Dewetting of surfactant solutions close to receding three–phase contact lines

Entnetzung von Tensidlösungen nahe zurückweichender Dreiphasenkontaktlinien
Zur Erlangung des akademischen Grades Doktor-Ingenieur (Dr.-Ing.)
Genehmigte Dissertation von Benedikt Benjamin Straub aus Hadamar
Tag der Einreichung: 10.11.2020, Tag der Prüfung: 12.01.2021

1. Gutachten: Prof. Dr. Steffen Hardt
2. Gutachten: Prof. Dr. Hans-Jürgen Butt
Darmstadt – D17

TECHNISCHE
UNIVERSITÄT
DARMSTADT

Fachbereich Maschinenbau

Dewetting of surfactant solutions close to receding three–phase contact lines
Entnetzung von Tensidlösungen nahe zurückweichender Dreiphasenkontaktlinien

Accepted doctoral thesis by Benedikt Benjamin Straub

1. Review: Prof. Dr. Steffen Hardt
2. Review: Prof. Dr. Hans-Jürgen Butt

Date of submission: 10.11.2020
Date of thesis defense: 12.01.2021

Darmstadt – D17

Bitte zitieren Sie dieses Dokument als:
URN: urn:nbn:de:tuda-tuprints-186174
URL: http://tuprints.ulb.tu-darmstadt.de/id/eprint/18617

“An expert is a person who has made all the mistakes that can be made in a very narrow field.” — Niels Bohr

Erklärung

Hiermit erkläre ich, dass ich die vorliegende Arbeit, abgesehen von den in ihr ausdrücklich genannten Hilfen, selbständig verfasst habe.

10.11.2020, Benedikt Benjamin Straub

Zusammenfassung

Das Be– und Entnetzungsverhalten von Tensidlösungen spielt eine wichtige Rolle in vielen natürlichen Prozessen und industriellen Anwendungen, wie z.B. industriellen Druck– und Beschichtungsprozesse. Ein genaues Verständnis des Be– und Entnetzungsverhaltens von Tensidlösungen ist wichtig, um diese Prozesse zu kontrollieren und zu optimieren. Vorangegangene Arbeiten zeigten einen großen Einfluss von Tensiden auf das Be- und Entnetzungsverhalten wässriger Lösungen. Dieser Einfluss ist ebenfalls für geringe Tensidkonzentrationen unterhalb der kritischen Mizellenkonzentration vorhanden und nimmt mit steigender Konzentration zu. Es wurde die Hypothese aufgestellt, dass Marangoni Kräfte nahe der bewegten Dreiphasenkontaktlinien für die Veränderung des Benetzungsverhaltens von wässrigen Tensidlösungen verantwortlich sind. Diese Hypothese konnte bisher nicht experimentell überprüft werden, da die Dynamik bzw. das Strömungsfeld von wässrigen Tensidlösungen nahe zurückschreitender Dreiphasenkontaktlinien bisher nicht gemessen wurde.

Aus diesem Grund wurde in dieser Arbeit das dynamische Entnetzungsverhalten von wässrigen Tensidlösungen nahe zurückschreitender Dreiphasenkontaktlinien in Abhängigkeit von der Tensidkonzentration untersucht und die bestehende Hypothese getestet. Dazu wurden zwei komplementäre experimentelle Aufbauten erstellt, die es ermöglichen, Strömungsfelder auf der 10 µm Skala nahe der sich bewegenden Dreiphasenkontaktlinie zu messen. Ein schnelles konfokales Laser–Scanning–Mikroskop wurde entwickelt und gebaut. Es basiert auf zwei anstatt der üblichen einen Rastereinheiten und kann zweidimensionale Bilder mit bis zu 1 kHz in horizontale und 200 Hz in vertikale Richtung aufnehmen. Damit ist es deutlich schneller als vergleichbare kommerzielle Mikroskope. Zusätzlich wurde die Methode der astigmatischen Partikelverfolgung angewendet, indem ein bestehendes kommerzielles Mikroskop modifiziert wurde. Da diese Methode im Vergleich zum gebauten konfokalen Mikroskop die direkte Messung von dreidimensionalen Strömungsfeldern ermöglicht, wurde diese zum Testen der Hypothese verwendet.

Die Messung der Strömungsfelder erfolgte nahe der zurückweichenden Dreiphasenkontaktlinie von Tropfen bestehend aus wässrigen Tensidlösungen mit variierenden Konzentrationen unterhalb der kritischen Mizellenkonzentration. Die Strömungsfelder wurden mit einer bestehenden hydrodynamischen Theorie für Wasser verglichen. Ich habe herausgefunden, dass insbesondere nahe der Luft/Wasser Grenzfläche des Tropfens im Bereich bis zu 112 µm entfernt von der bewegten Dreiphasenkontaktlinien die Strömungsfelder der Tensidlösungen von der zu erwarteten Strömung für reines Wasser abweichen. Die gemessenen Strömungsfelder lassen sich nur erklären, wenn die freie Oberfläche nicht als spannungsfrei angenommen wird. Die gemessene Spannung entlang der freien Oberfläche entspricht einer Marangoni Spannung, die durch eine räumlich variable Tensidkonzentration hervorgerufen wird. Diese Beobachtung entspricht der eingangs formulierten Hypothese, welche somit grundsätzlich verifiziert ist. Aus den Strömungsfeldern konnte die Marangoni Spannung und der Gradient der Oberflächenspannung entlang der freien Oberfläche berechnet werden. Beide Parameter nehmen mit steigender Tensidkonzentration zu. Obwohl die ermittelte Oberflächenkonzentration des Tensids nahe der Kontaktlinie weniger als 0.01 % von der Gleichgewichtskonzentration abweicht, hatte dies erkennbaren Einfluss auf die Strömungsfelder. Die gemessenen Effekte treten ebenfalls für absolute Tensidkonzentrationen kleiner als 1 ppm auf. Dies impliziert, dass selbst kleinste Verunreinigungen, welche häufig unvermeidbar sind, einen entscheidenden Einfluss auf das dynamische Entnetzungsverhalten von Flüssigkeiten haben.

Abstract

The wetting and dewetting behaviour of aqueous surfactant solutions is important for many natural processes and industrial applications like printing and coating processes. In order to control and optimize these processes, in–depth knowledge of the topic is required. Preliminary studies showed a significant influence of surfactants on the wetting and dewetting behaviour of aqueous solutions. This influence is also present for concentrations below the critical micelle concentration and increases with higher surfactant concentration. One hypothesis proposes that Marangoni effects close to the receding three–phase contact line of aqueous surfactant solutions are the cause for the altered dewetting behaviour. As of yet, this hypothesis could not be tested, since the dynamics and hence the flow field of aqueous surfactant solutions close to receding three–phase contact lines were not measured.

Therefore, in this work, the dynamic dewetting behaviour of aqueous surfactant solutions close to receding three–phase contact lines depending on the surfactant concentration was studied and the aforementioned hypothesis tested. For this purpose, two complementary experimental setups were developed making it possible to measure flow fields on the 10 µm scale close to receding three–phase contact lines. For one thing, a fast laser scanning confocal microscope was developed and built. It utilizes two instead of the usual one scan unit. Two–dimensional images can be recorded with a frame rate up to 1 kHz in the horizontal direction and up to 200 Hz in the vertical direction. Thus, it is significantly faster than comparable commercially available state–of–the–art microscopes. Additionally, astigmatism particle tracking velocimetry was used by modifying a commercial microscope. Since this method, in contrast to the confocal microscope, enables the direct measurement of three–dimensional flow fields, it was used to test the hypothesis.

This way, flow fields close to the receding three–phase contact line of drops consisting of aqueous surfactant solutions were measured with varying concentrations below the critical micelle concentration. The resulting flow fields were compared to an existing hydrodynamic theory for water. I discovered that especially close to the liquid/air interface of the drop at a distance of up to 112 µm from the three–phase contact line the flow fields of surfactant solutions differed from the expected flow field of water. The measured flow fields can only be explained if the free surface is not considered to be stress–free. This stress along the free surface corresponds to a Marangoni stress caused by a spatially differently distributed surfactant concentration. Thus, the initially presented hypothesis is verified. The Marangoni stress, as well as the gradient of surface tension along the free surface, were calculated based on the measured flow fields. Both parameters increase with increasing surfactant concentration. Even though the surface surfactant concentration close to the contact line only differs by 0.01 % from the equilibrium value, the observed influence on the flow fields is substantial. The measured effects occur even for absolute surfactant concentrations below 1 ppm. This indicates that even small impurities, which are in practice often unavoidable, have a significant influence on the dynamic dewetting behaviour of liquids.

Contents

List of Figures

List of Tables

Nomenclature

Latin symbols

Symbol	Units	Description
a	$\mathrm{mol\,m^{-3}}$	Activity
a_x	m	x–axis diameter of the particle image
a_y	m	y–axis diameter of the particle image
Ai		Airy function
A_{res}		Amplitude of the resonant scanner
b	m	Breadth
c	mol	Concentration
c_{abs}	ppm	Absolute concentration
d	m	Distance
d_{ad}	m	Distance between adsorption sides on the solid surface
$d_{ax,\,col}$	m	Axial resolution of the colloid
$d_{ax,\,e}$	m	Experimental axial resolution
$d_{ax,\,fwhm}$	m	Axial resolution using full width at half maximum
$d_{ax,\,t}$	m	Theoretical axial resolution
d_{fwhm}	m	Resolution calculated with the full width at half maximum
$d_{lat,\,col}$	m	Lateral resolution of the colloid
$d_{lat,\,e}$	m	Experimental lateral resolution
$d_{lat,\,fwhm}$	m	Lateral resolution using the full width at half maximum
$d_{lat,\,grid}$	m	Lateral resolution of the calibration grid
$d_{lat,\,t}$	m	Theoretical lateral resolution
d_{ph}	m	Pinhole diameter
$d_{slice,\,e}$	m	Experimental optical slice thickness
$d_{slice,\,t}$	m	Theoretical optical slice thickness
d_{Ab}	m	Abbe resolution limit
d_{Ra}	m	Rayleigh resolution limit
d_{Sp}	m	Sparrow resolution limit
D	$\mathrm{m^2\,s^{-1}}$	Diffusion coefficient
D_{ph}	AU	Modified pinhole diameter

Continued on next page

Latin symbols continued from previous page

Symbol	Units	Description
e		Euler's number
f_0	Hz	Characteristic frequency
f	m	Focal length
f_{cam}	Hz	Frequency of the camera signal
f_{galvo}	Hz	Frequency of the galvanometer motion
f_{hyp}		Hyperbolic function
f_{res}	Hz	Frequency of the resonant motion
f_{Mo}		Function used in Moffatt's theory
F_c	N	Capillary force
F_{xz}	m	Position of the xz–focal plane
F_{yz}	m	Position of the yz–focal plane
g	$\mathrm{m\,s^{-2}}$	Gravitational constant
H	deg	Contact angle hysteresis
I		Intensity
I_0		Maximum intensity
J_1		First–order Bessel function
k		Correction factor
k_B	$\mathrm{J\,K^{-1}}$	Boltzmann constant
l	m	Length
l_c	m	Capillary length
L	m	Length
L_{dec}	m	Decay length of the surface tension
L_{non}	m	Non–equilibrium region along liquid/air interface
L_M	m	Microscopic length
M		Magnification
M_d		Relative magnitude of the deviation
n		Index of refraction
N_f		Frame number
N_{lines}		Number of lines
NA		Numerical aperture
$\mathrm{NA_{cond}}$		Numerical aperture of the condenser
p		Fitting parameter
Pe_α		Peclet number calculated with the diffusion length α
r	m	Radius
R	$\mathrm{J\,mol^{-1}\,K^{-1}}$	Ideal gas constant
s_1		Parameter

Continued on next page

Latin symbols continued from previous page

Symbol	Units	Description
S	$\mathrm{N\,m^{-1}}$	Spreading parameter
t	s	Time
t_{dwell}	s	Dwell time
t_A	s	Advective time scale
t_D	s	Diffusive time scale
t_R	s	Ratio between diffusive and advective time scales
T	K	Temperature
u	$\mathrm{m\,s^{-1}}$	Velocity component in x–direction
U	$\mathrm{m\,s^{-1}}$	Contact line velocity
v_p	$\mathrm{m\,s^{-1}}$	Velocity component parallel to the liquid/air interface
$\vec{v}$	$\mathrm{m\,s^{-1}}$	Velocity vector
V	$\mathrm{m\,s^{-1}}$	Surface velocity
w	$\mathrm{m\,s^{-1}}$	Velocity component in z–direction
x	m	Cartesian coordinate
x_{Int}	m	Coordinate axis along the liquid/air interface
y	m	Cartesian coordinate
y_{PS}	m	Coordinate axis of the piezoelectric stage
z	m	Cartesian coordinate

Concluded

Greek symbols

Symbol	Units	Description
α	m	Diffusion length
β	deg	Diffraction angle
γ	$\mathrm{N\,m^{-1}}$	Interfacial tension
γ_0	$\mathrm{N\,m^{-1}}$	Interfacial tension of the solvent
γ_{rec}	$\mathrm{N\,m^{-1}}$	Interfacial tension of the receding side of the drop
γ_{Bulk}	$\mathrm{N\,m^{-1}}$	Interfacial tension of the bulk liquid
γ_L	$\mathrm{N\,m^{-1}}$	Interfacial tension of the liquid/air interface
γ_S	$\mathrm{N\,m^{-1}}$	Interfacial tension of the solid/air interface
γ_{SL}	$\mathrm{N\,m^{-1}}$	Interfacial tension of the solid/liquid interface
γ_{Tear}	$\mathrm{N\,m^{-1}}$	Interfacial tension of the liquid tear

Continued on next page

Greek symbols continued from previous page

Symbol	**Units**	**Description**
Γ	$\mathrm{mol\,m^{-2}}$	Surface excess
δ		Reduced capillary number
Θ	deg	Contact angle
Θ_{adv}	deg	Advancing contact angle
$\Theta_{adv,\ s}$	deg	Static advancing contact angle
Θ_{rec}	deg	Receding contact angle
$\Theta_{rec,\ s}$	deg	Static receding contact angle
Θ_D	deg	Dynamic contact angle
Θ_M	deg	Microscopic contact angle
Θ_S	deg	Static contact angle
λ	m	Light wavelength
λ_{em}	m	Emission light wavelength
λ_{ex}	m	Excitation light wavelength
λ_m	m	Median light wavelength
μ	$\mathrm{kg\,m^{-1}\,s^{-1}}$	Dynamic viscosity
ν	$\mathrm{m^2\,s^{-1}}$	Kinematic viscosity
ρ	$\mathrm{kg\,m^{-3}}$	Density
ρ_{ps}	$\mathrm{kg\,m^{-3}}$	Density of polystyrene
τ	$\mathrm{N\,m^{-2}}$	Shear stress
φ	deg	Phase shift
Φ	deg	Angle of the polar coordinate system
ψ	deg	(Half)angular aperture of the objective

Concluded

Dimensionless groups

Symbol	**Name**	**Definition**	**&**	**Meaning**
Ca	Capillary number	$Ca = \frac{\mu\ u}{\gamma}$	$\widehat{=}$	$\frac{\text{viscous forces}}{\text{surface tension forces}}$
Pe	Péclet number	$Pe = \frac{u\ l}{D}$	$\widehat{=}$	$\frac{\text{advective transport rate}}{\text{diffusive transport rate}}$

Continued on next page

Dimensionless groups continued from previous page

Symbol	Name	Definition	&	Meaning
Re	Reynolds number	$Re = \frac{u\,l}{\nu}$	$\widehat{=}$	$\frac{\text{inertial forces}}{\text{viscous forces}}$
				Concluded

Mathematical symbols

Symbol	Units	Description
∇	m^{-1}	Gradient
$\nabla_{\parallel}$	m^{-1}	Gradient parallel to the liquid/air interface
$\nabla_{\perp}$	m^{-1}	Gradient perpendicular to the liquid/air interface
Δ		Difference
$\lvert \bullet \rvert$		Vector length
		Concluded

Subscripts

Subscript	Description
air	Air
d	Deviation
e	Experiment
i	Ith order or parameter
Im	Coordinate system of the image
Ob	Objective
Oc	Ocular
t	Theory
$water$	Water
x	x–direction
y	y–direction
	Concluded

Abbreviations

Abbreviation	Description
2D	Two–dimensional
3D	Three–dimensional
AIP	American Institute of Physics
APTV	Astigmatism particle tracking velocimetry
AU	Airy unit
C_8E_3	Octyl triglycole
$C_{12}E_5$	Dodecyl pentaglycole
CC BY 4.0	Creative Commons Attribution 4.0 International license
CMC	Critical micelle concentration
CMOS	Complementary metal–oxide–semiconductor
CTAB	Cetrimonium bromide
e.g.	For example
FWHM	Full width at half maximum
HDT	Hydrodynamic theory
i.e	That is
LSCM	Laser scanning confocal microscope
MKT	Molecular–kinetic theory
MPIP	Max Planck Institute for Polymer Research
NA	Numerical aperture
O1	Objective 1
O2	Objective 2
O3	Objective 3
O	Oxygen
OH	Hydroxide
PDMS	Polydimethylsiloxane
PIV	Particle image velocimetry
PSF	Point spread function
PTV	Particle tracking velocimetry
vs.	Versus
VI	Virtual Instrument
	Concluded

1. Introduction and Motivation

Wetting phenomena play a crucial role in our daily life as well as in natural and industrial processes. Raindrops running down a window or beads of dew sitting on a leaf are only two everyday examples of wetting. How the liquid, e.g. the rain, disperses and spreads on the solid surface depends on the wettability of the solid. In order to quantify this attribute, the so–called contact angle, which is defined as the angle between the wetted surface of the solid and the free surface of the liquid drop, is used. If the solid surface has high wettability, the liquid drop spreads on a large area of the solid surface and the contact angle is small. However, if the solid surface has a low wettability, only a small area of the solid is wetted and the liquid drop has a large contact angle.

Knowledge about the spreading behaviour of liquids on solid surfaces is used in agriculture to minimize the necessary amount of pesticides while maintaining high coverage of the leaves [189]. The coating industry needs profound knowledge of wetting as well to create uniform coatings [25] e.g. of car bodies. Further examples of industrial processes relying on wetting phenomena are cleaning, printing or oil recovery processes [27, 101].

Wetting phenomena are differentiated into static and dynamic wetting. Static wetting describes all phenomena with the liquid in a local energy minimum and thus with no movement. If the liquid is moving, it is described by the field of dynamic wetting. This means that the three–phase contact line, i.e. the line where all three phases (liquid, solid, gas) meet, is moving. In this case, a liquid has two different contact angles: The advancing contact angle where the solid surface is wetted by the liquid and the receding contact angle where the solid surface is dewetted by the liquid. In dynamic wetting, two wetting mechanisms are further differentiated: Spontaneous and forced wetting.

In the case of spontaneous wetting, also referred to as spreading, a drop of liquid is gently placed on top of a solid substrate. As long as the interfacial forces are not in equilibrium, the drop spreads further until an equilibrium state is reached. Next to ambient conditions like temperature and humidity, the acting interfacial forces during dynamic dewetting depend on the properties of the solid surface and the liquid.

In the case of forced wetting, an external force is applied deforming the interfacial area. This leads either to an advancing or receding contact line, i.e. the liquid moves over the solid. An example is the immersion and retraction of a plate in and out of a liquid pool. At a critical dewetting velocity the receding contact angle reaches an angle of 0° and film formation starts. This means that the removed plate is covered by a liquid film with a constant film height [55, 107]. This knowledge is used in modern dip coating processes to reach uniform coatings with extremely thin layers [25].

The dynamic wetting of simple one–component liquids has been intensively studied for both mechanisms [27, 164]. Hereby, the correct measurement and description of contact angles played a crucial role and are still a topic of current research [27, 61, 68]. Two main theoretical approaches exist to describe moving contact lines: The molecular kinetic theory [24, 39] describes the movement of the contact line based on the kinetic energy of liquid molecules. In contrast, the hydrodynamic theory [46, 88, 177] describes the movement based on fluid–mechanics, i.e. the Navier–Stokes equation [106]. Several theories combine both approaches [32, 50, 138].

However, the dynamic wetting of multi–component liquids, e.g. surfactant solutions, is less explored [27, 101, 115]. Surfactants adsorb to the free surface of liquids lowering the surface tension [33, 147]. Thus, surfactants change the wetting behaviour of liquids. For example, a change of the hydrodynamic boundary condition at the free surface of the liquid was observed [5, 38, 118]. Due to the addition of surfactants, changes to the surface flow [16] and bulk flow [102, 121] of liquids were reported. Furthermore, the spontaneous wetting behaviour of liquids, e.g. in terms of wetting speed and wetted area, is adaptable with surfactants [27, 34, 90, 168, 179].

Especially the forced dewetting behaviour of surfactant solutions is important for industrial processes, e.g. printing and coating, since surfactants can be used to adapt the wetting behaviour of the liquid. For example, the addition of surfactants increases the thickness of the coated layer on the solid surface [143, 157]. Motivated by the industrial importance of the problem several groups investigated the forced wetting behaviour of different surfactant solutions on various solids [69, 70, 71, 83, 84, 85, 112, 116, 175]. They all found that the critical speed for film formation and the dynamic contact angle decrease for increasing surfactant concentration.

Those macroscopic observations indicate that changes to the wetting behaviour of liquids due to surfactants occur on the microscopic scale as well. However, the dynamics close to the receding contact line are unknown. Fell et al. [69] proposed the hypothesis that the newly created liquid surface at the receding contact line is initially free of surfactants. They present two possible mechanisms to equilibrate the surface surfactant concentration of the new liquid/air interface with the bulk concentration. Either molecules diffuse from the bulk towards the liquid/air interface or molecules that were adsorbed to the solid are directly transferred to the newly created liquid/air interface at the contact line. The authors assume that the latter effect is negligible and thus assume diffusion to be the dominating equilibration mechanism. The result of this equilibration process is a surface tension gradient along the free surface resulting in a Marangoni stress. The authors propose that this Marangoni stress opposes the surface flow and is the reason for possible changes in the flow field and the reduction of the contact angle.

However, the hypothesis could not be tested, since the dynamics of surfactant solutions close to receding contact lines are still unknown. The reason for this is the lack of suitable experimental methods with sufficient spatial and temporal resolution. Henrich [84] built an experimental setup that enables measurements close to locally stable receding contact lines. Here, a liquid drop is pinned to a specific position while the solid substrate is moved underneath it. An inverted confocal laser scanning microscope was used to measure the dynamics close to the contact line. Yet, Henrich was limited by the insufficient axial scanning capacities of the confocal microscope and the dynamics close to receding contact lines of surfactant solutions remained unknown.

Therefore, the aim of my thesis was to build a suitable experimental setup for measuring flow fields close to the receding contact lines of moving drops. I built two complementary experimental setups for this purpose. The first setup is a custom–built fast re–scan laser scanning confocal microscope and the second one is an astigmatism particle tracking velocimetry (APTV) setup. Both setups were successfully built and have sufficient spatial and temporal resolution to measure the required flow fields. Due to practical reasons, the APTV setup was used to measure the flow fields and test the aforementioned hypothesis.

I measured flow fields of aqueous solutions of the nonionic surfactants dodecyl pentaglycole ($\mathrm{C}_{12}\mathrm{E}_5$) and octyl triglycole ($\mathrm{C}_8\mathrm{E}_3$) with different concentrations closer than 100 µm to the contact line. The concentrations were varied from zero to 30 % of the critical micelle concentration (CMC) of the surfactant. Since the size of the surfactant molecules differs significantly between the used surfactants, the CMCs differed by two orders of magnitude. Hence, the absolute amount of surfactant molecules differed considerably between the aqueous solutions. Even so, the relative concentration regarding the CMC (% CMC) was identical. This enabled studying the influence of the absolute amount of surfactant molecules and the influence of the relative concentration (% CMC) on the dynamics close to receding contact lines. In order to compare the measured flow fields of surfactant solutions with the predicted flow fields for water according to the hydrodynamic theory of Moffatt [127], smooth hydrophobized glass substrates were used as solid substrates. The deviation between the flow fields showed the influence of surfactants on wetting behaviour. The results were used to determine the existence of a Marangoni stress and thus to test and judge the aforementioned hypothesis [69].

The structure of this work is as follows: At first, fundamentals of wetting and surfactants, microscopy and measurement of fluid velocity are presented. Following, the custom–built confocal microscope is presented as well as the built APTV setup. Subsequently, the methods are compared regarding their capacities to measure flow fields close to receding three–phase contact lines. The flow field measurements of aqueous surfactant solutions are presented in chapter 4. Based on this data, the aforementioned hypothesis, which tries to explain the dynamics close to receding three–phase contact lines of surfactant solutions, is examined. Finally, the results are summarized and an outlook on further studies is presented.

2. State of the art

In this chapter important fundamentals for the present work are presented. In the beginning, the basics of static and dynamic wetting as well as theoretical approaches to describe wetting are presented. Thereafter, properties of surfactants and their influence on forced dewetting are shown. Then, a short introduction to optical resolution and confocal microscopy is given. Finally, techniques to measure the fluid velocity are presented.

2.1. Static wetting

The study of how a liquid spreads on a solid (or liquid) surface, is referred to as wetting [50]. When a liquid drop is placed on top of a solid surface, the liquid spreads on the surface. Depending on the properties of the solid, liquid, and gas, the drop either covers the surface completely (contact angle $\Theta = 0$) or takes over a static equilibrium state with a finite static contact angle Θ. In the latter case, a three–phase contact line is formed where all three phases (solid, liquid, gas) are in contact (Figure 2.1 (a)). Thus, wetting describes the interplay between three phases, of which at least two are fluids [33].

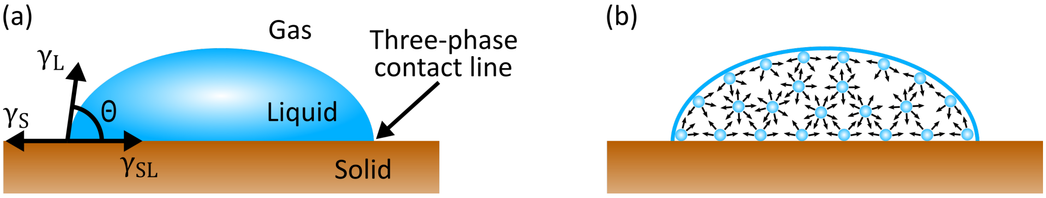

Figure 2.1.: (a) Sketch of a drop wetting a solid substrate with a finite contact angle Θ. (b) The reason for the dome shape of drops is the surface tension of the liquid which is caused by unbalanced forces acting on molecules at the surface.

The reason for the spherical shape of small droplets and bubbles is the surface tension of the liquid. The molecules in the midst of the bulk of a pure liquid interact with their surrounding molecules and the net force acting on these molecules is zero (Figure 2.1 (b)). However, molecules at the surface of the liquid are only to one side surrounded by liquid molecules and therefore, the net force acting on the surface molecules is directed inwards, i.e. pulling the molecules inwards. Since the energetic state of these surface molecules is energetically unfavourable, the liquid minimizes its surface area leading to the spherical shape of small drops. The surface tension can be considered the force that is required to bring a molecule from the bulk to the surface, i.e. to increase the surface area. A good example is the difference between dry and wet hair. Whereas dry hair has volume, wet hair sticks together. The term surface tension is used to describe the interfacial tension between a liquid and gas. Interfacial tensions are present at solid/liquid, solid/gas, liquid/gas and liquid/liquid interfaces.

In an ideal configuration (thermodynamic equilibrium and an ideal solid that is chemically homogeneous, rigid and flat to an atomic scale) the contact angle can be related to the interfacial tensions of the solid γ_S, liquid γ_L and solid/liquid γ_{SL} via the Young's equation [191]

$$\gamma_L \ \cos(\Theta) = \gamma_S - \gamma_{SL}. \tag{2.1}$$

Figure 2.2 shows different wetting behaviours of drops on surfaces which can be explained by the Young's equation. In the case $\gamma_S > \gamma_{SL}$ the contact angle has to be smaller than 90°. This is called a hydrophilic material behaviour. If the contact angle is 0° the surface is completely wetted by the liquid. A hydrophobic behaviour is present for $\gamma_S < \gamma_{SL}$ and a contact angle larger than 90°. The maximum reachable contact angle is 180°

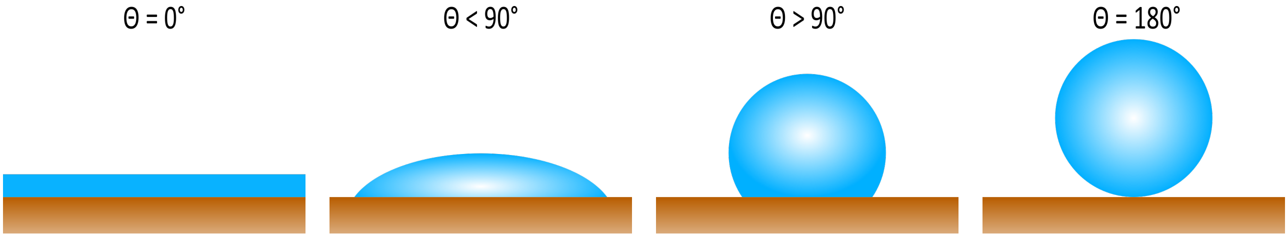

Figure 2.2.: Drops sitting on different substrates with different contact angles.

In non–equilibrium conditions the spreading parameter S is used to describe whether a liquid is completely wetted ($\Theta = 0°$) or if the liquid forms a finite contact angle. The spreading parameter is a measure of whether the dry (γ_S) or wetted $(\gamma_{SL} + \gamma_L)$ state of a substrate is energetically more favourable and is defined as [33, 50, 74]

$$S = \gamma_S - (\gamma_{SL} + \gamma_L). \tag{2.2}$$

If $S < 1$ the substrate is partially wetted by the liquid and a finite contact angle is formed. The substrate is completely wetted if $S > 1$.

2.2. Dynamic wetting and dewetting

Many natural phenomena, like raindrops running down a window, show a dynamic wetting and dewetting behaviour. A drop running down a tilted plate has two different dynamic contact angles: the advancing contact angle Θ_{adv} and the receding contact angle Θ_{rec} (Figure 2.3 (a)). In the following, contact angle measurement techniques, the contact angle hysteresis, as well as the dynamic dewetting behaviour of liquid films and drops, are presented.

2.2.1. Measurement of contact angles

The characterization and measurement of contact angles are of crucial importance for describing wetting phenomena. Several different definitions of contact angles and measurement techniques exist, see [33, 50, 67, 92, 192].

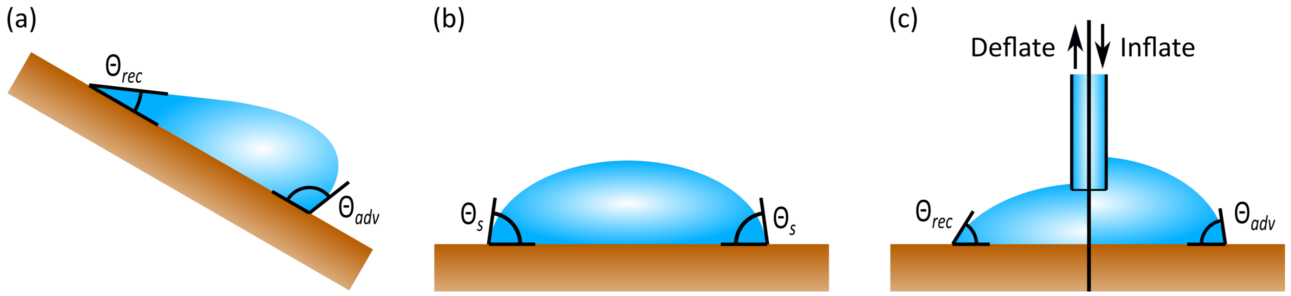

Figure 2.3.: (a) Sketch of a drop running down a tilted plate with the dynamic advancing Θ_{adv} and receding contact angle Θ_{rec}. (b) Measurement of the static contact angle Θ_s. (c) Measurement of the static advancing $\Theta_{adv,\ s}$ and receding $\Theta_{rec,\ s}$ contact angles by inflating or deflating of a sessile drop an a substrate.

The static contact angle is measured by placing a drop on a substrate (Figure 2.3 (b)). The light source is placed behind the drop and a picture of the drop is taken from the front. The measured contact angle is called the static contact angle Θ_s. However, this static contact angle is not the contact angle used in the Young's equation since this equation is only valid in an ideal configuration, see [104] for a detailed description.

The advancing Θ_{adv} and receding Θ_{rec} contact angles can be measured by inflating and deflating a sessile drop on a substrate (Figure 2.3 (c)). For example, a syringe pump is used to control the flow rate of the added or removed liquid from the drop. This type of measurement is called the sessile drop method, see [92, 103, 104]. If the droplet is deflated, its volume decreases. The angle just before the contact line starts to recede, due to the decreasing volume, is the static receding contact angle $\Theta_{rec,\ s}$. The angle just before the contact line starts to advance while inflating the drop is defined as the static advancing contact angle $\Theta_{adv,\ s}$. Thus, the static advancing $\Theta_{adv,\ s}$ and receding $\Theta_{rec,\ s}$ contact angles are defined as the angles just before the contact line starts to move, i.e. for zero contact line velocity. The dynamic advancing Θ_{adv} and receding Θ_{rec} contact angles are measured during the movement of the contact line. These dynamic angles depend on the speed of the contact line, see Figure 2.4 in section 2.2.2.

Another option to measure the static contact angles $\Theta_{adv,\ s}$ and $\Theta_{rec,\ s}$ is the tilted plate method [117]. A drop is placed on top of a plate and the tilt angle of this plate is increased until the drop starts to move (Figure 2.3 (a)). The contact angles just as the drop starts to move are the static advancing and receding contact angle. The tilt angle of the plate is called the roll of angle.

In general, the contact angle depends on the length scale at which it is measured [27]. Due to the bending of the meniscus, the microscopic contact angle (nanometre–scale) can differ significantly from the macroscopic contact angle (millimetre–scale), see [21, 27] and section 2.3.2. The above–described measurement techniques measure macroscopic angles and if not differently stated, the term contact angle in this work refers to the macroscopic contact angle.

2.2.2. Contact angle hysteresis

The static advancing contact angle $\Theta_{adv,\ s}$ is necessarily larger than the static receding contact angle $\Theta_{rec,\ s}$ (Figure 2.4). The difference between those angles at zero contact line velocity is called the contact angle hysteresis [33, 61]

$$H = \Theta_{adv,\ s} - \Theta_{rec,\ s} > 0^\circ \tag{2.3}$$

The reason for this is that the observed system is not ideal. In an ideal system with an ideal solid that is chemically homogeneous, rigid, and flat to an atomic scale without being perturbed by chemical interactions or by vapour or liquid adsorption, the receding $\Theta_{rec,\ s}$ and advancing $\Theta_{adv,\ s}$ would be equal [25, 61, 67]. However, solid surfaces have a specific roughness and the surface can be chemically or structurally heterogeneous. This leads to pinning of the contact line and thus to the described hysteresis. Because of its importance, the contact hysteresis has been intensively studied, e.g. [23, 25, 33, 61, 67, 68, 93, 192].

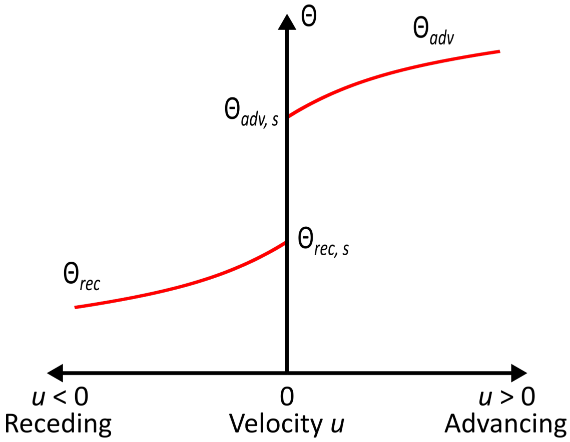

Figure 2.4.: Velocity dependence of the advancing and receding contact and contact angle (after [33, 61])

The dynamic contact angles depend on the velocity, i.e. the speed of the contact line [25, 33, 61]. If the absolute velocity of the advancing contact line is increased, the dynamic advancing contact angle is increased as well (Figure 2.4). The opposite is true for the receding contact angle. If the absolute velocity of the receding contact line is increased, the receding contact angle decreases.

Besides the velocity u, the contact angle also depends on the dynamic viscosity μ and the surface tension of the liquid γ_L [33]. These parameters are combined in the capillary number

$$Ca = \frac{\mu\ u}{\gamma_L} \tag{2.4}$$

which is the ratio between the viscous and surface forces.

2.2.3. Dewetting behaviour of liquid films and drops

For high capillary numbers, e.g. high velocities, the receding contact angle is 0° (Figure 2.4). In the case of a plate being immersed and then removed from a liquid pool, the solid substrate, i.e. the plate, is covered by a liquid film with a specific film thickness (Figure 2.5 (a)). Those films are called Landau–Levich–Derjaguin films [55, 107]. The thickness of the film can be controlled by the viscosity, density, and surface tension of the liquid. This is used in industry to create uniform coatings.

In the case of dewetting of a complex liquid (e.g. liquid with surfactants) with low capillary numbers, it is possible to deposit a monolayer (monomolecular film) of the surfactants on the solid surface [26]. This film is called Langmuir–Blodgett film [26, 73, 75]. The dewetting velocity must be closely monitored so that the deposited film stays in equilibrium. Otherwise, the monolayer would collapse [80].

Similar observations were made for the dewetting behaviour of drops [109, 139]. At low capillary numbers the drops have a classical rounded shape while moving (Figure 2.5 (b)). For higher capillary numbers the drops become longer and thinner but remain the same height. At some point, the drops depart from their rounded shape and develop a corner at the receding side. For even higher capillary numbers, i.e. velocities above the maximum speed of dewetting, the corner changes into a cusp, and small droplets are left behind.

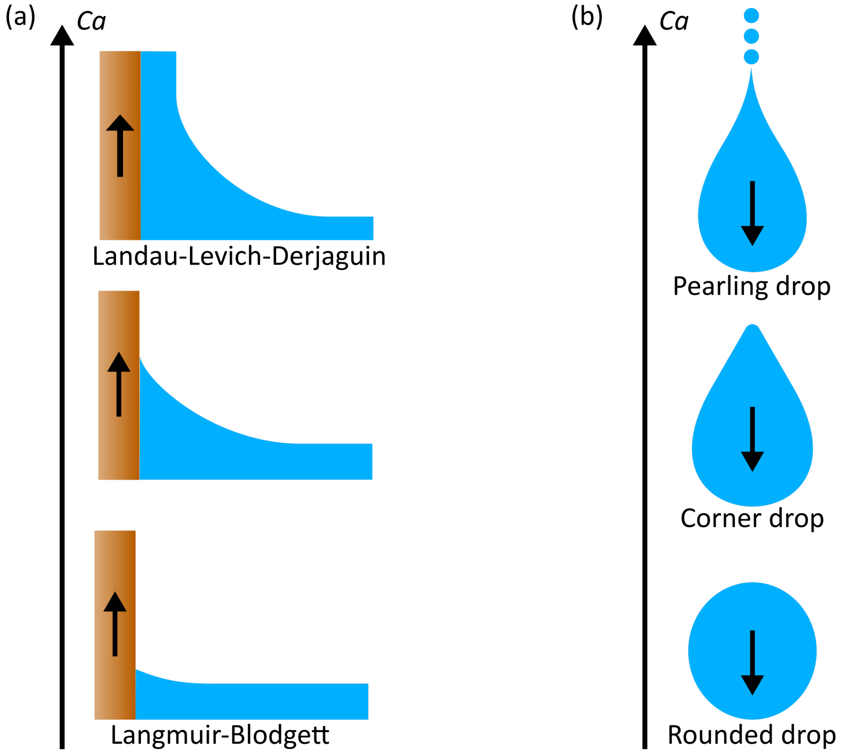

Figure 2.5.: (a) Different dewetting behaviours of liquid films and (b) drops running down a plate depending on their capillary numbers.

2.2.4. Wetting mechanism

Dynamic (de)wetting can be split into spontaneous and forced wetting.

Spontaneous wetting is also called spreading. A liquid that is placed on a solid takes a thermodynamic equilibrium shape without externally imposed forces. The contact line moves until an equilibrium state is reached.

In forced (de)wetting an external force is applied which results in a deformation of the interfacial area and thus in wetting or dewetting, e.g. the sessile drop method from section 2.2.1. Forced (de)wetting plays a crucial role in many industrial processes like coating and printing. By controlling the contact line velocity or the properties of the liquid and substrate, different (de)wetting behaviours are achievable. Forced dewetting of drops consisting of aqueous surfactant solutions is the subject of this work.

2.3. Modeling

In this section, theories are presented that describe the movement of the three–phase contact line. These theories are the molecular–kinetic theory (MKT) and the hydrodynamic theory (HDT). Each of these theories is based on a theoretical system: either on fluid–mechanics or on the kinetic energy of liquids [21]. However, none of these models can describe the movement of the contact line on all length scales.

2.3.1. Molecular–kinetic theory

The molecular–kinetic model, developed by [24, 39], describes the motion of the contact line by the process of attachment or detachment of liquid molecules from or to the solid surface [21] (Figure 2.6). If the adsorption and desorption of liquid molecules to or from the solid surface is in equilibrium, the contact line is static with no velocity. If this equilibrium is disturbed, the contact line moves. If more liquid molecules adsorb to the solid surface, the contact line advances. On the other hand, if more liquid molecules desorb from the solid, the contact line recedes. Thus, the disturbance of the ad– and desorption equilibrium defines the contact line motion. The MKT model divides the problem area into two length scales: the molecular scale where the adsorption and desorption process occurs and the macroscopic length scale where the effects are seen. The contact angle is assumed to be the same on the macroscopic and molecular length scales. The contact line velocity can be calculated with

$$U = 2 f_0 \, d_{ad} \, \sinh\left(\frac{\gamma_L \left(\cos\left(\Theta_S\right) - \cos\left(\Theta_D\right)\right) \, d_{ad}^2}{2 \, k_B \, T}\right) \tag{2.5}$$

where f_0 is the characteristic frequency, d_{ad} the distance between the adsorption sides on the solid surface, γ_L the surface tension of the liquid, Θ_S the static contact angle (contact angle for zero velocity), Θ_D the dynamic contact angle (either the advancing Θ_{adv} or receding Θ_{rec} contact angle), k_B the Boltzmann constant and T the absolute temperature [21].

Since the MKT theory describes wetting only on a molecular length scale, no hydrodynamic effects, which occur on a larger length scale, are taken into account. The dissipation arises from the friction due to the moving contact line. Viscous dissipation due to the confined flow of the liquid is ignored [54].

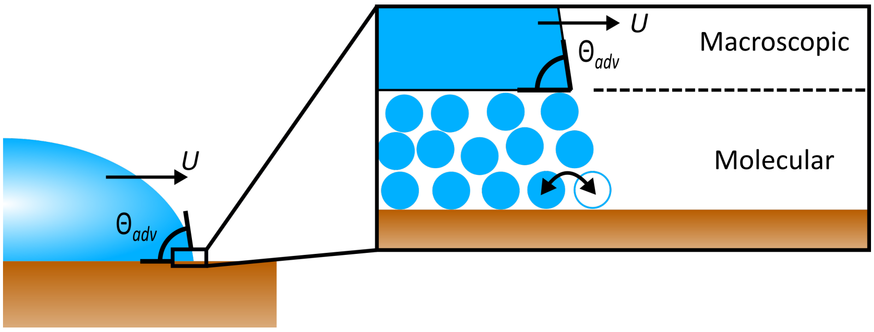

Figure 2.6.: The molecular kinetic theory describes the movement of the contact line by adsorption and desorption of liquid molecules to the solid surface on a molecular level [33]. Model sketches after [21].

2.3.2. Hydrodynamic theory

Early hydrodynamic studies and approaches could not describe the flow close to moving three–phase contact lines physically correct. Experimental studies neglected viscous forces near the contact line while evaluating their data, e.g. West (1911) [182], Yarnold (1938) [190], Bikerman (1950) [19], Schwartz (1964) [155]. Creeping flow analysis of a wedge–shaped liquid with a moving solid shows singularity effects, e.g. Moffatt (1964) [127], Bhattacharji (1965) [18], Bataille (1965) [14]. The reason for the singularity is the conflict between a moving contact line and the standard no–slip boundary condition between a solid and a liquid. The results are unbounded shear stresses, pressure, and viscous dissipation at the contact line and an infinite force that is exerted by the liquid on the solid [88]. Several approaches to deal with the singularity are available. One option is to exclude the microscopic region from hydrodynamic considerations [81, 177]. It is also possible to allow slippage of the liquid with respect to the solid, i.e. the no–slip boundary is relaxed [46, 61, 88].

The simplest form of the hydrodynamic solution is called the Cox–Voinov law [46]. This model describes the wetting behaviour by considering the viscous flow dissipation close to the three–phase contact line and allowing slippage of the liquid with respect to the solid [21, 46, 66, 177]. The general idea is that changes in the macroscopic observable contact angle occur due to the viscous bending of the liquid/gas interface on a mesoscopic length scale. The microscopic contact angle Θ_M is assumed to depend on short–ranged intermolecular forces and to be equal to the contact angle Θ_S for zero velocity. Thus, the model divides the problem into three length scales with different contact angles (Figure 2.7). The Cox–Voinov law [46] can be written in terms of the capillary number as

$$\Theta_D^3 = \Theta_M^3 \pm 9\, Ca \ln\left(\frac{L}{L_M}\right), \; \Theta_M = \Theta_S \tag{2.6}$$

where L and L_M are macroscopic and microscopic length scales [21]. The microscopic contact angle is assumed to be equal to the static macroscopic contact angle. The second term in equation 2.6 is positive for advancing contact lines and negative for receding contact lines.

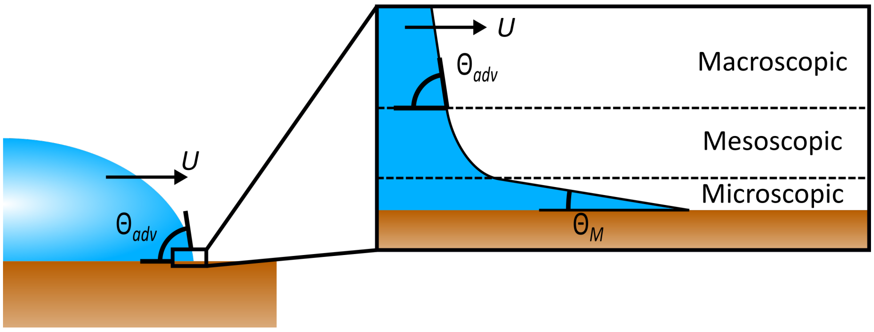

Figure 2.7.: The hydrodynamic model divides the problem into three length scales and describes the contact line motion within the wedge of the liquid with viscous flow dissipation [21, 46, 66, 177]. Model sketches after [21].

The model is valid for capillary numbers and Reynolds numbers less than one and is most satisfactory in a small velocity regime [22, 138]. The Reynolds number Re is defined as the ratio between inertial forces and viscous forces [145]

$$Re = \frac{u\,l}{\nu} \tag{2.7}$$

where u is the velocity of the liquid, ν is the kinematic viscosity of the liquid and l is a characteristic length. The Reynolds number can be used to predict whether a flow is laminar or turbulent. Above a critical value of the Reynolds number the flow is turbulent and below the critical value the flow is laminar [106, 140]. The critical value depends on the specific problem properties.

A main drawback of the hydrodynamic theory is that it neglects characteristics of the solid surface [46, 136, 137]. Based on the above–described model, further hydrodynamic theories were developed that take additional boundary conditions into account, e.g. Shikmurzaev [160, 161] and Billingham [20, 100]. In addition, combined models were developed to overcome the individual restrictions of the HDT and MKT theory, e.g. Petrov and Petrov [138] and Brochard–Wyart and de Gennes [32, 50].

Although equation 2.6 was derived for advancing contact lines, it is also applicable to receding contact lines. Eggers [63, 64] and Snoeijer [163] derived an approximate solution for receding contact lines for small Θ_S and the contact angle follows

$$\frac{\Theta_D}{\Theta_S} = \frac{2^{\frac{2}{3}}\delta^{\frac{1}{3}}}{Ai\left(s_1\right)}\frac{dAi\left(s_1\right)}{dx}. \tag{2.8}$$

Here, Ai is the Airy function and $\delta = 3Ca/\Theta_S^3$ is a reduced capillary number. The parameter s_1 is the largest root of [63, 64, 163]

$$\frac{2}{\Theta_S\delta^{\frac{1}{3}}} + \frac{2^{\frac{2}{3}}}{Ai\left(s_1\right)}\frac{dAi\left(s_1\right)}{dx} - \frac{2^{\frac{1}{6}}\exp^{\frac{-1}{3s_1}}\Theta_S}{3\pi Ai^2\left(s_1\right)L_M} = 0 \tag{2.9}$$

with the length of the microscopic regime L_M and the static contact angle at zero velocity Θ_S are adjustable parameters.
All length scales of equations 2.8 and 2.9 are rescaled with the capillary length

$$l_c = \sqrt{\frac{\gamma_L}{\Delta\rho g}}. \tag{2.10}$$

Here $\Delta\rho$ is the density difference between the liquid and the surrounding gas and g is the gravitational constant. The capillary length is used to determine whether surface or gravitational forces are dominant. In systems that are smaller than the capillary length, e.g. a drop with a radius $r < l_c$, surface forces dominate. If the system is larger than the capillary length, e.g. a drop with a radius $r > l_c$, gravitational forces dominate and surface forces become less significant. The capillary length is often a convenient reference or characteristic length for wetting problems.

Moffatt's theory

Moffatt [127] provided one of the first hydrodynamic theories. Although it was shown that his theory fails close to the contact line on the microscopic level [88], the solution is still valid on the macroscopic level. The measured flow fields in this work have a distance of around 10 µm to the contact line. Thus, singularity effects at the contact line have a negligible influence on the flow field. Therefore, Moffatt's theory can be used to evaluate the measured flow fields and agrees with the other theory solutions in the outer region. The derivation of the solution can be found in [88, 127]. In general, Moffatt's theory is based on the creeping flow model, thus it is only valid for $Re \ll 1$. In the following, his solution for the problem geometry shown in Figure 2.8 (a) is presented without its derivation.

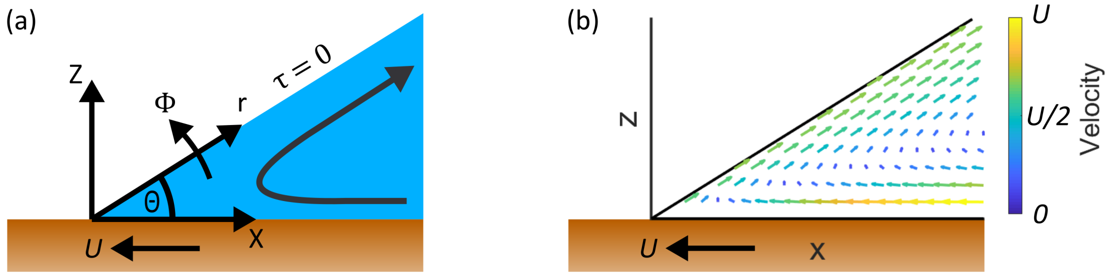

Figure 2.8.: (a) Geometry of the problem with polar and Cartesian coordinate systems, contact angle Θ, velocity of the solid U, stress free liquid/air interface $\tau = 0$, and bulk streamline. (b) Calculated velocity profile for the problem geometry of (a) after Moffatt [127].

The shown problem geometry consists of a plate that is withdrawn from a liquid pool. It is assumed that the free surface of the liquid is straight and the liquid has the form of a wedge. The solid moves with a constant velocity U, the free surface of the liquid is stress–free and the liquid has a distinct contact angle Θ. The theory is written in polar coordinates and the axis orientation is given in Figure 2.8 (a). The solution for the fluid velocity components is given by

$$u = U \; f'_{Mo} \left(\Phi \right) , \quad w = -U \; f_{Mo} \left(\Phi \right) \tag{2.11}$$

with

$$f_{Mo} \left(\Phi \right) = \frac{\Phi \cos \left(\Phi \right) \sin \left(\Theta \right) - \Theta \cos \left(\Theta \right) \sin \left(\Phi \right)}{\sin \left(\Theta \right) \cos \left(\Theta \right) - \Theta} . \tag{2.12}$$

Thus, the necessary input parameters to calculate the solution are the contact line velocity U and the contact angle Θ. A predicted flow field is shown in Figure 2.8 (b). The color code indicates the magnitude of the velocity and the arrow direction indicates the flow direction.

2.4. Surfactants

Surfactants (blend of surface–active–agents) are chemical compounds that usually lower the interfacial tension between two immiscible phases [147]. A schematic sketch of a typical surfactant structure is shown in Figure 2.9 (a). The surfactant molecule is amphiphilic, meaning it consists of a hydrophobic tail and a hydrophilic head group [33, 147]. Depending on the charge of the head group, surfactants are classified either anionic, cationic, zwitterionic, or nonionic [147]. In this work the nonionic surfactants dodecyl pentaglycole ($C_{12}E_5$) and octyl triglycole (C_8E_3) are used. Their chemical structure can be seen in Figure 2.9 (b) and (c). The reason for choosing those surfactants is explained in section 4.1.

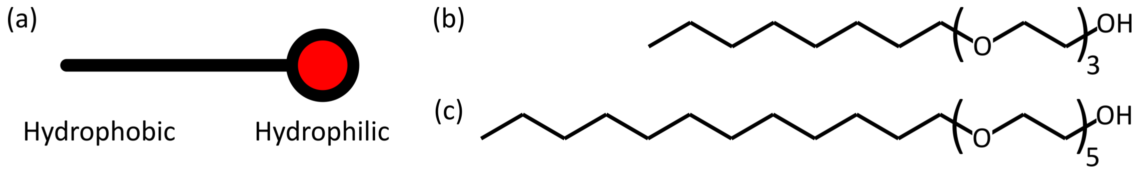

Figure 2.9.: (a) Schematic structure of a surfactant with a hydrophilic head group and a hydrophobic tail. Chemical structure of C_8E_3 (b) and $C_{12}E_5$ (c).

2.4.1. Critical micelle concentration

Surfactants diffuse in aqueous solutions and adsorb to the liquid/air interface since the hydrophobic tail seeks to stick out of the water. If the maximum surface concentration of surfactant molecules is reached, i.e. the whole surface is covered by surfactants, the surfactants aggregate to form a surfactant cluster that is called micelle [33, 147]. This surfactant concentration is called the critical micelle concentration (CMC). This situation is shown in Figure 2.10. Inside these micelles, hydrophobic substances, e.g. oil, can be accommodated and a stable emulsion, e.g. of water and oil, can be formed [33]. In general, surfactants increase the cleaning ability of water (also below the CMC) and are therefore used in many cleaning agents [33, 147].

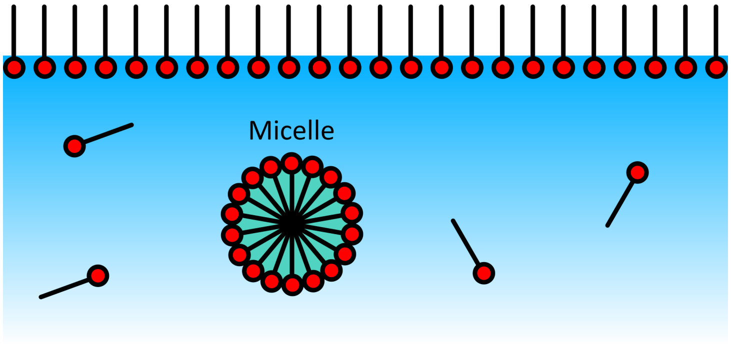

Figure 2.10.: If the maximum surface coverage of surfactant molecules is reached, micelles are formed. In these structures, hydrophobic materials can accommodate. This enhances the cleaning abilities of the solvent since dirt, oil or similar hydrophobic material stays in a stable emulsion with the solvent and can be removed.

2.4.2. Gibbs adsorption isotherm

The change in surface tension due to the adsorption of surfactant molecules to the surface can be described by the Gibbs adsorption isotherm.This isotherm correlates the surface tension with the surface excess. The latter is defined as the surface concentration of the surfactant molecules and is given as the number of molecules per unit area. It is only valid for surfaces whose deformation is reversible, e.g. liquid surfaces. In a two–component system the surface excess of the solute (i.e. a surfactant) in the solvent (i.e. water) is defined as

$$\Gamma = -\frac{a}{R\,T}\frac{\partial \gamma}{\partial a}\bigg|_T \tag{2.13}$$

with the activity a, the temperature T and the ideal gas constant R. If $\Gamma > 0$, the solute is enriched at the interface and the surface tension of the solvent decreases. Such solutes are called surface–active, i.e. surfactants. In the case of $\Gamma < 0$, the solute avoids the interface and the surface tension of the solvent is increased. For low activities, the activity a can be replaced approximately by the concentration c of the solute. [33]

2.4.3. Measurement of the surface tension

Since surfactants decrease the surface tension of water, it is important to measure the surface tension of surfactant solutions. Several standard methods to measure the surface tension exist, see [33, 50, 67, 120]. In this work, the Wilhelmy–plate method, named after Ludwig Wilhelmy who studied the force acting on a plate in detail [185], was used to measure the surface tension of liquids. A Wilhelmy–plate is a small platinum plate (Figure 2.11). This plate is attached to a fine balance. To measure the surface tension this plate is halfway immersed into the liquid. The capillary force acting on the plate is given by the following equation

$$F_c = 2\gamma\,(b + l)\cos(\Theta) \tag{2.14}$$

with the breadth b and length l of the plate. The plate is so thin that its breadth can be neglected and the formula to measure the surface tension simplifies to

$$\gamma = \frac{F_c}{2\,l\cos(\Theta)}. \tag{2.15}$$

Since the capillary force F_c is measured by the fine balance, the only unknown parameter is the contact angle Θ. The easiest way to eliminate the contact angle from the equation is to maintain a contact angle of 0°. This is achieved by using platinum as the material of the plate because most liquids have a contact angle of 0° on it. The second reason to use platinum is that it is chemically very stable and most contamination on the plate is easily cleaned by heating the plate.

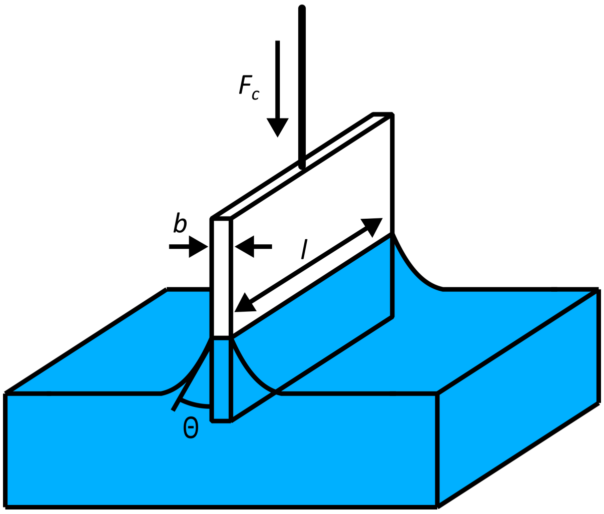

Figure 2.11.: Wilhelmy–plate method to measure the surface tension of liquids.

2.4.4. Marangoni effect

A Marangoni effect occurs due to a gradient in surface tension along an interface which can be caused by a concentration or temperature gradient. This Marangoni effect is noticeable either as a flow of mass, the so–called Marangoni flow, or in form of a stress, the so–called Marangoni stress. It can be observed e.g. after swirling a glass of wine (Figure 2.12). It is assumed that wine is a mixture of water and ethanol. Pure water has a higher surface tension than the mixture. Due to the swirling, a thin wine film spreads on the glass. This film has a large surface area compared to its volume. Thus, evaporation is faster in this region than in the bulk region of the wine. Since ethanol evaporates faster than water, the solution in this area depletes of ethanol and the surface tension is locally increased. The result is a gradient in surface tension that points toward the high energy surface since it seeks to reduce its surface area. The gradient leads to a flow of mass, i.e. a Marangoni flow, opposing the gravitational forces and is responsible for the shown accumulation of wine in form of small drops at the rim. At some point, the drops are too big and they slide down towards the bulk liquid due to gravity. These observations are referred to as tears of wine [87, 176, 178]. The Marangoni effect was first described in 1855 by the physicist James Thomsen [91] and named after the physicist Carl Marangoni who published his first observations of the effect in 1865 [119].

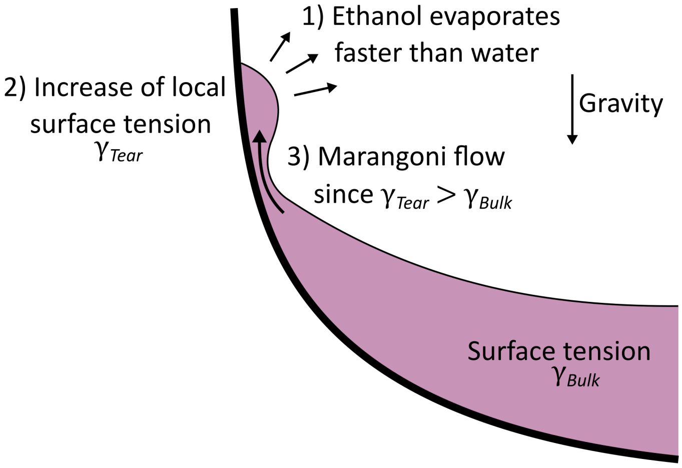

Figure 2.12.: Tears of wine effect to explain the Marangoni effect.

2.5. Dewetting of surfactant solutions

In the following, important results of macroscopic studies on the dewetting behaviour of aqueous surfactant solutions and the hypothesis [69] trying to explain the dynamics close to the contact line of dewetting surfactant solutions are presented.

2.5.1. Macroscopic influence

Preliminary studies [69, 70, 71, 83, 84, 85, 112, 175] used a rotating drum setup to measure the dynamic receding and advancing contact angle of surfactant solutions (Figure 2.13 (a)). The setup enabled measurement of the advancing and receding contact angles over a large velocity regime. The contact angles were recorded with high–speed cameras and macro optics.

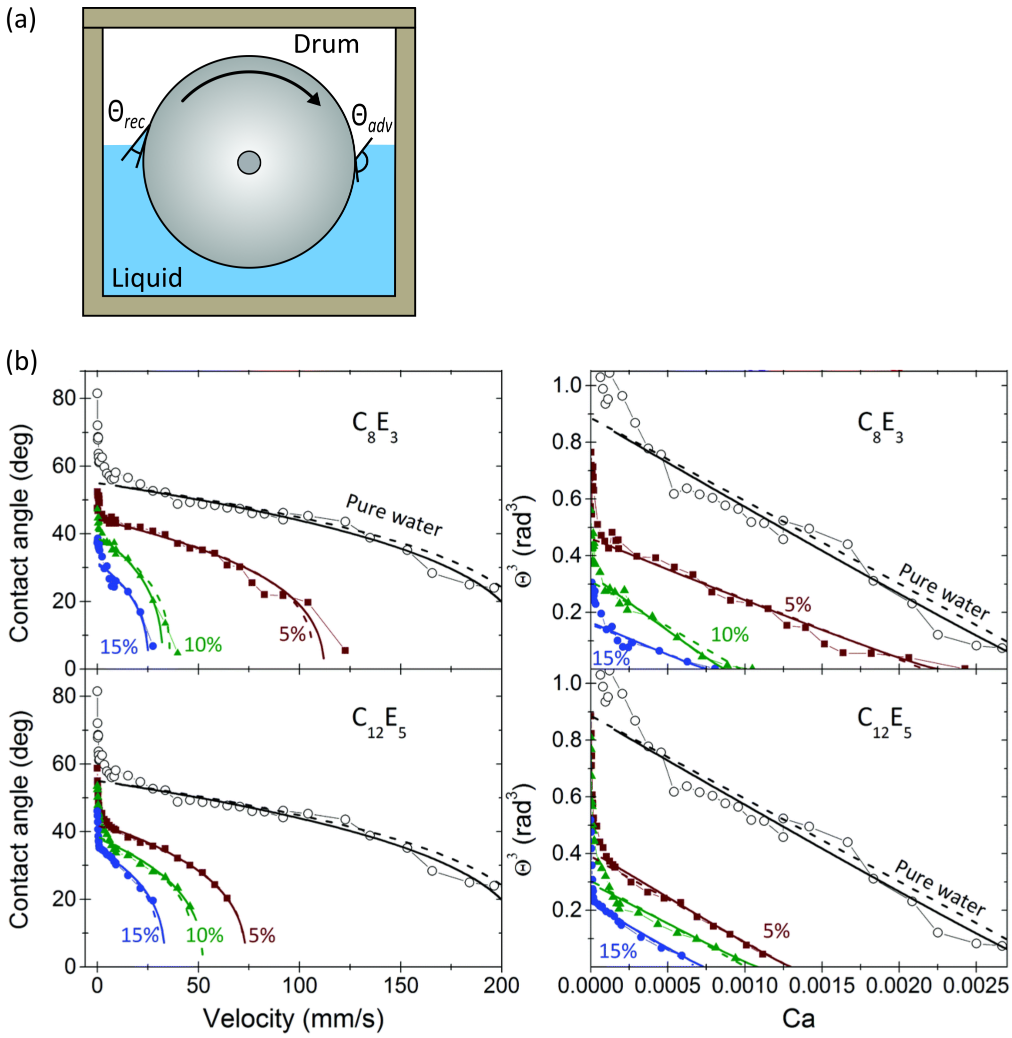

Figure 2.13.: (a) Sketch of the rotating drum setup after [69]. It enables the simultaneous measurement of the advancing and receding contact angle. (b) Left: dynamic receding contact angles versus the velocity for pure water and different aqueous surfactant solutions for $C_{12}E_5$ and C_8E_3. Right: Cubic contact angle versus the capillary number (calculated with the viscosity of water $\mu = 1\,\mathrm{mPa\,s}$). Solid lines are fits using the hydrodynamic model of Eggers and Snoijer (equation 2.8) and dashed lines are fits using the hydrodynamic Cox–Voinov law (equation 2.6). [83] - Published by the Royal Society of Chemistry. This figure shows a part of the original.

Measurements with water showed that the receding contact angle decreases and the advancing contact angle increases with an increasing rotation speed of the drum [69, 71, 83, 84]. Already the addition of small amounts of surfactants well below the CMC changed the dynamic receding contact angle significantly [69, 83]. This can be seen in Figure 2.13 (b) for two exemplary nonionic surfactants $C_{12}E_5$ and C_8E_3. On the left side, the dynamic receding contact angle above the contact line velocity for measurements of pure water and different aqueous surfactant solutions is shown. An increase of surfactant concentration and velocity leads to smaller contact angles. Truszkowska et al. [175] showed the same behaviour for high molecular weight surfactants. The plots on the right side of Figure 2.13 (b) show the cubic dynamic contact angle above the capillary number and the data is represented by straight lines. The capillary number of the measurements were in the order of 10^{-6} and thus in the region between the Langmuir–Blodgett and Landau–Levich–Derjaguin film formation (Figure 2.5). Henrich et al. [83] showed the described behaviour also for the surfactants cetrimonium bromide (CTAB, ionic), sodium 1–decanesulfonate (anionic) and butyl glycole (nonionic). It was found that the charge of the surfactant does not influence the dynamic behaviour. The hydrodynamic Cox–Voinov law [46] (equation 2.6) and the model of Eggers and Snoeijer [63, 163] (equation 2.8) were fitted to the data and are represented by the dashed and solid line respectively. Excellent agreement was found for velocities greater than $10\,\mathrm{mm\,s^{-1}}$.

2.5.2. Hypothesis

To explain the influence of even small amounts of surfactants on the dynamic contact angles, Fell et al. [69, 71] proposed a hypothesis. The model was again described in [83, 84] and extended in [85]. The hypothesis simplifies the problem to two dimensions and assumes that diffusion is the dominating effect. Hydrodynamic effects are completely neglected by the hypothesis.
A sketch of the process close to the receding contact line is shown in Figure 2.14 (a). It is assumed that the liquid/air interface is a straight line without curvature. The general fluid flow (bulk flow) follows the expected hydrodynamic behaviour. Close to the solid, the fluid moves parallel to the solid surface towards the contact line. At the contact line, the liquid changes its direction and flows backwards along the liquid/air interface. The authors of the hypothesis assume that close to the three–phase contact line a new liquid/air interface is continuously generated. This new liquid/air interface is not covered by surfactant molecules. There are two possible mechanisms to equilibrate the surface surfactant concentration of the new liquid/air interface with the bulk concentration [85]. Either molecules diffuse from the bulk towards the liquid/air interface or molecules that were adsorbed to the solid are directly transferred to the newly created liquid/air interface at the contact line. The authors assume that the latter effect is negligible and that diffusion is the dominating equilibration mechanism. This leads to a region close to the three–phase contact line with lower surface concentration of surfactants [69, 83, 85], as sketched in Figure 2.14 (a). It is claimed that the size of this region depends on two characteristic length scales that describe the equilibrium conditions and the advection–diffusion dynamics.

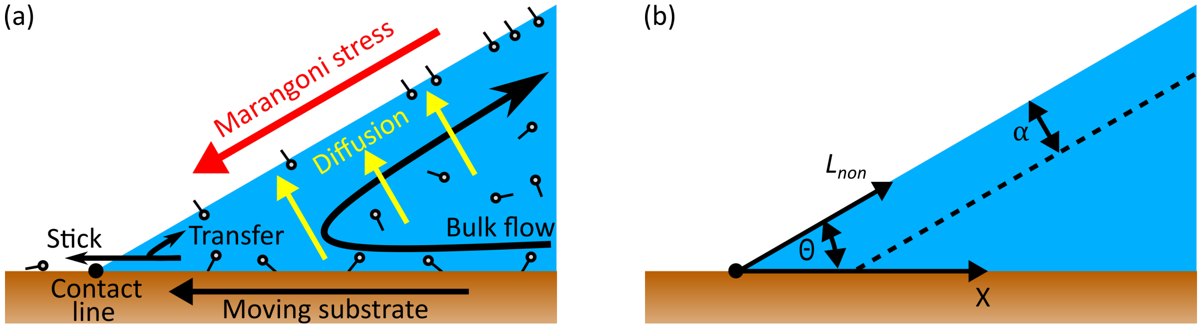

Figure 2.14.: (a) Schematic sketch of the process close to the receding three–phase contact line in the presence of surfactant molecules. (b) Definition of the parameters needed for the analysis. Sketches after [69, 71, 84, 85].

In equilibrium, the characteristic length scale α defines the thickness of a liquid layer that contains as many surfactant molecules as the liquid/air interface. Thus, the length α is a good measure of the diffusion length and therefore in the following referred to as such. By assuming a linear dependence of the equilibrium surface excess

$$\Gamma = \alpha c \tag{2.16}$$

on the bulk concentration c, the integration of Gibbs adsorption isotherm

$$\Gamma = -\frac{c}{RT}\frac{\partial \gamma}{\partial c} \tag{2.17}$$

between $c = 0$ and the equilibrium bulk surfactant concentration c, gives the characteristic length scale [69, 85]

$$\alpha = \frac{\Delta \gamma}{RTc} = \frac{\gamma_0 - \gamma}{RTc}. \tag{2.18}$$

Here, γ_0 is the surface tension of pure water and γ the equilibrium surface tension of the surfactant solution. Depending on the individual properties of the surfactant the diffusion length α can differ significantly.
The definition of the diffusion length α enables an approximation of the non–equilibrium region close to the contact line. Due to the problem geometry, the diffusion length α is smaller close to the contact line. At the contact line geometry considerations lead to [85]

$$L_{non} = \frac{2\alpha}{\tan(\Theta)}. \tag{2.19}$$

This equation defines a region that contains enough surfactant molecules to refill the newly generated liquid/air interface at the contact line. The prefactor 2 is needed to account for the reduction of the diffusion length α due to the wedge–shaped geometry. Thus, the concentration of surfactant molecules is lower close to the contact line and the surface tension is locally increased. This concentration gradient along the interface and the resulting gradient in surface tension lead to a Marangoni effect (section 2.4.4). The resulting Marangoni stress opposes the fluid flow close to the liquid/air interface and as a consequence, the contact angle changes.
Surfactant molecules are transported to the liquid/air interface by diffusion to equilibrate the surface concentration. This diffusion process is mostly perpendicular to the bulk flow (Figure 2.14 (a)). The characteristic diffusive time scale is estimated by [69, 71, 85]

$$t_D = \frac{\alpha^2}{2D} \tag{2.20}$$

with the diffusion coefficient D. This time scale has to be compared to the advective time scale [85]

$$t_A = \frac{L_{non}}{U} = \frac{2\alpha}{U\tan(\Theta)} \tag{2.21}$$

with contact line speed U. While the diffusive time scale t_D defines the time needed to equilibrate the surface concentration, the advective time scale t_A defines the time needed to create new liquid/air interface in the size of L_{non}. The ratio between both time scales

$$t_R = \frac{t_D}{t_A} = \frac{1}{4}\tan(\Theta)\,\frac{U\,\alpha}{D} \tag{2.22}$$

indicates the relative importance of these processes [85]. If the advective time scale is shorter than the diffusive time scale ($t_R > 1$), diffusion is not fast enough to equilibrate the newly generated liquid/air interface and the non–equilibrium region is expanded.

An additional dimensionless number to study transport phenomena is the Péclet number, named after the French physicist Jean Claude Eugène Péclet. The Péclet number defines the ratio between advective and diffusive transport rate and is defined as

$$Pe = \frac{u\,l}{D}. \tag{2.23}$$

Here, l is a characteristic length, u is the characteristic velocity and D is the diffusion coefficient. It can be seen that the above described ratio between the advective and diffusive time scale t_R (equation 2.22), is, apart from the prefactor, identical to the definition of the Péclet number with $u = U$ and $l = \alpha$.

2.5.3. Surfactant transport on large length scales

The above–presented hypothesis explains the surfactant transport process on a small length scale close to the receding contact line. Surface tension gradients result in a Marangoni effect which affects the dynamics of dewetting surfactant solutions.
However, surfactant transport on larger scales might also influence the dewetting behaviour of surfactant solutions. Fell et al. [70, 71] studied the influence of large scale surfactant transport processes with different configurations of the rotating drum setup (Figure 2.15). Depending on the filling height of the drum the surface flow, i.e. the surface surfactant transport between the advancing and receding side, can be blocked (Figure 2.15 (b) and (c)). Also, by using an additional barrier the bulk flow and thus the bulk surfactant transport can be blocked (Figure 2.15 (c)). Measurements for pure water showed no difference between the three setup configurations. In the case of surfactant solutions, blocking of the long–range surfactant transport processes significantly changes the contact angle dynamics [70, 71]. Even only blocking the surface surfactant transport increased the dynamic contact angle hysteresis. By blocking the surface and bulk transport, the measured contact angle hysteresis was further increased [70, 71]. Thus, the dewetting of surfactant solutions depends on processes at different length scales [70, 71].

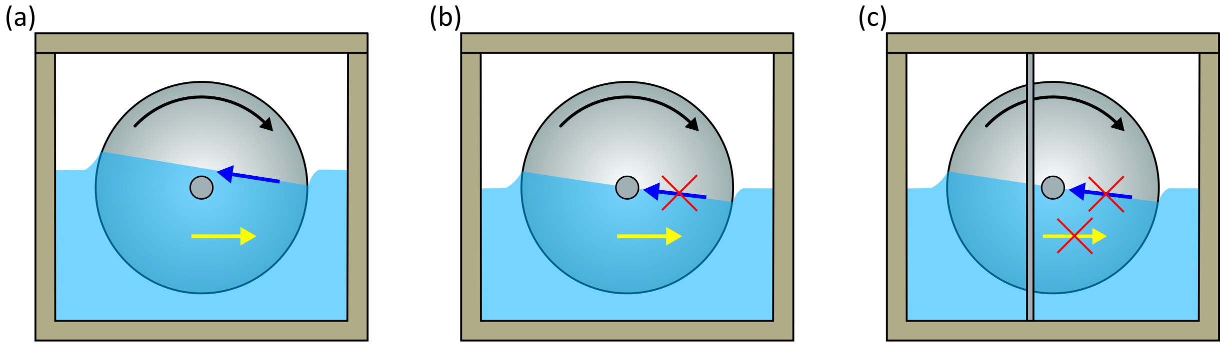

Figure 2.15.: Possible surfactant transport processes depending on the setup configuration. (a) Surface (blue arrow) and bulk transport (yellow arrow) are possible (b) Surface transport is blocked by the rotation axis of the drum. (c) Axis blocks the surface transport and an additional barrier blocks the bulk transport. After [71].

2.5.4. Microscopic influence

In section 2.5.2, I presented the hypothesis [69] which proposes that a Marangoni stress, arising from a surface tension gradient, opposes the surface flow close to the contact line. The hypothesis can be tested either by measuring the surface tension gradient close to the contact line or by measuring the influence of the Marangoni stress on the flow field. Since a measurement of the surface tension gradient is hardly possible, the flow profile close to the receding contact line should be measured.

An estimation of the needed measurement volume close to the receding contact line is possible with the hypothesis. In the case of a 0.9 % CMC CTAB surfactant solution, the non–equilibrium region close to the contact line has a size of 20.3 µm [69]. As a result, velocity measurements should be done in an area $<100\,\mu$m close to the receding contact lines. This necessitates the use of optical imaging systems, e.g. microscope, with a sufficient spatial and temporal resolution. In the following, an experimental setup which enables to measure the dynamics close to moving contact lines over long times is presented.

Measurement setup

Henrich [84] designed a measurement setup to measure flow profiles close to receding three–phase contact lines of surfactant solutions (Figure 2.16). The main idea of this setup is to create locally stable moving contact lines. This is necessary since a confocal microscope with a fixed objective position was used to measure the flow close to the moving three–phase contact line. A free moving contact line would move out of the field of view of the microscope objective, reducing the measurement time. Thus, the moving contact line must be locally stable above the objective.

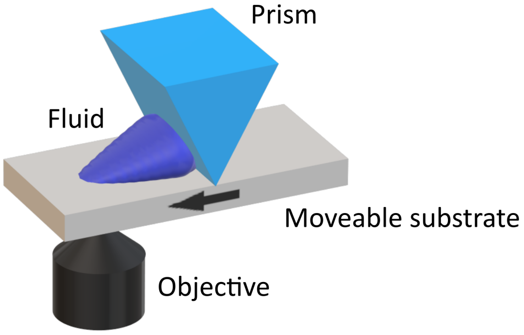

Figure 2.16.: The shown setup is used to create locally stable moving contact lines. [170] (Creative Commons Attribution 4.0 International license (CC BY 4.0)).

In the following, the working principle and the components of the setup are presented. Since several experimental methods and setups were built and used in this work, all components are listed in Appendix A.4. When describing the methods or setups, reference is made to the tables in the appendix for more details about the components.

A locally stable moving three–phase contact line is realized in the following way: A liquid drop is placed on top of a glass substrate. The substrate can be moved by a piezoelectric stage (A.3.1). While the substrate can be moved back and forth, the drop is pinned to the prism. Thus, it is possible to create advancing or receding contact lines that are locally stable since the drop is pinned to the prism. Therefore, it is possible to use fixed optical elements, e.g. the objective of a confocal microscope, to study the area close to a moving contact line. This enables studying the area close to moving three–phase contact lines on a microscopic

scale.
The setup was designed so that it fits on a fluorescence microscope (A.2.7) or a custom–built laser scanning confocal microscope [151, 181]. All important parts of this setup are mounted on kinematic units allowing a precise alignment of the setup. The prism can be moved vertically by a translation stage (A.3.3) and a kinematic mount (A.3.4) enables angular adjustment. Three preloaded fine thread screws (A.3.5) allow vertical and angular adjustment of the piezoelectric stage and the substrate. A substrate holder is screwed to the piezoelectric stage and the measurement substrate is placed on top of this holder. The piezoelectric stage has a maximum travel range of 25 mm with a velocity range between $0.001\,\mathrm{mm\,s^{-1}}$ and $10\,\mathrm{mm\,s^{-1}}$. Henrich [84] analysed the linearity of the motion with the following results: For high velocities $>1.33\,\mathrm{mm\,s^{-1}}$ the movement of the stage is smooth. A one millimetre thick polydimethylsiloxane (PDMS) dampening layer is used for lower velocities. This layer is placed between the piezoelectric stage and the substrate holder. That way a smooth movement is possible down to a velocity of $0.2\,\mathrm{mm\,s^{-1}}$.

Preliminary studies with the setup

First velocity measurements close to receding contact lines using the above described setup were performed using a confocal laser scanning microscope [84]. Polystyrene particles with a diameter of $4\,\mu\mathrm{m}$ were added to the liquid and tracked to measure the flow velocity. Due to limitations of the axial scanning capacities of the used confocal microscope the measurement volume was limited to a horizontal two–dimensional plane close to the moving substrate (out–of–plane distance to substrate $<10\,\mu\mathrm{m}$). Furthermore, no out–of–plane velocity data could be measured and the measurement time was limited by the used high–speed camera. Therefore, the amount of data was low and the statistical significance poor. A first conclusion of the these first measurements was that the velocity close to the solid of dewetting surfactant solutions differs from the velocity of pure water [84]. However, due to the above mentioned points, the conclusion is based on sparse amount of data.
Thus, a measurement method with sufficient temporal and spatial resolution is needed to investigate the dynamics of surfactant solutions close to moving contact lines.

Measurement of flow fields in moving drops

The choice of a suitable experimental method is limited by the three–dimensional shape of the drop and the optical accessibility of the measurement setup. Moving drops have complex three–dimensional shapes and different wetting behaviours depending on the contact line velocity [62, 109, 139, 141, 165] (section 2.2.3). Only a few studies report velocity measurements close to receding contact lines of moving drops since a free moving drop does not remain long in the field of view of the optical measurement device. Furthermore, due to the unknown dynamic interface of the drop, only the solid substrate is an optically defined interface. Since the solid substrate is flat, no optical aberrations occur. Thus, the only option to measure dynamics inside the drop without optical aberrations is by illuminating and detecting through the solid substrate.
Rio et al. [146] measured the two–dimensional flow close to the solid substrate of drops running down a tilted plate. Qian et al. [142] used flood illumination and total internal reflection fluorescence to measure flow fields close to moving contact lines. They subsequently measured the flow in different horizontal planes in the liquid while moving the liquid back and forth. The three–dimensional flow field was reconstructed by combining the measurements of multiple horizontal planes. Kim et al. [97, 98] used a tomographic particle image velocimetry (PIV) setup with four PIV cameras mounted to a custom made microscope to measure the three–dimensional internal flow of moving water drops. Similar to the setup of Henrich [84], they pinned the drop to a locally stable position while moving the substrate underneath it.

Although the multi–camera method of Kim et al. enables three–dimensional measurements of flow fields, I decided to minimize the complexity by using experimental methods that only need one camera or detection unit like a confocal microscope.

2.6. Microscopy

Microscopy is a standard tool in every natural science and industry to magnify objects. The invention of the compound microscope is generally attributed to a Dutch spectacle maker Zacharias Janssen of Middleburg (1590) and the second place is taken by Galilei, who announced his invention of the compound microscope in 1610 [82]. The lens system of a compound microscope is shown in Figure 2.17. The object is magnified to a real, inverted intermediate image. This intermediate image is further magnified by the ocular. The ocular is arranged so that the intermediate image falls on its focal plane. The total magnification M of the compound microscope is the product of the two partial magnifications of the objective M_{Ob} and ocular M_{Oc} [28, 82]

$$M = M_{Ob}\, M_{Oc}. \tag{2.24}$$

Thus, high magnifications are easily reachable and images can be recorded by placing a camera behind the ocular.

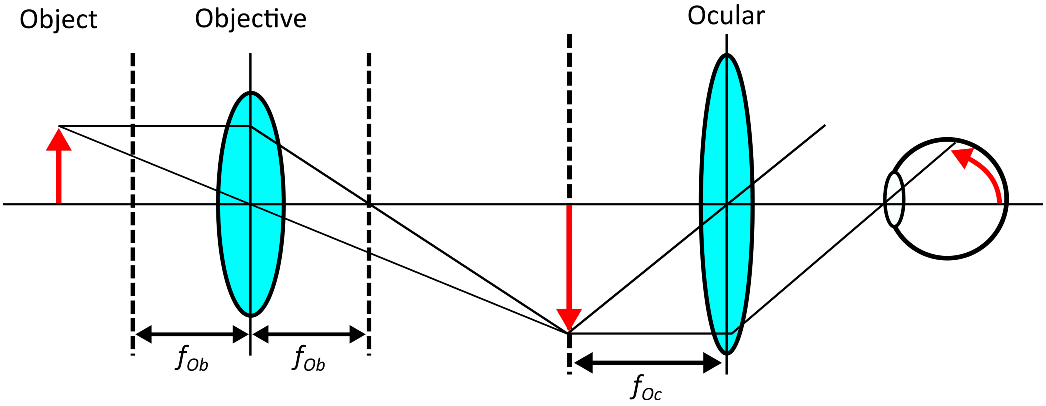

Figure 2.17.: Lens assembly of a compound microscope. The object is magnified to a real, inverted intermediate image. This intermediate image is further magnified by the ocular.

2.6.1. Optical resolution

An important property of microscopes or any optical imaging device is its resolution. The optical resolution is the ability of an optical imaging system to resolve details of the observed object. The definition of optical resolution is a matter of convention and different resolution criteria exist [28, 82, 89]. In the following commonly used standard criteria are presented.

Abbe's criterion

Basic concepts of light microscopy were established by the physicist Ernst Abbe (1840-1905) [2].These are visualized by the diffraction of light at a grating (Figure 2.18). The light with a wavelength λ is diffracted into multiple orders i at a grating with a constant spacing d. To quantify the light collecting properties of the objective, Abbe introduced the numerical aperture (NA) of the objective

$$\mathrm{NA} = n \sin(\psi) \tag{2.25}$$

with the (half)angular aperture α and the index of refraction of the surrounding medium n. Hence, the numerical aperture describes the range of angles from which the objective can accept or emit light.

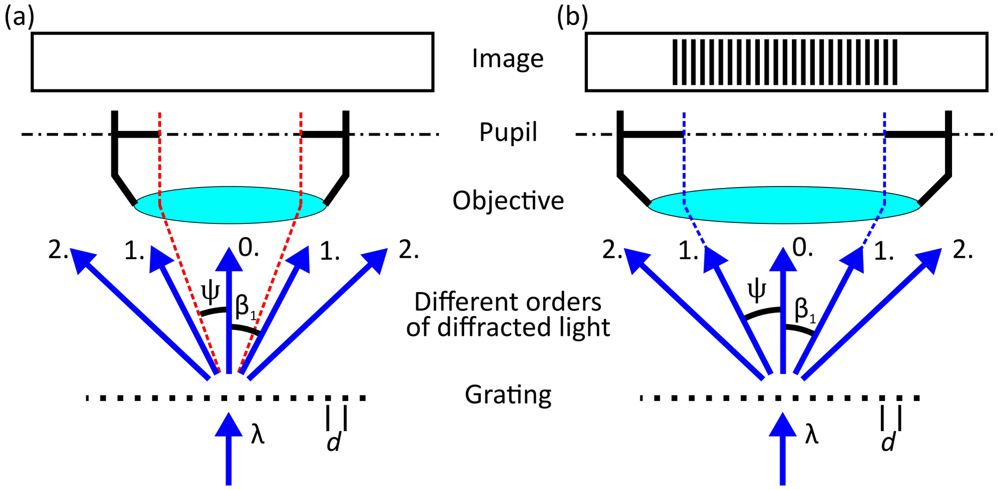

Figure 2.18.: Diffraction of light at a grating to visualize Abbe's resolution criterion, after [28]. (a) Resolution criterion is not fulfilled and the grating is not resolved in the image plane. (b) Resolution criterion is fulfilled and the grating is resolved.

At least two orders of the diffracted light, i.e. at least the 0th an the 1st orders of diffracted light, must be collected by the objective to resolve the grating. By using the diffraction equation at a grating $\sin(\beta_i) = i\ \lambda / nd$, the minimal distance d between two lines of the grating that can be resolved is

$$d = \frac{\lambda}{\mathrm{NA}}. \tag{2.26}$$

Since the resolution is defined as the ability to resolve details and the distance d is the minimal distance between two lines of grating that can be revolved, d is a measure of the lateral, i.e. in–plane, resolution. Thus, the lateral resolution d is proportional to the used wavelength of the light λ and inverse proportional to the numerical aperture NA of the objective. Equation 2.26 is Abbe's resolution criterion in the case of a central incident beam. In Figure 2.18 (a) the resolution criterion is not fulfilled and the grating is not resolved, whereas in (b) the criterion is fulfilled and the grating is resolved in the image plane.
If instead of a central incident beam, a condenser is used to illuminate the grating, Abbe's resolution criterion is defined as

$$d_{Ab} = \frac{\lambda}{\mathrm{NA} + \mathrm{NA}_{\mathrm{cond}}} \tag{2.27}$$

with the numerical aperture of the condenser $\mathrm{NA}_{\mathrm{cond}}$. The best resolution is reached in the case of $\mathrm{NA} = \mathrm{NA}_{\mathrm{cond}}$. No additional resolution is gained if the numerical aperture of the condenser $\mathrm{NA}_{\mathrm{cond}}$ exceeds the numerical aperture of the objective NA.

Rayleigh and Sparrow criterion

Instead of using a grating, small luminous point objects, e.g. stars, can be used to define resolution criteria. We cannot resolve any details of stars since they are too far away with exception of the sun. Already early astronomers realized that the images of stars observed with their telescopes do not appear as infinitesimal small points, but as dots with dim rings around them [28] (Figure 2.19 (a)).

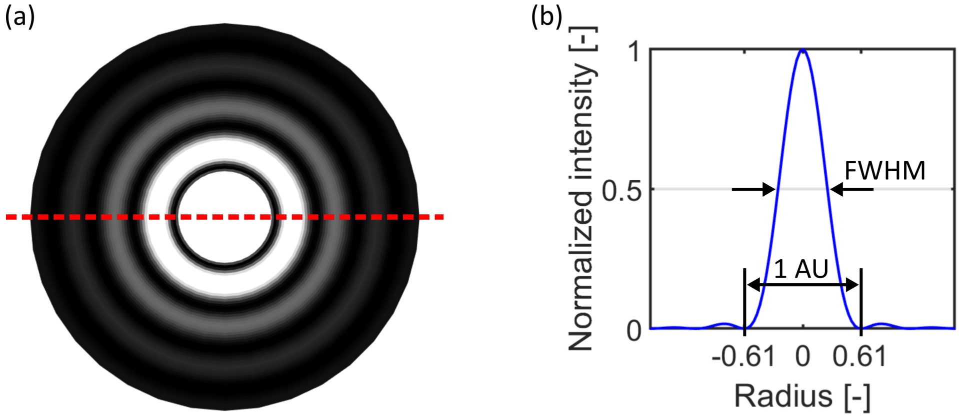

Figure 2.19.: (a) Two–dimensional intensity distribution of a diffraction pattern of a small luminous point recorded with a circular aperture. Pattern is calculated with equation 2.28. (b) Profile through the middle of (a) along the dashed line with the marked full width at half maximum (FWHM) and one Airy unit (AU).

The observed diffraction pattern can be calculated using the Fraunhofer approximation of wave–optics, named in honour of the physicist Joseph von Fraunhofer (1787-1826). The Fraunhofer condition is fulfilled if the diffraction pattern is observed at a great distance from the diffraction object (e.g. circular aperture of a telescope) or at the focal plane of an imaging lens (that is placed in the circular aperture) [82]. The illuminating light waves are cropped by the aperture and only a circular segment is used to create an image in the focal plane. This is the same process that takes place in an eye, microscope, or camera [82]. Since the condition is fulfilled, the illumination and diffraction light waves can be treated as plane waves. The diffraction pattern is described by the function [28, 82]

$$I = I_0 \left(\frac{2\, J_1\,(r)}{r} \right)^2 . \tag{2.28}$$

Here, I is the intensity (brightness) of the pattern depending on the radius r, I_0 is the maximum intensity peak at the centre of the pattern and J_1 is a first–order Bessel function. The intensity distribution of the diffraction pattern of equation 2.28 is called point spread function (PSF) since it describes how a point is spread into a two–dimensional pattern by an optical instrument [28]. The PSF of equation 2.28 is shown in Figure 2.19 (b). The profile (b) is called Airy pattern and the middle of the two–dimensional image (a) is called an Airy disc in honour of the mathematician Sir George Biddell Airy (1801–1892), who was the first to derive equation 2.28 [4]. The first dark ring around the centre dot in Figure 2.19, i.e. the first zero crossing of function 2.28, is defined as the diameter of the Airy disc or as the Airy unit (AU) [28, 82, 89, 180, 187]

$$\mathrm{AU} = 1.22 \frac{\lambda}{\mathrm{NA}} \tag{2.29}$$

Equation 2.29 describes the diameter of the image of a point–like object. Thus, the diameter reduces for a small wavelength λ and a large numerical aperture.

Knowing this, an argument about the requirements to distinguish between two infinitesimal small luminous objects, e.g. stars, that are close together is possible. The superposition of two PSFs for distant incoherent point light sources can be calculated for different distances between them (Figure 2.20). The black curve is the superposition of two light sources at the same position. The superposition just has an increased intensity. If the spacing between the PSFs is increased, at a certain distance d_{Sp} the red curve is reached. The superposition has a plateau, i.e. the function is constant for a certain distance, and an infinitesimal increase of the spacing would lead to two maxima and a minimum in between. So the distance d_{Sp} is the true limit whether one or two objects can be seen. The distance d_{Sp} is called the Sparrow criterion in honour of C. M. Sparrow and can be calculated via [28, 82, 167]

$$d_{Sp} = 0.51 \frac{\lambda}{\mathrm{NA}} \tag{2.30}$$

which is nearly identical to Abbe's resolution limit in the case of $\mathrm{NA} = \mathrm{NA}_{\mathrm{cond}}$ (equation 2.27).
If the distance between the light sources is further increased, at a distance d_{Ra} the maximum of one PSF lies in the first minimum of the second PSF (blue curve). This distance d_{Ra} is called the Rayleigh criterion in honour of John William Strutt, 3rd Baron Rayleigh (1842–1919). Since the function 2.28 is symmetric, the distance d_{Ra} is half the diameter of the Airy disc [28, 82, 114, 180]

$$d_{Ra} = 0.61 \frac{\lambda}{\mathrm{NA}}. \tag{2.31}$$

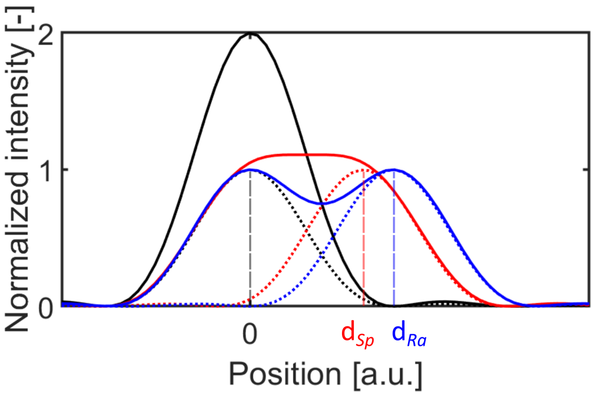

Figure 2.20.: Superposition of two point spread functions (dashed lines) for distant incoherent point light sources for varying distances between them. Two point light sources at the same position lead to the black curve. The red curve shows the superposition of two light sources (black and red dashed curves) at a distance corresponding to the Sparrow resolution limit d_{Sp} and the blue curve shows the superposition at a distance corresponding to the Rayleigh resolution limit d_{Re}.

Full width at half maximum

The previous mentioned criteria are based on the distance between two points. Although the criteria are good, in reality, it would take an exaggerated amount of work to control the distance of two points in the range of nanometres. Furthermore, the PSF of both points is identical. Thus, all information is already given by one PSF from function 2.28 and the superposition does not give additional information. Therefore, a resolution criterion merely based on the PSF would serve. A commonly used parameter d_{fwhm} is the full width at half maximum (FWHM) of the PSF (Figure 2.19 (b)). The distance d_{fwhm} is defined as a criterion for resolution [28]

$$d_{fwhm} = 0.515\frac{\lambda}{\mathrm{NA}}. \tag{2.32}$$

The advantage of the FWHM is that it can be measured with images of objects that are not resolved by the imaging objects.

2.6.2. Confocal microscopy

Confocal microscopy, introduced by Minsky in 1957 [126], was invented to overcome the optical limitations of wide–field microscopy. Since in wide–field illumination the whole specimen is permanently illuminated, up to 90 % of the observed fluorescence can originate from out of focus positions, leading to a reduced depth resolution and high background noise [44]. Confocal microscopy solves this problem by blocking most out of focus information by use of a pinhole. Figure 2.21 shows the working principle of confocal microscopy. The light emitted from the point light source is focused by an objective to illuminate a small focal spot in the focal plane in the specimen. The same objective collects the emitted/reflected light which is imaged on a pinhole before being detected. The confocal condition is that the pinhole is positioned at the plane that is optically conjugated to the illumination focal spot [6, 28, 89]. This configuration blocks most out of focus light from being detected. Thus, confocal microscopes detect light only in an area around

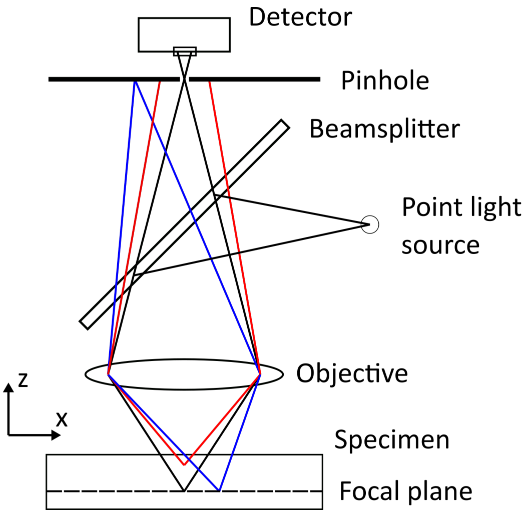

Figure 2.21.: Sketch of a confocal microscope to show the confocal condition. The focused illumination point in the focal plane and the observed point in the plane of the pinhole lie on optically conjugated planes. Thus, most out–of–focus light coming from planes above or below the focal plane is blocked by the pinhole.

the focal plane. This area is called the optical slice thickness. The optical slice thickness is defined as a three-dimensional volume (with the focal plane in its middle) from which light is detected. Conventional microscopes have no optical slice thickness since these devices also detect out–of–focus light. As a result, confocal microscopy enhances lateral/axial resolution and allows true three–dimensional–imaging.

Laser scanning confocal microscopy

Since its invention different designs of confocal microscopes were introduced. The laser scanning confocal microscope (LSCM) or confocal laser scanning microscope with a moving laser beam appeared in the 1980s, see Åslund et al. [9, 10], Carlsson et al. [35], Amos et al. [7] and White et al. [183]. The LSCM scans each position of the focal plane with a moving focus point. This is done by a pair of moving mirrors (galvanometer or resonant scanner) or acousto–optical deflectors. The focal plane can be moved axially through the sample either by moving the objective or the sample holder. This point scanning dramatically reduces the contribution of out–of–focus fluorescence. Therefore, LSCM is the method of choice to measure densely packed fluorescent samples or biological samples [89]. The major advantage of LSCM is that it can scan arbitrary planes through the sample by controlling each scanning unit individually. Thus, arbitrary planes through the sample can be measured and analysed.

A disadvantage of LSCM is its speed limitation. The scanning speed is limited by the movement of the fastest scan axis. Modern resonant scanner or acousto–optical modulators can be used to increase the scanning speed. The important point is that when the scanning speed is increased the focal spot spends less time at a specific position of the sample. Thus, less time is available to detect photons coming from the sample and the recorded image gets noisy. To increase the image quality the laser intensity can be increased. More excitation photons would reach the sample and thus more photons are emitted or reflected from the sample. However, high laser intensities at the focal spot can damage the sample. Another option is to scan the same line twice and average the recorded data. But to maintain the scanning speed, the scanned area of the probe has to be reduced. As a result, it is not possible to achieve high temporal resolution, high spatial resolution, large pixel numbers, and a wide grey scale simultaneously [89].

To enable high scanning speeds several multi–beam confocal microscope were developed, e.g. slit scanning microscopes [36, 173], spinning disk microscopes [128, 162, 173] or pinhole array setups [94]. These designs also have drawbacks like high bleaching rates of slit scanning microscopes or low light transmission and reflections from the disc of spinning disc microscopes [89, 173, 188]. Additionally, multi–beam setups have the drawback of crosstalk between the beams, leading to high background noise when recording densely packed fluorescent samples [76, 188]. Another single–beam design of a confocal microscope which enables fast scanning is a re–scan laser scanning confocal microscope. This design enables high scanning speeds while only using a single laser beam. The re–scan design is presented in detail in section 3.1.1.

Three–dimensional scanning capacities

A further limitation are the axial scanning capacities of current confocal microscope designs. A confocal microscope achieves axial scanning by moving the focal plane through the sample. A common way to accomplish this is by moving the objective up and down by using piezoelectric scanners. The maximum axial scanning speed of these scanners is limited by the inertia of the moving objective. Also, fast movements of the objective can induce vibrations on the sample, affecting the image quality [60, 77]. This effect is enhanced if immersion objectives are used since the immersion oil mechanically couples objective and sample. Several techniques to enable high speed axial and three–dimensional scanning without disturbing the sample were developed. These techniques move the focal plane without moving the objective and are referred to as remote focus techniques. Various electric tunable lenses based on electrowetting [17] or liquids [77, 130, 159] exist. Also, lenses based on acousto–optic deflectors or scanners [59, 96], tunable acoustic lenses [60, 125], liquid–crystal lenses [113] and diffractive tunable lenses [15] are available. These lenses are placed in the back aperture of the objective and allow for shifting the focal plane in the axial direction without moving the objective. Besides lenses, a spatial light modulator [49], a second objective with a moveable mirror [29, 30] or the addition of two objectives [48] can be used to remotely move the focal plane. All of these techniques add optical elements to the beam path adding possible refraction, diffraction, and reflection interfaces and therefore lowering the signal intensity. Also, some of the techniques alter the field of view or add optical aberrations, e.g. chromatic aberration due to missing corrections of the optical elements. Several of these techniques are also not suitable for applications with a high numerical aperture objective [15]. Aberration free and usable for high numerical aperture applications are the remote focus techniques of [29, 30, 48].

Resolution of confocal microscopes

The maximally available resolution is limited by the wavelength of the light and in the case of laser scanning microscopes by the spot size of the laser focus [134]. The latter accounts for the fact that the laser focus cannot be infinitesimal small but has a finite size. Table 2.1 lists the theoretical formulas to calculate the lateral/axial resolution and optical slice thickness for conventional and confocal microscopes. As already mentioned, confocal microscopes block most out–of–focus light and thus enable three–dimensional imaging. The optical slice thickness defines the axial thickness of the specimen's volume from which light is led through by the pinhole and recorded. Since conventional microscopes have no pinhole, a slice thickness cannot be defined.

Table 2.1.: Lateral and axial resolution and optical slice thickness for conventional and confocal microscopes [6, 28, 89, 132, 134, 156, 180, 184, 187]

		Conventional microscope	Geometric–optical confocal microscope 1 AU $< D_{ph} < \infty$	Wave–optical confocal microscope $D_{ph} <$ 0.25 AU
Lateral resolution		$\frac{0.61\lambda_{em}}{\mathrm{NA}}$	$\frac{0.51\lambda_{ex}}{\mathrm{NA}}$	$\frac{0.37\lambda_{m}}{\mathrm{NA}}$
Axial resolution	$\mathrm{NA} \geq 0.5$	$\frac{2n\lambda_{em}}{\mathrm{NA}^2}$	$\frac{0.88\lambda_{ex}}{n-\sqrt{n^2-\mathrm{NA}^2}}$	$\frac{0.64\lambda_{m}}{n-\sqrt{n^2-\mathrm{NA}^2}}$
	$\mathrm{NA} < 0.5$	$\frac{2n\lambda_{em}}{\mathrm{NA}^2}$	$\frac{1.77n\lambda_{ex}}{\mathrm{NA}^2}$	$\frac{1.28n\lambda_{m}}{\mathrm{NA}^2}$
Optical slice thickness		Not definable	$\sqrt{\left(\frac{0.88\lambda_{em}}{n-\sqrt{n^2-\mathrm{NA}^2}}\right)^2+\left(\frac{\sqrt{2}nD_{ph}}{\mathrm{NA}}\right)^2}$	$\frac{0.64\lambda_{m}}{n-\sqrt{n^2-\mathrm{NA}^2}}$

The resolution depends on the index of refraction n, the numerical aperture (NA) of the microscope objective, and the wavelength of the light λ. For the latter is distinguished between excitation λ_{ex}, emission

λ_{em}, and a median wavelength [132, 156]

$$\lambda_m = \frac{\sqrt{2}\lambda_{ex}\lambda_{em}}{\sqrt{\lambda_{ex}^2 + \lambda_{em}^2}}. \tag{2.33}$$

The modified pinhole diameter D_{ph} is measured in Airy units (AU) and defined as [133, 187]

$$D_{ph} = \frac{d_{ph}}{M_{Ob}} \tag{2.34}$$

with the physical pinhole diameter d_{ph} and the magnification of the objective M_{Ob}. Depending on the modified pinhole diameter of the setup, either a geometric– or wave–optical analysis is used to describe the resolution of the setup [6, 132, 156, 184, 187]. Standard confocal microscopes do not use infinitesimal small pinholes and work with $D_{ph} > 0.25\,\text{AU}$.

2.7. Measurement of fluid velocity

Several standard techniques [122] and volumetric techniques [31, 41, 43, 58, 99, 194] are available to measure the fluid velocity. In the following, particle–based techniques are presented that were used in this work.

2.7.1. Particle–based techniques

Particle–based techniques [174] rely on tracking particles that follow the fluid flow. These particles have to fulfil several conditions to provide good measurement data: The particles have to follow the fluid flow truthfully without disturbing it. Thus, an important point is to match the density of the particle and the density of the measurement fluid to avoid sedimentation effects. In addition, the fluid motion should exceed any Brownian motion [65, 108, 110, 135, 171] of the particle. The Brownian motion is significant for particle diameters smaller than 1 µm and adds an error to the determination of the velocity [131]. The error due to Brownian motion can be eliminated using correlation averaging [111]. Furthermore, the particles have to scatter or emit enough light to detect them properly. If possible, fluorescent tracer particles should be used since they significantly improve the quality of the recording [123]. Since the camera has a significant impact on the image quality, the camera should have the highest possible quantum efficiency [79, 111]. The particle size should be chosen so that the motion of a particle between two frames is less than half the particle diameter [47]. A sufficient amount of particles should be added to the fluid, to measure the velocity with the desired temporal and spatial resolution.

2.7.2. Particle image velocimetry and particle tracking velocimetry

Particle image velocimetry (PIV) and particle tracking velocimetry (PTV) are off–the–shelf experimental tools to measure fluid velocities [3]. If the measurements take place on the micro–scale, as in this work, the methods are referred to as µPIV or µPTV. Depending on the density of tracer particles in the image, the evaluation of the velocities is done differently. PTV algorithms are used to calculate the velocities for small particle densities and PIV algorithms are used to calculate the velocity for high particle densities [3].

The fluid volume is illuminated and observed with the microscope objective. Fluorescence particles emit light that is collected by the microscope. The two–dimensional image of the particles is recorded by the camera. After a small–time interval, Δt a second image is recorded. If a flow occurs, the particles have moved some distance Δd. The velocity u can be calculated with

$$u = \frac{\Delta d}{\Delta t}. \tag{2.35}$$

This can be done for consecutive frames and the velocity of the particles can be calculated for all recorded time frames. PTV tracks the trajectories of single particles and delivers the velocity and acceleration along the trajectory. This is the reason why PTV is also referred to as lagrangian particle tracking. However, particles can move in three dimensions during the time interval Δt. Thus, for volume illumination (all tracer particles emit light) only the light from the particles in the focal plane should be collected. This can be easily done by using a confocal microscope, see section 2.6.2.
Standard PIV/PTV are two–dimensional techniques that can be used to measure velocities in the focal plane (e.g. xy–, xz– or yz–plane). Several options are available to use PIV/PTV as three–dimensional techniques, see [41, 58, 174].

2.7.3. Astigmatism particle tracking velocimetry

Defocusing techniques [12, 13, 58], like astigmatism particle tracking velocimetry (APTV), use the size or shape of the particle images to calculate the third out–of–plane (axial) position of the particle. The first defocusing technique was used by Willert and Gharib [186]. They used a three–pinhole aperture to deform the recorded particle shapes and were able to measure three–dimensional velocities. The first APTV setup is described by Kao and Verkman [95] who used a cylindrical lens to deform the particle shapes and measured the three–dimensional position of particles in living cells. APTV was further improved and nowadays is an established technique for microfluidics called µAPTV [12, 13, 40, 41, 42, 43, 148].

In Figure 2.22 (a) a sketch of an APTV setup is shown. A fluorescent microscope is changed into an APTV setup by placing a cylindrical lens in front of the camera. Due to the cylindrical lens, instead of one focal plane, two focal planes F_{xz} and F_{xy} exist (Figure 2.22 (b)). The images of fluorescent tracer particles are deformed either horizontally or vertically, depending on their distance to the focal planes. For this reason, the shape of the particle image can be used to determine the axial position of the particle. Therefore, a calibration of the APTV setup is needed. This is done by recording particle image shapes of reference particles with known axial positions. Recorded particle image shapes of measurements are compared to the calibration data to calculate the axial particle position. Hence, APTV measures three–dimensional trajectories of particles with two–dimensional images of the particle shapes.

The big advantage of APTV, or defocusing techniques in general, is that only one camera and no moving parts are needed to measure a three–dimensional velocity field. The only necessary addition to standard fluorescence microscopes is a cylindrical lens that is placed in front of the camera chip. The three–dimensional frame rate of APTV setups equals the reachable two–dimensional frame rate, since three–dimensional information is calculated with a two–dimensional image.

However, there are a few important points to keep in mind. The optical path is disturbed on purpose by adding a cylindrical lens. Thus, the resolution of the setup is reduced compared to standard fluorescent setups since the particle images are deformed. Since the intensity of the emitted fluorescence light of one particle is distributed over several camera pixels due to its elliptical shape, the quantum efficiency of the

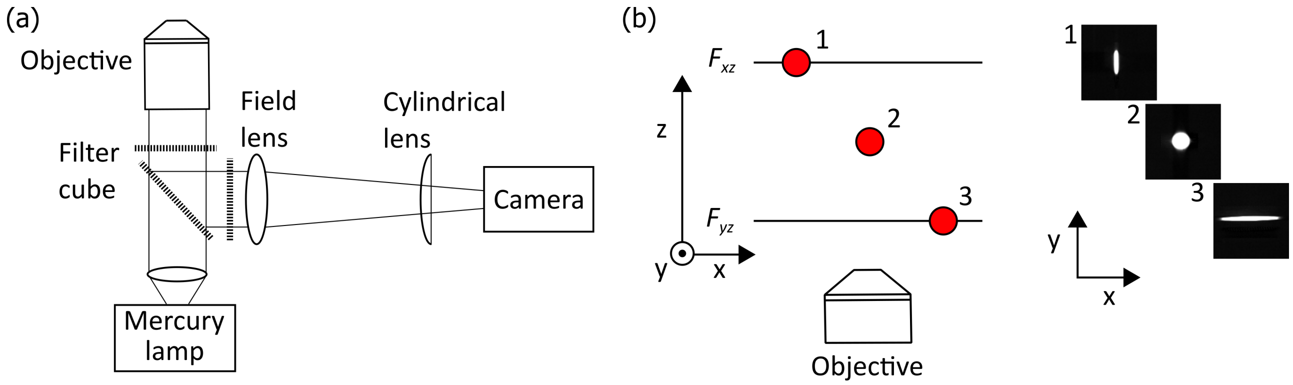

Figure 2.22.: (a) Sketch of a fluorescent microscope with a cylindrical lens in front of the camera. (b) The image of a fluorescent labelled particle changes depending on its distance to the objective lens due to the cylindrical lens. Adapted from [170] (under review) ©2020 American Physical Society (CC BY 4.0).

camera is even more important than in standard PTV. Furthermore, the size of tracer particles has to be monodisperse because otherwise, the technique fails. APTV works with low seeding rates since the shape of each particle has to be recorded.

3. Experimental methods

In this chapter, two experimental methods that I developed and built during this work are presented. The first method, which is presented in the first part of this chapter, is a custom–built fast re–scan laser scanning confocal microscope that I developed and built. In the second part of this chapter, an astigmatism particle tracking velocimetry (APTV) setup that I built is presented. Both setups were designed by me and all necessary software codes to control the setups and analyse the recorded data were written by me as well. Both methods were built to enable the measurement of flow fields close to moving three–phase contact lines. At the end of this chapter, the methods are compared regarding their capabilities to measure the flow fields.

The appendix contains an overview of all commercial components (Appendix A.4), technical drawings (Appendix A.8), used software programmes (Appendix A.6) and consumables (Appendix A.5). When describing the methods or setups, reference is made to the tables in the appendix for more details on the components, software or consumable material.

3.1. Fast re–scan laser scanning confocal microscope

Commercially available state–of–the–art confocal microscopes offer full–frame two–dimensional imaging with tens of hertz and good resolution. They include control and analysis software and several illumination wavelengths [1, 45, 193]. Whereas these microscopes deliver very good resolution and image quality for low frame rates, they are limited in high–speed acquisition. Table 3.1 lists the high–speed specifications of three commercially available state–of–the–art confocal microscopes. In particular, the field of view is severely restricted, which limits the use of these microscopes. It is also worth mentioning that at the time the here presented custom–built microscope was planned (2017), none of the mentioned commercial microscopes were available and the high–speed capacities of older generations of commercial microscopes were even worse.
A further limiting factor of commercial microscopes is the limited axial scanning speed. The axial scanning is either done by moving the objective or the sample up and down. The fast mechanical movement of the objective can induce vibrations on the sample. Next to affecting the image quality, this can lead to distortions of liquid samples, e.g. drops. The movement of the sample stage leads to even greater distortions of liquid samples.

Therefore, despite all the benefits of commercially available confocal laser scanning microscopes, I decided to build a new high–speed confocal microscope. The last entry in Table 3.1 shows the high–speed specifications of the custom–built setup that are clearly above the commercially available standard. A custom–built microscope has also the advantage that the beam path is easily accessible and customizable. Two extensions of the built microscope to measure three–dimensional dynamics without disturbing the sample are presented in section 3.1.5.
During the construction of the microscope, I supervised a Bachelor thesis [105] which had a part in

Table 3.1.: High–speed capacities of state–of–the–art commercially available confocal laser scanning microscopes [1, 45, 193] compared to the custom–built microscope.

Company	Model	Release	Max. frame rate [Hz]	Field of view [px^2]	Line speed [lines/s]
Nikon	A1R HD25	08.2018	720	512 × 16	7800
Zeiss	LSM 980	04.2019	425	512 × 16	6380
Leica	Stellaris 8	04.2020	428	No information	No information
MPIP	Fast mode	10.2018	1000	1024 × 125	31400

constructing the confocal microscope. Most of the content in the following sections about the custom–built confocal microscope is published in [169].

3.1.1. Re–scan laser scanning confocal microscope

The custom–built microscope is a re–scan laser scanning confocal microscope. This is a special design of a laser scanning confocal microscope. De Luca et al. [51, 52, 53] published the design 2013 and named it "Re–scan confocal microscopy". Auernhammer et al. [11] published a high–speed design of an re–scan confocal microscope in a patent from 2013. Also, commercial re–scan confocal microscope modules are available with a recording speed of 4 Hz [144].

The general design of a re–scan configuration is shown in Figure 3.1. The incoming laser beam is redirected by a beam splitter towards the sample scan unit. This unit is used to scan the sample in lateral direction, i.e. x– and y–direction. The imaging optics are used to scan the sample in axial direction. The emitted light from the sample is captured by the imaging optics and redirected towards the beam splitter. Behind the beam splitter, the light penetrates a pinhole and reaches the detection scan unit. This scan unit depicts the sample information on a two–dimensional camera chip. It is necessary that the scan units and the camera are frequency– and phase–locked.

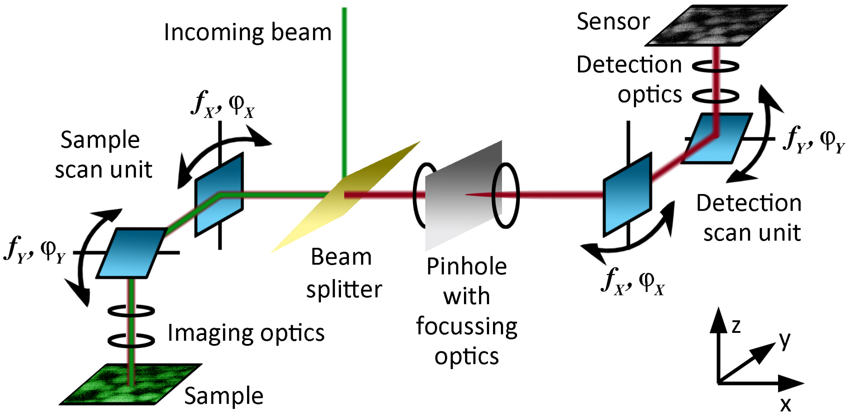

Figure 3.1.: Schematic beam path of a re–scan confocal laser scanning microscope. Reprinted from [169], with the permission of AIP Publishing.

The difference between the design of a standard laser scanning confocal microscope and the re–scan design is the detection beam path. In a standard design, a photomultiplier tube or photon counter is placed behind the pinhole and used to detect the signal. Since the laser signal at this position is purely temporal, software is needed to reconstruct a two–dimensional image of this temporal data. A re–scan configuration on the other hand directly records a two–dimensional image, because the second scan unit depicts the data on the two–dimensional camera chip. Thus, the re–scan design does not need complex image reconstruction software.

3.1.2. Setup requirements and design decisions

The aim of this work is the measurement of flow fields close to receding three–phase contact lines. The main requirement of the custom–built microscope is enabling the measurement of those flow fields with sufficient spatial and temporal resolution. To fulfil this requirement a vertical scan (xz– or yz–scan) with at least a frame rate of $\geq$50 Hz is necessary. In general, the following points would be desirable:

- High scanning speeds with highest possible resolution
- Fast axial scanning speed without disturbing the sample
- Simple and quick adjustment of the optical components with a minimum number of optical elements
- Compatibility with various experimental setups

Some of these points conflict with each other. In section 2.6.2, it was already shown that it is not possible to achieve high temporal resolution, high spatial resolution, large pixel numbers, and a wide grey scale simultaneously [89]. As a result, a design compromise was necessary:
I chose to realize the highest possible scanning speed. Therefore, I had to use small scanning mirrors to enable the fastest possible mirror movement. Due to the small mirror size, the pupil of the objective could be barely fully illuminated which reduced the usable numerical aperture of the objective and thus the resolution of the setup. The optical properties of the setup are characterized in section 3.1.4.
I chose the fastest available objective scanner to enable fast axial scanning. To circumvent the disturbance of the sample during the measurement of flow fields, I built two configurations of the setup which are explained in detail in section 3.1.5.
The adjustment of optical assemblies is a time–consuming process that should be reduced to a minimum. In order to achieve this, I reduced the number of optical elements as much as possible. Since I connected every optical element by optical rails and rods, the mechanical drift of the components is low. This also reduced the adjustment time compared to other custom–built microscopes that were used in previous studies [151, 181].
The design of the sample table of the microscope offers maximum compatibility with various experimental setups. Several mounting plates and a common 25 mm hole grid around the measurement area provide maximum flexibility.

3.1.3. Description of the setup

In this section, the beam path, important assembly groups, the control software, and the motion of the synchronized scanners of the custom–built microscope are presented.

Beam path and its components

This section provides detailed information about the components of the custom–built microscope. After a description of the whole beam path, important assembly groups are explained in detail.

Figure 3.2 (a) shows a detailed schematic sketch of the standard configuration of the microscope. In (b) the completely assembled microscope is shown and (c) shows the microscope with removed sample table and overlaid beam path. The components are arranged compactly, leaving around a third of the available

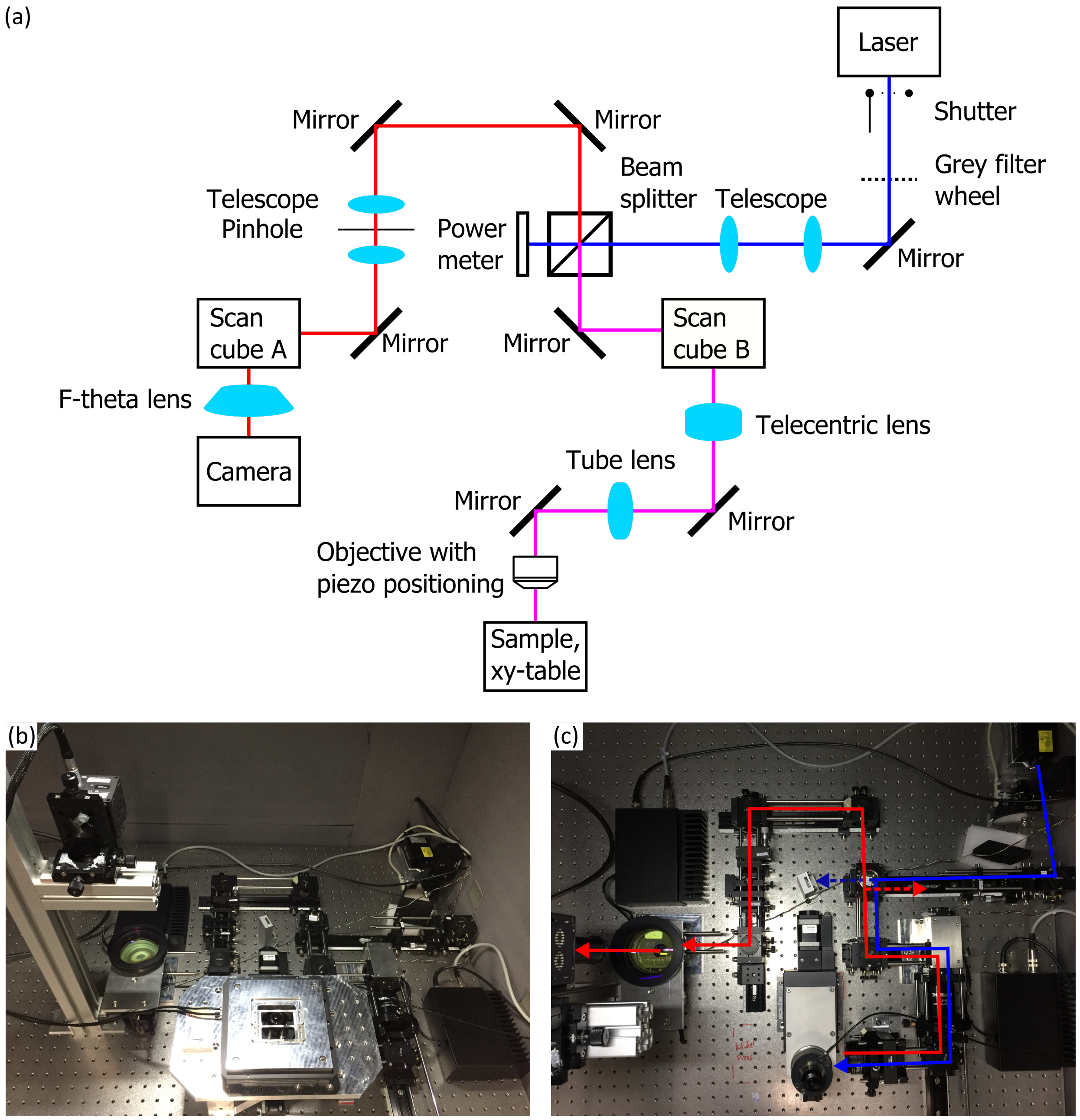

Figure 3.2.: (a) Sketch of the beam path of the standard configuration of the custom–built microscope. (b) Completely assembled microscope. (c) Assembled microscope with removed sample table. The blue line marks the excitation laser beam and the red line marks the reflected or emitted laser beam from the sample. The magenta line in (a) marks the part of the beam path where both, excitation and reflected/emitted, laser beams overlap.

breadboard (A.1.47) space free. Thus, enough space for future extensions is available. The laser (A.1.46) emits green light with a wavelength of 532 nm that passes a shutter (A.1.14) and a motorized grey filter wheel (A.1.23, A.1.16). Both shutter and filter wheel can be controlled remotely, enabling safe regulation of the laser intensity. The first telescope consists of two achromatic doublet lenses (A.1.17, A.1.27) with focal lengths of 19 mm and 100 mm. This increases the laser beam diameter from 0.7 mm to 3.7 mm. The following 50:50 beam splitter (A.1.24) directs half of the laser intensity to a power meter (A.1.13) which is used to monitor the laser power in realtime. The other half of the laser intensity is lead towards scan cube B in which the oscillating mirrors are mounted. The oscillating mirrors create an array of diverging laser beams. This array enters a telecentric lens system (A.1.8, A.1.9). The telecentric system transforms the diverging beams into a parallel array of laser beams. The advantage of a telecentric lens system is that the microscope objective can be moved in a range of 70 to 170 mm behind the telecentric system. Therefore, the axial scanning of the sample can be done by moving the objective back and forth.

The parallel light array is reflected vertically into the pupil of the objective. The movement of the objective can be controlled by two devices. A rough height adjustment can be done by an elevator stage (A.1.31). For fine adjustments, two different piezoelectric positioning devices are available. The first piezoelectric motor (A.1.39) has a sub–nanometre positioning resolution with a travel range of 400 µm. The second device (A.1.35) enables fast axial scanning with an oscillation frequency of 100 Hz with a travel range of 100 µm. The sample can be moved with a motorized xy–table (A.1.37). The xy–table is placed on a sample table.

The sample reflects/emits light which follows the same path back to the beam splitter. Half of its intensity is redirected towards the laser and is lost. The other half is lead towards a second telescope which focuses the beam on a pinhole. The light passing through the pinhole (A.1.22) is scanned by scan cube A onto a complementary metal–oxide–semiconductor (CMOS) sensor (A.1.48). An f–theta lens (A.1.51) is used to transform the diverging beam into a parallel array of laser beams and focus the light on the camera chip.

Several mirrors (A.1.25, A.1.26) in the setup are needed to guide and correct the laser beam. The mirrors are necessary because the beam deviates from its optimal position when passing through optical elements. The mirrors are silver–coated resulting in a high reflectance >98.5 % in the case of the used laser light wavelength. All optical elements, e.g. lenses and beam splitter, have an anti–reflective coating to minimize losses due to reflection.

The description above is true for the reflectance mode of the confocal microscope. To use the setup in fluorescence mode, either the beam splitter can be replaced by a suitable dichroic mirror or an appropriate chromatic filter is placed between scan cube A and the beam splitter. The latter one is only suitable if enough fluorescent light is emitted by the probe, because 50 % of the emitted light is lost due to the beam splitter.

Assembly group: Scan cubes

The scan cubes are the main part of the built confocal microscope. Technical drawings of the scan cubes can be found in Appendix A.8. Each scan cube contains one resonant scanner (A.1.34) and one galvanometer scanner (A.1.19). The scan cubes protect the mirrors from physical damage and dust and have a sound absorbing effect. Figure 3.3 shows both scan cubes with removed top plates. Scan cube A (Figure 3.3 (a)) scans the chip of the camera. Therefore, the scan cube reflects the laser beam, which enters the cube horizontally from the right, vertically upwards. The second scan cube B (Figure 3.3 (b)) scans the sample. The laser beam enters the cube from the left and exits through the lower side.

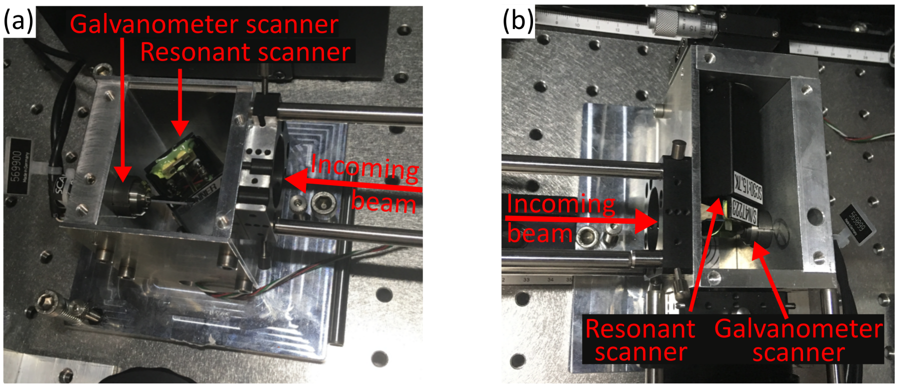

Figure 3.3.: (a) Scan cube A and (b) scan cube B. Each of the scan cubes contains a resonant and a galvanometer scanner.

Several important points had to be considered during the design of those scan cubes. The rotation axis of the resonant and galvanometer scanner must be perpendicular to each other. Otherwise, the mirrors would not create a uniform array of laser beams. Furthermore, the incoming laser beam must meet at first the resonant mirror when entering the cube. The reason for this is the size of the mirror. The resonant mirror has a size of $4 \times 5\,\mathrm{mm}^2$ and the incoming laser beam has a thickness of 3.7 mm. The first moving mirror transforms the incoming laser beam into a line that is reflected to the second moving mirror. The length of this reflected line is larger than the size of the resonant mirror. Thus, the first mirror that is encountered by the incoming laser beam must be the resonant mirror and the second mirror is the large galvanometer mirror.

An unavoidable error source is the spacing between the moving mirrors. In an ideal case, the axes of rotation of both resonant and galvanometer mirrors should cross each other. In reality spacing between the axes of rotation is unavoidable due to the size of the mirrors. To minimize the influence of the spacing, the spacing between the mirrors should be reduced as much as possible. The spacing between the mirrors was set to 12 mm. Additionally, the spacing shifts the height of the laser beam. The standard height of the laser beam was 60 mm, since this height is the available height of the used optomechanical system (A.1.21) on which the setup is based. This beam height was used in the entire setup, except in the area between scan cube B and the objective. In this area, the laser beam height was reduced to 48 mm. The optomechanical system also had compatible elements for a beam height of 40 mm. 8 mm thick adapter plates and optomechanical components with a beam height of 40 mm were used in this area.

The most crucial alignment spot is scan cube B. After the scan cube, the laser light has to move through the telecentric lens system and the objective. A good alignment of the mirrors in scan cube B is necessary since the number of alignment mirrors after the scan cube is limited to two. The reason for this is that the lenses of the telecentric systems need a fixed distance to the moving mirrors inside of the scan cube and to the microscope objective. To enable adjustment of the moving mirrors, both, the resonant mirror and the galvanometer mirror, have an adjustable rotation axis. The galvanometer scanner can be rotated in its mounting hole and is fixed with two screws. The resonant scanner is mounted on a rotation mount (A.1.11) that enables free rotation of the mirror. These alignment options enhance the correct propagation of the laser beam through the following telecentric lens system.

To further optimize the alignment of the scan cubes with other optical elements, the scan cubes are compatible with the chosen optomechanical system. In Figure 3.2 (b) and (c) it can be seen that the optical elements are connected with rods in a cage system. This connection significantly reduces the drift between the optical elements and simplifies the alignment. Therefore, the design of the scan cubes also enables the connection of the cubes via rods to other optomechanical elements (Figure 3.3).

Assembly group: Sample table

The assembled sample table is shown in Figure 3.4 (a) and a sectional view through the assembly group can be seen in (b). To move the sample a xy–table (A.1.37) is mounted on the sample table. Different sample plates are available to mount different experimental setups, e.g. the setup to create locally stable moving contact lines (Figure 2.16), on the table. The whole assembly was designed so that the elevator stage (A.1.31), fine positioning units (A.1.35, A.1.39) and the xy–table fit together and are aligned with the laser beam path (Figure 3.4 (b)). To enable further assemblies and modifications a common 25 mm hole grid is available on two sides of the sample table (Figure 3.4 (a)).

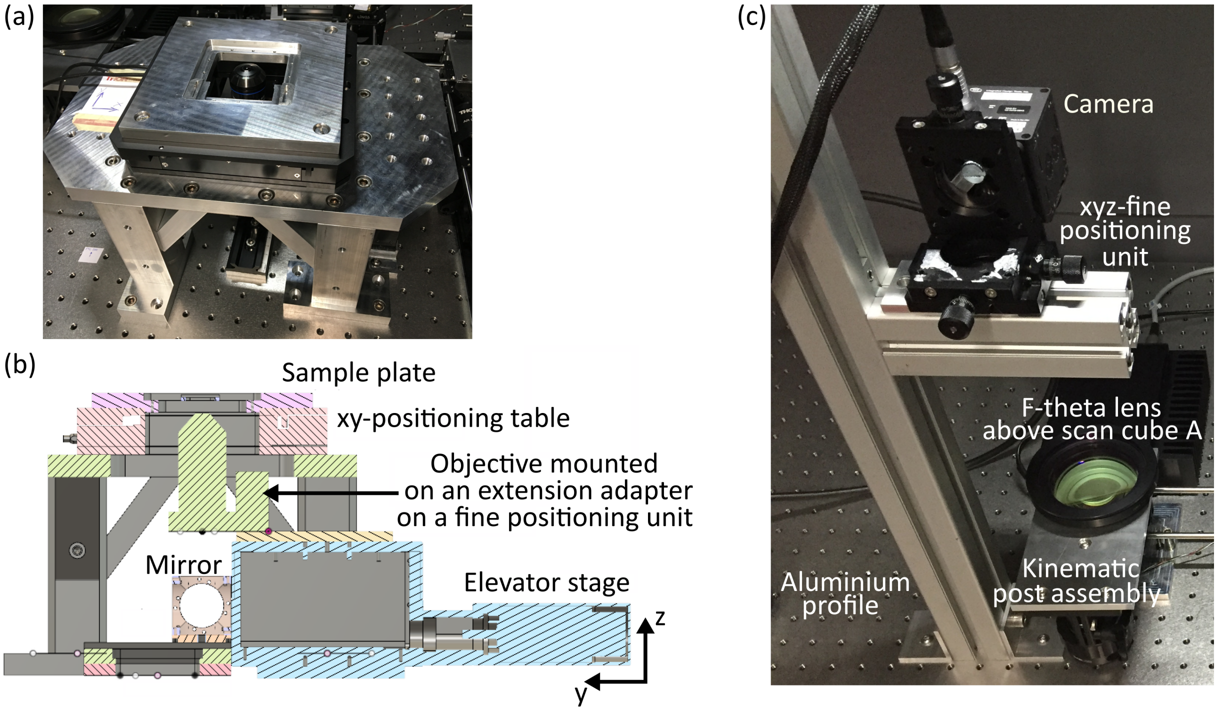

Figure 3.4.: (a) Assembled sample table. (b) Sectional view through the assembly group of the sample table (a). Adapted from [105]. (c) Assembly group camera.

Assembly group: Camera

This assembly group aligns the camera (A.1.48) and the f–theta lens (A.1.51) correctly to the beam path after scan unit A (Figure 3.4 (c)). The height of the f–theta lens is adjustable by a post assembly (A.1.6, A.1.7). The camera is mounted on a xyz–fine positioning unit (A.1.30). Rough positioning of the camera is possible by adjustment of the aluminium profile (A.4.15). Since all component joints of the assembly are perpendicular to each other, the camera sensor is placed parallel to the breadboard and perpendicular to the laser beam.

Housing box

The whole setup is encapsulated in a housing box (A.1.45). The box blocks all ambient light from disturbing any measurements. Furthermore, it blocks all laser radiation from leaving the housing and thus makes it save to work with high laser radiation. On the inside, the housing has a foam layer (A.1.53). This foam layer is fireproof and adsorbs acoustic noise. The cable openings are sealed with cable entries (A.1.52). Furthermore, the box protects optical elements like lenses, mirrors, and objectives from dust, since dust can reduce the resolution of the optical system significantly by creating interference patterns or dark spots on the image. A temperature and humidity sensor (A.1.44) is placed inside the box to monitor these values.

Control software and synchronized motion of the scanning units

The majority of electronic elements are either controlled via their manufacturer's software or via a graphical user interface (Appendix A.1.1) programmed in LabVIEW (A.6.1). The scan units and the camera are controlled via synchronized waveform generators (A.1.49, A.1.1). The wiring of the components can be found in Appendix A.1.2.

Figure 3.5 shows the synchronized motion of the scanning units. The resonant scanners are responsible for the x–motion, the galvanometer scanners for the y–motion and the objective fine positioning units for the z–motion of the laser focus point in the sample. All axes are scanned bidirectionally. The number of lines per two–dimensional frame and the number of two–dimensional frames per three–dimensional stack is adjustable by the frequencies driving the motion of the galvanic mirrors and the z–motion of the focus.

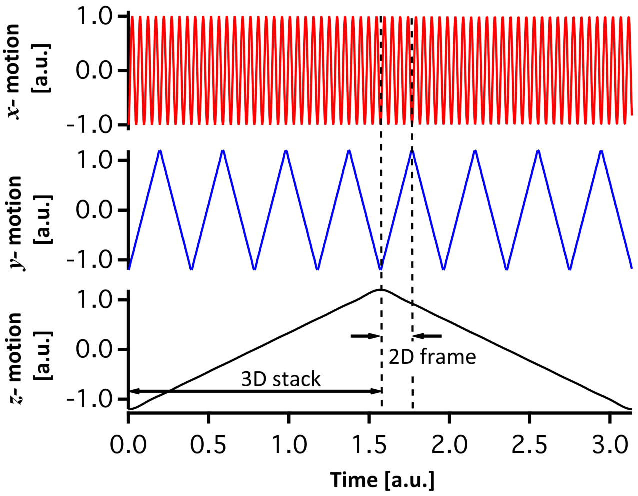

Figure 3.5.: Synchronized motion of the scanning units in the case of the three–dimensional scanning mode. Reprinted from [169], with the permission of AIP Publishing.

The resonant scanners oscillate with a fixed frequency of 15.7 kHz in a sinusoidal motion with a maximum scan angle of ±5°. A remote control (A.1.41) was designed and built to adjust the amplitude and relative phase of the resonant scanners. Both resonant scanners should oscillate with the same amplitude because otherwise, the image would be distorted and the relative phase between the mirrors must be adjusted to synchronize their motion.

The galvanometer scanners oscillate with an adjustable frequency up to 500 Hz. The motion of the scanners is controlled with a waveform generator (A.1.1) and a triangular signal with smoothed edges is used to oscillate the mirrors. This signal is superior to sinusoidal signals because it leads to an equal intensity distribution along the linear slope of the signal (Figure 3.6). The Figure shows an image of a calibration slide (A.4.12), recorded with a frame rate of 100 Hz with an oil immersion objective (A.4.19) and immersion oil

(A.5.15). The x–direction is scanned by the resonant scanners with a sinusoidal motion and the y–direction by the galvanometer scanners with the shown 80 % triangular motion. The blue rectangle marks the image area where the intensity distribution is equally distributed. The triangular signal leads to a broader area with an equal intensity distribution and a reduced peak intensity area at the smoothed edges of the reversal point compared to the sinusoidal motion. A pure triangular signal would lead to a perfectly equal intensity distribution in x–direction, but the rotation motor of the galvanometer scanners cannot follow this signal at high frequencies. Therefore, the edges are smoothed and a 80 % triangular signal is used. In standard acquisition mode, the reversal points of both the resonant and the galvanometer scanners are placed out of the field of view to increase the area with an equal intensity distribution. The z–motion of the objective follows a triangular signal for the before–mentioned reasons.

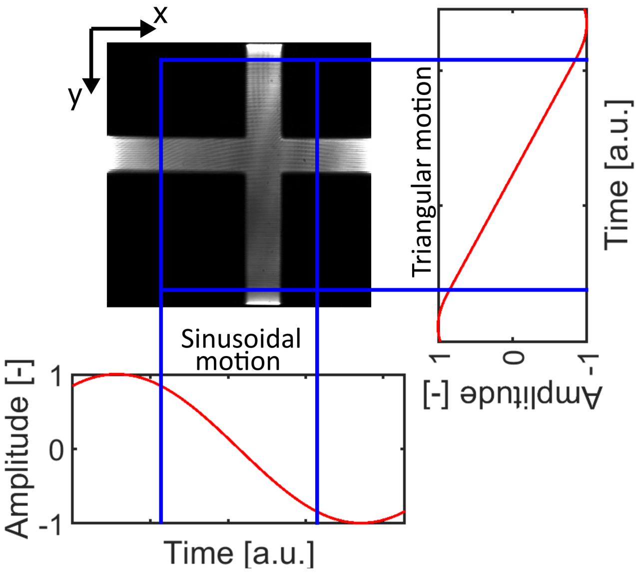

Figure 3.6.: Image of a calibration slide to show the influence of the sinusoidal and triangular mirror oscillation on the intensity distribution. The galvanometer scanners, y–direction, perform a 80 % triangular motion whereas the resonant scanners, x–motion, perform a sinusoidal motion. The area of equal intensity distribution is marked by the blue rectangle.

The camera is controlled with the manufacturer's software (A.6.5). A rectangular signal can be used to trigger the camera externally. The camera is triggered at each reversal point of the triangular signal of the galvanometer scanners. Hence, the frequency of the camera trigger signal, which equals the frame rate of the recording, is twice the frequency of the galvanometer scanners. Thus, the maximal frame rate of the setup is 1 kHz. The camera trigger signal is generated with the second output of the waveform generator.

3.1.4. Optical properties

In this section, the optical properties of the built re–scan confocal laser scanning microscope are characterized. These properties are the lateral and axial resolution, optical slice thickness, and field of view. The latter depends on the line frequencies and thus on the frame rate. Also, the dwell time of the setup is characterized and a measurement of a dense colloidal sample is shown to demonstrate the three–dimensional scanning capacities of the setup. Furthermore, a criterion to calculate the actual measurement resolution is presented.

Table 3.2 lists the parameters of the confocal microscope that are used for the calculation of the optical properties.

Table 3.2.: Parameters for the calculation of the optical properties.

Parameter	Symbol	Value
Laser wavelength	λ_{ex}	532 nm
Emitted wavelength	λ_{em}	607 nm
Numerical aperture	NA	1.35
Index of refraction	n	1.518
Pinhole diameter	d_{ph}	20 µm
Objective magnification	M_{Ob}	60

Pinhole diameter

The pinhole is the central element of a confocal microscope and its size determines the amount of collected light and the resolution of the setup. Smaller pinhole diameters increase the resolution but the amount of collected light decreases. To determine the optimal pinhole diameter for a specific optical setup, the modified pinhole diameter D_{ph} is used. The modified pinhole diameter is expressed in terms of the Airy unit (AU). 1 AU is the inner disc of the lateral diffraction pattern, see Figure 2.19. If the modified pinhole diameter is set to 1 AU, then just the inner disc of the diffraction pattern can pass the pinhole and is detected [28, 133]. In this case around 80 % of the light coming from the sample is accepted and a 10 % gain in lateral resolution, compared to the Abbe resolution limit, is achieved [37]. A general optimal pinhole size for a laser scanning confocal microscope does not exist. The pinhole diameter should be chosen to have the optimal compromise between signal strength and lateral/axial resolution [37]. The pinhole diameter should be $>$0.5 AU [133] and pinhole diameters of 0.63 AU [158] or 0.8 AU [37] are recommended.
To determine the optical properties of the setup, a pinhole diameter of $d_{ph} = 20\,\mu\text{m}$ was found to provide sufficient signal strength. The size of an Airy unit and the modified pinhole diameter for the present setup are calculated with

$$\text{AU} = 1.22\frac{\lambda_{ex}}{NA} = 473\,\text{nm} \tag{3.1}$$

$$D_{ph} = \frac{d_{ph}}{M_{Ob}} = 333.3\,\text{nm} = 0.7\,\text{AU}. \tag{3.2}$$

Resolution

The used pinhole with a modified parameter $D_{ph} = 0.7\,\text{AU}$ neither fulfils the condition for wave–optical or geometric–optical analysis (Table 2.1). However, since the used pinhole is not infinitesimal small and the geometric–optical analysis is more conservative, the theoretical resolution is calculated with the formulas for geometric–optical confocal microscopes. The theoretical lateral and axial resolution and optical slice thickness are calculated with the following formulas:

$$d_{lat,\ t} = 0.51\frac{\lambda_{ex}}{\text{NA}} = 201\,\text{nm} \tag{3.3}$$

$$d_{ax,\ t} = 0.88\frac{\lambda_{ex}}{n - \sqrt{n^2 - \text{NA}^2}} = 568\,\text{nm} \tag{3.4}$$

$$d_{slice,\ t} = \sqrt{\left(0.88 \frac{\lambda_{em}}{n - \sqrt{n^2 - \mathrm{NA}^2}}\right)^2 + \left(\frac{\sqrt{2} n D_{ph}}{\mathrm{NA}}\right)^2} = 837\,\mathrm{nm}. \tag{3.5}$$

Experimental resolution is given by the width of the focal spot in axial and lateral direction [134]. The experimental lateral resolution is determined by using the line width of the laser at the focal plane (Figure 3.7 (a)). A fully reflective calibration slide (A.4.12) is used to record the lines. The lines are separated by increasing the y–amplitude of the galvanometer scanners with a frame rate of 800 Hz. The full width at half maximum of such a line is $d_{lat,\ fwhm} = (3.8 \pm 0.2)\,\mathrm{px}$. The magnification of the setup M, i.e. the transition of pixel to micrometre, is determined with the calibration slide to $M = (17.00 \pm 1.09)\,\mathrm{px\,\mu m^{-1}}$. The experimental lateral resolution is calculated with the full width at half maximum of the intensity profile of the laser line $d_{lat,\ fwhm}$ and the setup magnification M

$$d_{lat,\ e} = \frac{d_{lat,\ fwhm}}{M} = (223.9 \pm 8.9)\,\mathrm{nm}. \tag{3.6}$$

A way to experimentally determine the axial resolution is an axial two–dimensional scan of an infinitesimal small reflection, e.g. mirror or fully reflective surface [86]. To measure the axial resolution, the surface of a blank glass slide (A.5.1) is used as the reflective surface. Since an oil immersion objective is used, the glass–air boundary reflects sufficient light and is assumed to be an infinitesimal thin plane. Figure 3.7 (b) shows the axial two–dimensional–scan through the glass boundary with the corresponding intensity profile perpendicular to the glass surface. The full width at half maximum of this intensity profile is $d_{ax,\ fwhm} = (10.2 \pm 0.4)\,\mathrm{px}$ and the experimental axial resolution is calculated with

$$d_{ax,\ e} = \frac{d_{ax,\ fwhm}}{M} = (602.4 \pm 25.1)\,\mathrm{nm}. \tag{3.7}$$

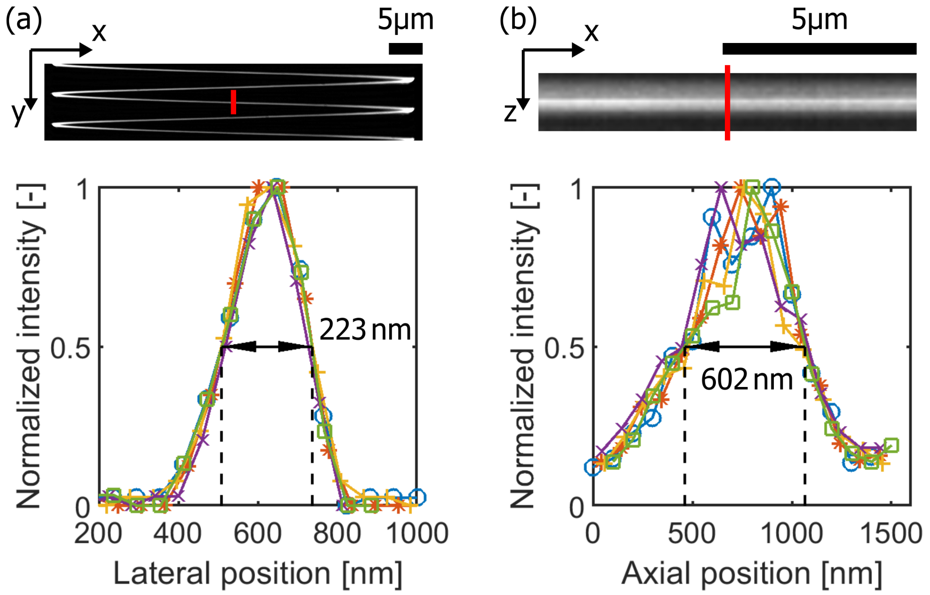

Figure 3.7.: Experimental determination of the (a) lateral and (b) axial resolution of the custom–built confocal microscope. The resolutions were averaged over five different measurements.

Both experimentally determined values are slightly worse than the theoretical values. This is expected since the present setup only barely fully illuminates the objective pupil and therefore the usable numerical aperture of the objective is reduced.

The field of view depends, next to the used objective, on the sampling rate of lines per picture. The size of the camera sensor is $1024 \times 1024\,\text{px}^2$. With a line width of four pixel ($d_{lat,\ fwhm} = (3.8 \pm 0.2)\,\text{px}$), the optimum amount of lines per picture should be 256. In practice, however, the lines cannot be equally distributed in the image. The frequency of the galvanometer scanners sets the line distribution in the image. Since a 80 % triangular signal is used, the line density at the image borders is higher than in the centre. However, for optimal results, the distribution should be equal in the entire image. A simple way to optimize the line distribution is to cut off the image borders or to adjust the amplitude of the signal so that the reversal points lie outside of the image.
The number of possible lines N_{lines} per image depends on the desired frame rate and can be calculated via

$$N_{lines} = \frac{f_{res}}{f_{galvo}} = \frac{2f_{res}}{f_{cam}} = \frac{31\,400\,\text{Hz}}{f_{cam}}\text{lines} \tag{3.8}$$

with the fixed frequency of the resonant scanners f_{res}, the adjustable frequency of the galvanometer scanners f_{galvo} and the frequency of the camera f_{cam}. The latter is twice the frequency of the galvanometer scanners because a picture is taken at each turning point of the galvanometer signal.
Depending on the camera frequency the number of lines changes and the field of view varies (Figure 3.8). Figure 3.8 (a) to (d) show images of a reflective line grid (A.4.13), recorded with varying frame rates (f_{cam}). In the case of $f_{cam} = 100\,\text{Hz}$ (Figure 3.8 (a)), the number of lines could be 317. This would lead to a slight oversampling which has no disadvantage when static samples are recorded but it would lead to blurred images in case of dynamic processes. To prevent this oversampling the number of lines is reduced to 256. The number of lines for a frequency of $f_{cam} = 800\,\text{Hz}$ (Figure 3.8 (c)) is 39.25 which would lead to a strong undersampling. To circumvent this, the amplitude of the galvanometer scanner and thus the field of view is reduced (see the yellow lines in Figure 3.8 (b) to (d)).

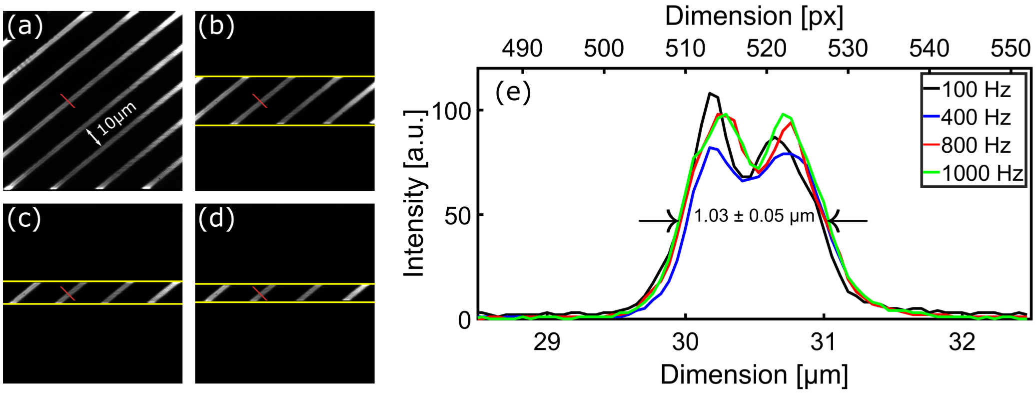

Figure 3.8.: (a) to (d) give the same area of a reflective line grid with a $10\,\mu\text{m}$ spacing between the lines and $1\,\mu\text{m}$ thick lines at different frame rates. The thickness of the grid line is correctly recorded for all frame rates and the averaged value at the full width of half maximum is $(1.03 \pm 0.05)\,\mu\text{m}$. The yellow lines mark the reduced width of the field of view at high frame rates. (e) The superposition of the line profiles along the red line in (a) to (d) illustrates the independence of the lateral resolution of the frame rate. Reprinted from [169], with the permission of AIP Publishing.

Independent of the camera frequency the thickness of the grid line is correctly recorded for all frame rates with an averaged value of the full width at half maximum of $(1.00 \pm 0.05)\,\mathrm{\mu m}$ (Figure 3.8 (e)). Thus, the magnification M and the resolution of the setup are independent of the frame rate.

Realistic sample: fluorescently labelled colloids

To show the three–dimensional scanning capacities of the built microscope, a volume of a colloidal probe was recorded. Figure 3.9 (a) shows a xz–cut through a recorded volume of colloidal particles. The colloids are silica particles labelled with rhodamine B (A.5.10). They have a mean diameter of $(10.0 \pm 1.7)\,\mathrm{\mu m}$ and details about their preparation are given in [151, 181]. An index matching solution of sodium thiocyanate (A.5.11) in water was prepared with a mismatch of the refraction index $\Delta n \leq 0.0005$. Larger mismatches would lead to scattering and diffraction within the first layers of the sample and would prohibit the scanning of deep layers [57]. The colloids are dispersed in the solution and sediment to the bottom of the measurement cell due to gravity. The probe was recorded with a three–dimensional stack rate of 0.4 Hz and a two–dimensional frame rate of 800 Hz. The focal plane was moved in axial direction by moving the objective with a piezoelectric stage. The colloids are correctly recorded with a full width at half maximum around $10\,\mathrm{\mu m}$ (Figure 3.9 (b)).

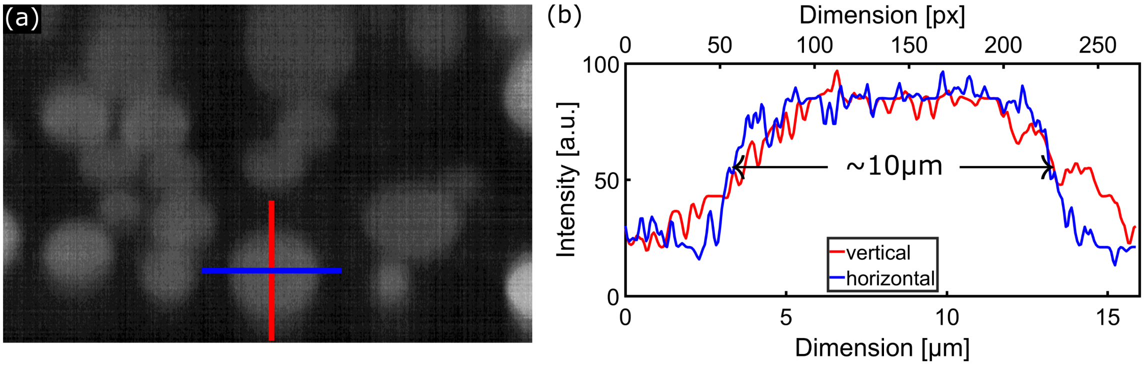

Figure 3.9.: Image and analysis of a three−dimensional sample of sedimented fluorescent colloids with a mean diameter of $10\,\mathrm{\mu m}$. (a) shows a xz−cut through the measured three−dimensional volume and (b) shows the intensity values along the blue (lateral or x−direction) and red (z−direction, vertical to the sample plane) line. The lateral and vertical full width at half maximum of the marked colloid is $10\,\mathrm{\mu m}$ in both directions. Reprinted from [169], with the permission of AIP Publishing.

Photobleaching

The loss of the ability to fluoresce of fluorescent dyes is called photobleaching [56]. This results in the weakening of the fluorescent signal coming from the sample during measurements. To reduce the amount of photobleaching either the excitation light intensity is reduced or the excitation time, i.e. the dwell time t_{dwell}, is reduced [56, 76]. However, both, reduction of the excitation light intensity and excitation time still lead to a reduction of the fluorescent signal.

The dwell time of the present setup is the time that is needed to scan an area of the size of the optical resolution ($d_{ax,\ fwhm} = 3.8\,\mathrm{px}$). The frequency of the resonant scanners is constant at 31 400 Hz and thus, the focal spot scans 31 400 lines s^{-1}. The dwell time depends on the scanned area, i.e. the field of view. The width of the field of view depends on the amplitude of the resonant scanners A_{res}. If the whole camera chip is used, the maximum field of view corresponds to 1024 px which is scanned by a single motion of the scanner, i.e. by one line. The dwell time of the setup can be calculated if a triangular motion of the resonant scanners is assumed via

$$t_{dwell} = \frac{d_{ax,\ fwhm}}{f_{res}\ A_{res}} = \frac{3.8\,\mathrm{px}}{31\,400\,\mathrm{lines\,s^{-1}}\ 1024\,\mathrm{px\,line^{-1}}} = 118\,\mathrm{ns}. \tag{3.9}$$

This dwell time is significantly shorter when compared to other setups. Spinning disc setups have dwell times in the microsecond range and most confocal laser scanning microscopes working with single–photon counting have dwell times higher than 1 µs. Short dwell times reduce photo toxicity and bleaching [56, 76]. This is verified by comparing the lifetime of the sample when using different microscopes. The present setup has a high intensity around 11 mW $\mu\mathrm{m}^{-2}$ in the focus of the objective. Still, it was possible to measure sedimented colloidal particles (silica labelled with rhodamine B, see the previous section) more than 8000 times without a significant amount of bleaching. Identical samples were measured in previous works [151, 181] with a different laser scanning confocal microscope. Although the intensity in the focal spot was only around 90 nW $\mu\mathrm{m}^{-2}$, the same spot could only be measured around 600 times due to a dwell time around 5 µs.

Sample quality

As already mentioned, the best possible resolution of the confocal microscope is limited by the wavelength of the light, the numerical aperture, and the spot size of the laser focus in axial and lateral direction [134]. Although the earlier presented theoretical and experimental calculation of the resolution is correct, the calculated resolution values can hardly be reached in experiments. The reason is that the sample itself has an influence on the image quality, i.e. signal–to–noise ratio, and resolution. Especially in three–dimensional scanning even a slight refractive index mismatch lowers the resolution drastically [57]. Therefore, a criterion to calculate the resolution of any measurement sample would be beneficial.

The calculation of the resolution with the full width at half maximum (Figure 3.7) primarily depends on the edge steepness of the detected intensity profile. Thus, a valid option to calculate the resolution of any measured intensity profile is the usage of its edge steepness. Here, the width of the edge steepness is used as a criterion for axial/lateral resolution. For this purpose, the slope of the intensity profile is fitted with a hyperbolic function

$$f_{hyp} = p_1 \pm p_2 \tanh\left(\frac{x - p_3}{p_4}\right),\ \pm \text{ rising or falling edge} \tag{3.10}$$

with the fitting parameters p_i. A hyperbolic function was chosen since it is suited perfectly to fit the slopes of intensity profiles for most specimen. The resolution is defined as the lateral distance between the 10 % and 90 % value of the maximum amplitude of the hyperbolic function.

This criterion is used to calculate the resolution of the lines of the reflective grid (Figure 3.8). The lateral resolution of the calibration grid is calculated by fitting the hyperbolic function to the intensity profiles of Figure 3.8 (e) to $d_{lat,\ grid} = (329 \pm 35)\,\mathrm{nm}$. The lateral resolution of the calibration grid strongly depends on the manufacturing quality of the grid lines.

The intensity profiles of the sedimented colloids (Figure 3.9 (b)) were fitted with the hyperbolic function as shown in Figure 3.10. A lateral resolution $d_{lat,\ col} = (1.34 \pm 0.23)\,\mu\mathrm{m}$ and an axial resolution $d_{ax,\ col} = (4.12 \pm 0.10)\,\mu\mathrm{m}$ were calculated. At first glance, the calculated resolution for the colloids seems low. However, it is important to emphasize the meaning of these numbers. The resolution indicates the minimum required distance between two objects in order to distinguish between them. Since the colloids have a diameter of $(10.0 \pm 1.7)\,\mu\mathrm{m}$, the calculated resolution shows that it is possible to tell each individual colloid in lateral and axial direction apart, i.e. to resolve each colloid. Also, those resolution values are only valid for the measured colloids (Figure 3.9 (b)). Other samples, e.g. the grid lines, have different individual resolutions as shown above. The best reachable resolution of the current microscope configuration for any sample is limited by the resolution calculated with the full width at half maximum (Figure 3.7).

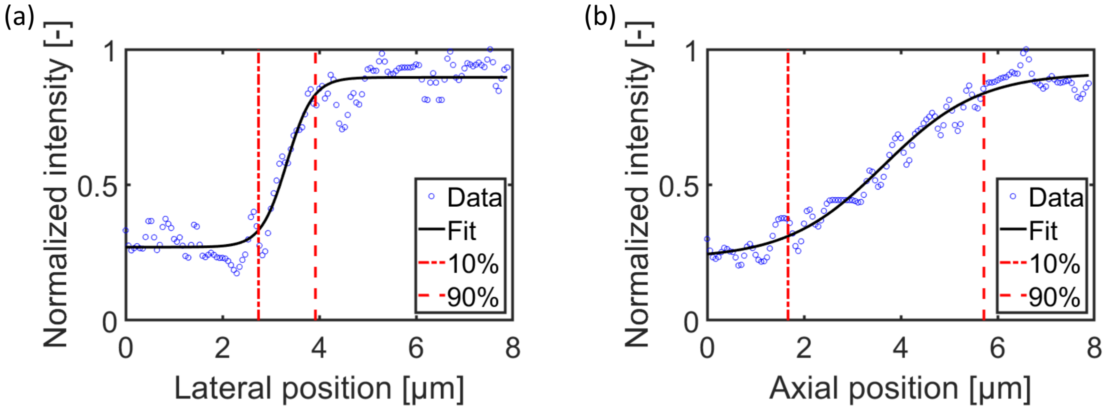

Figure 3.10.: Fits using equation 3.10 to the (a) lateral and (b) axial intensity slopes of the measured sedimented colloid (Figure 3.9 (b)). The vertical lines mark the 10 % and 90 % value of the maximum amplitude of the hyperbolic function and the distance between the vertical lines is defined as the resolution.

All calculated sample resolutions are worse than the best possible resolution that was calculated with the full width at half maximum. However, it is expected that the resolution of a real sample is worse than the best possible resolution for the following reasons: The quality of the sample, e.g. grid lines or labelled colloids, plays a major role. The colloids have a finite surface roughness and the distribution of the dye might have gradients close to the surface, leading to a relatively flat edge steepness and thus a low resolution. A major influence has the index–matching solution. Minor imperfections of the index–matching could lead to refraction at each optical interface. Thus, each particle surface and the surfaces of the measurement cell could lead to refraction effects. These effects reduce the image quality greatly and result in a reduced signal–to–noise ratio and thus in a reduction of the resolution. This particularly affects the axial resolution. Overall, the detected fluorescent light from the colloids has a lower signal intensity than reflected light, further reducing the signal–to–noise ratio.

It was shown that depending on the used resolution criterion, e.g. full width at half maximum or hyperbolic fitting, different resolutions were calculated. Since the resolution depends crucially on the quality of the sample, the resolution should be recalculated for every measurement probe.

3.1.5. Extensions

The above described standard configuration of the setup enables fast two–dimensional scanning with a frame rate up to 1 kHz. Axial scanning is realized by moving the objective with a piezoelectric scanner. An xz–scan is possible with a frame rate of 200 Hz with a z–amplitude of 100 µm. However, fast movements of the objective can disturb the sample. Several remote focus techniques exist, e.g. tunable lenses or addition of objectives in the beam path. These techniques enable movement of the focal plane through the sample without disturbing it. Preliminary tests with a tunable lens (A.1.3) lead to unsatisfactory results due to optical aberrations caused by the lens.

A remote focus technique based on the idea of [48] was added to the setup. Two additional objectives are placed face to face in the beam path. By moving one of these additional objectives, the focal plane is moved through the sample. Thus, the movement of the objective is decoupled from the sample. Since only high-quality objectives are added to the beam path, no additional optical aberrations occur. The technique is aberration–free and usable for high numerical aperture objectives [48].

The mentioned remote focus techniques aim to scan the whole three–dimensional volume by moving the focal plane. This is necessary if dense colloidal probes (Figure 3.9) or biological samples are measured. However, the measurement of flow fields is also possible without scanning the entire three–dimensional volume. In section 2.7.3 the method APTV was presented. This method enables the measurement of three–dimensional flow fields without the need for a moving focal plane. Thus, no moving parts at all are necessary. Because an APTV setup was also built in this work (section 3.2), the combination with the custom–built confocal microscope was a matter of course. Since APTV works with out–of–focus information, the method cannot be used with the standard design of the confocal microscope. This is because the pinhole blocks most out–of–focus light. However, since the beam path is easily accessible an additional fluorescent detection beam path could be added to the confocal microscope. This approach combines confocal detection with synchronized fluorescence detection. By using a cylindrical lens in the fluorescence beam path, synchronized high–resolution confocal and APTV measurements are possible.

The realization of the remote focus technique is presented in the following section. Thereafter, the combination of confocal and APTV measurements is presented.

Remote focusing using two additional objectives

This extension is based on ideas of [48] and utilizes two additional objectives in the beam path to change the position of the focal plane. The changed part of the beam path is shown in Figure 3.11. Two additional objectives O2 and O3 (A.4.20) and two tube lenses (A.1.10) are added to the beam path. The objectives are placed face to face and objective O3 can be moved with a piezoelectric stage (A.1.35). Objective O2 is mounted in a xyz–translation unit (A.1.4) to align the objectives. If objective O3 is moved, the focal plane is moved through the sample.

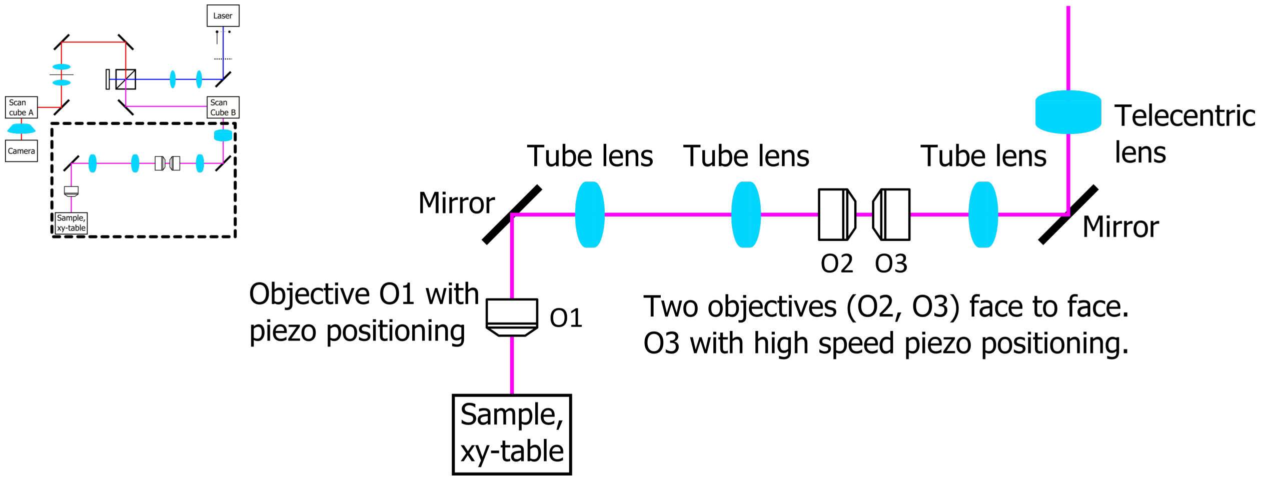

Figure 3.11.: Optical assembly of the remote focus technique. The marked region on the left shows the changed region of the beam path as part of the standard configuration (Figure 3.2).

Measurements of polystyrene particles with a diameter of 2 µm (A.5.14) embedded in a PDMS matrix are shown in Figure 3.12. All images show the same field of view. Figure 3.12 (a) shows the image of a particle in the reference position of objectives O1 and O3. By moving the objective O1 18 µm downwards, the focal plane is moved and the particle is no longer detected. The movement of objective O3 by 14 µm leads to the detection of the particle (Figure 3.12 (a) bottom image). Thus, the movement of objective O3 moved the focal plane and an image of the particle is recorded. The same is shown in Figure 3.12 (b) for a second particle with different objective positions.

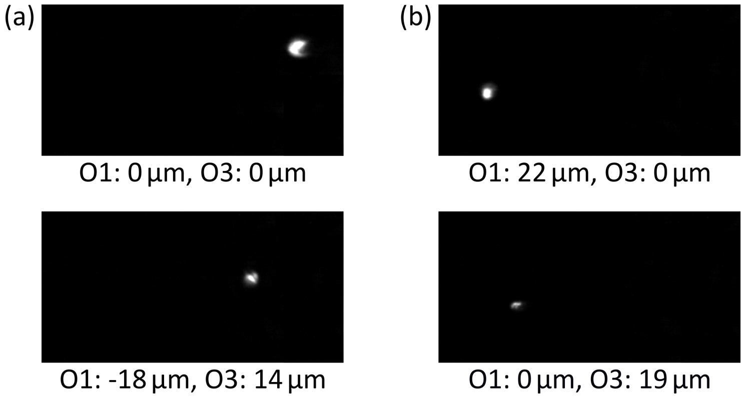

Figure 3.12.: Recorded particle image shapes using the remote focus extension. All images show the same field of view. (a) Particle images of the same particle but with different objective positions. (b) Images of a second particle with different objective positions.

It is possible to remotely move the focal plane through the sample with the above–described assembly. However, the optical path is not aberration–free. The lateral position of the particle image differs in the top and bottom images (Figure 3.12). Since [48] showed that the method works without aberrations, the here used alignment of the objectives is imperfect. A minor pitch angle between the objectives is likely the reason for the observed aberration. To correct this error, objective O2 was mounted on a five–axes table (A.1.5). Yet, it was not possible to correct the aberration.

Further changes to the beam path and the mounting of the objectives are necessary to eliminate the aberration. Additional mirrors could be placed before and after the objectives O2 and O3 to align the laser beam perfectly with the objective assembly. The correct alignment of the objectives to each other is crucial.

Astigmatism particle tracking velocimetry

The idea of this extension is to combine a high–resolution confocal detection with a synchronized APTV measurement. Since, next to the confocal microscope, an APTV setup was built in this work (section 3.2), the idea to combine both methods was a matter of course. Figure 3.13 shows the beam path of the APTV configuration of the built confocal microscope. The general idea is to detect the emitted fluorescent light with a second camera while the reflected light is detected by the camera of the confocal microscope. For this purpose, a dichroic mirror (A.1.15) was placed between the telecentric and the tube lens. This dichroic mirror reflects only the emitted fluorescent light while the reflected light penetrates and is used for the standard confocal detection. Behind the dichroic mirror is an additional longpass filter (A.1.18) placed in order to eliminate remaining excitation light. The fluorescent light is detected by a second camera (A.4.9) with a cylindrical lens (A.2.11) in front of the camera chip. The APTV camera is triggered by the same signal being used for the standard camera and thus, a parallel confocal and APTV recording is possible.

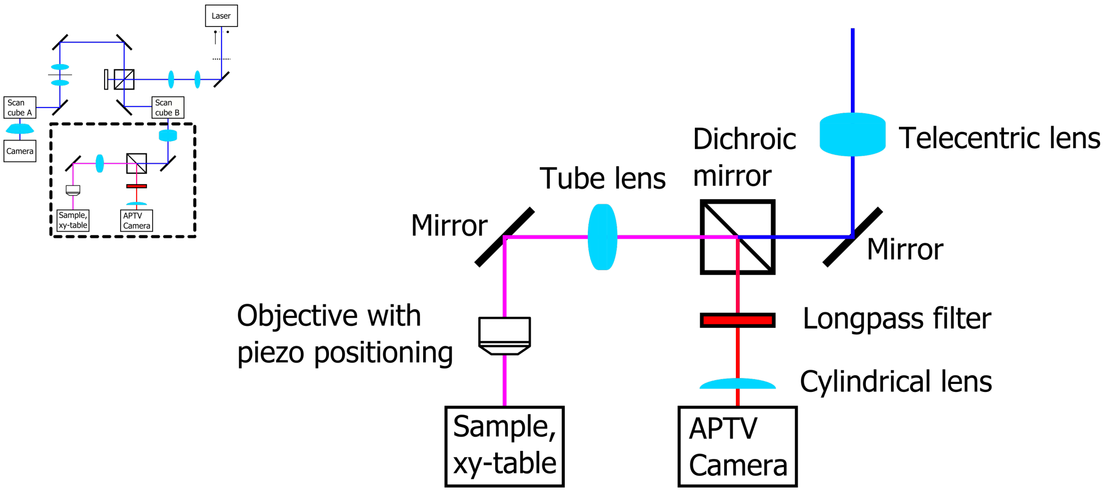

Figure 3.13.: Optical assembly of APTV configuration. On the left, the changed region of the beam path as part of the standard configuration (Figure 3.2) is marked.

Images of different axial positions of fluorescently labelled particles with a diameter of 4 µm (A.5.14) were recorded with a 20 X objective (A.4.18) and a cylindrical lens with a focal length of 50 mm (Figure 3.14). The first row shows the confocal reflection and the second row shows the APTV images of the particles for different axial positions. The confocal beam path can only record particle images when the particles are within the focal plane of the objective at position $z = 0\,\mu\text{m}$ due to the pinhole. On the other hand, APTV records images for various axial positions since this part of the beam path equals a fluorescent microscope and has no pinhole to block out–of–focus information. The images of the particles are deformed to distinguishable ellipsoidal shapes, depending on the relative distance of the particle from the focal plane. The out–of–plane particle position can be calculated using the particle image shape. A detailed description of the APTV data analysis is given in section 3.2. These images also proof that both cameras record the same field of view.

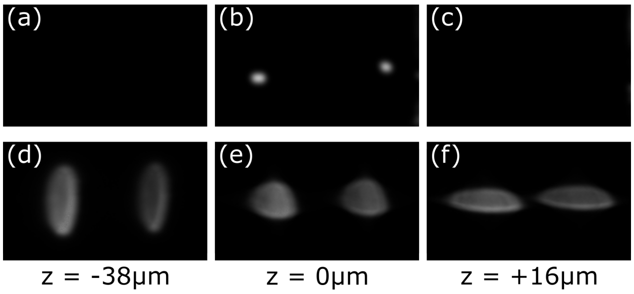

Figure 3.14.: Comparison of (a, b, c) confocal and (d, e, f) APTV images of fluorescently labelled particles for different focus heights (z). The confocal microscope can only detect particle images when they are within the focal plane ($z = 0\,\mu\text{m}$). APTV detects different particle image shapes depending on their axial position. Reprinted from [169], with the permission of AIP Publishing.

The main advantage of this configuration is, next to the three–dimensional image capacity of the APTV, its combination with a parallel confocal measurement. Thus, it combines all advantages of a confocal microscope with an APTV device. The confocal detection can be used to record a specific two–dimensional plane through the sample with high accuracy while the APTV detection records three–dimensional trajectories of tracer particles around the focal plane. Further measurement options are possible, if additional excitation wavelengths, i.e. additional lasers, are added to the setup. Then, both, confocal and APTV, can be used in fluorescent mode, enabling further measurement possibilities.

3.1.6. Possible improvements to the setup

The described custom–built re–scan confocal laser scanning microscope with the mentioned configurations has unused potential. Several design aspects could be changed to improve resolution and scanning capacities.

The main design compromise of the setup is between high–speed capacities and resolution. To enable the high scanning speeds, resonant mirrors with a small mirror size were used. Due to the small mirror size, the pupil of the objective is barely fully illuminated and thus the resolution of the setup decreases. An over–illumination of the objective pupil would increase the resolution, but larger mirrors would limit the resonance frequency and thus, the maximum frame rate of the setup. Another option to increase the illumination of the objective aperture is to include additional optical elements, i.e. a telescope, after scan cube B to increase the beam diameter and over–illuminate the pupil. However, this would further increase the needed alignment and adjustment effort.
The whole setup is placed inside a housing box to minimize the influence of stray light. Since the camera and other electrical elements emit heat, the temperature in the housing box increases during measurements. Repeated heating and cooling of the optical elements cause them to drift leading to additional alignment and adjustment efforts. A cooling system with active temperature control and dust filtering could solve this problem.
Furthermore, the pixel size of the camera sensor should be adapted to the spot size of the laser beam. The used camera has a relatively small sensor and a pixel size of $13.9 \times 13.9\,\mu\text{m}^2$ leading to a spot size diameter of around 3.8 px. For optimal usage of the camera sensor, the spot size should be one pixel or slightly larger. Smaller pixel sizes should be evaded since this would lead to oversampling. An optimal pixel size would increase the sensitivity of the setup and signal–to–noise ratio.

The three–dimensional scanning capacities of the setup could be further improved. The standard configuration uses piezoelectric stages to move the objective up and down. The fast piezoelectric stage enables axial scanning speeds with several hundred hertz. However, the coupling between objective and sample due to the immersion oil limits the axial scanning speed. Air objectives could be used to circumvent this problem at the expense of resolution. Another option to circumvent the coupling problem is the use of tunable lenses [15, 17, 59, 60, 77, 96, 113, 125, 130, 159]. These lenses are placed at the aperture of the objective and alter the laser beam enabling axial scanning of different planes without moving the objective. Although preliminary tests with a tunable lens lead to unsatisfactory results, new generations of tunable lenses might be suitable.
Two configurations were presented to enable fast three–dimensional measurements. It was shown that the remote focus technique using two additional objectives is working but optical aberrations occur. The positioning and alignment of the additional elements need to be redesigned, as explained in the previous section about this configuration. The alignment of the APTV configuration needs improvement to enhance the image quality of the APTV camera. The APTV camera must be replaced with a high–speed camera

since the utilized camera was a webcam with relatively low quantum efficiency. The additional dichroic mirror can be optimized to reduce the loss of light intensity.

3.2. Astigmatism particle tracking velocimetry

In this section, the built APTV setup is presented. The general working principle of APTV was described in section 2.7.3. Since it is possible to measure three–dimensional velocity fields without any moving parts with APTV, I decided to built an APTV setup.

In the following, the setup components and the developed measurement and data processing software are described. Furthermore, the calibration of the setup is explained and the uncertainty of the particle detection is calculated. As before, when describing the methods or setups, reference is made to the tables in the appendix for more details on the components, software or consumable material.

3.2.1. Description of the setup

In this work, a Leica DMI6000 B inverted research microscope (A.2.7) was transformed into an APTV setup. The only part that needed to be changed was the standard camera adapter (A.2.8) because the cylindrical lens (A.2.11) must be included in front of the camera chip. Since the used camera (A.2.3) weighed around 8 kg, a camera mount was also needed.

Camera adapter

Every camera chip has, depending on its size, an optimal distance to the internal components of a microscope. The microscope manufacturer's camera adapter is designed that way. The main requirement for the new camera adapter is that the distance between the camera chip and microscope does not change. Furthermore, it is beneficial to be able to rotate the cylindrical lens in the APTV adapter. That way it is easier to adjust the cylindrical lens.
The designed APTV camera adapter consists of different lens tube components (A.2.9), a rotation mount (A.2.10) for the cylindrical lens and a microscope connector (A.2.2) to connect the adapter with the camera port of the microscope. Depending on the measurement requirements, the adapter can be easily disassembled and reassembled. Therefore, the cylindrical lens or the distance between the lens and camera chip can be changed. Figure 3.15 shows the APTV camera adapter.

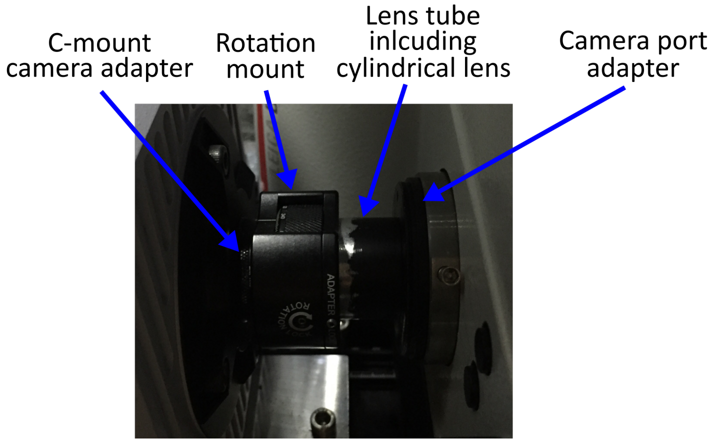

Figure 3.15.: The designed and built APTV camera adapter enables a free rotation of the cylindrical lens and has the same length as the standard adapter.

Camera mount

The construction of a camera mount was necessary to support the weight of the camera and align the camera chip perpendicular to the light beam coming from the microscope. Mounting plates were designed to mount the camera on a linear rail system (A.2.1). The whole rail system and the microscope were placed on top of a breadboard (A.2.6) and the microscope was fixed to a specific position and height. The height adjustment was necessary since the camera chip position is higher than the camera port of the microscope when both the camera and microscope are placed on the same surface. Figure 3.16 shows an overview of the final APTV setup.

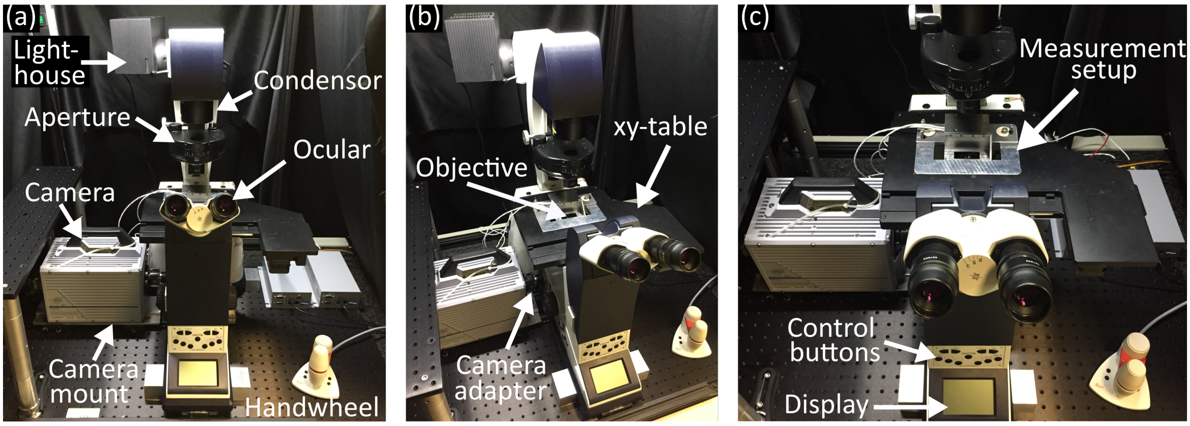

Figure 3.16.: (a-c) Different pictures of the built APTV setup with the mounted measurement setup (Figure 2.16).

Miscellaneous components

To further improve the image quality and reduce intensity losses several components were added: A new filter cube (A.2.1) was designed and installed in the fluorescence microscope. The components of this filter cube were chosen to fit the excitation (530 nm) and emission (607 nm) light wavelengths of the used tracer particles perfectly that are used for the flow field measurements. New high–quality objectives (A.4.16, A.4.17) were added to the setup to increase the image quality.
The whole setup was encapsulated with a housing box (A.2.5) to block ambient light and airflow from disturbing the measurements. It also protects the optical elements from dust. The housing consists of an aluminium frame (A.4.15) with a laser curtain. The whole setup was placed on top of a dampening table (A.2.4). Furthermore, a temperature and humidity sensor (A.2.12) is placed next to the measurement area.

3.2.2. Software

The usage of APTV required the programming of two extensive software packages. The first software package, i.e. the control software, was written in LabVIEW to control the Leica DMI6000 B inverted research microscope. Especially an automated calibration routine was necessary to enable fast and simple calibration of the setup. The graphical user interface of the programmed control software can be found in Appendix A.2.2. The second software package, the data processing software, was written in Matlab (A.6.2) to analyse the recorded images. In the following, the control software, a calibration routine, the data processing software and the uncertainty of the particle detection are presented.

Control software

The programming of the control software was necessary to enable fast and easy calibration of the APTV setup. For this purpose, the motorized stages, i.e. xy–table and z–positioning unit of the objective, of the microscope must be controlled. In addition, the high–speed camera must be either controlled or triggered with the software to record the calibration images. The available manufacturer's software (A.6.7) was not sufficient for these applications. The manufacturer's software can be used to change some basic settings of the microscope like the sensitivity of the handwheel or the settings of the objective revolver. However, the available software could not be used to control the motorized stages which is necessary to calibrate the APTV setup. Therefore, I programmed a software package to control the microscope using LabVIEW. The programmed user interface of the control software can be seen in Appendix A.2.2. All important parameters of the microscope are monitored in realtime and several automated calibration routines are available. In the following, the control software and thereafter an automated calibration routine are briefly presented. The written programmes in LabVIEW are called virtual instruments (VIs) and in the following the term VI or VIs refers to the written programmes.

Directly after the initialization of the connection between the control software and the microscope, the xy–table and the z–positioning unit of the microscope objective carry out a reference run. This guarantees that all motorized stages, i.e. the xy–table and the z–positioning unit, are correctly referenced and the correct position of the stages is shown in the user interface of the VIs. The status of all microscope parameters, i.e. position of motorized stages, handwheel status, etc., is updated every 250 ms. A temperature and humidity sensor is also connected via a serial connection and the data is updated every 250 ms. The software allows moving every motorized stage and component of the microscope. Furthermore, the movement speed of the xy–table and z–positioning unit can be controlled. A motorized stage can be moved either to an absolute position regarding the travel range of the stage or to a position relative to its current position. The excitation light shutter and the handwheel of the microscope can be switched on and off via the user interface. When the connection is terminated, the z–positioning unit automatically moves to the lowest possible position and the microscope can be turned off. This is necessary to prevent collisions between the xy–table and the mounted objective.
The high–speed camera is controlled via the manufacturer's software (A.6.6) and not directly via VIs. However, it is necessary that the VIs can trigger the camera, i.e. the VIs send a signal to the camera to take a picture or start a recording. This is crucial for the calibration of the APTV setup as will be shown later. For this reason, the measurement computer is equipped with a multifunction I/O device (A.2.13) which is connected to a break–out board (A.2.14). With these components, the VIs can send or receive additional digital or analogous signals. The break–out board is connected to the camera and thus enables the communication between the camera and the VIs. This connection enables triggering the camera via the VIs. In addition, the camera sends a signal every time a picture is taken. Therefore, it is possible to control whether the correct amount of pictures was taken, e.g. during a calibration. It is also possible to trigger and synchronize multiple cameras with the developed VIs.
Every APTV measurement and calibration is started by the VIs. The VIs trigger the connected camera and the recording of the measurement starts. The software automatically creates a data–sheet for each measurement and calibration. This data–sheet includes every important measurement detail, i.e. type of camera adapter, the focal length of the cylindrical lens, type of measurement, information about the measurement solution, etc. This information must be entered into specified input boxes of the user interface. Several options are available via dropdown menus but individual entries are also possible. During measurements, the VIs automatically records the current temperature, relative humidity, and position of all motorized stages in the data–sheet. A new entry of these values is made every second during a measurement. The

information saved in the data–sheet is used by the data processing software. An exemplary data–sheet can be seen in Appendix A.2.3.

Calibration

As already mentioned in section 2.7.3, a calibration of the APTV setup is needed. Depending on the distance between the microscope objective and the particle, different particle image shapes are recorded. To calculate the out–of–plane coordinates of particle images a calibration is needed. Therefore, reference particles are recorded with known axial positions. The detected particle image shapes and corresponding axial positions are combined and this way a calibration is compiled. The calibration is used to calculate the axial position of particle images that were recorded during measurement. In this section, the recording of a calibration dataset is explained.

The VIs enable different calibration routines. It is possible to do only a z–calibration, meaning that only the objective is moved by the z–positioning unit of the microscope with a known step size, and after each motion, an image is taken by the camera. It is also possible to do a xyz– or zxy–calibration. In the following a standard z–calibration is explained in detail.
During a z–calibration the focal plane is moved stepwise through a sample of sedimented fluorescent particles with a predetermined distance between each step. A sketch of a calibration measurement is shown in Figure 3.17 (a). Before it is possible to start the calibration, it is necessary to define the start position of the z–positioning unit, the number of steps, and the step size. To exclude possible errors like moving one motorized stage into the electronic or mechanical stop, the input parameters are checked by the VIs before it is possible to start the calibration. The VIs disable the handwheel and the xy–table to prevent any disturbances during the calibration. The VIs check if with the current settings an existing calibration data–sheet would be overwritten and prevents this by adjusting the name of the new data–sheet. Then, a new calibration data–sheet is created and the main loop of the calibration starts. The z–positioning unit is moved to the start position and after a brief delay time, the camera is triggered. The VIs wait until confirmation of the camera is send that a picture was taken. If this confirmation is missing the loop ends and an error message pops up. Otherwise, the current position of the z–positioning unit is entered into the data–sheet. Then, the z–positioning unit is moved to the next position and the calibration loop does another iteration until the last picture has been taken. If the last iteration step has been carried out, the loop ends, the internal shutter of the microscope is closed to prevent bleaching of the fluorescent particles, and all control units, e.g. handwheel and xy–table, are enabled. During the calibration measurement, a progress bar shows duration and progress.

Recorded particle image shapes of a z–calibration can be seen in Figure 3.17 (b). The sedimented fluorescent tracer particles had a diameter of $2\,\mu\text{m}$ (A.5.14) and were recorded with a 40 X objective (A.4.16) and a cylindrical lens with a focal length of $150\,\mu\text{m}$. Illumination was provided by the mercury lamp of the microscope. Depending on the out–of–plane particle position (z–position) the particle images were deformed to different elliptical shapes. The position of the z–positioning unit was increased from left to right (Figure 3.17 (b)). However, since the objective was moved upwards, and the recorded particle stays at the same position, the distance between the objective and the particle decreases from left to right. The origin of the relative z–axis is defined at the particle that has the lowest distance to the objective (particle on the right). It is directed towards the particle with the highest distance to the objective (particle on the left).

The above–described calibration routine moves the objective to record the shape of reference particles.

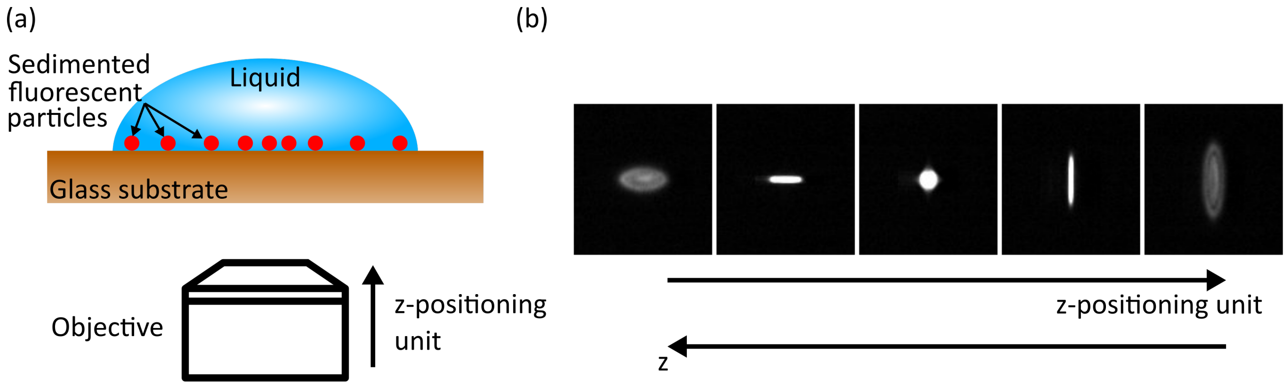

Figure 3.17.: (a) Sketch of a calibration measurement. (b) Recorded particle image shapes depending on their distance to the objective with the distance decreasing from left to right.

However, this is not an in–situ calibration. In the case of an in–situ calibration the calibration target, i.e. the fluorescent particles, are moved in the measurement liquid while the objective remains at a fixed position. Since the calibration is not done using an in–situ calibration target, an additional correction of the axial particle position is needed, if the immersion medium of the objective and the measurement fluid have different refractive indices. Since the used objectives use air as an immersion medium ($n_{air} = 1$) and the measurement fluids are aqueous solutions ($n_{water} = 1.33$ [172]), a correction is needed. The correction using the correct trigonometric relation with the numerical aperture of the objective lens is [31, 124, 150]

$$z_{water} = k\ z_{air} = \sqrt{\frac{n_{water}^2 - \mathrm{NA}^2}{n_{air}^2 - \mathrm{NA}^2}} z_{air} = 1.48\ z_{air} \tag{3.11}$$

with the correction factor k, the numerical aperture $\mathrm{NA} = 0.6$ of the used microscope objective. The axial position z_{air} equals the known step sizes of the z–positioning unit. The simplified version of the correction is [31, 150]

$$z_{water} = k\ z_{air} = \frac{n_{water}}{n_{air}} z_{air} = 1.33\ z_{air}. \tag{3.12}$$

The simplified version is widely used for objectives with a low numerical aperture. In this work, I used the exact correction of equation 3.11. Since all measurements were done with aqueous solutions, all axial positions were corrected for water. In this work, all axial positions z refer to the corrected values z_{water}. A correction for the used glass substrates is not necessary since the used objectives are coverslip corrected.

Data processing software

The data processing software was written in Matlab. The software is needed to analyse the recorded particle image shapes, calculate calibration curves and combine the detected particle coordinates to trajectories, and finally calculate the velocity. Furthermore, the cylindrical lens deforms, next to the particle image shapes, the whole image. A correction for this deformation is also needed. In the following, the particle detection and analysis, calculation of calibration curves and the correction of the image deformation are presented. The particle shape detection and the creation of the calibration curves is based on ideas of [42, 78, 148] and further details can be found in the mentioned references.

Particle detection and shape analysis

The particle detection works iteratively and consists of several steps. At first, the brightness of the original image is changed by using a threshold value to simplify the following processing steps. Depending on the quality of the images a median filter and/or Gaussian filter is used. The kernel size of these filters is adjusted depending on the magnification of the objective, size of the tracer particles, focal length of the cylindrical lens, and image quality. Some of this information, i.e. the objective magnification and size of the tracer particles, is read out of the measurement data–sheet by the software. Then, the particle images are detected by standard binary analysis. This detection provides the particle position, size, and length of the principal axes of the detected particle image. The particle coordinates and principle particle axes determined from the binary detection are used as start parameters for a two–dimensional fitting to the intensity distribution I of the particle image shape with the following formula [78]

$$I\left(x,y\right)=p_1\exp\left(-8.0\frac{\left(p_2-x\right)^2}{p_3}-8.0\frac{\left(p_4-y\right)^2}{p_5}\right)+p_6 \tag{3.13}$$

with the fitting parameters p_i. This fitting is applied to the original image to prevent the influence of filter operations on the particle position and shape. The principal axes in x– and y–direction, i.e. the width and height, of the particles are given by $a_x=\sqrt{p_3}$ and $a_y=\sqrt{p_5}$. The fitting is done iteratively for each particle image. Only a specific cut–out area of the entire picture around the particle image is used for fitting. The size of the cut–out area around the particle is also altered during each iteration step. The size of the cut–out area is twice as big as the detected particle diameter from the previous iteration. This way the influence of the size of the cut–out area on the fitting is minimized. Figure 3.18 shows an image of sedimented fluorescent particles. The principal particle axes are marked in the magnified image of a particle image shape. The yellow ellipse marks the border of the field of view. Particle image shapes that touch the image border are removed from further analysis since the particle image might be incomplete. Overlapping particle images are also removed from further analysis.

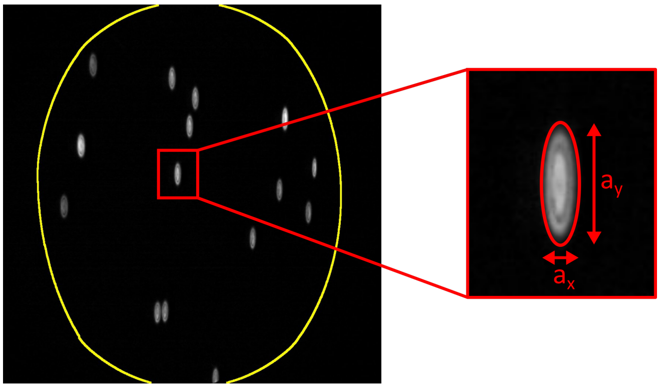

Figure 3.18.: Image of sedimented fluorescent particles with a magnified image of a particle image shape. The yellow ellipse marks the border of the field of view.

Calibration curves

The creation of calibration curves requires calibration measurements. Fluorescently labelled particles are placed on top of a glass substrate. The focal plane of the objective is moved through the sample with a known step size. At each step, an image is recorded with a known axial position of the objective. As already mentioned, this process was automated by a written software package. The recorded particle image shapes are analysed and combined with the known axial positions to calculate calibration curves. The formulas for these curves are [42]

$$a_x\left(z\right) = \sqrt{p_1^2 \left(z - F_{xz}\right)^2 + p_2^2} + p_3 \tag{3.14}$$

$$a_y\left(z\right) = \sqrt{p_4^2 \left(z - F_{yz}\right)^2 + p_5^2} + p_6 \tag{3.15}$$

with the fitting parameters p_i. The first formula is the deformation of the principle axis in x–direction with the position of the xz–focal plane F_{xz}. The second formula is the deformation of the second principle axis in y–direction with the corresponding focal plane F_{yz}. Figure 3.19 (a) shows the fitted particle image shapes with the above mentioned equations. The individual fits only depend on the axial variable z. The scatter plot of the particle diameters in x– and y–direction collapse on a single curve (Figure 3.19 (b)). This calibration curve depends only on the axial variable z. Thus, this calibration curve can be used to calculate the axial position of a particle by using the detected shape of the particle image described by the x– and y–particle diameter. If a detected particle image shape deviates too far from a calibration curve, the particle is removed from further analysis.

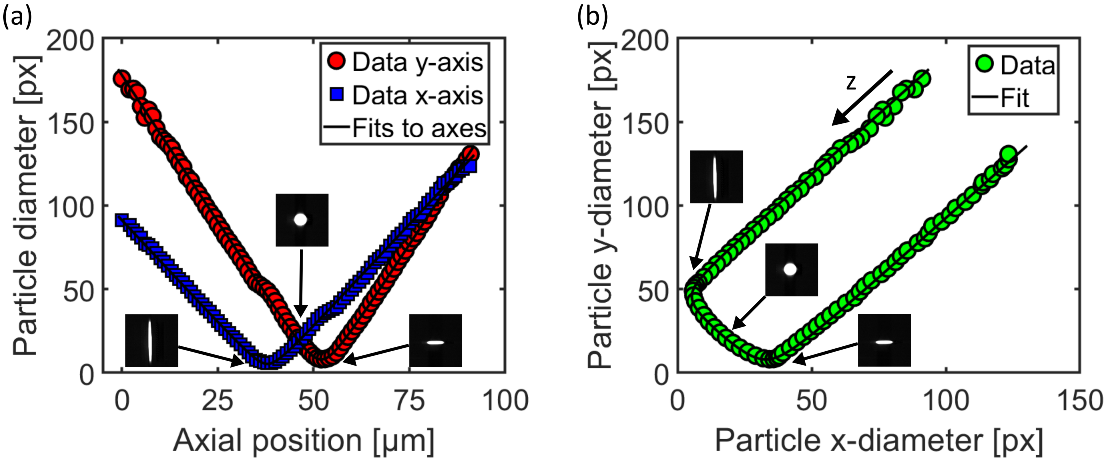

Figure 3.19.: Analysed calibration data of 2 µm fluorescent labelled particles that were recorded with a 40 X objective and a cylindrical lens with a focal length of 150 µm. (a) Detected particle shapes depending on the axial position z. The individual particle axes are fitted with equations 3.14 and 3.15. (b) Scatter plot of the detected particle shapes. The data collapses on a single curve that is only dependent on the axial variable z.

The shown curves of Figure 3.19 are only valid for the lateral position, i.e. xy–position, of the analysed particle. The deformation of the particle shape differs depending on the lateral particle position. The reason for this is that the two focal planes F_{xz} and F_{xy} are not flat but deformed [42]. The overlay of several detected particle shapes for different lateral particle positions can be seen in Figure 3.20 (a) and (b). It can be seen that the curves do not collapse on a single master curve but differ slightly. This is more obvious in Figure 3.20 (c) and (d). These show calibration data which was recorded with a 20 X objective (A.4.17), a cylindrical lens with a focal length of 50 µm and particles with a diameter of 4.5 µm (A.5.14). The individual detected particle shapes collapse on different curves, depending on their lateral position as shown in (d). The same is true for the data shown in (b). Thus, depending on the lateral particle position, different calibration curves are needed to determine the axial particle position correctly. Therefore, a calibration file consists of several calibration curves and depending on the lateral particle position the corresponding curve is applied.

A comparison of the different calibrations of Figure 3.20 (a) and (b) vs. (c) and (d) shows further important points. The shape of the curves differs between (b) and (d), i.e. the particle image shapes are deformed differently. Furthermore, the axial range of the second calibration (c) is larger than the one shown in (a). The usable axial volume of the calibration also varies for the two calibrations. In theory, it would be possible to use the whole recorded axial volume of the particle shapes. However, close to the minimum and maximum of the axial volume, the detection of the particle shapes is more prone to detection errors. Thus, this area should not be used. This reduces the usable axial measurement volume to around 60 µm for the data shown in (a) and (b) and to around 100 µm for the second dataset. Thus, depending on the planned measurement, the correct combination of objective magnification, cylindrical lens, and particle size needs to be found.

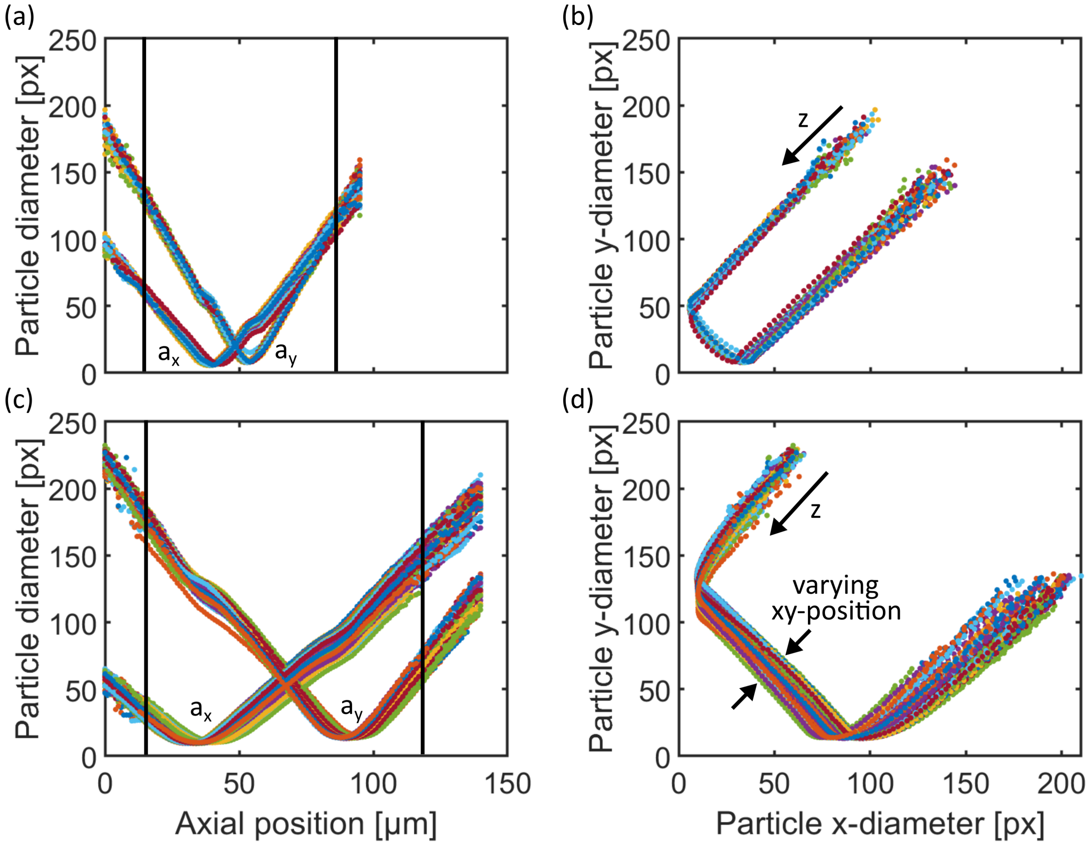

Figure 3.20.: Scatterplots of the detected particle image shapes for different particles with varying lateral positions depending on the axial variable z. (a-b) Data were recorded with a magnification of 40 X, a cylindrical lens with a focal length of 150 µm and a particle size of 2 µm. (c-d) Data were recorded with a magnification of 20 X, a cylindrical lens with a focal length of 50 µm and a particle size of 4.5 µm. Vertical lines in (a) and (c) mark the used axial volume of the calibration.

Next to the above–shown calibration method, other ways to calibrate an APTV system are possible which are presented in [148]. Different parameters are presented that can help to choose which calibration method is most suitable for the combination of objective magnification, the focal length of the cylindrical lens, and the particle size. Here, the above presented calibration with equations 3.14 and 3.15 leads to the best results for the used setup parameters.

Global image deformation

Due to the cylindrical lens, the image is also globally deformed (Figure 3.21). The figure shows the images of a calibration grid (A.4.12) without a cylindrical lens in the beam path (a) and with a cylindrical lens (b). The round outline of the image shown in figure (a) gets deformed to an elliptical shape in the image shown in (b). However, the grid lines remain straight and the vertical and horizontal lines remain perpendicular to each other. Thus, the image shown in (b) is downscaled in x–direction, resulting in a smaller magnification than the image shown in (a). In y–direction the scale of the image does not change. Only a small lateral displacement due to imperfections of the lens occurs. The magnification of the image shown in (a) is 43.44 in x– and y–direction. However, in the image shown in figure (b) the magnification in y–directions remains the same while it is reduced in x–direction to 30. This difference in scale means that the same physical distance between two points is recorded differently in x– and y–direction. This can be seen directly by comparing the grids of (a) and (b). The grid of the image shown in (a) consists of equidistant squares. However, in figure (b) the squares are deformed to rectangles.

All measurements are done with a cylindrical lens. Thus, the lateral particle positions are in the deformed coordinate system of the image shown in (b). Therefore, it is necessary to transform the deformed coordinates back into the real physical coordinate system as shown in figure (a). Knowing that both figures (a) and (b) show the same part of a physical object, i.e. the grid, a transformation matrix can be calculated. This is done by using the plugin bUnwarpJ [8, 166] of ImageJ [152, 153, 154]. With this plugin, it is possible to calculate the transformation matrix from the deformed coordinate system shown in (b) to the real physical system of (a). In figure (c) the image of a grid without a cylindrical lens shown in (a) (blue channel) is superimposed on the mathematically transformed grid from image (b) (red channel). Since the grid lines overlap perfectly, it is shown that the transformation matrix is correct.

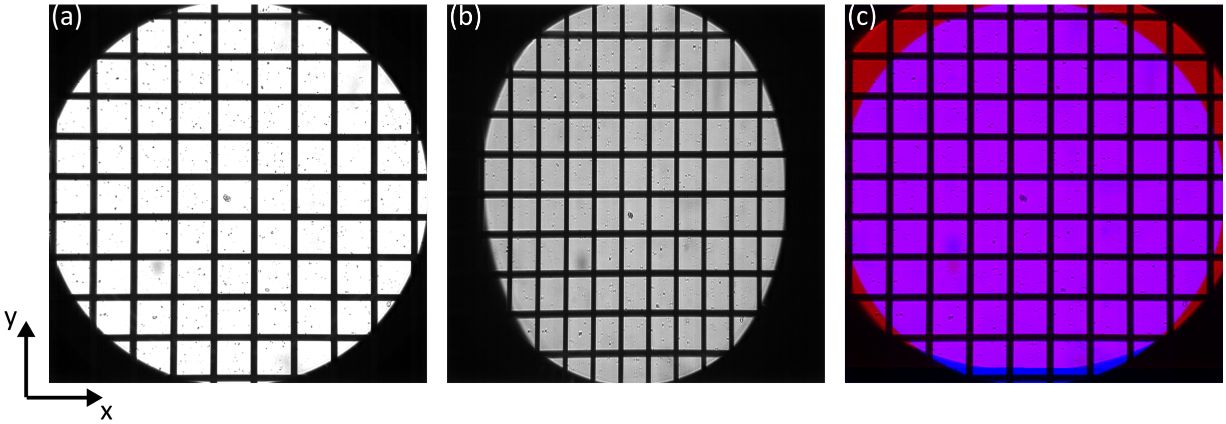

Figure 3.21.: (a) Image of a calibration grid without a cylindrical lens in the beam path. (b) Image of the deformed calibration grid due to the cylindrical lens. (c) Overlay of image (a) (blue channel) and the mathematically transformed grid from image (b) (red channel).

Particle tracking velocimetry

After the detection of the particle shape, the usage of the calibration curve, and the correction of the global deformation, all three spatial particle coordinates are available. The data processing is done for each recorded image of a measurement. The known time interval between two images is used to calculate the temporal particle coordinate. The spatial and temporal particle coordinates are combined to trajectories by use of the track algorithm [47]. The velocities were calculated via equation 2.35.

Uncertainty of the particle detection

The error of the particle detection differs in lateral and axial direction. The detection error of the axial particle positions depends on the quality of the calibration. The inherent error of the calibration is calculated by using test data. This test data is recorded in the same way as a calibration. Thus, the particle images for different known axial positions are recorded. The calibration is now used on this test data and the axial position of the particles is calculated. The calculated axial position is compared to the known axial position of the particles. All calibrations that are used in this work have an axial standard deviation lower than ±1 µm. The uncertainty of the determination of the lateral particle position is around ±0.5 px. With a 40 X magnification and a pixel size of $20 \times 20\,\mu\text{m}^2$ the lateral standard deviation is ±0.25 µm.

3.3. Conclusion on the experimental methods

In this chapter, two experimental methods that were built during this work were described. The first part of the chapter described the development of a fast re–scan laser scanning confocal microscope. The second part was about the establishment of an astigmatism particle tracking velocimetry setup. Both setups were built to find a suitable experimental method enabling the measurement of flow profiles close to receding contact lines of surfactant solutions. In the following, both methods are summarized and thereafter compared.

In the first part of this chapter, I described the built high–speed re–scan laser scanning confocal microscope. This setup enables high–speed confocal recordings while using only a single laser beam preventing any crosstalk. In contrast to standard single beam laser scanning confocal microscopes, which use one scanning unit to scan the sample, it utilizes two scanning units in a re–scan configuration. This means that one scan unit scans the sample and the other scan unit projects the image on a two–dimensional camera sensor. Thus, a two–dimensional image is directly recorded, without the need for image reconstruction software. As with any laser scanning confocal microscopes, the maximum scanning speed is limited by the speed of the moving mirrors. The resonant scanners oscillate with a fixed frequency of 15.7 kHz leading to a line frequency of 31.4 kHz since the scanning is done bidirectionally. This fast scanning speed results in a small dwell time of around 118 ns leading to reduced bleaching of the sample.
All three scanning axes, i.e. the resonant scanners, galvanometer scanners, and objective scanner, can be controlled individually. This enables scanning arbitrary planes through the sample, which is one of the big advantages of laser scanning confocal microscopes. The highest possible two–dimensional frame rates are 1 kHz in the lateral direction, i.e. xy–scan, and 200 Hz in the vertical direction, i.e. xz–scan, with a z–amplitude of 100 µm. The axial scanning speed can be increased by decreasing the z–amplitude. Three–dimensional xyz–stacks can be recorded with frame rates up to 40 Hz. The high–speed capacities of the custom–built microscope are superior to comparable commercial state–of–the–art microscopes (Table 3.1).
The optical properties of the setup were theoretically and experimentally determined (section 3.1.4). It was shown that the resolution of the microscope is independent of the frame rate. The best measured lateral resolution is (223.9 ± 8.9) nm and the best axial resolution is (602.4 ± 25.1) nm. Since the resolution depends crucially on the sample quality, i.e. quality of the fluorescent dye and quality of the index matching, a new resolution criterion was defined (page 46). This criterion utilizes the edge steepness of the recorded intensity profiles, e.g. of fluorescently labelled particles, to calculate the resolution. A hyperbolic function

is fitted to the rising and falling slopes of the intensity profile. The resolution is defined as the distance between the 10 % and 90 % value of the maximum amplitude of the hyperbolic fitting. Since the criterion uses the measured intensity profile of the sample, it can be easily applied to every measurement to calculate the resolution.

The custom–built microscope still has unused potential and possible improvements to the optical setup were presented in section 3.1.6. A major limiting factor of many microscopes is the axial scanning capacity. A common way to accomplish axial scanning is by moving either the objective or the sample up and down. This can lead to mechanical vibrations and thus to disturbances of the sample. To circumvent this, I added two extensions to the present setup which enable fast axial scanning without disturbing the sample (section 3.1.5).

The first extension is a remote focus technique based on ideas of [48]. Two additional objectives are added to the beam path. By moving one of those objectives, the focal plane is moved through the sample. Thus, the focal plane is moved through the sample without moving the sample or the objective that detects the light coming from the sample. Hence, the sample is not disturbed by mechanical vibrations. It was shown that the method works and ideas to improve the image quality were given. The second extension is a combination of the confocal microscope with astigmatism particle tracking velocimetry which was presented in section 2.7.3. Since additionally an APTV setup was built during this work (section 3.2), the combination of both methods was a matter of course. For this purpose, an additional fluorescent detection beam path was added to the optical assembly of the microscope. By placing a cylindrical lens in the fluorescent beam path, APTV could be used. Thus, this extension combines the advantages of confocal microscopy, i.e. high–quality images of a specific plane through the sample, with the three–dimensional detection capacities of APTV.

In the second part of this chapter, I described the built APTV setup. The advantage of astigmatism particle tracking velocimetry, or defocusing techniques in general, is that only one camera and no moving parts are needed to measure three–dimensional dynamics (section 2.7.3). I modified a commercial Leica DMI6000B inverted research microscope to be used as an APTV setup by placing a cylindrical lens in the beam path of the microscope. To use APTV I had to write two extensive software packages (section 3.2.2). The first software package was written with LabVIEW to control the microscope. The programmed software enables remote control of every motorized component of the microscope. Automated calibration routines are available allowing easy and fast calibration of the setup. During measurements, data–sheets, which include all important measurement parameters, are automatically created by the software. The second software package was written in Matlab to analyse the recorded particle image shapes, calculate and use calibration curves, and to track the particles. The uncertainty of the three–dimensional particle detection is lower than 1 µm in axial direction and around 0.25 µm in lateral direction.

Three–dimensional flow profiles can be measured with frame rates up to a few hundred Hertz. The reachable frame rate depends on the quality of the fluorescent dye and the combination of objective magnification, focal length of the cylindrical lens, and size of the tracer particles. The combination of the mentioned parameters also determines the size of the measurement volume. Thus, the size of the measurement volume can be adapted to fulfil the individual measurement requirements by changing the combinations of the mentioned components.

In general, both setups can be used to measure the required flow fields close to receding three–phase contact lines. Each setup has its individual advantages and disadvantages: The custom–built confocal microscope has the advantages of any laser scanning confocal microscopes, i.e. arbitrary scans through the sample and only detection of light coming from the focal plane. Thus, high concentrations of tracer particles can be used to track the flow motion. Two–dimensional flow fields can be calculated by using standard particle image or tracking velocimetry methods. If a two–dimensional flow field, e.g. a vertical or horizontal scan through the sample, is sufficient, the confocal microscope is the method of choice. Besides tracking the flow motion, the slope of the liquid/air interface, and the position of the contact line can be measured directly. By stepwise detection of horizontal planes, three–dimensional flow profiles can be reconstructed. High image quality and spatial resolution are secured by using objectives with a high numerical aperture and blocking most out–of–focus information. The major disadvantage of the custom–built microscope is the necessity to repeatedly adjust and align the optomechanical components and the possible disturbances of the sample due to mechanical vibrations.

Astigmatism particle tracking velocimetry enables direct measurement of three–dimensional particle positions without the need for moving parts. However, the amount of tracer particles is, compared to the custom–built microscope, low since every particle in the three–dimensional volume is detected. Thus, overlapping particle image shapes should be avoided. This leads to a reduced concentration of tracer particles. As a result, APTV detects fewer particles per frame compared to the custom–built microscope. However, the detected information of the APTV setup is three–dimensional. A sufficient amount of information, i.e. particle trajectories, is needed for a good spatial resolution. This can be achieved by increasing the measurement time. In the present work, this is possible since the moving drop reaches a dynamic equilibrium state. In contrast to the custom–built microscope, no adjustment and alignment effort is needed to use APTV. Additionally, no index matching of the tracer particles with the measurement fluid is necessary. Furthermore, no moving parts are needed and thus no mechanical disturbance of the sample is possible. However, calibration of the setup and detection of the particle image shapes are necessary. This was considered a minor disadvantage compared to the alignment effort and the possible disturbance of the sample when using the custom–built confocal microscope. As a result, I used the APTV setup to directly measure three–dimensional flow fields close to receding three–phase contact lines of aqueous surfactant solutions.

4. Influence of surfactants on forced dewetting

In this chapter the influence of surfactant solutions on flow fields close to receding three–phase contact lines is investigated. At the beginning of this chapter, the materials and methods as well as the data processing is presented. Thereafter, the measured flow fields are discussed and the hypothesis [69] (section 2.5.2) which tries to explain the dynamics close to receding contact lines of surfactant solutions is tested. Furthermore, the model of the hypothesis is expanded and a new model describing an additional surfactant transport mechanisms is proposed. Most of the content of the following sections is published in [170].

The appendix contains an overview of all commercial components (Appendix A.4), used software programmes (Appendix A.6) and consumables (Appendix A.5). When describing the material and the experimental setup, reference is made to the tables in the appendix for more details on the components, software or consumable material.

4.1. Material

Table 4.1 shows the properties of the used surfactants (A.5.8, A.5.9) in this work. To avoid charge effects, only nonionic surfactant solutions were used. Since Henrich et al. [83] showed that the charge does not influence the dewetting behaviour of surfactant solutions, the use of nonionic surfactants in this work is sufficient. The surfactants were used without further purification. The surfactants were selected due to their significantly different critical micelle concentration. In section 4.1.1 the different surfactant solutions are discussed in detail.

Table 4.1.: Properties of the surfactants. Values of the diffusion coefficients from [83].

Name	Formula	Type	CMC [mM]	Molecular weight [$\mathrm{g\,mol^{-1}}$]	Surface tension at CMC [$\mathrm{mN\,m^{-1}}$]	Diffusion coefficient [$\mathrm{m^2\,s^{-1}}$]
Dodecyl pentaglycole	$C_{12}E_5$	Nonionic	0.07	406.60	30.7	2.9×10^{-10}
Octyl triglycole	C_8E_3	Nonionic	7.5	262.39	27.3	4.6×10^{-10}

Silanized cover slides (A.5.1) were used as substrates. In a first step, these slides were mechanically cleaned with acetone (A.5.6), isopropanol (A.5.7) and ethanol (A.5.5) with clean room wipes. Then, the slides were placed in a closed box and hydrophobized with (trichloro(1H, 1H, 2H, 2H–perfluorooctyl)silane (A.5.4) via the gas phase for two minutes. Two 10 µL drops of the silane were placed in the box and a magnetic stirrer ensured a homogeneous coating of the cover slides.

Fluorescently labelled polystyrene particles with diameters of either 2 µm or 4 µm were used to measure the flow motion. The latter were synthesized at the MPIP (A.5.13) and have an excitation wavelength of 550 nm and an emission wavelength of 600 nm. The 2 µm particles were commercial particles (A.5.14) with an excitation wavelength of 530 nm and an emission wavelength of 607 nm. The particles were dispersed in the surfactant solutions. The sedimentation of the particles was avoided by using a 1:1 mixture of deuterium oxide (A.5.12) and ultra–pure water (A.4.1, A.4.2). The polystyrene particles are only slightly denser than water ($\rho_{ps} = 1050\,\mathrm{kg\,m^{-1}}$). Due to this small density difference, the sedimentation time is much larger than the time scales of the measured phenomena. Thus, even without a density match, it can be safely assumed that the particles follow the fluid [149].

4.1.1. Characterisation of the surfactant solutions

Table 4.2 shows the properties of the used measurement solutions with concentrations of 5, 15 and 30 % CMC. A fine balance (A.4.11) was used to create aqueous solutions with the mentioned concentrations. Due to the difference of the CMC between both surfactants, the absolute concentration c_{abs} of surfactant molecules in parts per million (ppm) differs significantly. The equilibrium surface tension γ of the aqueous surfactant solutions was measured by using the Wilhelmy–method with a tensiometer (A.4.7). The measured surface tension of pure water was 72.4 $\mathrm{mN\,m^{-1}}$. The surface tension of the surfactant solutions decreases with increasing surfactant concentration. The equilibrium surface excess Γ is calculated using equation 2.13 and increases with increasing surfactant concentration.

The Capillary and Reynolds numbers were also calculated for the surfactant solutions. A characteristic velocity of 200 $\mathrm{\mu m\,s^{-1}}$ was used to calculate the dimensionless numbers. This value equals the contact line velocity of the measurements. Furthermore, the dynamic viscosity of water ($\mu = 1\,\mathrm{mPa\,s}$) was used to calculate the dimensionless numbers. Since the surfactant concentration is low and even temperature effects have a higher influence on the viscosity than the small amounts of surfactant molecules, the viscosity of water can be used to calculate the dimensionless numbers for the surfactant solutions. The Capillary numbers Ca are calculated using equation 2.4 and are in the order of 10^{-6} for all solutions. This indicates that surface forces are dominant compared to viscous forces. The Reynolds numbers Re were calculated using equation 2.7. The size of the measurement volume (100 $\mathrm{\mu m}$) was used as a characteristic length. The Reynolds numbers are in the order of 10^{-2}, indicating that viscous forces are dominant.

Table 4.2.: Properties of the surfactant solutions: absolute concentration c_{abs}, equilibrium surface tension γ and equilibrium surface excess Γ.

Surfactant	[% CMC]	c_{abs} [ppm]	γ [$\mathrm{mN\,m^{-1}}$]	Γ [$\mathrm{mol\,m^{-2}}$]
$C_{12}E_5$	5	0.06	58.21	0.9×10^{-6}
$C_{12}E_5$	15	0.19	47.45	2.6×10^{-6}
$C_{12}E_5$	30	0.38	40.18	5.1×10^{-6}
C_8E_3	5	6.78	53.16	0.9×10^{-6}
C_8E_3	15	20.32	43.36	2.8×10^{-6}
C_8E_3	30	40.65	35.38	5.6×10^{-6}

4.2. Experimental setup

Figure 4.1 shows the experimental setup, which was already described in detail in section 2.5.4. In this study measurements with a contact line velocity of 200 µm s^{-1} are done and thus a 1 mm thick PDMS dampening layer is used to guarantee a smooth motion of the piezoelectric stage (see section 2.5.4 for details about the linear motion of the stage).

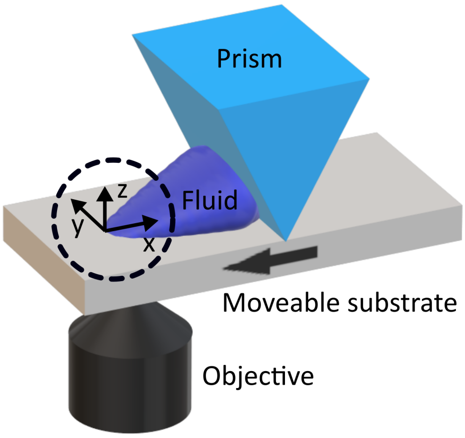

Figure 4.1.: The setup enables measuring flow fields in the circled area close to moving contact lines that are locally stable. Adapted from [170] (CC BY 4.0).

The prism must be hydrophobized like the used glass substrates to prevent spreading of the liquid on the prism. In a first step, the prism is cleaned and afterwards hydrophobized with trichloro(1H, 1H, 2H, 2H-perfluorooctyl)silane in a closed box via the gas phase. The cleaning and hydrophobization process of the prism is of crucial importance since the prism has direct contact with the liquid and can contaminate it. Thus, after each measurement, the prism is at least rinsed with pure water.
The focus of the present work was on measurements close to the receding contact line as shown in Figure 4.1. The movement of the substrate is to the left and a receding contact line is created in the circled area of the drop. Since the distance between the prism and the circled measurement area is larger than at least 30 times the measurement area, no influence of the prism on the flow close to the receding contact line is expected. The calculation of flow profiles is presented in section 4.4.

4.3. Experimental procedure

In this work 5, 15 and 30 % CMC surfactant solutions of $\mathrm{C_{12}E_5}$ and $\mathrm{C_{12}E_5}$ are used. The measurement volume of the drop is always 2.5 µL. These volumes are measured with pipettes (A.5.2) and the drop is placed on top of the hydrophobized glass substrates. Up to four measurements are done on the same substrate. Each measurement is done at a different position and with a new drop of the measurement liquid. Flow profiles are measured for the surfactant solutions and water at a constant contact line velocity of 200 µm s^{-1}. The contact line velocity is controlled by the movement of the piezoelectric stage (A.3.1) which is controlled by changing a frequency in the control software (A.6.4) of the motor. In this work the frequency is set to 500 Hz which yields a contact line velocity of 200 µm s^{-1}. The PDMS dampening layer is used to guarantee a smooth motion of the contact line. Further details about the properties of the piezoelectric stage can be found in section section 2.5.4 or [84]. For the APTV measurements a 40 X times

objective (A.4.16), a cylindrical lens (A.2.11) with a focal length of 150 mm and 2 µm sized fluorescently labelled polystyrene particles (A.5.14) are used. The excitation light is provided by the mercury lamp of the microscope (A.2.7). The new internal filter cube (A.2.1) of the microscope is used to maximize the usable fluorescent light. The high–speed camera (A.2.3) records images with a frame rate of 50 Hz which yields a good spatial and temporal resolution. The field of view in this configuration is around $400 \times 450 \times 60\,\mu m^3$ and the uncertainty of the determination of the particle position is less than $\pm 0.25\,\mu m$ in lateral direction and less than $\pm 1\,\mu m$ in axial direction. The measurement area is protected from ambient airflow and stray light by a laser curtain.
The measurements of water, $C_{12}E_5$ and 5 % CMC C_8E_3 were done by me with the above described setup. Measurements of water and 15 % CMC and 30 % CMC C_8E_3 were done by F. Henrich and M. Rossi at the Bundeswehr University Munich with a second setup. The setup in Munich consists of an inverted microscope Axio Observer Z1 (Carl Zeiss AG) in combination with an Imager sCMOS camera (LaVision GmbH). It uses a 150 µm cylindrical lens and a 40 X microscope objective (LD Plan—Neofluar, Carl Zeiss AG). A high–power green light–emitting diode was used as illumination and 4 µm sized polystyrene particles (A.5.13) are used to track the flow. The calibration of this setup can be found in [12]. The uncertainty of this setup is $\pm 0.7\,\mu m$ in the axial direction, and $\pm 0.1\,\mu m$ in the lateral direction with a measurement volume of around $380 \times 430 \times 70\,\mu m^3$. All measurements were analysed by me.

4.3.1. Effects of contamination

The first series of velocity measurements showed an unexpected behaviour of the flow field. The flow field of pure water close to a receding three–phase contact line should look like Figure 4.2 (a). Instead, the measured flow field of water looked like the one shown in Figure 4.2 (b). The surface flow at the liquid/air interface pointed towards the contact line and a so–called dividing [16] or split–ejection streamline [72] was present in the liquid bulk. A similar observation was made on the advancing side of drops. There, the surface flow pointed away from the contact line and a so–called split–injection streamline [72] was present. After the addition of surfactants to the measurement solution, the dividing streamline was not present any more. Although this behaviour was observed in other studies [16, 72], the here observed behaviour may be due to contamination of the liquid or sample. Thus, possible sources of contamination were systematically identified and eliminated.

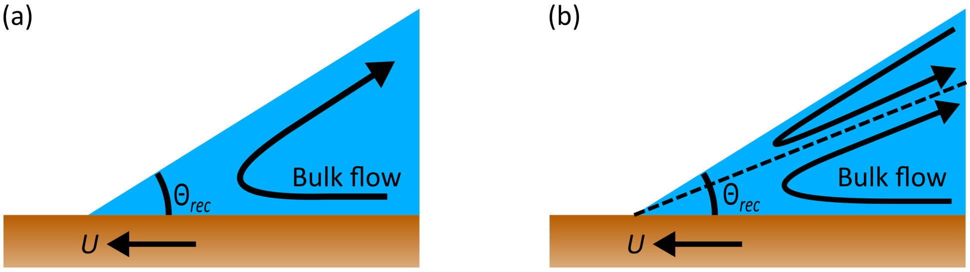

Figure 4.2.: (a) Expected flow field of water with the contact line velocity U, the receding contact angle Θ_{rec} and the bulk flow motion. (b) Measured flow field of water during the first measurement series with a dividing streamline.

The three most likely ways to contaminate the measurement were the used pipette (A.5.2) and tips (A.5.3), the tracer particles (A.5.14) and the silanization process of the solid substrate. The pipettes and the tips are shared for all co–workers in a lab. Both pipettes and tips can be easily contaminated by minor mistakes, e.g. by leaving the container of the tips open or filling too much liquid into the pipette. Since these mistakes often happen unnoticed, all subsequent work with the pipette and tips is affected. Thus, I ordered a new set of pipettes and tips only for these experiments and stored them in a closed box to prevent any contamination. Commercially bought polystyrene particles (A.5.14) were used to track the flow. These particles were delivered in a storage liquid from the manufacturer. Upon request, the manufacturer assured that the particles were washed several times and that no residues of the particles' synthesis were left. To be on the safe side, the particles were washed again several times. This was done by letting the particles sediment to the bottom of the storage container, removing the excess liquid, adding new ultra–pure water and mixing particles and water by use of an ultrasonic bath (A.4.10). This process was repeated several times. Another way to distort the measurements is the substrate. Before and after the silanization process the substrate was cleaned to prevent any contamination.

After taking care of the mentioned points, the flow fields of water showed the expected behaviour without the dividing streamline. Thus, the here observed dividing streamline was due to some contamination. It was not possible to measure or create the dividing streamline on purpose in a controllable manner. Hence, no statement about the creation or physics behind dividing streamlines is possible. However, other studies showed the streamline for pure water [72] as well as for surfactant solutions [16].

4.4. Data processing

The results of the APTV measurements are particle trajectories whose xy–positions are in the coordinate system of the recorded images (Figure 4.3). In the shown system, the substrate motion is directed from high to low y_{Im} values. Several additional steps of data processing, next to the in section 3.2.2 presented standard APTV processing steps, are required before the data can be analysed. The additional steps are the correction of the inclination of the solid substrate, changing the coordinate system, and finally the creation of flow fields. In the following, these data processing steps are presented.

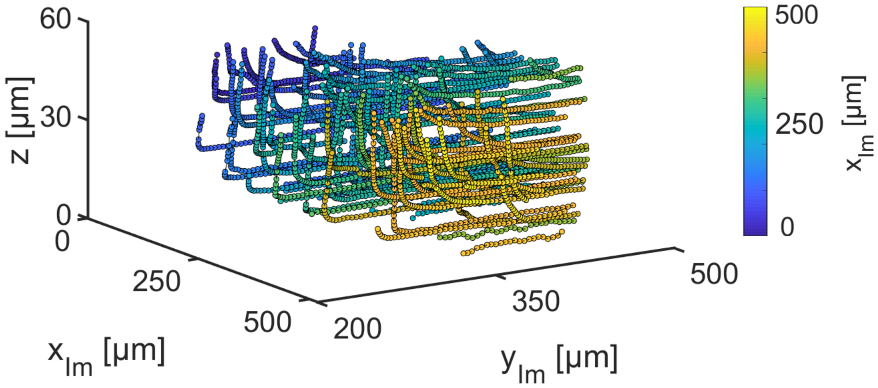

Figure 4.3.: Detected particle trajectories. The trajectories are color coded depending on the x_{Im}–position of the data points.

4.4.1. Correction of inclination

In the first step, the inclination of the substrate must be corrected. To visualize the inclination, the y_{Im}–position of the particles has to be scaled since the motion of the piezoelectric stage is parallel to the y_{Im}–axis. Figure 4.4 shows the same data as Figure 4.3, but the y_{Im}–axis position of each particle was scaled to show the inclination. The y_{Im}–axis position of each particle i for every recorded frame N_f, i.e. $y_{Im}\left(i, N\right)$, was scaled with the following equation

$$y_{PS}\left(i, N_f\right) = y_{Im}\left(i, N_f\right) + \frac{N_f\, U}{\Delta t} \tag{4.1}$$

and the contact line velocity U and the time interval between two successive frames Δt. Thus, the particle position $y_{PS}\left(i, N_f\right)$ is the absolute position of the particle in the coordinate system of the piezoelectric stage which has a travel range up to 26 mm. From the scaled trajectories of the particles, it is evident that some sort of inclination exists. Therefore, a two–dimensional plane was fitted to the particles with the lowest z–values, i.e. the particles that stick to the solid. This plane represents the glass substrate and all axial particle positions are corrected regarding this plane (with $z = 0\,\mu\mathrm{m}$ corresponding to the glass substrate).

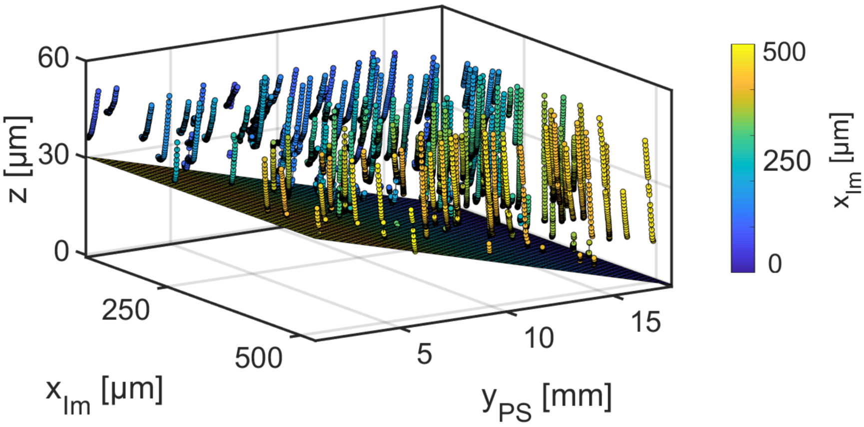

Figure 4.4.: Detected particle trajectories in the coordinate axis of the piezoelectric stage y_{PS}. The inclination of the glass substrate is corrected by fitting a two–dimensional plane to the particles that stick at the glass substrate.

In the case of the shown measurement, the inclination is around 30 $\mu\mathrm{m}$ over the travel range of 17 mm which equals an inclination angle of around 0.1°. Possible reasons for the inclination are the PDMS dampening layer and small manufacturing inaccuracies of the substrate holder. It is not possible to correct these error sources due to the lack of adjustment options. Also, the substrate itself is an error source. The used glass substrates (A.5.1) are only $(170 \pm 5)\,\mu\mathrm{m}$ thick. Although these substrates are of the best quality, they are not perfectly flat and can be bent easily. The substrates are glued to the sample holder to guarantee the best possible flatness of the substrate. However, a small error will remain and contribute to the observed inclination.

The influence of the inclination on the measured dynamic is negligible. However, the inclination further influences the usable axial volume during the measurement. It can be seen that for small y_{PS} values the axial volume is only around 30 $\mu\mathrm{m}$. It increases during the measurement until it reaches around 60 $\mu\mathrm{m}$ which is around the maximum usable axial volume of the used calibration.

4.4.2. Change of coordinate system

In the next step, the coordinate system has to be changed. Until now, the data points are still represented in the image coordinate system with corrected z–values. A presentation of the data in the co–moving frame of the contact line is beneficial for further analysis. The origin of this coordinate system is placed on the moving three–phase contact line. Thus, the contact line must be detected for each recorded frame. This is done by using several segmentation and edge detection techniques. The detected data points of the contact line are fitted with a second–order polynomial function. Since the contact line is tracked in the distorted image system, the contact line position has to be transformed back to the real system by using the transformation matrix (section 3.2.2). An image with a marked detected contact line can be seen in Figure 4.5 (a). The particle coordinates are transformed using the contact line position. The representation of the trajectories in the co–moving frame of the contact line can be seen in Figure 4.5 (b). The streamwise variable x represents the distance between the data point and the contact line (with $x = 0$ corresponding to the contact line).

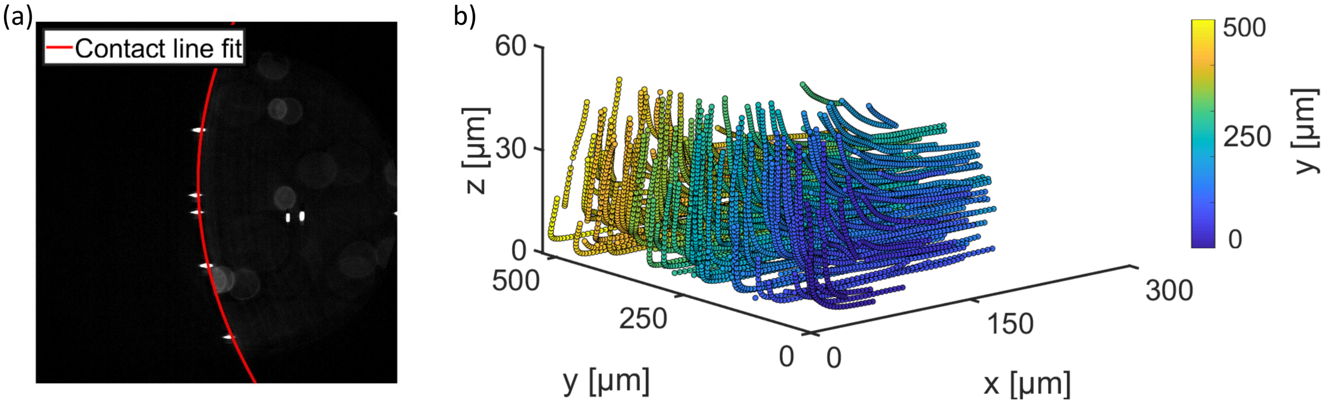

Figure 4.5.: (a) Recorded image with different particle images and the fitted contact line. (b) Representation of the detected particle trajectories in the co–moving frame of the contact line. The origin of the system is placed on the moving three–phase contact line.

4.4.3. Calculation of velocity fields

The velocity components of the final particle coordinates (Figure 4.5 (b)) were calculated via equation 2.35. Since the measured data showed that the flow in y–direction is negligible, all trajectories were projected on the xz–plane. It is assumed that the shape of the liquid close to the three–phase contact line is a wedge and thus, the liquid/air interface is a straight line. The receding contact angle is fitted by the use of the trajectories that move parallel to the liquid/air interface. The pitch of the particle trajectories is used to calculate the contact angle. The measurement uncertainty of this procedure is around ±5°. The correct contact line velocity for each measurement is calculated by analysing the tracer particles that are stuck at the substrate. The velocity of these particles is equal to the contact line velocity. Finally, all measured particle velocities were averaged to equidistant grid points with a spacing of 5 µm. Each measurement solution was measured at least three times. An average of 168 particles were tracked in each measurement and analysed with the written software. The average number of sample points per equidistant grid point is around 13. The velocity fields are discussed in section 4.6.

4.5. Macroscopic contact angle measurements

As mentioned in the previous section, the receding contact angle was calculated by using the trajectories that move parallel to the liquid/air interface. Since the contact angle was not measured directly during the measurement, it must be controlled if the calculated values are reasonable. Therefore, additional contact angle measurements were done.

Measurements of the static advancing and receding contact angles were made using the sessile drop method on a goniometer (A.4.6). The measured static receding contact angles are around 20° larger than the measured receding contact angles for a velocity of $200\,\mu\mathrm{m\,s^{-1}}$.

Macroscopic measurements of the dynamic contact angles were done using the in section 4.2 presented experimental setup. Figure 4.6 (a) shows an image of a $5\,\%$ $\mathrm{C_{12}E_5}$ drop while the substrate is moved with $200\,\mu\mathrm{m\,s^{-1}}$. To record those images, the drop was illuminated from behind using a light–emitting diode (A.4.8). The image was recorded from the front using a webcam (A.4.9) mounted on a three–axes table (A.4.5). The imaging optics of the webcam were a 2 X objective (A.4.4) and a tubus (A.4.3).

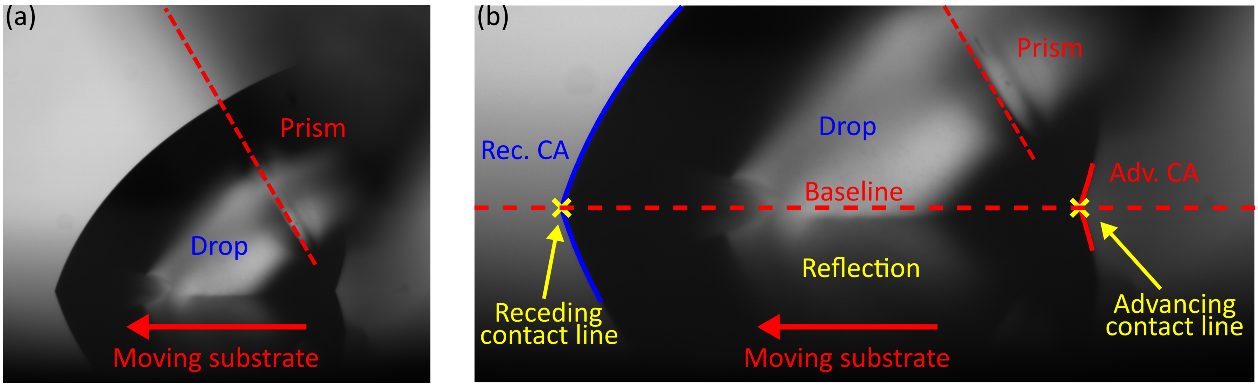

Figure 4.6.: (a) Macroscopic image of a $5\,\%$ $\mathrm{C_{12}E_5}$ drop while the substrate is moved with $200\,\mu\mathrm{m\,s^{-1}}$. (b) Detection of the contact angles.

The drop is pinned to the prism and a locally stable moving three–phase–contact line is created. The detection of the contact angles is shown in Figure 4.6 (b). An edge detection algorithm is used to detect the outline of the drop and its reflection on the substrate. The reversal points, i.e. the advancing and receding contact lines, are calculated to define a baseline. The contact angles are measured between the drop outline and the baseline. The measurement uncertainty of the contact angle detection is around ±3°. Detection of the drop shape and calculation of the contact angle is based on an available software package [129] with slight modifications.

The shown configuration of the measurement setup in Figure 4.6 is used to measure the receding contact angle. It is also possible to calculate an advancing contact angle. However, since the distance between the prism and the advancing side is rather small, the prism has a huge influence on the advancing contact angle. Thus, the calculated values for the advancing side are not reliable.

The macroscopic measured receding contact angle for $5\,\%$ $\mathrm{C_{12}E_5}$ is around 76°. The receding contact angle, calculated with the particle trajectories, is around 74°. The different methods show good agreement in determining the receding contact angle. This is also true for other measured solutions. The maximum error amplitude between the macroscopic measured contact angles and the calculated contact angles with trajectories is around ±7°. The results show that the method of calculating the contact angle with trajectories is valid.

4.6. Velocity fields

In this section the measured velocity fields close to receding three–phase contact lines are presented. As mentioned before, since the measured data showed that the flow in y–direction is negligible, all trajectories were projected on the xz–plane. It is assumed that the shape of the liquid close to the three–phase contact line is a wedge and thus, the liquid/air interface is a straight line. All measured particle velocities were averaged to equidistant grid points with a spacing of 5 µm.

4.6.1. Water

A measured velocity field for pure water can be seen in Figure 4.7. The data is shown in the co–moving frame of the contact line, in which the origin of the coordinate system corresponds to the moving three–phase contact line. The flow direction is given by the angular orientation of the arrows and the velocity is given by the color code. The black solid line marks the liquid/air interface and the contact angle for the measurements of water is around 78°. The velocity field shows that fluid enters the measurement volume from the right, moves in the direction of the contact line, is redirected to flow parallel to the liquid/air interface, and leaves the measurement volume.

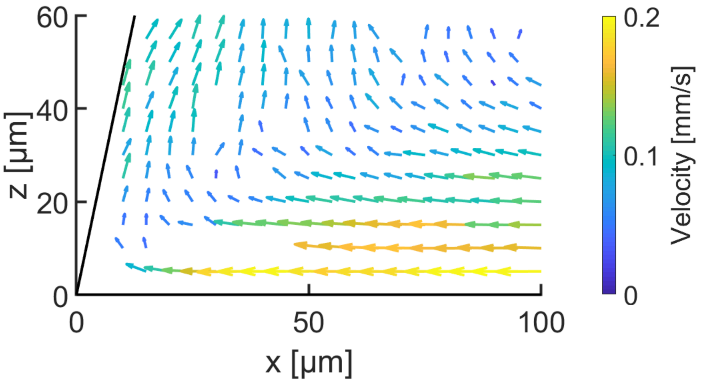

Figure 4.7.: Measured velocity field of water in the co–moving frame of the contact line. The straight black line is the liquid/air interface. Adapted from [170] (CC BY 4.0).

4.6.2. Surfactant solutions

Two exemplary velocity fields for 30 % CMC surfactant solutions of $\mathrm{C_{12}E_5}$ and $\mathrm{C_8E_3}$ are shown in Figure 4.8. The first observation is that the receding contact angle decreases from 78° (water) to 54° in the case of $\mathrm{C_{12}E_5}$ and 25° in the case of $\mathrm{C_8E_3}$. The general fluid motion is similar for water and surfactant solutions. Flow fields for all surfactant solutions can be found in Appendix A.3.1.

Further quantitative statements are not possible from the comparison of the flow profiles. The reason is that the receding contact angles differ between the measurements. Thus, the measured flow magnitudes of water and surfactant solutions cannot be compared quantitatively. For this reason, a different approach is necessary to enable quantitative statements.

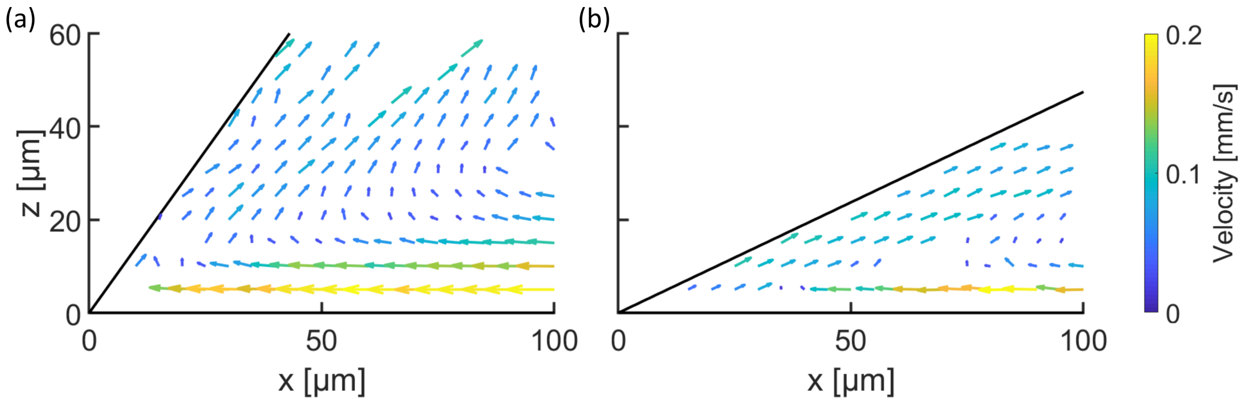

Figure 4.8.: (a) Velocity field of 30 % CMC $C_{12}E_5$ solution with a receding contact angle of 54°. (b) Velocity field of 30 % CMC C_8E_3 solution with a receding contact angle of 25°. Adapted from [170] (CC BY 4.0).

4.7. Deviation fields

The idea behind deviation fields is to compare the measurements to available hydrodynamic theories. For the simplified two–dimensional wedge geometry near the contact line, hydrodynamic theories for simple liquids exist [46, 88, 127, 177]. These theories provide an analytical solution for the region directly at the contact line on a nanometre scale (inner solution) and for the bulk flow (outer solution). Since the used tracer particles are micrometre sized, the measurements are in the range of the outer solution. Because the outer solution is basically the same for the mentioned theories, the measured velocity data is compared only to the theory of Moffatt [127] for a stress–free liquid/air interface with a constant contact line velocity which was presented in section 2.3.2. A deviation field shows the velocity difference between theory and measurement and the velocity deviation is calculated via equations

$$u_d = u_e - u_t, \quad w_d = w_e - w_t, \tag{4.2}$$

$$M_d = \frac{|\vec{v}_d|}{|\vec{v}_t|} = \frac{\sqrt{u_d^2 + w_d^2}}{\sqrt{u_t^2 + w_t^2}}. \tag{4.3}$$

with the mean local velocity components u and w in x– and z–direction at a given $(x,\ z)$–position. The indices indicate the type of data, e.g. deviation d, experiment e, and theory t. The relative magnitude of the deviation M_d is calculated by simple vector analysis.

4.7.1. Water

The calculation of a deviation field for water is shown in Figure 4.9. Figure 4.9 (a) shows a measured velocity field with a contact angle of 78°. The contact angle and contact line velocity of the measurement are used to calculate the theoretical velocity field using Moffatt's solution (b). The information of (a) and (b) is used to create the deviation field (c) using equations 4.2 and 4.3. As already mentioned, this deviation field shows the deviation between the measurement and the theoretical prediction by Moffatt. The color code and length of the arrows represent the relative magnitude of the deviation M_d. The angular deviation is given by the arrow direction. The relative magnitude of the deviation between the measurement of water and the theory is between 5–30 %. The angular deviation is randomly distributed and no distinct regions with the same angular deviation exist. This randomness and the small absolute deviation show that measurement and theory agree well. The random noise shows that no bias error occurred. Close to the free surface of the liquid, only a small deviation occurs. Thus, the liquid/air interface seems to be stress–free since the theoretical solution was calculated for a stress–free liquid/air interface.

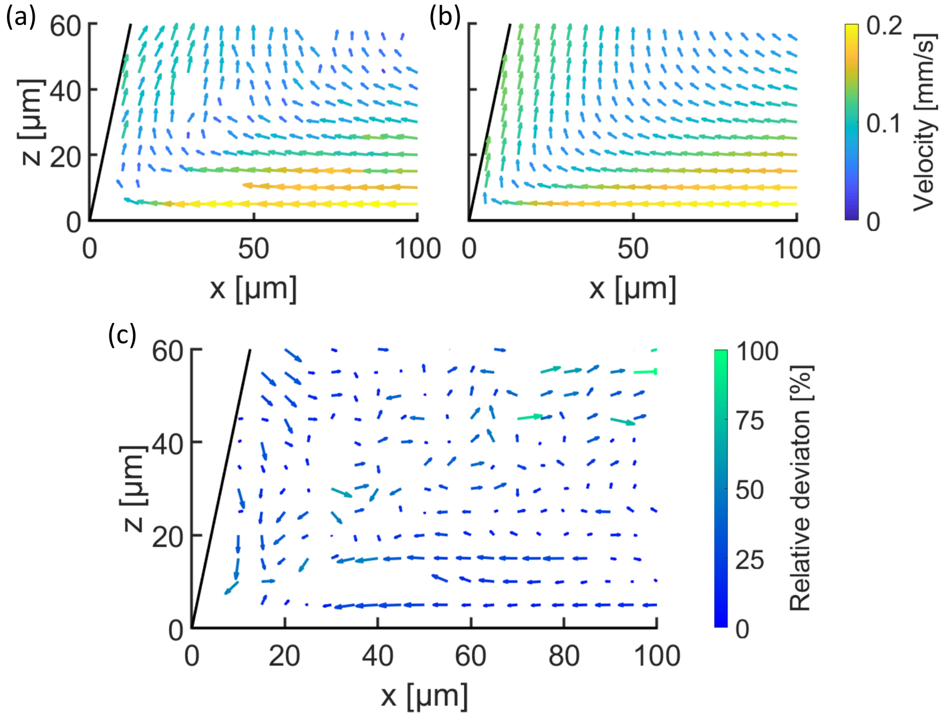

Figure 4.9.: (a) Measured velocity field of water. (b) Theoretical velocity field of water calculated with the theory of Moffatt [127] (section 2.3.2). (c) Deviation field calculated with equations 4.2 and 4.3 and the information from (a) and (b). Adapted from [170] (CC BY 4.0).

4.7.2. Surfactant solutions

Since it was shown that the measurements of water and the theory of Moffatt match well, it is possible to compare the measurements of surfactant solutions to the theory of Moffatt for water. Since the theoretical prediction can be calculated for any contact angle, a direct qualitative comparison using deviation fields is possible. The deviation fields for surfactant solution should show angular and absolute deviations since a theoretical solution for pure water is compared to a measurement for a surfactant solution.

Deviation fields of 30 % CMC $C_{12}E_5$ and C_8E_3 solutions are shown in Figure 4.10 (a) and (b). It can be seen that the angular deviation is no longer randomly distributed. Large regions with the same angular deviation exist close to the liquid/air interface (region A) and in the liquid bulk (region B).
In the region close to the liquid/air interface (region A) the arrows point towards the three–phase contact line and thus, in opposite direction of the surface flow. The reduced surface velocity is explainable by a Marangoni stress (section 2.4.4) at the liquid/air interface. This Marangoni stress opposes the surface flow and thus the surface flow is reduced. The Marangoni stress is caused by a surface tension gradient and corresponding gradient in surface surfactant concentration, i.e. gradient in surface excess, along the liquid/air interface. Therefore, the flow near the liquid/air interface is reduced in the case of aqueous

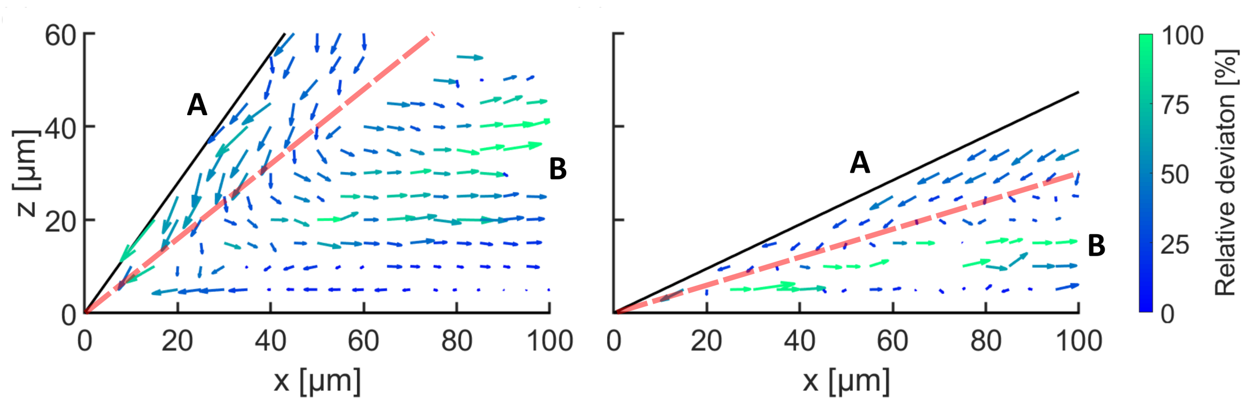

Figure 4.10.: (a) Deviation field of a 30 % CMC $C_{12}E_5$ solution with an absolute surfactant concentration of $0.38\,\mathrm{ppm}$. (b) Deviation field of a 30 % CMC C_8E_3 solution with an absolute surfactant concentration of 40 ppm. The red dashed line separates the deviation close the free surface (region A) from the bulk deviation (region B). Deviation fields for all surfactant solutions can be found in Appendix A.3.1. Adapted from [170] (CC BY 4.0).

surfactant solution compared to water. As a result, the liquid/air interface of aqueous surfactant solutions is not stress–free. The surface tension gradients are quantified in section 4.8.
In the bulk region (B) the arrows point to the right, i.e. in opposite flow direction. This means that the velocity in this region is also reduced compared to water. The reason for this second region can be explained by the conservation of mass. The shown liquid volume is defined as a control volume and the conservation of mass must be fulfilled. Since the outflow is reduced due to the Marangoni stress in region A, the inflow in region B must be reduced as well to fulfil mass conservation. This is the reason why the bulk flow in region B is reduced. It is remarkable that these pronounced deviations are created by an absolute surfactant concentration of only $c_{abs} = 0.38\,\mathrm{ppm}$ and 40 ppm for $C_{12}E_5$ and C_8E_3 respectively.

4.8. Surface tension gradient

As shown in the previous section, the surface flow of aqueous surfactant solutions is reduced compared to the expected flow behaviour of pure water. The reason for this is a surface tension gradient leading to a Marangoni stress which opposes the surface flow. Thus, the liquid/air interface of aqueous surfactant solutions is not stress–free. It is possible to quantify the surface tension gradient by calculating the shear stress, i.e. Marangoni stress, at the liquid/air interface which is necessary to cause the measured flow fields. Figure 4.11 (a) shows a sketch of the liquid wedge with the direction of the important parameters. The shear stress τ at the liquid/air interface, i.e. the free surface of the liquid, can be calculated by using the measured velocity data of the surfactant solutions

$$\tau = \mu \nabla_{\perp} v_p|_{Int} \tag{4.4}$$

with the dynamic viscosity of the liquid μ and the derivative of the velocity component parallel to the free surface v_p at the liquid/air interface, i.e. the surface velocity. In the present case, the surface tension gradient $\nabla_{\parallel}\gamma$ along the free surface can be equated to the shear stress

$$\nabla_{\parallel}\gamma = \tau = \mu \nabla_{\perp} v_p|_{Int} \tag{4.5}$$

because any stress occurring at a surface originates from a surface tension gradient [106].

To calculate the velocity derivative $\nabla_{\perp} v_p$, the measured velocity is fitted by a cubic polynomial in the direction normal to the liquid/air interface. The shear stress τ is calculated by differentiating the polynomial and using the viscosity of water $\mu = 1\,\mathrm{mPa\,s}$. Since the absolute surfactant concentration is low and even temperature effects have a higher influence on the viscosity than the small amounts of surfactant molecules, the viscosity of water can be used to calculate the shear stress for the surfactant solutions. Even though the polynomial fitting is done with a fair amount of data points, the uncertainty of the calculated shear stress is around 20 %. The area closer than $x_{Int} = 20\,\mathrm{\mu m}$ to the three-phase contact line is excluded from further analysis due to large statistical errors. The reason for these errors is the size of the tracer particles. Close to the three–phase contact line the liquid area is limited by the opening angle of the wedge. The tracer particles interact with the fluid flow and thus do not correctly indicate the flow motion (see discussion in the following paragraph). Therefore, a region closer than $x_{Int} = 20\,\mathrm{\mu m}$ is excluded from further analysis. The change in surface tension $\Delta\gamma$ is calculated by integration of the shear stress τ in negative x_{Int}–axis direction along the free surface.

Figure 4.11 (b) to (d) show the calculated change in surface tension $\Delta\gamma$ for different solutions. The change in surface tension $\Delta\gamma$ is plotted above the interface variable x_{Int}. The curves are exponential fits to the data and the dotted lines are the corresponding confidence intervals. For pure water, a change in surface tension is not expected. Yet, the shown curve for pure water shows a slight increase when approaching the contact line (Figure 4.11 (b)). It is assumed that the minimal increase is due to the interaction of the tracer particles with the flow motion close to the contact line. In the vicinity of the sharp corner, the tracer particle might not follow the fluid motion correctly but disturbs the fluid motion due to its size. Thus, it is assumed that the small measured increase of the surface tension of water is a systematic error due to the interaction of the tracer particles with the flow motion in the vicinity of the sharp corner. This assumption is supported by several points. For distances larger than $x_{Int} = 30\,\mathrm{\mu m}$ the $\Delta\gamma$ values of pure water are around zero. The calculated change in surface tension for the 5 % CMC surfactant solutions are already a factor three larger than values of pure water. The slopes of these solutions also start to increase further away from the contact line. The curves of higher concentrated surfactant solutions show significant changes in surface tension that are more than a factor 100 larger than the values of water and also start to increase substantially further away from the contact line (Figure 4.11 (c) and (d)). Hence, the assumption that the slight increase in the calculated surface tension gradient for water is a small systematic error is valid. Since the calculated changes in surface tension for surfactant solutions are significantly higher and start to appear farther away from the contact line, the systematic error has a negligible influence on the calculated values.

The calculated gradient in surface tension for all surfactant solutions occurs up to several tens of micrometres from the contact line. At a certain distance each surfactant solution shows a vanishing change in surface tension $\Delta\gamma$ (Figure 4.11 (c) and (d)). This indicates that the surface surfactant concentration, i.e. the surface excess of surfactant, is in equilibrium with the bulk concentration at large distances from the contact line. It can be seen that this distance is increased with increasing surfactant concentration. Thus, the non–equilibrium region at the free surface, i.e. the region where a change in surface tension occurs, is increased with increasing surfactant concentration for all solutions and both surfactants. Since the data were fitted with an exponential function, the decay length L_{dec}, i.e. the inverse of the decay constant, is a good characteristic length to compare the surfactant solutions. The decay length is the distance at which the change in surface tension $\Delta\gamma$ has decreased to $1/e \approx 0.37$ times its initial value. The decay lengths L_{dec} are shown by the coloured boxes in Figure 4.11 (c) and (d). For all surfactant solutions these lengths are around 10–25 $\mathrm{\mu m}$. Thus, independent of the surfactant concentrations, all surface tension gradients decay over a similar distance for both surfactants.

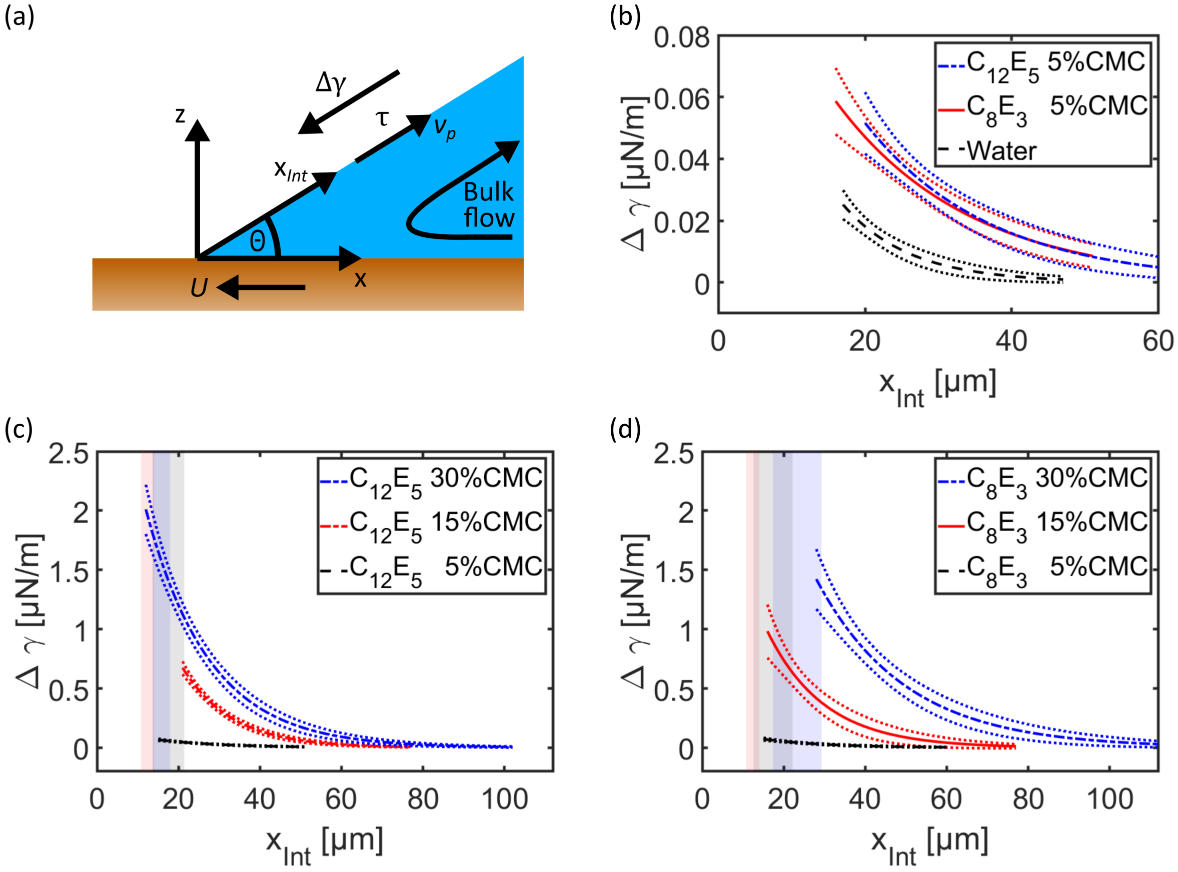

Figure 4.11.: (a) Sketch of the area close to the receding three−phase contact line to show the orientation of the shear stress τ, the velocity component parallel to the free interface v_p and x_{Int}−axis. (b-d) Calculated change in surface tension $\Delta\gamma$ of water and aqueous surfactant solutions along the free surface. The origin of the plots is the moving contact line. Change in surface tension of (b) 5 % CMC solutions and water, (c) $\mathrm{C_{12}E_5}$ solutions, and (d) $\mathrm{C_8E_3}$ solutions. The data was fitted with an exponential function and the dotted lines are the corresponding confidence intervals. The decay lengths of the exponential functions are shown by the coloured boxes in (c) and (d). Adapted from [170] (CC BY 4.0).

When approaching the contact line, $\Delta\gamma$ increases showing that the local surface tension increases compared to the equilibrium surface tension. This behaviour is observed for all measured surfactant solutions showing the generic behaviour of this phenomena. Although the maximum increase in surface tension is only around $2\,\mu\mathrm{N\,m^{-1}}$ (30 % CMC $\mathrm{C_{12}E_5}$), the corresponding gradient in surface tension is around $130\,\mathrm{mN\,m^{-2}}$. The magnitude of the surface tension gradient is increased with increasing surfactant concentration for both surfactants. The reason for the higher surface tension near the contact line is a decreasing surface excess of surfactant molecules, i.e. decreasing surface surfactant concentration, close to the three–phase contact line. The local surface excess of each surfactant solution, calculated with the maximum values of the surface tension from Figure 4.11 (c) and (d), is only 0.01 % lower than the equilibrium surface excess Γ (Γ is listed in Table 4.2 for all solutions). Hence, although only small changes of the surface excess occur, the influence on the receding contact angle and the flow fields is significant (see deviation fields in Figure 4.10). This means that even the smallest impurities in pure fluids have a huge impact on the dynamics at the free surfaces and the bulk velocity field.

4.9. Test of hypothesis

In section 2.5.2 a hypothesis [69, 85] to explain the influence of surfactants on forced dewetting was presented. In this section, the hypothesis and the corresponding scaling arguments are tested with the measured data. Furthermore, a new model is proposed describing an additional surfactant transport process.

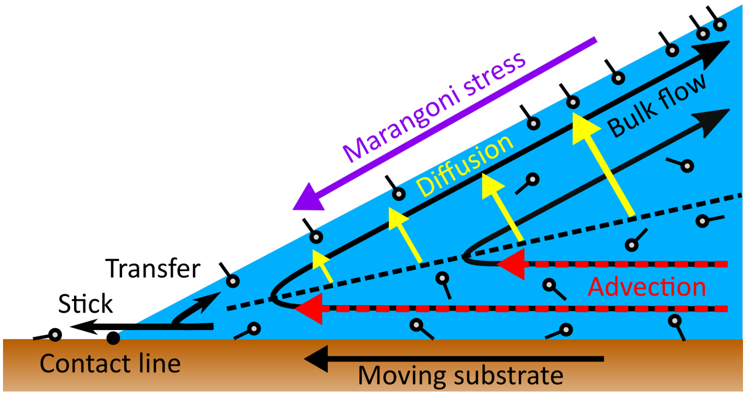

Figure 4.12.: Sketch showing the processes close to a receding three–phase contact line in the presence of surfactant molecules. Adapted from [170] (CC BY 4.0).

In Figure 4.12 an adaptation of Figure 2.14 (section 2.5.2) is shown. In the following, the main arguments of the hypothesis are briefly repeated by referring to Figure 4.12. The sketch shows the region at a receding contact line with a wedge–shaped liquid volume and the possible surfactant transport mechanisms. The bulk flow is represented by the black arrows and the surfactant molecules are represented by the small circles with a tail. A new liquid/air interface is continuously created at the receding contact line. This new interface is covered less with surfactants than the liquid interface in equilibrium further away from the contact line. Surfactants adsorb to the new interface in two ways: (1) Some surfactant molecules are stuck at the liquid/solid interface. These molecules are either transferred to the new interface or they stick to the solid surface and move out of the liquid volume. (2) Diffusion transports surfactant molecules from the bulk solution towards the new interface. This process is supported by advection due to the bulk flow. Thus, a region underneath the new liquid/air interface is depleted of molecules (above the dashed line in Figure 4.12). In the vicinity of the solid, advection transports the equilibrium surfactant concentration of the bulk liquid towards the contact line (below the dashed line). The result of this equilibration process is a difference in surfactant concentration along the liquid/air interface and therefore a concentration gradient. The resulting surface tension gradient leads to a Marangoni stress (section 2.4.4) along the liquid/air interface opposing the surface flow.

The main argument of the hypothesis [69] that a Marangoni effect opposes the bulk flow is verified by the flow field measurements. The deviation fields, which indicate the velocity deviation between the measured flow of aqueous surfactant solutions and the expected flow of water, show a huge velocity deviation of the surfactant solutions underneath the free surface. Thus, the surface flow of surfactant solutions is lower compared to the expected surface flow of pure water. It was shown that the reason for this reduced surface flow is a Marangoni stress which opposes the surface flow. The cause of the Marangoni stress, the gradient in surface tension, was also quantified. In accordance with the hypothesis, it was found that the strength of the Marangoni effect increases with increasing surfactant concentration.

4.9.1. Scaling arguments

Since it was possible to quantify the change in surface tension and surface excess (Figure 4.11), the scaling arguments [85] of the hypothesis can be tested. These scaling arguments are based on the assumption that diffusion perpendicular to the free surface is dominant while neglecting hydrodynamic flow effects. The scaling arguments were presented in section 2.5.2 in detail. The scaling arguments were calculated using the measured receding contact angles (Appendix A.3.1), equilibrium surface tensions (Table 4.2) and a contact line velocity of $200\,\mu\mathrm{m\,s^{-1}}$. In the following, the scaling arguments are compared to the measured data.

Time scales

In this section, the time scale arguments are discussed. The diffusive time scale t_D defines the time needed to equilibrate the free surface by the diffusion component that is normal to the surface. The advective time scale t_A was defined as the time needed to create a new liquid/air interface which has the length of the non–equilibrium region L_{non} [85]. L_{non} is the predicted size of the region close to the contact line where the surface surfactant concentration is not in equilibrium with the concentration in the bulk. The calculated advective t_A and diffusive t_D time scales differ up to several orders of magnitude for the surfactants due to their different molecular properties (Table 4.3).
The ratio $t_R = t_D/t_A$ indicates whether diffusion is fast enough to equilibrate the newly created interface over the length of the non–equilibrium region L_{non} or not. In the case of $t_R > 1$, diffusion is not fast enough and the non–equilibrium region would expand along the interface. If $t_R < 1$, diffusion is fast enough to equilibrate the interface within the length L_{non}. The here calculated ratios t_R predict that diffusion is not fast enough to equilibrate the surface within the length L_{non} for all $C_{12}E_5$ surfactant solutions. This indicates that the diffusive surfactant transport perpendicular to the liquid/air interface is not enough to equilibrate the interface within the length L_{non}. In the case of C_8E_3, diffusion can be fast enough to equilibrate the the interface concentration.

Table 4.3.: Time scale arguments for the aqueous surfactant solutions: diffusive t_D time scale, advective t_A time scale, time scale ratio t_R and calculated Péclet numbers for the diffusion length α.

Surfactant	[%CMC]	t_D [s]	t_A [s]	t_R	Pe_α
$C_{12}E_5$	5	103	0.6	173.3	168.5
$C_{12}E_5$	15	103	2.3	44.1	168.5
$C_{12}E_5$	30	103	2.3	45.2	168.5
C_8E_3	5	6×10^{-3}	14×10^{-3}	0.5	1
C_8E_3	15	6×10^{-3}	22×10^{-3}	0.3	1
C_8E_3	30	6×10^{-3}	52×10^{-3}	0.1	1

It was earlier shown that the ratio t_R (equation 2.22) is, apart from the prefactor, identical to the definition of the Péclet number (equation 2.23). If the ratio t_R is interpreted like a Péclet number, it indicates whether the advective or diffusive transport rate is dominant along the length α. The diffusion length α defines a region that contains as many surfactant molecules as the surface, when the surface and the volume concentrations are in equilibrium. In the case of $\mathrm{C_{12}E_5}$ solutions, the message remains the same. The ratio t_R indicates that diffusion is not enough to equilibrate the interface over the length α with the bulk concentration. For convenience, also the Péclet numbers Pe_α are calculated using the diffusion length α and the contact line velocity U. These numbers only differ due to the above–mentioned prefactor from the values of t_R. These Péclet numbers indicate as well that diffusion is not enough to equilibrate surface surfactant concentration of the new liquid/air interface since $Pe_\alpha > 1$. In the case of $\mathrm{C_8E_3}$ surfactant solutions, the Péclet numbers are $Pe_\alpha = 1$ which means that advective and diffusive transport are equally important to equilibrate the interface concentration. This indicates that, next to diffusion, also advective transport is important for $\mathrm{C_8E_3}$ surfactant solutions.

These results imply that the diffusive surfactant transport perpendicular to the liquid/air interface is not enough to equilibrate the surface surfactant concentration of the newly created liquid/air interface with the bulk concentration. Especially, in the case of the surfactant $\mathrm{C_{12}E_5}$, diffusion is inefficient. Hence, the assumption of the scaling arguments, that diffusion is the dominant surfactant transport mechanism, might be wrong. The scaling arguments are based on several assumptions and simplifications. The assumption that diffusion is dominant is reasonable when the problem is simplified to the two–dimensional wedge–shaped liquid as shown in Figure 4.12. In this case, only diffusion can transport sufficient surfactant molecules to the liquid/air interface. No direct advective surfactant transport to the interface is possible since the flow is parallel to the liquid/air interface. Since the above–mentioned results indicate that diffusion is not enough to equilibrate the liquid/air interface, an additional transport mechanism is necessary. The only remaining surfactant transport process is the transfer of molecules that were stuck at the solid surface to the newly created interface at the contact line. However, in accordance with the hypothesis it can be assumed that this surfactant transport is negligibly small. Thus, the simplification to two dimensions allows no further significant surfactant transport processes. Hence, the simplification of the problem to two dimensions might be wrong. Similar observations are made when the predicted length scales are discussed.

Length scales

The above–described time scales were calculated with the length scales α and L_{non} (section 2.5.2). As mentioned above, in equilibrium, the diffusion length α (equation 2.18) defines the thickness of a liquid layer underneath the liquid/air interface that contains as many surfactant molecules as the liquid/air interface. The non–equilibrium region L_{non} (equation 2.19) defines a region that contains enough surfactant molecules to refill the newly generated liquid/air interface at the contact line. In this region, close to the receding contact line, the surfactant concentration at the liquid/air interface is not in equilibrium with the bulk concentration. As already mentioned, the calculation of the length scales is based only on diffusive arguments and neglects hydrodynamic effects.

In Table 4.4 the values of the length scales are shown. It can be seen that the diffusion length α and the non–equilibrium region L_{non} differ up to two orders of magnitude between the aqueous surfactant solutions of $\mathrm{C_{12}E_5}$ and $\mathrm{C_8E_3}$.
In the case of $\mathrm{C_{12}E_5}$, the non–equilibrium region L_{non} predicts that the surfactant concentration of the liquid/air interface is in equilibrium with the bulk concentration at distances higher than $100\,\mu\mathrm{m}$ from the contact line. However, the calculated decay lengths L_{dec} of the surface tension gradients are around $15\,\mu\mathrm{m}$. Thus, equilibrium is reached for significantly shorter distances to the contact line than predicted by the non–equilibrium region. Hence, next to diffusion, additional surfactant transport is needed to equilibrate

Table 4.4.: Length scale arguments for the aqueous surfactant solutions: diffusion length α, non–equilibrium region L_{non} and decay length L_{dec}.

Surfactant	[%CMC]	α [µm]	L_{non} [µm]	L_{dec} [µm]
$C_{12}E_5$	5	244.4	118.9	17.5 ± 3.9
$C_{12}E_5$	15	244.4	466.6	12.4 ± 1.6
$C_{12}E_5$	30	244.4	455.8	15.8 ± 2.1
C_8E_3	5	2.5	2.8	17.4 ± 4.8
C_8E_3	15	2.5	4.5	15.9 ± 5.5
C_8E_3	30	2.5	10.4	23.3 ± 6.0

the surface surfactant concentration. In the case of C_8E_3, the non–equilibrium region L_{non} is smaller than the decay length L_{dec}. Hence, diffusion might be fast enough to equilibrate the interface.
The above–mentioned points indicate that in the case of $C_{12}E_5$ diffusion is not enough to equilibrate the surface while in the case of C_8E_3 diffusion might be enough. However, the decay lengths L_{dec} of the surface tension gradients are similar for all solutions and both surfactants, although the diffusion lengths α and therefore the availability of surfactant molecules in the measurement volume deviate considerably between the surfactants. The similar decay lengths L_{dec} for all solutions and both surfactants can not be explained by the diffusive scaling arguments.

In accordance with the results of the previous section, the above–described results indicate molecular properties of the surfactants, e.g. size and diffusion coefficient, have a small influence on the dynamics of dewetting surfactant solutions. A two–dimensional theory based on the assumption that diffusion is the dominant surfactant transport process is not capable of describing the dewetting dynamics of aqueous surfactant solutions correctly. As mentioned earlier, the simplification to two dimensions allows no further surfactant transport processes besides diffusion. Therefore, the results indicate that an additional transport process is needed to equilibrate the liquid/air interface. Thus, the problem analysis should be extended to three dimensions.

4.9.2. Possible three–dimensional surfactant transport

Until now, the dewetting behaviour of surfactant solutions was only explained by the dynamics close to the receding three–phase contact line in two dimensions. It was found that a Marangoni effect arises due to a surface tension gradient. This Marangoni effect is responsible for the observed dynamics of the surfactant solutions. However, the results indicate that a two–dimensional approach is not sufficient to describe the whole dynamics.

Previous studies [70] (section 2.5.3) reported that the dynamic dewetting behaviour of aqueous surfactant solutions also depends, next to the dynamics close to the contact line, on surfactant transport on large length scales, i.e. the three–dimensional surfactant transport from the advancing to the receding side. The same might be true for the present case of moving drops consisting of aqueous surfactant solutions.
Figure 4.13 shows a horizontal cut through a moving drop. At the receding side of the drop, a new liquid/air interface is continuously created, and at the advancing side the molecules forming the liquid/air interface return to the bulk liquid. At the sides of the moving drop, the liquid flow is parallel to the contact line as shown by others [146]. It can be assumed that in this region the surface surfactant concentration is in equilibrium with the bulk surface. Thus, the surface surfactant concentration at the sides of the drop

is higher than at the receding side of the drop. This results in a surface tension gradient tangential to the contact line since $\gamma_{rec} > \gamma$. This surface tension gradient would cause a Marangoni effect that drives surfactant transport from the drop's sides to the receding side of the moving drop. This effect occurs over the entirety of the drop's surface. This surfactant transport would contribute to the equilibration process of the newly created interface at the receding contact line.

Further studies are needed to investigate the advection–diffusion dynamics of moving drops of aqueous surfactant solutions. Especially the above described possible three–dimensional surfactant transport around the drop's surface might play an important role in the complex dynamics of dewetting surfactant solutions.

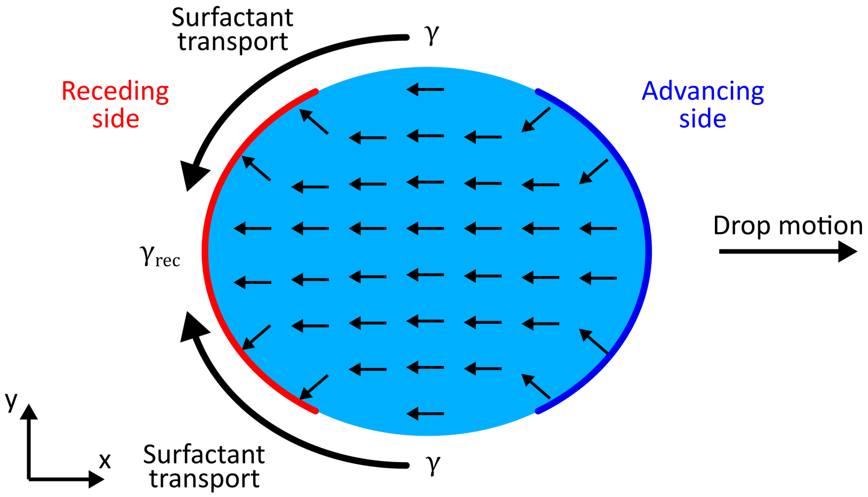

Figure 4.13.: Possible three–dimensional surfactant transport around the drop's surface. Shown is a horizontal plane through the drop with assumed internal flow of the drop. [170] (CC BY 4.0).

4.10. Conclusion of the influence of surfactant on forced dewetting

In this chapter, I investigated the dynamic dewetting behaviour of surfactant solutions. Three–dimensional flow fields close to receding contact lines were measured using the in section 3.2 described APTV setup. The measured data indicated that the flow in the direction parallel to the contact line is negligible in the measurement area. Thus, the three–dimensional velocity data was projected onto a two–dimensional plane. To compare the measured flow fields with theoretical calculations, I assume that the liquid has a straight liquid/air interface and thus a wedge–shaped form. The measured flow fields are compared to the theoretical solution of Moffatt [127] for the case of water and a stress–free liquid/air interface (page 12). The measured flow fields of water match well with the theoretical solution indicating that the liquid/air interface is indeed stress–free in the case of pure water.

Aqueous surfactant solutions of the nonionic surfactants dodecyl pentaglycole ($\mathrm{C_{12}E_5}$) and octyl triglycole ($\mathrm{C_8E_3}$) with concentrations well below the critical micelle concentration were investigated. In accordance with previous studies [69, 83], the receding contact angles decrease with increasing surfactant concentrations. Since the shape of the liquid wedge differs between surfactant solutions and water, due to different receding contact angles, a direct comparison of the measured flow fields between the water and surfactant solutions is not possible. However, since the measurements of water agreed well with the theoretical solution of Moffatt [127], it is valid to compare the measured flow fields of the surfactant solutions with the theoretical prediction for water. This comparison revealed pronounced deviations between the measured flow fields of surfactant solutions and the theoretical solution for pure water (section 4.7.2). Especially the flow at the liquid/air interface is reduced for surfactant solutions. The reduction of the surface flow is explainable by a shear stress at the liquid/air interface opposing the surface flow. Hence, the assumption of a stress–free liquid/air interface does not apply for aqueous surfactant solutions. This so–called Marangoni stress (2.4.4) is caused by a surface tension gradient, i.e. a gradient in surface surfactant concentration, along the liquid/air interface.

The surface tension gradient was quantified by calculating the shear stress, i.e. the Marangoni stress, at the liquid/air interface which is necessary to cause the measured velocity fields (section 4.8). It was found that the strength of the Marangoni stress increases with increasing surfactant concentration.
Despite the absolute concentrations of the solutions differing up to a factor of 100 and the typical diffusion lengths up to a factor of 1000, it was found that the surface tension gradients for all solutions and both surfactants decrease over approximately the same decay length. This indicates that molecular properties of the surfactant molecules, i.e. size or structure, have a small influence on the dynamics. Thus, an additional surfactant transport process, next to diffusion, is necessary to explain the equilibration of the surfactant concentration at the liquid/air interface with the bulk concentration. A possible Marangoni stress driven three–dimensional surfactant transport around the drop's surface was proposed in section 4.9.2.
Although the maximum observed increase of surface tension close to the contact line is only around $2\,\mu\mathrm{N\,m^{-1}}$ higher than the equilibrium value, the corresponding surface tension gradient is $130\,\mathrm{mN\,m^{-2}}$. Even though the surface excess, i.e. the surface surfactant concentration, only varies by 0.01 % from the equilibrium value for all solutions, the measured influence on the flow fields is immense. This, together with the fact that the measured effects occur even for absolute surfactant concentrations below 1 ppm, shows that even the smallest impurities in pure fluids, which are often unavoidable, have a huge influence on the dynamic dewetting behaviour of liquids.

In section 4.9, the above–described observations were used to test the in section 2.5.2 presented hypothesis [69]. The hypothesis proposed that a Marangoni stress opposes the surface flow close to the receding contact line of dewetting surfactant solutions. This argument is verified by the measured flow fields.

5. Conclusion and outlook

In this work, I measured flow fields close to receding three–phase contact lines to study the dynamic dewetting behaviour of aqueous surfactant solutions. Hereby, the dependence of the dynamic dewetting behaviour on the surfactant concentration was investigated. Furthermore, an existing hypothesis [69], which proposes that a Marangoni stress opposes the surface flow close to the receding three–phase contact line of aqueous surfactant solutions, was tested. Thus, a major objective of my work was to build an experimental setup with sufficient spatial and temporal resolution to measure the flow fields close to receding three–phase contact lines.

For this purpose, I developed and successfully built two complementary experimental setups: a fast re–scan laser scanning confocal microscope and an astigmatism particle tracking velocimetry (APTV) setup. Both setups can be used to measure the required flow fields with sufficient spatial and temporal resolution. However, each setup has its individual advantages and disadvantages.
The custom–built fast re–scan laser scanning confocal microscope enables measuring two–dimensional flow fields with a frame rate up to 1 kHz in the horizontal and up to 200 Hz in the vertical direction. These high–speed capacities are superior to comparable commercial state–of–the–art microscopes. Next to tracking the flow motion, the slope of the liquid/air interface, and the position of the contact line can be measured directly. Furthermore, arbitrary planes through the sample can be scanned and high concentrations of tracer particles can be used to track the flow motion. The major disadvantage of the custom–built microscope is the necessity to repeatedly adjust and align the optomechanical components. Otherwise, the image quality is greatly reduced. An additional drawback is the possible disturbance of the sample due to mechanical vibrations.
Astigmatism particle tracking velocimetry enables direct measurements of three–dimensional flow fields without the need for moving parts. However, the amount of tracer particles is, compared to the custom–built confocal microscope, low, since every particle in the three–dimensional volume is detected simultaneously. Thus, overlapping particle image shapes should be avoided leading to a reduced concentration of tracer particles. As a result, APTV detects fewer particles per frame compared to the custom–built microscope. However, a sufficient amount of particle trajectories is needed for a good spatial resolution. This was achieved by increasing the measurement time. In contrast to the custom–built microscope, no adjustment and alignment effort is needed to use APTV. Furthermore, no index matching of the measurement fluid with the tracer particles is necessary. Moreover, no moving parts are needed and thus no mechanical disturbance of the sample is possible. However, a calibration of the setup and the detection of the particle image shapes are necessary. For the purpose of this work, this was considered a minor disadvantage compared to the alignment effort and possible disturbance of the sample when using the confocal microscope. Therefore, I used the APTV setup to directly measure three–dimensional flow fields close to receding three–phase contact lines of aqueous surfactant solutions.

The conducted experiments showed that the measured flow fields for pure water agree well with the hydrodynamic theory of Moffatt [127] which assumes a stress–free liquid/air interface. This indicates that the liquid/air interface of pure water is indeed stress–free.

Aqueous surfactant solutions of the nonionic surfactants dodecyl pentaglycole ($C_{12}E_5$) and octyl triglycole (C_8E_3) with concentrations well below the critical micelle concentration were investigated. In accordance with previous studies [69, 83], it was found that the receding contact angles decrease with increasing surfactant concentrations. Moreover, the measurements showed that surfactants reduce the flow velocity close to the free surface. Thus, the surface flow of the liquid was reduced. This is explainable by a shear stress at the liquid surface opposing the surface flow. Hence, the assumption of a stress–free liquid air interface does not apply for aqueous surfactant solutions. This so–called Marangoni stress is caused by a surface tension gradient resulting from a gradient in surface surfactant concentration along the liquid/air interface. Consequently, the hypothesis [69], which proposed the existence of a Marangoni stress opposing the surface flow, was verified. By calculating the shear stress necessary to cause the measured flow fields, it was possible to quantify the change in surface tension and corresponding surface tension gradient along the liquid/air interface. Despite the calculated maximum increase in surface tension close to the contact lines being only around $2\,\mu\mathrm{N\,m^{-1}}$ higher than the equilibrium surface tension, the corresponding surface tension gradient is around $130\,\mathrm{mN\,m^{-2}}$. Even though, the surfactant concentration at the surface, i.e. the surface excess, only varies by 0.01 % from the equilibrium value, the measured influence on the flow fields is significant. The measured effects occur even for absolute surfactant concentrations below 1 ppm. This indicates that even the smallest amounts of impurities in fluids, which are often unavoidable, have a huge influence on the dynamic dewetting behaviour of liquids.

Furthermore, it was found that the range and magnitude of the surface tension gradient increase with increasing surfactant concentration. Although the absolute concentrations of the aqueous surfactant solutions differ up to a factor of 100 and typical diffusion lengths up to a factor of 1000, the surface tension gradients for all solutions and both surfactants decay over nearly the same decay length. This indicates that the molecular properties of the surfactant molecules, i.e. structure and size, have only a small influence on the dewetting dynamics. Thus, an additional surfactant transport mechanism besides diffusion seems to be necessary to explain the equilibration of the surfactant concentration at the surface with the surfactant concentration in the bulk.

For this reason, a possible three–dimensional surfactant transport around the drop's surface was proposed. It is assumed that the liquid flow at the sides of the drop is parallel to the contact line and thus the surface surfactant concentration at the drop's sides is in equilibrium with the bulk. This means that the surface surfactant concentration on the sides of the drop is higher than in the receding part of the drop. As a result, a surface tension gradient arises parallel to the contact line. This leads to a Marangoni effect driving surfactant transport from the sides of the drop to the receding part of the drop. This effect occurs over the entirety of the drop's surface. This surfactant transport might contribute to the equilibration process of the newly created liquid/air interface at the receding contact line.

In conclusion, flow fields of aqueous surfactant solutions close to receding three–phase contact lines were measured and the hypothesis [69], which proposed the existence of a Marangoni stress, was verified. Moreover, a significant influence of very low surfactant concentrations below 1 ppm on the dynamic dewetting behaviour of liquids was shown. The results indicate that, next to diffusion, an additional surfactant transport process is necessary. A possible three–dimensional surfactant transport mechanism acting over the entire surface of the drop was proposed.

In the course of this work, smooth substrates were used. However, dynamic wetting on rough or structured substrates should be investigated as well since in practice the wetted surface is usually not perfectly smooth. This could be done with the here developed confocal microscope. In addition, the wetting behaviour of other one– or more–component liquids should be studied because in technical applications the liquids vary greatly.

Furthermore, the observed dividing streamline necessitates further investigations. In this case, the surface flow along the liquid/air interface was reversed. This means that the surface flow pointed towards the contact line. Other studies [16, 72] reported the dividing streamline as well. In this work, the reason for the dividing streamline was some sort of unknown contamination. It was not possible to create the dividing streamline on purpose. However, being able to create or suppress the dividing streamline in a controlled manner would be of great scientific interest.

Moreover, further investigations of the possible three–dimensional surfactant transport on the drop's surface are needed. In accordance with a previous study [70], a large–scale surfactant transport mechanism is likely and would significantly contribute to understanding the dynamics of dewetting surfactant solutions.

Bibliography

[1] *A1R HD25. Confocal Microscope System*. 2018. URL: https://www.microscope.healthcare.nikon.com/en_EU/products/confocal-microscopes/a1hd25-a1rhd25 (visited on 06/08/2020).

[2] E. Abbe. “Beiträge zur Theorie des Mikroskops und der mikroskopischen Wahrnehmung”. In: *Archiv für Mikroskopische Anatomie* 9 (1 1835), pp. 413–468. ISSN: 0176–7364. DOI: 10.1007/BF02956173. URL: https://doi.org/10.1007/BF02956173.

[3] R. J. Adrian. “Twenty years of particle image velocimetry”. In: *Experiments in Fluids* 39.2 (2005), pp. 159–169. ISSN: 1432–1114. DOI: 10.1007/s00348-005-0991-7. URL: https://doi.org/10.1007/s00348-005-0991-7.

[4] G. B. Airy. “On the diffraction of an object-glass with circular aperture”. In: *Transactions of the Cambridge Philosophical Society* 5 (1835), pp. 283–291. URL: https://archive.org/details/cbarchive_120424_onthediffractionofanobjectglas9999/page/n1/mode/2up.

[5] Y. Amarouchene, G. Cristobal, and H. Kellay. “Noncoalescing Drops”. In: *Phys. Rev. Lett.* 87 (Oct. 2001), p. 206104. DOI: 10.1103/PhysRevLett.87.206104. URL: https://link.aps.org/doi/10.1103/PhysRevLett.87.206104.

[6] B. Amos, G. McConnell, and T. Wilson. “2.2 Confocal Microscopy”. In: *Comprehensive Biophysics*. Ed. by E. H. Egelman. Vol. 2. Amsterdam: Elsevier, 2012, pp. 3–23. ISBN: 978-0-08-095718-0. DOI: https://doi.org/10.1016/B978-0-12-374920-8.00203-4. URL: http://www.sciencedirect.com/science/article/pii/B9780123749208002034.

[7] W. B. Amos, J. G. White, and M. Fordham. “Use of confocal imaging in the study of biological structures”. In: *Appl. Opt.* 26.16 (Aug. 1987), pp. 3239–3243. DOI: 10.1364/AO.26.003239. URL: http://ao.osa.org/abstract.cfm?URI=ao-26-16-3239.

[8] I. Arganda–Carreras, C. O. S. Sorzano, R. Marabini, J. M. Carazo, C. Ortiz–de Solorzano, and J. Kybic. “Consistent and Elastic Registration of Histological Sections Using Vector-Spline Regularization”. In: *Computer Vision Approaches to Medical Image Analysis*. Ed. by R. R. Beichel and M. Sonka. Vol. 4241. Springer Berlin Heidelberg, 2006, pp. 85–95. ISBN: 978-3-540-46258-3. URL: %3CGo%20to%20ISI%3E://WOS:000241602500008.

[9] N. Åslund, K. Carlsson, A. Liljeborg, and L. Majlöf. “PHOIBOS, a Microscope Scanner Designed for Micro-Fluorometric Applications, Using Laser Induced Fluorescence”. In: *Proceedings of the Third Scandinavian Conference on Image Analysis, Studentliteratur* (1983), p. 338.

[10] N. Åslund, A. Liljeborg, P.-O. Forsgren, and S. Wahlsten. “Three–dimensional digital microscopy using the PHOIBOS Scanner”. In: *Scanning* 9.6 (1987), pp. 227–235. DOI: `10.1002/sca.4950090603`. eprint: `https://onlinelibrary.wiley.com/doi/pdf/10.1002/sca.4950090603`. URL: `https://onlinelibrary.wiley.com/doi/abs/10.1002/sca.4950090603`.

[11] G. K. Auernhammer, M. Roth, and H.-J. Butt. *Optical scanning microscope having two scanning units*. webside. patent application, application number: DE102012101344. 2013. URL: `https://depatisnet.dpma.de/DepatisNet/depatisnet?action=bibdat%5C&docid=DE102012101344A1`.

[12] R. Barnkob, C. J. Kähler, and M. Rossi. “General defocusing particle tracking”. In: *Lab on a Chip* 15.17 (2015), pp. 3556–3560. DOI: `10.1039/C5LC00562K`. URL: `http://dx.doi.org/10.1039/C5LC00562K`.

[13] R. Barnkob and M. Rossi. “General defocusing particle tracking: fundamentals and uncertainty assessment”. In: *Experiments in Fluids* 61.4 (2020), p. 110. ISSN: 1432-1114. DOI: `10.1007/s00348-020-2937-5`. URL: `https://doi.org/10.1007/s00348-020-2937-5`.

[14] J. Bataille. “Etude de l’écoulement au voisinage du ménisque séparant deux fluides se déplaçant lentement entre deux plaques planes paralléles ou dans un tube capillaire”. In: *C. R. Acad. Sci. (Paris) A* 262 (1966), pp. 843–846. URL: `https://gallica.bnf.fr/ark:/12148/bpt6k6413222n/f305.item`.

[15] M. Bawart, M. A. May, T. Öttl, C. Roider, S. Bernet, M. Schmidt, M. Ritsch-Marte, and A. Jesacher. “Diffractive tunable lens for remote focusing in high-NA optical systems”. In: *Opt. Express* 28.18 (Aug. 2020), pp. 26336–26347. DOI: `10.1364/OE.400784`. URL: `http://www.opticsexpress.org/abstract.cfm?URI=oe-28-18-26336`.

[16] B. K. Beppler, K. S. Varanasi, S. Garoff, G. Evmenenko, and K. Woods. “Influence of fluid flow on the deposition of soluble surfactants through receding contact lines of volatile solvents”. In: *Langmuir* 24 (13 2008), pp. 6705–6711. ISSN: 0743-7463. DOI: `10.1021/la8004882`. URL: `https://doi.org/10.1021/la8004882`.

[17] B. Berge and J. Peseux. “Variable focal lens controlled by an external voltage: An application of electrowetting”. In: *The European Physical Journal E* 3.2 (2000), pp. 159–163. ISSN: 1292-8941. DOI: `10.1007/s101890070029`. URL: `https://doi.org/10.1007/s101890070029`.

[18] S. Bhattacharji and P. Savic. “Real and apparent non-Newtonian behaviour in viscous pipe flow of suspensions driven by a fluid piston”. In: *Proceedings of the 1965 Heat Transfer and Fluid Mechanics Institute* 248 (1965), pp. 248–262.

[19] J. Bikerman. “Sliding of drops from surfaces of different roughnesses”. In: *Journal of Colloid Science* 5.4 (1950), pp. 349–359. ISSN: 0095-8522. DOI: `https://doi.org/10.1016/0095-8522(50)90059-6`. URL: `http://www.sciencedirect.com/science/article/pii/0095852250900596`.

[20] J. Billingham and A. King. “The interaction of a moving fluid/fluid interface with a flat plate”. In: *Journal of Fluid Mechanics* 296 (1995), pp. 325–351. DOI: `10.1017/S002211209500214X`.

[21] T. D. Blake. “The physics of moving wetting lines”. In: *Journal of Colloid and Interface Science* 299.1 (2006), pp. 1–13. ISSN: 0021–9797. DOI: `https://doi.org/10.1016/j.jcis.2006.03.051`. URL: `http://www.sciencedirect.com/science/article/pii/S0021979706002463`.

[22] T. D. Blake, A. Clarke, and K. J. Ruschak. “Hydrodynamic assist of dynamic wetting”. In: *AIChE Journal* 40.2 (1994), pp. 229–242. DOI: `10.1002/aic.690400205`. eprint: `https://aiche.onlinelibrary.wiley.com/doi/pdf/10.1002/aic.690400205`. URL: `https://aiche.onlinelibrary.wiley.com/doi/abs/10.1002/aic.690400205`.

[23] T. D. Blake and J. M. Haynes. “Contact–Angle Hysteresis”. In: ed. by J. Danielli, M. Rosenberg, and D. Cadenhead. Vol. 6. Progress in Surface and Membrane Science. Elsevier, 1973, pp. 125–138. DOI: `https://doi.org/10.1016/B978-0-12-571806-6.50009-X`. URL: `http://www.sciencedirect.com/science/article/pii/B978012571806650009X`.

[24] T. D. Blake and J. M. Haynes. “Kinetics of liquid/liquid displacement”. In: *Journal of Colloid and Interface Science* 30.3 (1969), pp. 421–423. ISSN: 0021-9797. DOI: `https://doi.org/10.1016/0021-9797(69)90411-1`. URL: `http://www.sciencedirect.com/science/article/pii/0021979769904111`.

[25] T. D. Blake and K. J. Ruschak. “Wetting: Static and Dynamic Contact Lines”. In: *Liquid Film Coating: Scientific principles and their technological implications*. Ed. by S. Kistler and P. Schweizer. Dordrecht: Springer Netherlands, 1997, pp. 63–97. ISBN: 978-94-011-5342-3. DOI: `10.1007/978-94-011-5342-3_3`. URL: `https://doi.org/10.1007/978-94-011-5342-3_3`.

[26] K. B. Blodgett. “MONOMOLECULAR FILMS OF FATTY ACIDS ON GLASS”. In: *Journal of the American Chemical Society* 56.2 (1934), pp. 495–495. DOI: `10.1021/ja01317a513`. eprint: `https://doi.org/10.1021/ja01317a513`. URL: `https://doi.org/10.1021/ja01317a513`.

[27] D. Bonn, J. Eggers, J. Indekeu, J. Meunier, and E. Rolley. “Wetting and spreading”. In: *Reviews of Modern Physics* 81 (2 2009), pp. 739–805. ISSN: 0034-6861. DOI: `10.1103/RevModPhys.81.739`. URL: `https://link.aps.org/doi/10.1103/RevModPhys.81.739`.

[28] R. T. Borlinghaus. *The White Confocal. Microscopic Optical Sectioning in all Colors*. Springer International Publishing, 2017. DOI: `10.1007/978-3-319-55562-1`. URL: `https://doi.org/10.1007/978-0-387-45524-2`.

[29] E. J. Botcherby, R. Juškaitis, M. J. Booth, and T. Wilson. “An optical technique for remote focusing in microscopy”. In: *Optics Communications* 281.4 (2008), pp. 880–887. ISSN: 0030-4018. DOI: `https://doi.org/10.1016/j.optcom.2007.10.007`. URL: `http://www.sciencedirect.com/science/article/pii/S003040180701005X`.

[30] E. J. Botcherby, C. W. Smith, M. M. Kohl, D. Débarre, M. J. Booth, R. Juškaitis, O. Paulsen, and T. Wilson. "Aberration-free three-dimensional multiphoton imaging of neuronal activity at kHz rates". In: *Proceedings of the National Academy of Sciences* 109.8 (2012), pp. 2919–2924. ISSN: 0027-8424. DOI: `10.1073/pnas.1111662109`. eprint: `https://www.pnas.org/content/109/8/2919.full.pdf`. URL: `https://www.pnas.org/content/109/8/2919`.

[31] M. Bown, J. MacInnes, R. Allen, and W. Zimmerman. "Three–dimensional, three–component velocity measurements using stereoscopic micro–PIV and PTV". In: *Measurement Science and Technology* 17.8 (July 2006), pp. 2175–2185. DOI: `10.1088/0957-0233/17/8/017`. URL: `https://doi.org/10.1088%2F0957-0233%2F17%2F8%2F017`.

[32] F. Brochard and P. De Gennes. "Shear–dependent slippage at a polymer/solid interface". In: *Langmuir* 8.12 (1992), pp. 3033–3037. DOI: `10.1021/la00048a030`. eprint: `https://doi.org/10.1021/la00048a030`. URL: `https://doi.org/10.1021/la00048a030`.

[33] H.-J. Butt, K. Graf, and M. Kappl. *Physics and Chemistry of Interfaces*. John Wiley & Sons, Ltd, 2006. DOI: `10.1002/3527602313`. URL: `https://onlinelibrary.wiley.com/doi/book/10.1002/3527602313`.

[34] M. Cachile and A. M. Cazabat. "Spontaneous Spreading of Surfactant Solutions on Hydrophilic Surfaces: CnEm in Ethylene and Diethylene Glycol". In: *Langmuir* 15.4 (1999), pp. 1515–1521. DOI: `10.1021/la980840f`. eprint: `https://doi.org/10.1021/la980840f`. URL: `https://doi.org/10.1021/la980840f`.

[35] K. Carlsson, P. E. Danielsson, R. Lenz, A. Liljeborg, L. Majlöf, and N. Åslund. "Three-dimensional microscopy using a confocal laser scanning microscope". In: *Opt. Lett.* 10.2 (Feb. 1985), pp. 53–55. DOI: `10.1364/OL.10.000053`. URL: `http://ol.osa.org/abstract.cfm?URI=ol-10-2-53`.

[36] M. Castellano–Muñoz, A. W. Peng, F. T. Salles, and A. J. Ricci. "Swept Field Laser Confocal Microscopy for Enhanced Spatial and Temporal Resolution in Live–Cell Imaging". In: *Microscopy and Microanalysis* 18.4 (2012), pp. 753–760. DOI: `10.1017/S1431927612000542`.

[37] V. Centonze and J. Pawley. "Tutorial on Practical Confocal Microscopy and Use of the Confocal Test Specimen". In: *Handbook Of Biological Confocal Microscopy*. Ed. by J. B. Pawley. 3rd ed. Springer, Boston, MA, 2006, pp. 627–649. DOI: `10.1007/978-0-387-45524-2_35`. URL: `https://doi.org/10.1007/978-0-387-45524-2_35`.

[38] D. Y. C. Chan, E. Klaseboer, and R. Manica. "Dynamic deformations and forces in soft matter". In: *Soft Matter* 5 (2009), pp. 2858–2861. ISSN: 1744-683X. DOI: `10.1039/B907953J`. URL: `http://dx.doi.org/10.1039/B907953J`.

[39] B. Cherry and C. Holmes. "Kinetics of wetting of surfaces by polymers". In: *Journal of Colloid and Interface Science* 29.1 (1969). Symposium on Detergency, Solubilization and Micelles in Nonaqueous Media, pp. 174–176. ISSN: 0021-9797. DOI: `https://doi.org/10.1016/0021-`

9797(69)90367-1. URL: http://www.sciencedirect.com/science/article/pii/0021979769903671.

[40] C. Cierpka, R. Segura, R. Hain, and C. J. Kähler. "A simple single camera 3C3D velocity measurement technique without errors due to depth of correlation and spatial averaging for microfluidics". In: *Measurement Science and Technology* 21.4 (2010), p. 045401. DOI: 10.1088/0957-0233/21/4/045401. URL: https://doi.org/10.1088%2F0957-0233%2F21%2F4%2F045401.

[41] C. Cierpka and C. J. Kähler. "Particle imaging techniques for volumetric three-component (3D3C) velocity measurements in microfluidics". In: *Journal of Visualization* 15.1 (2012), pp. 1–31. ISSN: 1875–8975. DOI: 10.1007/s12650-011-0107-9. URL: https://doi.org/10.1007/s12650-011-0107-9.

[42] C. Cierpka, M. Rossi, R. Segura, and C. J. Kähler. "On the calibration of astigmatism particle tracking velocimetry for microflows". In: *Measurement Science and Technology* 22.1 (2011), p. 015401. ISSN: 0957-0233. DOI: 10.1088/0957-0233/22/1/015401. URL: https://doi.org/10.1088/0957-0233/22/1/015401.

[43] C. Cierpka, M. Rossi, R. Segura, F. Mastrangelo, and C. J. Kähler. "A comparative analysis of the uncertainty of astigmatism-μPTV, stereo-μPIV, and μPIV". In: *Experiments in Fluids* 52.3 (2012), pp. 605–615. ISSN: 1432-1114. DOI: 10.1063/1.5093310. eprint: 10.1007/s00348-011-1075-5. URL: https://doi.org/10.1007/s00348-011-1075-5.

[44] J.-A. Conchello and J. W. Lichtman. "Optical sectioning microscopy". In: *Nature Methods* 2 (2005), pp. 920–931. ISSN: 1548-7105. DOI: 10.1038/nmeth815. URL: https://doi.org/10.1038/nmeth815.

[45] *Confocal Microscope Platform STELLARIS. GET CLOSER TO THE TRUTH. Your Next Generation Confocal Microscope with Multiplex Mode*. 2020. URL: https://www.leica-microsystems.com/products/confocal-microscopes/p/stellaris-8/ (visited on 06/08/2020).

[46] R. G. Cox. "The dynamics of the spreading of liquids on a solid surface. Part 1. Viscous flow". In: *Journal of Fluid Mechanics* 168 (1986), pp. 169–194. ISSN: 0022-1120. DOI: 10.1017/S0022112086000332. URL: https://doi.org/10.1017/S0022112086000332.

[47] J. C. Crocker and D. G. Grier. "Methods of Digital Video Microscopy for Colloidal Studies". In: *Journal of Colloid and Interface Science* 179.1 (1996), pp. 298–310. ISSN: 0021-9797. DOI: 10.1006/jcis.1996.0217. URL: http://www.sciencedirect.com/science/article/pii/S0021979796902179.

[48] A. Curran, S. Tuohy, D. G. A. L. Aarts, M. J. Booth, T. Wilson, and R. P. A. Dullens. "Decoupled and simultaneous three-dimensional imaging and optical manipulation through a single objective". In: *Optica* 1.4 (Oct. 2014), pp. 223–226. DOI: 10.1364/OPTICA.1.000223. URL: http://www.osapublishing.org/optica/abstract.cfm?URI=optica-1-4-223.

[49] J. E. Curtis, B. A. Koss, and D. G. Grier. "Dynamic holographic optical tweezers". In: *Optics Communications* 207.1 (2002), pp. 169–175. ISSN: 0030-4018. DOI: `https://doi.org/10.1016/S0030-4018(02)01524-9`. URL: `http://www.sciencedirect.com/science/article/pii/S0030401802015249`.

[50] P.-G. de Gennes, F. Brochard-Wyart, and D. Quéré. *Capillarity and Wetting Phenomena*. Springer, New York, NY, 2004. DOI: `10.1007/978-0-387-21656-0`. URL: `https://doi.org/10.1007/978-0-387-21656-0`.

[51] G. M. R. De Luca, R. M. P. Breedijk, R. A. J. Brandt, C. H. C. Zeelenberg, B. E. de Jong, W. Timmermans, L. N. Azar, R. A. Hoebe, S. Stallinga, and E. M. M. Manders. "Re-scan confocal microscopy: scanning twice for better resolution". In: *Biomedical Optics Express* 4.11 (2013), pp. 2644–2656. ISSN: 2156-7085. DOI: `10.1364/boe.4.002644`. URL: `https://www.ncbi.nlm.nih.gov/pmc/articles/PMC3829557/pdf/2644.pdf`.

[52] G. M. R. De Luca, R. M. P. Breedijk, R. A. Hoebe, S. Stallinga, and E. Manders. "Re-scan confocal microscopy (RCM) improves the resolution of confocal microscopy and increases the sensitivity". In: *Methods and Applications in Fluorescence* 5.1 (2017), pp. 1–11. ISSN: 2050-6120. DOI: `10.1088/2050-6120/5/1/015002`. URL: `https://iopscience.iop.org/article/10.1088/2050-6120/5/1/015002/pdf`.

[53] G. M. R. De Luca et al. "Configurations of the Re-scan Confocal Microscope (RCM) for biomedical applications". In: *Journal of Microscopy* 266.2 (2017), pp. 166–177. ISSN: 0022-2720. DOI: `10.1111/jmi.12526`. URL: `https://onlinelibrary.wiley.com/doi/pdf/10.1111/jmi.12526`.

[54] M. J. De Ruijter, T. D. Blake, and J. De Coninck. "Dynamic Wetting Studied by Molecular Modeling Simulations of Droplet Spreading". In: *Langmuir* 15.22 (1999), pp. 7836–7847. DOI: `10.1021/la990171l`. eprint: `https://doi.org/10.1021/la990171l`. URL: `https://doi.org/10.1021/la990171l`.

[55] B. Derjaguin. "Thickness of liquid layer adhering to walls of vessels on their emptying and the theory of photo– and motion–picture film coating". In: *C. R. (Dokl.) Acad. Sci. URSS* 39 (1943), pp. 13–16.

[56] A. Diaspro, G. Chirico, C. Usai, P. Ramoino, and J. Dobrucki. "Photobleaching". In: *Handbook Of Biological Confocal Microscopy*. Ed. by J. B. Pawley. 3rd ed. Springer, Boston, MA, 2006, pp. 690–702. DOI: `10.1007/978-0-387-45524-2_39`. URL: `https://doi.org/10.1007/978-0-387-45524-2_39`.

[57] A. Diaspro, F. Federici, and M. Robello. "Influence of refractive-index mismatch in high-resolution three-dimensional confocal microscopy". In: *Appl. Opt.* 41.4 (Feb. 2002), pp. 685–690. DOI: `10.1364/AO.41.000685`. URL: `http://ao.osa.org/abstract.cfm?URI=ao-41-4-685`.

[58] S. Discetti and F. Coletti. “Volumetric velocimetry for fluid flows”. In: *Measurement Science and Technology* 29.4 (Mar. 2018), p. 042001. DOI: `10.1088/1361-6501/aaa571`. URL: `https://doi.org/10.1088%2F1361-6501%2Faaa571`.

[59] G. Duemani Reddy, K. Kelleher, R. Fink, and P. Saggau. “Three-dimensional random access multiphoton microscopy for functional imaging of neuronal activity”. In: *Nature Neuroscience* 11.6 (2008), pp. 713–720. ISSN: 1546-1726. DOI: `10.1038/nn.2116`. URL: `https://doi.org/10.1038/nn.2116`.

[60] M. Duocastella, G. Vicidomini, and A. Diaspro. “Simultaneous multiplane confocal microscopy using acoustic tunable lenses”. In: *Opt. Express* 22.16 (Aug. 2014), pp. 19293–19301. DOI: `10.1364/OE.22.019293`. URL: `http://www.opticsexpress.org/abstract.cfm?URI=oe-22-16-19293`.

[61] E. Dussan. “On the Spreading of Liquids on Solid Surfaces: Static and Dynamic Contact Lines”. In: *Annual Review of Fluid Mechanics* 11.1 (1979), pp. 371–400. DOI: `10.1146/annurev.fl.11.010179.002103`. eprint: `https://doi.org/10.1146/annurev.fl.11.010179.002103`. URL: `https://doi.org/10.1146/annurev.fl.11.010179.002103`.

[62] E. Dussan V. and R. Chow. “On the ability of drops or bubbles to stick to non–horizontal surfaces of solids”. In: *Journal of Fluid Mechanics* 137 (1983), pp. 1–29. DOI: `10.1017/S002211208300227X`.

[63] J. Eggers. “Existence of receding and advancing contact lines”. In: *Physics of Fluids* 17.8 (2005), p. 082106. DOI: `10.1063/1.2009007`. eprint: `https://doi.org/10.1063/1.2009007`. URL: `https://doi.org/10.1063/1.2009007`.

[64] J. Eggers. “Hydrodynamic Theory of Forced Dewetting”. In: *Phys. Rev. Lett.* 93 (9 Aug. 2004), p. 094502. DOI: `10.1103/PhysRevLett.93.094502`. URL: `https://link.aps.org/doi/10.1103/PhysRevLett.93.094502`.

[65] A. Einstein. “Über die von der molekularkinetischen Theorie der Wärme geforderte Bewegung von in ruhenden Flüssigkeiten suspendierten Teilchen”. In: *Annalen der Physik* 322.8 (1905), pp. 549–560. DOI: `10.1002/andp.19053220806`. eprint: `https://onlinelibrary.wiley.com/doi/pdf/10.1002/andp.19053220806`. URL: `https://onlinelibrary.wiley.com/doi/abs/10.1002/andp.19053220806`.

[66] H. Eral, D. ’t Mannetje, and J. Oh. “Contact angle hysteresis: a review of fundamentals and applications”. In: *Colloid and Polymer Science* 291.2 (2013), pp. 247–260. ISSN: 1435-1536. DOI: `10.1007/s00396-012-2796-6`. URL: `https://doi.org/10.1007/s00396-012-2796-6`.

[67] H. Erbil. *Surface Chemistry of Solid and Liquid Interfaces*. John Wiley & Sons, Ltd, 2009. ISBN: 9781444305401. DOI: `10.1002/9781444305401.ch1`. eprint: `https://onlinelibrary.wiley.com/doi/pdf/10.1002/9781444305401.ch1`. URL: `https://onlinelibrary.wiley.com/doi/abs/10.1002/9781444305401.ch1`.

[68] H. Erbil. “The debate on the dependence of apparent contact angles on drop contact area or three-phase contact line: A review”. In: *Surface Science Reports* 69.4 (2014), pp. 325–365. ISSN: 0167–5729. DOI: https://doi.org/10.1016/j.surfrep.2014.09.001. URL: http://www.sciencedirect.com/science/article/pii/S0167572914000223.

[69] D. Fell, G. Auernhammer, E. Bonaccurso, C. J. Liu, R. Sokuler, and H.-J. Butt. “Influence of Surfactant Concentration and Background Salt on Forced Dynamic Wetting and Dewetting”. In: *Langmuir* 27 (2011), pp. 2112–2117. ISSN: 0743-7463. DOI: 10.1021/la104675t. URL: https://doi.org/10.1021/la104675t.

[70] D. Fell, N. Pawanrat, E. Bonaccurso, H.-J. Butt, and G. K. Auernhammer. “Influence of surfactant transport suppression on dynamic contact angle hysteresis”. In: *Colloid and Polymer Science* 291 (2013), pp. 361–366. ISSN: 0303-402X. DOI: 10.1007/s00396-012-2759-y. URL: https://doi.org/10.1007/s00396-012-2759-y.

[71] D. Fell. “Dynamic wetting of complex liquids”. PhD thesis. Johannes Gutenberg–Universität Mainz, 2013.

[72] J. Fuentes and R. Cerro. “Flow patterns and interfacial velocities near a moving contact line”. In: *Experiments in Fluids* 38.4 (2005), pp. 503–510. ISSN: 1432–1114. DOI: 10.1007/s00348-005-0941-4. URL: https://doi.org/10.1007/s00348-005-0941-4.

[73] G. L. Gaines. “On the history of Langmuir-Blodgett films”. In: *Langmuir-–Blodgett Films, 1982*. Ed. by G. Roberts and C. Pitt. Thin Films Science and Technology. Oxford: Elsevier, 1983, pp. viii–xiii. DOI: https://doi.org/10.1016/B978-0-444-42173-9.50005-5. URL: http://www.sciencedirect.com/science/article/pii/B9780444421739500055.

[74] P. G. de Gennes. “Wetting: statics and dynamics”. In: *Rev. Mod. Phys.* 57 (3 1985), pp. 827–863. DOI: 10.1103/RevModPhys.57.827. URL: https://link.aps.org/doi/10.1103/RevModPhys.57.827.

[75] C. H. Giles, S. D. Forrester, and G. G. Roberts. “Historical Introduction”. In: *Langmuir–Blodgett Films*. Ed. by G. Roberts. Boston, MA: Springer US, 1990, pp. 1–15. ISBN: 978-1-4899-3716-2. DOI: 10.1007/978-1-4899-3716-2_1. URL: https://doi.org/10.1007/978-1-4899-3716-2_1.

[76] R. Gräf, J. Rietdorf, and T. Zimmermann. “Live Cell Spinning Disk Microscopy”. In: *Microscopy Techniques*. Ed. by J. Rietdorf. Vol. 95. Advances in Biochemical Engineering. Springer Berlin Heidelberg, 2005. Chap. 3, pp. 57–75.

[77] B. F. Grewe, F. F. Voigt, M. van ’t Hoff, and F. Helmchen. “Fast two-layer two-photon imaging of neuronal cell populations using an electrically tunable lens”. In: *Biomed. Opt. Express* 2.7 (July 2011), pp. 2035–2046. DOI: 10.1364/BOE.2.002035. URL: http://www.osapublishing.org/boe/abstract.cfm?URI=boe-2-7-2035.

[78] R. Hain, C. J. Kähler, and R. Radespiel. “Principles of a Volumetric Velocity Measurement Technique Based on Optical Aberrations”. In: *Imaging Measurement Methods for Flow Analysis*. Ed. by W. Nitsche and C. Dobriloff. Berlin, Heidelberg: Springer Berlin Heidelberg, 2009, pp. 1–10. ISBN: 978-3-642-01106-1.

[79] R. Hain, C. J. Kähler, and C. Tropea. “Comparison of CCD, CMOS and intensified cameras”. In: *Experiments in Fluids* 42.3 (2007), pp. 403–411. ISSN: 1432–1114. DOI: `10.1007/s00348-006-0247-1`. URL: `https://doi.org/10.1007/s00348-006-0247-1`.

[80] R. A. Hann. “Molecular Structure and Monolayer Properties”. In: *Langmuir–Blodgett Films*. Ed. by G. Roberts. Boston, MA: Springer US, 1990, pp. 17–92. ISBN: 978-1-4899-3716-2. DOI: `10.1007/978-1-4899-3716-2_2`. URL: `https://doi.org/10.1007/978-1-4899-3716-2_2`.

[81] R. Hansen and T. Toong. “Dynamic contact angle and its relationship to forces of hydrodynamic origin”. In: *Journal of Colloid and Interface Science* 37.1 (1971), pp. 196–207. ISSN: 0021-9797. DOI: `https://doi.org/10.1016/0021-9797(71)90280-3`. URL: `http://www.sciencedirect.com/science/article/pii/0021979771902803`.

[82] E. Hecht. *Optik*. Oldenbourg Wissenschaftsverlag GmbH, 2001. ISBN: 3-486-24917-7. DOI: `10.1515/9783110526653`. URL: `https://doi.org/10.1515/9783110526653`.

[83] F. Henrich, D. Fell, D. Truszkowska, M. Weirich, M. Anyfantakis, T. H. Nguyen, M. Wagner, G. K. Auernhammer, and H.-J. Butt. “Influence of surfactants in forced dynamic dewetting”. In: *Soft Matter* 12 (2016), pp. 7782–7791. ISSN: 1744-683X. DOI: `10.1039/C6SM00997B`. URL: `http://dx.doi.org/10.1039/C6SM00997B`.

[84] F. Henrich. “Dynamic dewetting of surfactant solutions”. PhD thesis. Technical University Darmstadt, 2017.

[85] F. Henrich, D. Linke, H. M. Sauer, E. Dörsam, S. Hardt, H.-J. Butt, and G. K. Auernhammer. “Forced dynamic dewetting of structured surfaces: Influence of surfactants”. In: *Phys. Rev. Fluids* 4 (12 Dec. 2019), p. 124202. DOI: `10.1103/PhysRevFluids.4.124202`. URL: `https://link.aps.org/doi/10.1103/PhysRevFluids.4.124202`.

[86] A. Hibbs, G. MacDonald, and K. Garsha. “Practical Confocal Microscopy”. In: *Handbook Of Biological Confocal Microscopy*. Ed. by J. B. Pawley. 3rd ed. Springer, Boston, MA, 2006, pp. 650–671. DOI: `10.1007/978-0-387-45524-2_36`. URL: `https://doi.org/10.1007/978-0-387-45524-2_36`.

[87] A. E. Hosoi and J. W. M. Bush. “Evaporative instabilities in climbing films”. In: *Journal of Fluid Mechanics* 442 (2001), pp. 217–239. DOI: `10.1017/S0022112001005018`.

[88] C. Huh and L. E. Scriven. “Hydrodynamic model of steady movement of a solid/liquid/fluid contact line”. In: *Journal of Colloid and Interface Science* 35.1 (1971), pp. 85–101. ISSN: 0021-9797. DOI: `10.1016/0021-9797(71)90188-3`. URL: `http://www.sciencedirect.com/science/article/pii/0021979771901883`.

[89] S. Inoué. “Foundations of Confocal Scanned Imaging in Light Microscopy”. In: *Handbook Of Biological Confocal Microscopy*. Ed. by J. B. Pawley. 3rd ed. Springer, Boston, MA, 2006, pp. 1–19. DOI: `10.1007/978-0-387-45524-2_1`. URL: `https://doi.org/10.1007/978-0-387-45524-2_1`.

[90] N. Ivanova and V. Starov. “Wetting and Spreading by Aqueous Surfactant Solutions”. In: *Surfactant Science and Technology*. Ed. by L. Romsted. CRC Press, 2014, pp. 169–189. DOI: `10.1201/b16802-8`. URL: `https://doi.org/10.1201/b16802`.

[91] J. Thomson A.M. C.E. “XLII. On certain curious motions observable at the surfaces of wine and other alcoholic liquors”. In: *The London, Edinburgh, and Dublin Philosophical Magazine and Journal of Science* 10.67 (1855), pp. 330–333. DOI: `10.1080/14786445508641982`. eprint: `https://doi.org/10.1080/14786445508641982`. URL: `https://doi.org/10.1080/14786445508641982`.

[92] T. D. B. Joël De Coninck. “Contact angle”. In: *Springer Handbook of Experimental Fluid Mechanics*. Ed. by C. Tropea, A. L. Yarin, and J. F. Foss. Springer, Berlin, Heidelberg, 2007, pp. 106–119. DOI: `10.1007/978-3-540-30299-5_3`. URL: `https://doi.org/10.1007/978-3-540-30299-5_3`.

[93] R. Johnson, R. Dettre, and D. Brandreth. “Dynamic contact angles and contact angle hysteresis”. In: *Journal of Colloid and Interface Science* 62.2 (1977), pp. 205–212. ISSN: 0021-9797. DOI: `https://doi.org/10.1016/0021-9797(77)90114-X`. URL: `http://www.sciencedirect.com/science/article/pii/002197977790114X`.

[94] K. Kagawa, M.-W. Seo, K. Yasutomi, S. Terakawa, and S. Kawahito. “Multi-beam confocal microscopy based on a custom image sensor with focal-plane pinhole array effect”. In: *Opt. Express* 21.2 (Jan. 2013), pp. 1417–1429. DOI: `10.1364/OE.21.001417`. URL: `http://www.opticsexpress.org/abstract.cfm?URI=oe-21-2-1417`.

[95] H. P. Kao and A. S. Verkman. “Tracking of single fluorescent particles in three dimensions: use of cylindrical optics to encode particle position”. In: *Biophysical Journal* 67 (1994), pp. 1291–1300. ISSN: 0006-3495. DOI: `10.1016/S0006-3495(94)80601-0`. URL: `https://doi.org/10.1016/S0006-3495(94)80601-0`.

[96] A. Kaplan, N. Friedman, and N. Davidson. “Acousto-optic lens with very fast focus scanning”. In: *Opt. Lett.* 26.14 (July 2001), pp. 1078–1080. DOI: `10.1364/OL.26.001078`. URL: `http://ol.osa.org/abstract.cfm?URI=ol-26-14-1078`.

[97] H. Kim, S. Große, G. E. Elsinga, and J. Westerweel. “Full 3D–3C velocity measurement inside a liquid immersion droplet”. In: *Experiments in Fluids* 51.2 (2 2011), pp. 395–405. ISSN: 1432–1114. DOI: `10.1007/s00348-011-1053-y`. URL: `https://doi.org/10.1007/s00348-011-1053-y`.

[98] H. Kim, C. Poelma, G. Ooms, and J. Westerweel. “Experimental and theoretical study of dewetting corner flow”. In: *Journal of Fluid Mechanics* 762 (2015), pp. 393–416. DOI: `10.1017/jfm.2014.623`.

[99] H. Kim, J. Westerweel, and G. E. Elsinga. “Comparison of Tomo–PIV and 3D–PTV for microfluidic flows”. In: *Measurement Science and Technology* 24.2 (2012), p. 024007. DOI: `10.1088/0957-0233/24/2/024007`. URL: `https://doi.org/10.1088%2F0957-0233%2F24%2F2%2F024007`.

[100] A. King, J. Billingham, and D. Popple. “The moving contact line between two wedges of fluid on a flat plate”. In: *The Quarterly Journal of Mechanics and Applied Mathematics* 52.3 (Sept. 1999), pp. 453–468. ISSN: 0033-5614. DOI: `10.1093/qjmam/52.3.453`. eprint: `https://academic.oup.com/qjmam/article-pdf/52/3/453/5318640/520453.pdf`. URL: `https://doi.org/10.1093/qjmam/52.3.453`.

[101] N. Kovalchuk and M. Simmons. “Surfactant–mediated wetting and spreading: Recent advances and applications”. In: *Current Opinion in Colloid & Interface Science* (2020). ISSN: 1359–0294. DOI: `https://doi.org/10.1016/j.cocis.2020.07.004`. URL: `http://www.sciencedirect.com/science/article/pii/S1359029420300583`.

[102] R. Krechetnikov and G. Homsy. “Surfactant effects in the Landau–Levich problem”. In: *Journal of Fluid Mechanics* 559 (2006), pp. 429–450. DOI: `10.1017/S0022112006000425`.

[103] D. Y. Kwok, T. Gietzelt, K. Grundke, H.-J. Jacobasch, and A. W. Neumann. “Contact Angle Measurements and Contact Angle Interpretation. 1. Contact Angle Measurements by Axisymmetric Drop Shape Analysis and a Goniometer Sessile Drop Technique”. In: *Langmuir* 13.10 (1997), pp. 2880–2894. DOI: `10.1021/la9608021`. eprint: `https://doi.org/10.1021/la9608021`. URL: `https://doi.org/10.1021/la9608021`.

[104] D. Kwok, R. Lin, M. Mui, and A. Neumann. “Low–rate dynamic and static contact angles and the determination of solid surface tensions”. In: *Colloids and Surfaces A: Physicochemical and Engineering Aspects* 116.1 (1996). A collection of papers presented at the Wetting and Interfacial Phenomena Symposium at the 69th Annual Colloid and Surface Science Symposium, pp. 63–77. ISSN: 0927-7757. DOI: `https://doi.org/10.1016/0927-7757(96)03590-X`. URL: `http://www.sciencedirect.com/science/article/pii/092777579603590X`.

[105] D. C. Lah. “Construction of a confocal microscope as well as implementing its control software for μ–PIV measurements”. Bachelor–Thesis. Technical University of Darmstadt, 2018.

[106] L. D. Landau and E. M. Lifshitz. *Fluid Mechanics*. 2nd ed. Vol. 6. Course of Theoretical Physics. Butterworth-Heinemann, 1987. ISBN: 978-0750627672.

[107] L. Landau and V. Levich. “Dragging of a liquid by a moving plate”. In: *Acta Physicochimica URSS* 17 (1942), pp. 42–47.

[108] P. Langevin. “Sur la theórie du mouvement brownien”. In: *C. R. Acad. Sci. (Paris)* 322.146 (1908), pp. 530–533. URL: `https://gallica.bnf.fr/ark:/12148/bpt6k3100t/f530.image`.

[109] N. Le Grand, A. Daerr, and L. Limat. “Shape and motion of drops sliding down an inclined plane”. In: *Journal of Fluid Mechanics* 541 (2005), pp. 293–315. DOI: `10.1017/S0022112005006105`.

[110] D. S. Lemons and A. Gythiel. “Paul Langevin’s 1908 paper “On the Theory of Brownian Motion” [“Sur la thóorie du mouvement brownien,” C. R. Acad. Sci. (Paris) 146, 530–533 (1908)]”. In: *American Journal of Physics* 65.11 (1997), pp. 1079–1081. DOI: `10.1119/1.18725`. eprint: `https://doi.org/10.1119/1.18725`. URL: `https://doi.org/10.1119/1.18725`.

[111] R. Lindken, M. Rossi, S. Große, and J. Westerweel. “Micro–Particle Image Velocimetry (μPIV): Recent developments, applications, and guidelines”. In: *Lab Chip* 9 (17 2009), pp. 2551–2567. DOI: `10.1039/B906558J`. URL: `http://dx.doi.org/10.1039/B906558J`.

[112] D. Linke. “Wetting of complex liquids”. PhD thesis. Johannes Gutenberg–Universität Mainz, 2017.

[113] M. Y. Loktev, V. N. Belopukhov, F. L. Vladimirov, G. V. Vdovin, G. D. Love, and A. F. Naumov. “Wave front control systems based on modal liquid crystal lenses”. In: *Review of Scientific Instruments* 71.9 (2000), pp. 3290–3297. DOI: `10.1063/1.1288256`. eprint: `https://doi.org/10.1063/1.1288256`. URL: `https://doi.org/10.1063/1.1288256`.

[114] Lord Rayleigh Sec. R. S. “XV. On the theory of optical images, with special reference to the microscope”. In: *The London, Edinburgh, and Dublin Philosophical Magazine and Journal of Science* 42.255 (1896), pp. 167–195. DOI: `10.1080/14786449608620902`. eprint: `https://doi.org/10.1080/14786449608620902`. URL: `https://doi.org/10.1080/14786449608620902`.

[115] G. Lu, X. D. Wang, and Y. Y. Duan. “A Critical Review of Dynamic Wetting by Complex Fluids: From Newtonian Fluids to Non-Newtonian Fluids and Nanofluids”. In: *Advances in Colloid and Interface Science* 236 (2016), pp. 43–62. ISSN: 0001-8686. DOI: `10.1016/j.cis.2016.07.004`. URL: `http://www.sciencedirect.com/science/article/pii/S0001868615300555`.

[116] B. B. Luokkala, S. Garoff, R. D. Tilton, and R. M. Suter. “Interfacial structure and rearrangement of nonionic surfactants near a moving contact line”. In: *Langmuir* 17 (19 2001), pp. 5917–5923. ISSN: 0743-7463. DOI: `10.1021/la010365c`. URL: `https://doi.org/10.1021/la010365c`.

[117] G. Macdougall, C. Ockrent, and J. P. Kendall. “Surface energy relations in liquid/solid systems I. The adhesion of liquids to solids and a new method of determining the surface tension of liquids”. In: *Proceedings of the Royal Society of London. Series A. Mathematical and Physical Sciences* 180.981 (1942), pp. 151–173. DOI: `10.1098/rspa.1942.0031`. eprint: `https://royalsocietypublishing.org/doi/pdf/10.1098/rspa.1942.0031`. URL: `https://royalsocietypublishing.org/doi/abs/10.1098/rspa.1942.0031`.

[118] O. Manor, I. U. Vakarelski, X. S. Tang, S. J. O’Shea, G. W. Stevens, F. Grieser, R. R. Dagastine, and D. Y. C. Chan. “Hydrodynamic Boundary Conditions and Dynamic Forces between Bubbles and Surfaces”. In: *Phys. Rev. Lett.* 101 (July 2008), p. 024501. DOI: `10.1103/PhysRevLett.101.024501`. URL: `https://link.aps.org/doi/10.1103/PhysRevLett.101.024501`.

[119] C. Marangoni. "Ueber die Ausbreitung der Tropfen einer Flüssigkeit auf der Oberfläche einer anderen". In: *Annalen der Physik* 219.7 (1871), pp. 337–354. DOI: `10.1002/andp.18712190702`. eprint: `https://onlinelibrary.wiley.com/doi/pdf/10.1002/andp.18712190702`. URL: `https://onlinelibrary.wiley.com/doi/abs/10.1002/andp.18712190702`.

[120] A. Marmur. "Surface Tension and Interfacial Tension of Liquids". In: *Springer Handbook of Experimental Fluid Mechanics*. Ed. by C. Tropea, A. L. Yarin, and J. F. Foss. Springer, Berlin, Heidelberg, 2007, pp. 96–106. DOI: `10.1007/978-3-540-30299-5_3`. URL: `https://doi.org/10.1007/978-3-540-30299-5_3`.

[121] H. C. Mayer and R. Krechetnikov. "Landau–Levich flow visualization: Revealing the flow topology responsible for the film thickening phenomena". In: *Physics of Fluids* 24.5 (2012), p. 052103. ISSN: 1070-6631. DOI: `10.1063/1.4703924`. eprint: `https://doi.org/10.1063/1.4703924`. URL: `https://doi.org/10.1063/1.4703924`.

[122] B. J. McKeon et al. "Velocity, Vorticity, and Mach Number". In: *Springer Handbook of Experimental Fluid Mechanics*. Ed. by C. Tropea, A. L. Yarin, and J. F. Foss. Springer, Berlin, Heidelberg, 2007, pp. 215–563. DOI: `10.1007/978-3-540-30299-5`. URL: `https://doi.org/10.1007/978-3-540-30299-5`.

[123] C. D. Meinhart, S. T. Wereley, and J. G. Santiago. "PIV measurements of a microchannel flow". In: *Experiments in Fluids* 27.5 (1999), pp. 414–419. ISSN: 1432–1114. DOI: `10.1007/s003480050366`. URL: `https://doi.org/10.1007/s003480050366`.

[124] C. Meinhart and S. Wereley. "The theory of diffraction-limited resolution in microparticle image velocimetry". In: *Measurement Science and Technology* 14.7 (June 2003), pp. 1047–1053. DOI: `10.1088/0957-0233/14/7/320`. URL: `https://doi.org/10.1088%2F0957-0233%2F14%2F7%2F320`.

[125] A. Mermillod-Blondin, E. McLeod, and C. B. Arnold. "High-speed varifocal imaging with a tunable acoustic gradient index of refraction lens". In: *Opt. Lett.* 33.18 (Sept. 2008), pp. 2146–2148. DOI: `10.1364/OL.33.002146`. URL: `http://ol.osa.org/abstract.cfm?URI=ol-33-18-2146`.

[126] M. Minsky. "Memoir on inventing the confocal scanning microscope". In: *Scanning* 10.4 (1988), pp. 128–138. ISSN: 0161-0457. DOI: `10.1002/sca.4950100403`. URL: `https://onlinelibrary.wiley.com/doi/pdf/10.1002/sca.4950100403`.

[127] H. K. Moffatt. "Viscous and resistive eddies near a sharp corner". In: *Journal of Fluid Mechanics* 18.1 (1964), pp. 1–18. ISSN: 0022-1120. DOI: `10.1017/s0022112064000015`. URL: `https://doi.org/10.1017/S0022112064000015`.

[128] A. Nakano. "Spinning–disk Confocal Microscopy – A Cutting-Edge Tool for Imaging of Membrane Traffic". In: *Cell Structure and Function* 27.5 (2002), pp. 349–355. DOI: `10.1247/csf.27.349`.

[129] Nis. *Drop shape analysis. Fit contact angle by double ellipses or polynomials*. 2020. URL: `https://www.mathworks.com/matlabcentral/fileexchange/57919-drop-shape-analysis-fit-contact-angle-by-double-ellipses-or-polynomials` (visited on 10/17/2020).

[130] H. Oku, K. Hashimoto, and M. Ishikawa. “Variable-focus lens with 1-kHz bandwidth”. In: *Opt. Express* 12.10 (May 2004), pp. 2138–2149. DOI: `10.1364/OPEX.12.002138`. URL: `http://www.opticsexpress.org/abstract.cfm?URI=oe-12-10-2138`.

[131] M. G. Olsen and R. J. Adrian. “Brownian motion and correlation in particle image velocimetry”. In: *Optics & Laser Technology* 32.7 (2000). Optical methods in heat and fluid flow, pp. 621–627. ISSN: 0030-3992. DOI: `https://doi.org/10.1016/S0030-3992(00)00119-5`. URL: `http://www.sciencedirect.com/science/article/pii/S0030399200001195`.

[132] J. S. Park, C. K. Choi, and K. D. Kihm. “Optically sliced micro–PIV using confocal laser scanning microscopy (CLSM)”. In: *Experiments in Fluids* 37 (2004), pp. 105–119. ISSN: 1432-1114. DOI: `10.1007/s00348-004-0790-6`. URL: `https://doi.org/10.1007/s00348-004-0790-6`.

[133] J. B. Pawley. “Fundamental Limits in Confocal Microscopy”. In: *Handbook Of Biological Confocal Microscopy*. Ed. by J. B. Pawley. 3rd ed. Springer, Boston, MA, 2006, pp. 20–42. DOI: `10.1007/978-0-387-45524-2_2`. URL: `https://doi.org/10.1007/978-0-387-45524-2_2`.

[134] J. B. Pawley, ed. *Handbook Of Biological Confocal Microscopy*. Springer, Boston, MA, 2006. DOI: `10.1007/978-0-387-45524-2`. URL: `https://doi.org/10.1007/978-0-387-45524-2`.

[135] J. Perrin. “Mouvement brownien et réalité moléculaire”. In: *Annales de Chimie et de Physique*. Vol. 18. 8. 1909, pp. 5–114.

[136] J. Petrov, J. Ralston, and R. Hayes. “Dewetting Dynamics on Heterogeneous Surfaces. A Molecular–Kinetic Treatment”. In: *Langmuir* 15.9 (1999), pp. 3365–3373. ISSN: 0743-7463. DOI: `10.1021/la971012+`. URL: `https://doi.org/10.1021/la971012+`.

[137] J. Petrov, J. Ralston, M. Schneemilch, and R. Hayes. “Dynamics of Partial Wetting and Dewetting in Well–Defined Systems”. In: *J. Phys. Chem. B* 107.7 (2003), pp. 247–260. ISSN: 1520–6106. DOI: `10.1021/jp026723h`. URL: `https://doi.org/10.1021/jp026723h`.

[138] P. Petrov and I. Petrov. “A combined molecular–hydrodynamic approach to wetting kinetics”. In: *Langmuir* 8.7 (1992), pp. 1762–1767. DOI: `10.1021/la00043a013`. eprint: `https://doi.org/10.1021/la00043a013`. URL: `https://doi.org/10.1021/la00043a013`.

[139] T. Podgorski, J.-M. Flesselles, and L. Limat. “Corners, Cusps, and Pearls in Running Drops”. In: *Phys. Rev. Lett.* 87 (3 June 2001), p. 036102. DOI: `10.1103/PhysRevLett.87.036102`. URL: `https://link.aps.org/doi/10.1103/PhysRevLett.87.036102`.

[140] S. Pope. *Turbulent Flows*. Cambridge University Press, 2000. DOI: `10.1017/CBO9780511840531`.

[141] B. Puthenveettil, V. Senthilkumar, and E. Hopfinger. “Motion of drops on inclined surfaces in the inertial regime”. In: *Journal of Fluid Mechanics* 726 (2013), pp. 26–61. DOI: `10.1017/jfm.2013.209`.

[142] B. Qian, J. Park, and K. S. Breuer. “Large apparent slip at a moving contact line”. In: *Physics of Fluids* 27.9 (2015), p. 091703. ISSN: 1070-6631. DOI: `10.1063/1.4931915`. eprint: `https://aip.scitation.org/doi/pdf/10.1063/1.4931915`. URL: `https://aip.scitation.org/doi/abs/10.1063/1.4931915`.

[143] D. Quéré, A. de Ryck, and O. Ou Ramdane. “Liquid coating from a surfactant solution”. In: *Europhysics Letters (EPL)* 37.4 (Feb. 1997), pp. 305–310. DOI: `10.1209/epl/i1997-00147-6`. URL: `https://doi.org/10.1209%2Fepl%2Fi1997-00147-6`.

[144] *Re-scan Confocal Microscope. RCM (1.1)*. 2019. URL: `https://www.confocal.nl/rcm-features/` (visited on 10/06/2020).

[145] O. Reynolds. “XXIX. An experimental investigation of the circumstances which determine whether the motion of water shall be direct or sinuous, and of the law of resistance in parallel channels”. In: *Philosophical Transactions of the Royal Society of London* 174 (1883), pp. 935–982. DOI: `10.1098/rstl.1883.0029`. eprint: `https://royalsocietypublishing.org/doi/pdf/10.1098/rstl.1883.0029`. URL: `https://royalsocietypublishing.org/doi/abs/10.1098/rstl.1883.0029`.

[146] E. Rio, A. Daerr, B. Andreotti, and L. Limat. “Boundary Conditions in the Vicinity of a Dynamic Contact Line: Experimental Investigation of Viscous Drops Sliding Down an Inclined Plane”. In: *Phys. Rev. Lett.* 94 (2 Jan. 2005), p. 024503. DOI: `10.1103/PhysRevLett.94.024503`. URL: `https://link.aps.org/doi/10.1103/PhysRevLett.94.024503`.

[147] M. Rosen and J. Kunjappu. “Characteristic Features of Surfactants”. In: *Surfactants and Interfacial Phenomena*. John Wiley & Sons, Ltd, 2012. Chap. 1, pp. 1–38. ISBN: 9781118228920. DOI: `10.1002/9781118228920.ch1`. eprint: `https://onlinelibrary.wiley.com/doi/pdf/10.1002/9781118228920.ch1`. URL: `https://onlinelibrary.wiley.com/doi/abs/10.1002/9781118228920.ch1`.

[148] M. Rossi and C. J. Kähler. “Optimization of astigmatic particle tracking velocimeters”. In: *Experiments in Fluids* 55 (2014), p. 1809. ISSN: 0723-4864. DOI: `10.1007/s00348-014-1809-2`. URL: `https://doi.org/10.1007/s00348-014-1809-2`.

[149] M. Rossi, A. Marin, and C. J. Kähler. “Interfacial flows in sessile evaporating droplets of mineral water”. In: *Phys. Rev. E* 100 (2019), p. 033103. DOI: `10.1103/PhysRevE.100.033103`. URL: `https://link.aps.org/doi/10.1103/PhysRevE.100.033103`.

[150] M. Rossi, R. Segura, C. Cierpka, and C. Kähler. “On the effect of particle image intensity and image preprocessing on the depth of correlation in micro–PIV”. In: *Experiments in Fluids* 52.4 (2012), pp. 1063–1075. ISSN: 1432–1114. DOI: `10.1007/s00348-011-1194-z`. URL: `https://doi.org/10.1007/s00348-011-1194-z`.

[151] M. Roth, M. Franzmann, M. D'Acunzi, M. Kreiter, and G. K. Auernhammer. "Experimental analysis of single particle deformations and rotations in colloidal and granular systems". In: *arXiv:1106.3623v2 [cond-mat.soft]* (2011).

[152] C. T. Rueden, J. Schindelin, M. C. Hiner, B. E. DeZonia, A. E. Walter, E. T. Arena, and K. W. Eliceiri. "ImageJ2: ImageJ for the next generation of scientific image data". In: *BMC Bioinformatics* 18 (2017), p. 529. ISSN: 1471-2105. DOI: `10.1186/s12859-017-1934-z`. URL: `https://doi.org/10.1186/s12859-017-1934-z`.

[153] J. Schindelin et al. "Fiji: an open-source platform for biological-image analysis". In: *Nature Methods* 9 (2012), pp. 676–682. ISSN: 1548-7091. DOI: `10.1038/nmeth.2019`. URL: `https://doi.org/10.1038/nmeth.2019`.

[154] C. A. Schneider, W. S. Rasband, and K. W. Eliceiri. "NIH Image to ImageJ: 25 years of image analysis". In: *Nature Methods* 9 (2012), pp. 671–675. ISSN: 1548-7091. DOI: `10.1038/nmeth.2089`. URL: `https://doi.org/10.1038/nmeth.2089`.

[155] A. Schwartz, C. Rader, and E. Huey. "Resistance to Flow in Capillary Systems of Positive Contact Angle". In: *Contact Angle, Wettability, and Adhesion*. Ed. by F. Fowkes. Chap. 17, pp. 250–267. DOI: `10.1021/ba-1964-0043.ch017`. eprint: `https://pubs.acs.org/doi/pdf/10.1021/ba-1964-0043.ch017`. URL: `https://pubs.acs.org/doi/abs/10.1021/ba-1964-0043.ch017`.

[156] S. M. Shah, J. Crawsaw, and E. Bork. "Three–dimensional imaging of porous media using confocal laser scanning microscopy". In: *Journal of Microscopy* 265.2 (2017), pp. 261–271. DOI: `10.1111/jmi.12496`. eprint: `https://onlinelibrary.wiley.com/doi/pdf/10.1111/jmi.12496`. URL: `https://onlinelibrary.wiley.com/doi/abs/10.1111/jmi.12496`.

[157] A. Shen, B. Gleason, G. McKinley, and H. Stone. "Fiber coating with surfactant solutions". In: *Physics of Fluids* 14.11 (2002), pp. 4055–4068. DOI: `10.1063/1.1512287`. eprint: `https://doi.org/10.1063/1.1512287`. URL: `https://doi.org/10.1063/1.1512287`.

[158] C. Sheppard, X. Gan, M. Gu, and M. Roy. "Signal-to-Noise Ratio in Confocal Microscopes". In: *Handbook Of Biological Confocal Microscopy*. Ed. by J. B. Pawley. 3rd ed. Springer, Boston, MA, 2006, pp. 442–452. DOI: `10.1007/978-0-387-45524-2`. URL: `https://doi.org/10.1007/978-0-387-45524-2`.

[159] S. Shian, R. M. Diebold, and D. R. Clarke. "Tunable lenses using transparent dielectric elastomer actuators". In: *Opt. Express* 21.7 (Apr. 2013), pp. 8669–8676. DOI: `10.1364/OE.21.008669`. URL: `http://www.opticsexpress.org/abstract.cfm?URI=oe-21-7-8669`.

[160] Y. Shikhmurzaev. "The moving contact line on a smooth solid surface". In: *International Journal of Multiphase Flow* 19.4 (1993), pp. 589–610. ISSN: 0301-9322. DOI: `https://doi.org/10.1016/0301-9322(93)90090-H`. URL: `http://www.sciencedirect.com/science/article/pii/030193229390090H`.

[161] Y. Shikhmurzaev. “Mathematical modeling of wetting hydrodynamics”. In: *Fluid Dynamics Research* 13.1 (1994), pp. 45–64. DOI: `10.1016/0169-5983(94)90063-9`. URL: `https://doi.org/10.1016%2F0169-5983%2894%2990063-9`.

[162] T. Shimozawa et al. “Improving spinning disk confocal microscopy by preventing pinhole cross-talk for intravital imaging”. In: *Proceedings of the National Academy of Sciences* 110.9 (2013), pp. 3399–3404. ISSN: 0027–8424. DOI: `10.1073/pnas.1216696110`. eprint: `https://www.pnas.org/content/110/9/3399.full.pdf`. URL: `https://www.pnas.org/content/110/9/3399`.

[163] T. Shing Chan, T. Gueudré, and J. Snoeijer. “Maximum speed of dewetting on a fiber”. In: *Physics of Fluids* 23.11 (2011), p. 112103. DOI: `10.1063/1.3659018`. eprint: `https://doi.org/10.1063/1.3659018`. URL: `https://doi.org/10.1063/1.3659018`.

[164] J. H. Snoeijer and B. Andreotti. “Moving Contact Lines: Scales, Regimes, and Dynamical Transitions”. In: *Annual Review of Fluid Mechanics* 45.1 (2013), pp. 269–292. DOI: `10.1146/annurev-fluid-011212-140734`. URL: `https://doi.org/10.1146/annurev-fluid-011212-140734`.

[165] J. Snoeijer, N. Le Grand–Piteira, L. Limat, H. Stone, and J. Eggers. “Cornered drops and rivulets”. In: *Physics of Fluids* 19.4 (2007), p. 042104. DOI: `10.1063/1.2722767`. eprint: `https://doi.org/10.1063/1.2722767`. URL: `https://doi.org/10.1063/1.2722767`.

[166] C. O. S. Sorzano, P. Thevenaz, and M. Unser. “Elastic registration of biological images using vector-spline regularization”. In: *IEEE Transactions on Biomedical Engineering* 52.4 (2005), pp. 652–663. ISSN: 0018-9294. DOI: `10.1109/tbme.2005.844030`. URL: `%3CGo%20to%20ISI%3E://WOS:000227712400011%20https://ieeexplore.ieee.org/document/1408122/`.

[167] C. M. Sparrow. “On Spectroscopic Resolving Power”. In: *Astrophysical Journal* 44 (1916), pp. 76–87. DOI: `10.1086/142271`.

[168] V. M. Starov, S. R. Kosvintsev, and M. G. Velarde. “Spreading of Surfactant Solutions over Hydrophobic Substrates”. In: *Journal of Colloid and Interface Science* 227.1 (2000), pp. 185–190. ISSN: 0021–9797. DOI: `https://doi.org/10.1006/jcis.2000.6851`. URL: `http://www.sciencedirect.com/science/article/pii/S0021979700968516`.

[169] B. B. Straub, D. C. Lah, H. Schmidt, M. Roth, L. Gilson, H.-J. Butt, and G. K. Auernhammer. “Versatile high–speed confocal microscopy using a single laser beam”. In: *Review of Scientific Instruments* 91.3 (2020), p. 033706. DOI: `10.1063/1.5122311`. eprint: `https://doi.org/10.1063/1.5122311`. URL: `https://doi.org/10.1063/1.5122311`.

[170] B. B. Straub, H. Schmidt, P. Rostami, F. Henrich, M. Rossi, C. J. Kähler, H.-J. Butt, and G. K. Auernhammer. *Flow profiles near receding three–phase contact lines: Influence of surfactants*. 2021. arXiv: `2105.12365 [physics.flu-dyn]`.

[171] W. Sutherland. “LXXV. A dynamical theory of diffusion for non–electrolytes and the molecular mass of albumin”. In: *The London, Edinburgh, and Dublin Philosophical Magazine and Journal of Science* 9.54 (1905), pp. 781–785. DOI: 10.1080/14786440509463331. eprint: https://doi.org/10.1080/14786440509463331. URL: https://doi.org/10.1080/14786440509463331.

[172] S. Theron and E. Zussman. “Electric and Magnetic parameters of Liquids and Gases”. In: *Springer Handbook of Experimental Fluid Mechanics*. Ed. by C. Tropea, A. L. Yarin, and J. F. Foss. Springer, Berlin, Heidelberg, 2007, pp. 158–166. DOI: 10.1007/978-3-540-30299-5_3. URL: https://doi.org/10.1007/978-3-540-30299-5_3.

[173] D. Toomre and J. Pawley. “Disk–Scanning Confocal Microscopy”. In: *Handbook Of Biological Confocal Microscopy*. Ed. by J. B. Pawley. 3rd ed. Springer, Boston, MA, 2006, pp. 221–237. DOI: 10.1007/978-0-387-45524-2_10. URL: https://doi.org/10.1007/978-0-387-45524-2_10.

[174] C. Tropea, F. Scarano, J. Westerweel, A. A. Cavone, J. F. Meyers, J. W. Lee, and R. Schodl. “Particle–Based Techniques”. In: *Springer Handbook of Experimental Fluid Mechanics*. Ed. by C. Tropea, A. L. Yarin, and J. F. Foss. Springer, Berlin, Heidelberg, 2007, pp. 309–342. DOI: 10.1007/978-3-540-30299-5. URL: https://doi.org/10.1007/978-3-540-30299-5.

[175] D. Truszkowska, F. Henrich, J. Schultze, K. Koynov, H. J. Rader, H.-J. Butt, and G. K. Auernhammer. “Forced dewetting dynamics of high molecular weight surfactant solutions”. In: *Colloids and Surfaces A: Physicochemical and Engineering Aspects* 521 (2017), pp. 30–37. ISSN: 0927-7757. DOI: 10.1016/j.colsurfa.2016.07.073. URL: http://www.sciencedirect.com/science/article/pii/S0927775716305957.

[176] D. C. Venerus and D. Nieto Simavilla. “Tears of wine: new insights on an old phenomenon”. In: *Scientific Reports* 5 (2015), p. 16162. DOI: 10.1038/srep16162. URL: https://doi.org/10.1038/srep16162.

[177] O. V. Voinov. “Hydrodynamics of wetting”. In: *Journal of Fluid Mechanics* 11 (1976), pp. 714–721. DOI: 10.1007/BF01012963. URL: https://doi.org/10.1007/BF01012963.

[178] R. Vuilleumier, V. Ego, L. Neltner, and A. M. Cazabat. “Tears of wine: the stationary state”. In: *Langmuir* 11.10 (1995), pp. 4117–4121. DOI: 10.1021/la00010a077. eprint: https://doi.org/10.1021/la00010a077. URL: https://doi.org/10.1021/la00010a077.

[179] X. Wang, L. Chen, and E. Bonaccurso. “Comparison of spontaneous wetting and drop impact dynamics of aqueous surfactant solutions on hydrophobic polypropylene surfaces: scaling of the contact radius”. In: *Colloid and Polymer Science* 293.1 (2015), pp. 257–265. ISSN: 1435-1536. DOI: 10.1007/s00396-014-3410-x. URL: https://doi.org/10.1007/s00396-014-3410-x.

[180] R. H. Webb. "Confocal optical microscopy". In: *Reports on Progress in Physics* 59.3 (1996), pp. 427–471. DOI: `10.1088/0034-4885/59/3/003`. URL: `https://doi.org/10.1088%2F0034-4885%2F59%2F3%2F003`.

[181] J. Wenzl, R. Seto, M. Roth, H. J. Butt, and G. K. Auernhammer. "Measurement of rotation of individual spherical particles in cohesive granulates". In: *Granular Matter* 15.4 (2013), pp. 391–400. ISSN: 1434-5021. DOI: `10.1007/s10035-012-0383-7`. URL: `https://link.springer.com/content/pdf/10.1007%2Fs10035-012-0383-7.pdf`.

[182] G. West and C. Lees. "On the resistance to the motion of a thread of mercury in a glass tube". In: *Proceedings of the Royal Society of London. Series A, Containing Papers of a Mathematical and Physical Character* 86.583 (1911), pp. 20–25. DOI: `10.1098/rspa.1911.0076`. eprint: `https://royalsocietypublishing.org/doi/pdf/10.1098/rspa.1911.0076`. URL: `https://royalsocietypublishing.org/doi/abs/10.1098/rspa.1911.0076`.

[183] J. G. White, W. B. Amos, and M. Fordham. "An evaluation of confocal versus conventional imaging of biological structures by fluorescence light microscopy." In: *Journal of Cell Biology* 105.1 (July 1987), pp. 41–48. ISSN: 0021-9525. DOI: `10.1083/jcb.105.1.41`. eprint: `https://rupress.org/jcb/article-pdf/105/1/41/1055159/41.pdf`. URL: `https://doi.org/10.1083/jcb.105.1.41`.

[184] S. Wilhelm, B. Gröbler, M. Gluch, and H. Heinz. *Confocal Laser Scanning Micrscopy: Principles*. 2003. URL: `http://zeiss-campus.magnet.fsu.edu/referencelibrary/laserconfocal.html` (visited on 04/07/2020).

[185] L. Wilhelmy. "Ueber die Abhängigkeit der Capillaritäts–Constanten des Alkohols von Substanz und Gestalt des benetzten festen Körpers". In: *Annalen der Physik* 195.6 (1863), pp. 177–217. DOI: `10.1002/andp.18631950602`. eprint: `https://onlinelibrary.wiley.com/doi/pdf/10.1002/andp.18631950602`. URL: `https://onlinelibrary.wiley.com/doi/abs/10.1002/andp.18631950602`.

[186] C. E. Willert and M. Gharib. "Three–dimensional particle imaging with a single camera". In: *Experiments in Fluids* 12.6 (1992), pp. 353–358. ISSN: 1432–1114. DOI: `10.1007/BF00193880`. URL: `https://doi.org/10.1007/BF00193880`.

[187] T. Wilson. "Resolution and optical sectioning in the confocal microscope". In: *Journal of Microscopy* 244.2 (2011), pp. 113–121. DOI: `10.1111/j.1365-2818.2011.03549.x`. eprint: `https://onlinelibrary.wiley.com/doi/pdf/10.1111/j.1365-2818.2011.03549.x`. URL: `https://onlinelibrary.wiley.com/doi/abs/10.1111/j.1365-2818.2011.03549.x`.

[188] P. W. Winter and H. Shroff. "Faster fluorescence microscopy: advances in high speed biological imaging". In: *Current Opinion in Chemical Biology* 20 (2014). Molecular imaging, pp. 46–53. ISSN: 1367–5931. DOI: `https://doi.org/10.1016/j.cbpa.2014.04.008`. URL: `http://www.sciencedirect.com/science/article/pii/S1367593114000544`.

[189] W. Wirth, S. Storp, and W. Jacobsen. “Mechanisms controlling leaf retention of agricultural spray solutions”. In: *Pesticide Science* 33.4 (1991), pp. 411–420. DOI: `10.1002/ps.2780330403`. eprint: `https://onlinelibrary.wiley.com/doi/pdf/10.1002/ps.2780330403`. URL: `https://onlinelibrary.wiley.com/doi/abs/10.1002/ps.2780330403`.

[190] G. Yarnold. “The motion of a mercury index in a capillary tube”. In: *Proceedings of the Physical Society* 50.4 (1938), pp. 540–552. DOI: `10.1088/0959-5309/50/4/307`. URL: `https://doi.org/10.1088%2F0959-5309%2F50%2F4%2F307`.

[191] T. Young. “III. An essay on the cohesion of fluids”. In: *Philosophical Transactions of the Royal Society of London* 95 (1805), pp. 65–87. DOI: `10.1098/rstl.1805.0005`. eprint: `https://royalsocietypublishing.org/doi/pdf/10.1098/rstl.1805.0005`. URL: `https://royalsocietypublishing.org/doi/abs/10.1098/rstl.1805.0005`.

[192] Y. Yuan and T. R. Lee. “Contact Angle and Wetting Properties”. In: *Surface Science Techniques*. Ed. by G. Bracco and B. Holst. Berlin, Heidelberg: Springer Berlin Heidelberg, 2013, pp. 3–34. ISBN: 978-3-642-34243-1. DOI: `10.1007/978-3-642-34243-1_1`. URL: `https://doi.org/10.1007/978-3-642-34243-1_1`.

[193] *ZEISS LSM 980 with Airyscan 2. Your Next Generation Confocal Microscope with Multiplex Mode*. 2019. URL: `https://www.zeiss.com/microscopy/int/products/confocal-microscopes/confocal-microscope-with-multiplex-mode-lsm-980-airyscan-2.html` (visited on 06/08/2020).

[194] Y. Zhou, M. Handley, G. Carles, and A. R. Harvey. “Advances in 3D single particle localization microscopy”. In: *APL Photonics* 4.6 (2019), p. 060901. DOI: `10.1063/1.5093310`. eprint: `https://doi.org/10.1063/1.5093310`. URL: `https://doi.org/10.1063/1.5093310`.

Acknowledgement

I want to thank Professor Steffen Hardt from the Institute for Nano- and Microfluidic at the Technical University of Darmstadt for the scientific supervision of the thesis.

Furthermore, I want to thank Professor Hans-Jürgen Butt from the Max Planck Institute of Polymer Research in Mainz and Dr. Günter Auernhammer from the Lebniz-Institut für Polymerforschung in Dresden for giving me the opportunity to work and research at the Max Planck Institute for Polymer Research in Mainz, as well as for their scientific supervision.

I also would like to thank my collaboration partners Prof. Christian Kähler from the Bundeswehr University in Munich and Dr. Massimiliano Rossi from the Technical University of Denmark.

I also thank my colleagues Henrik Schmidt, Laurent Gilson, Alexander Saal, Alexander Klasen from the Max Planck Institute for Polymer Research, and Felix Gerlach from the Technical University of Darmstadt for many helpful and interesting discussions.

Furthermore, I want to thank the employees of the electronic laboratory, the mechanical workshop, and the house technicians of the Max Planck Institute for Polymer Research for their help.

Finally, I want to thank my family and friends for their support. Special thanks to my wife Isabel for her support and proofreading my whole thesis.

A. Appendix

A.1. Fast re–scan confocal microscope

A.1.1. Graphical user interface

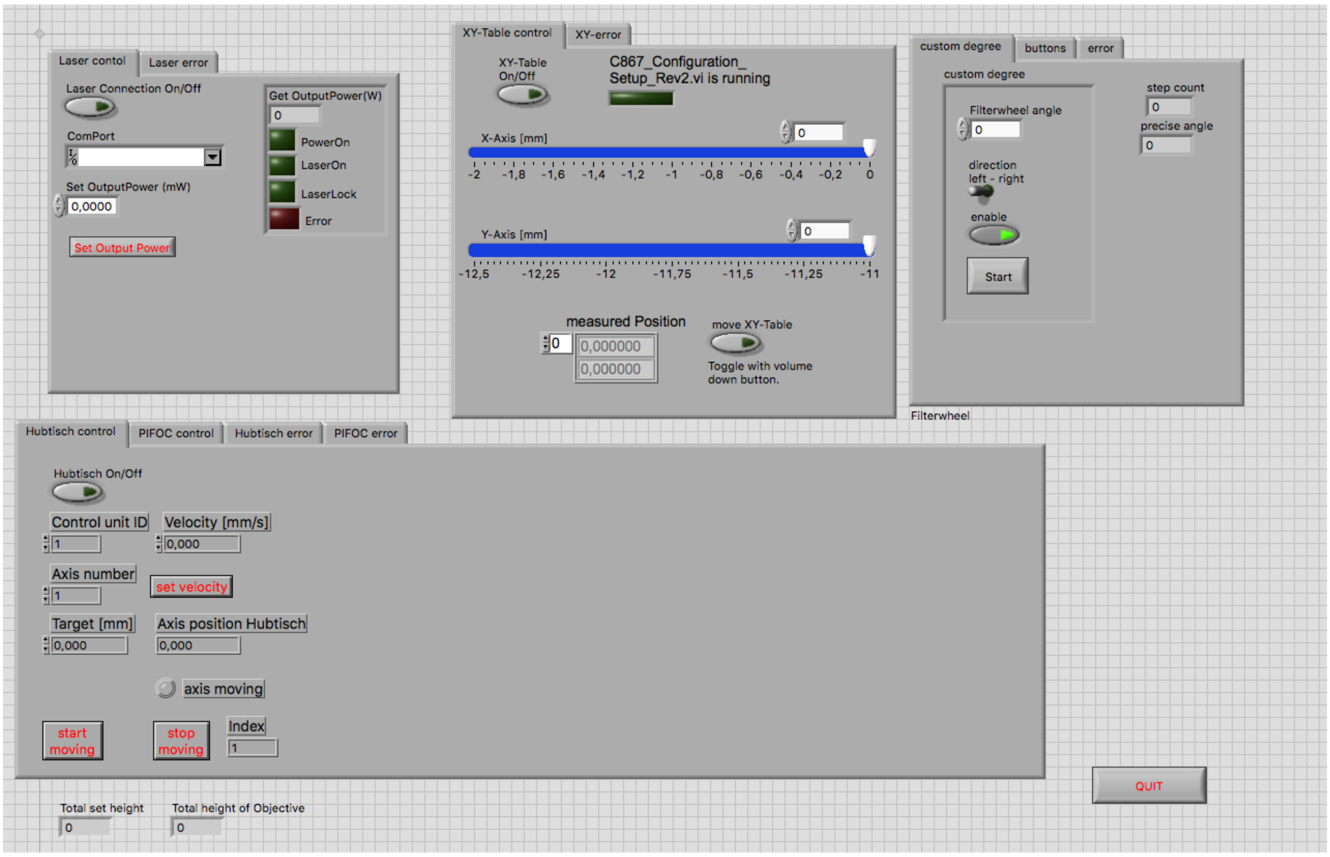

ComPort
Set OutputPower (mW) 0,0000
Get OutputPower(W) 0
X-Axis [mm] 0
Y-Axis [mm] 0
measured Position 0 0,000000 0,000000
Filterwheel angle 0
step count 0
precise angle 0
Control unit ID 1
Velocity [mm/s] 0,000
Axis number 1
Target [mm] 0,000
Axis position Hubtisch 0,000
Index 1
Total set height 0
Total height of Objective 0

Figure A.1.: Graphical user interface of the control software of the confocal microscope.

A.1.2. Wiring diagram

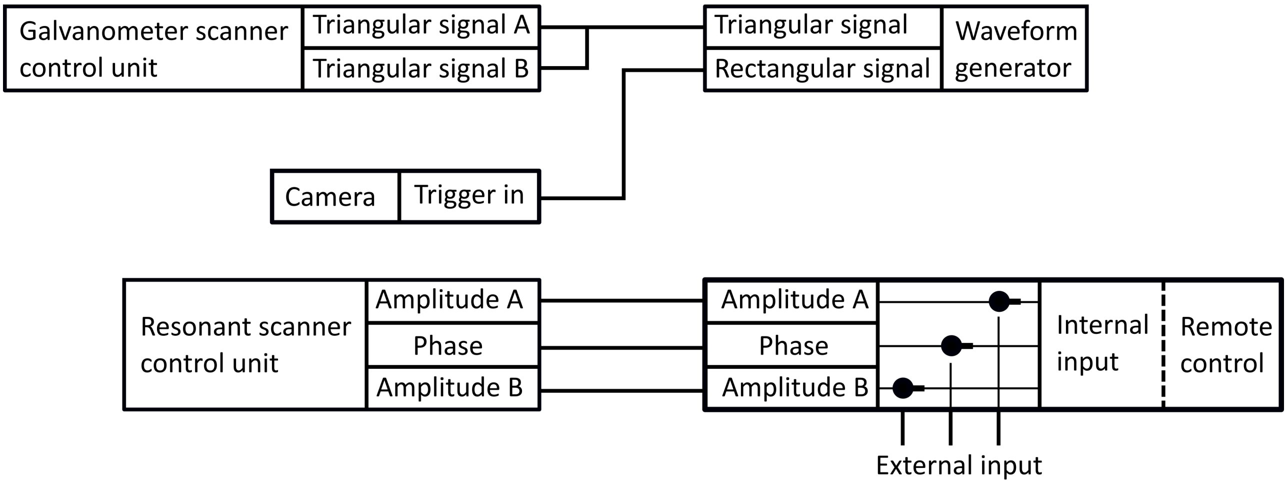

Figure A.2.: Wiring diagram of the confocal microscope.

A.2. Astigmatism particle tracking velocimetry

A.2.1. Filter Cube

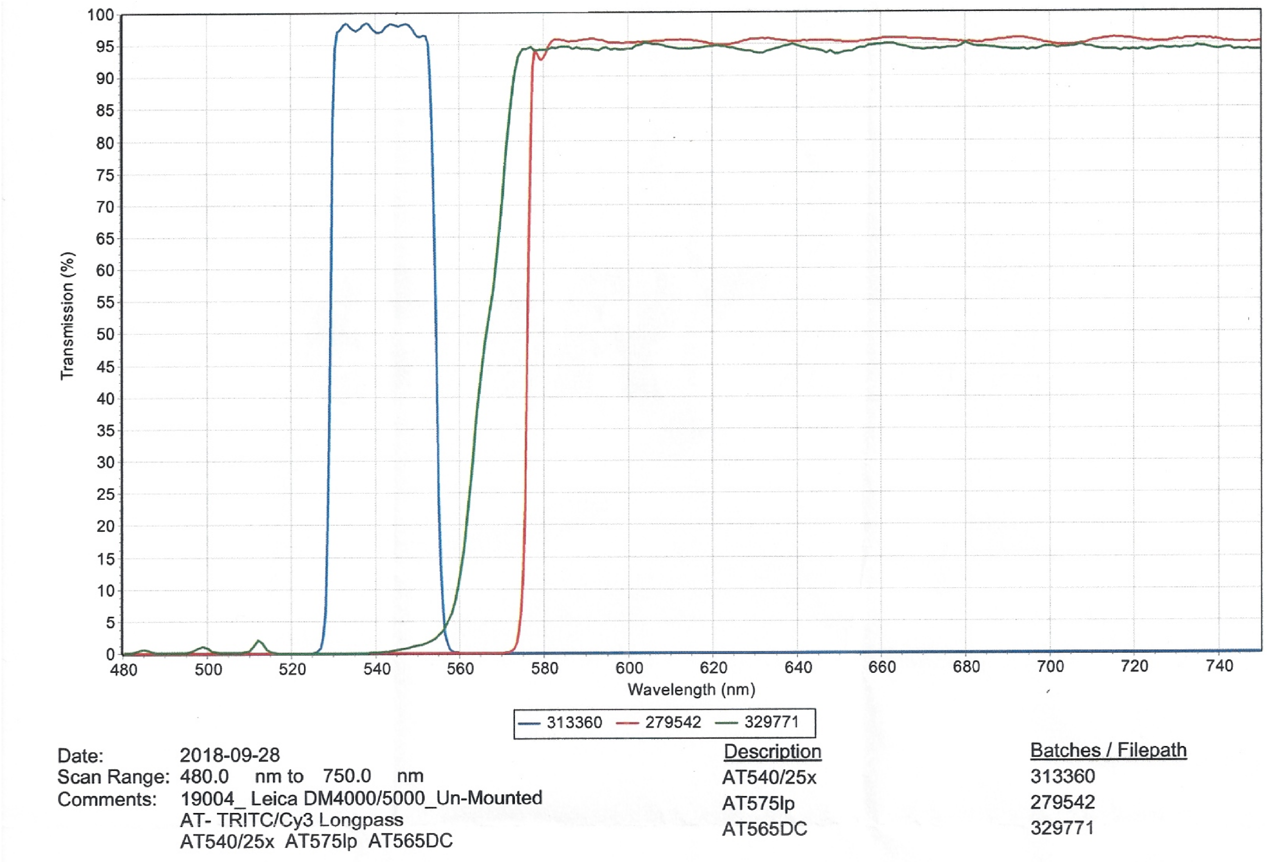

Date: 2018-09-28
Scan Range: 480.0 nm to 750.0 nm
Comments: 19004_ Leica DM4000/5000_Un-Mounted
AT- TRITC/Cy3 Longpass
AT540/25x AT575lp AT565DC

Description	Batches / Filepath
AT540/25x	313360
AT575lp	279542
AT565DC	329771

Figure A.3.: New filter cube of the microscope. Bought from AHF (A.7.1).

A.2.2. Graphical user interface

Measurement Type: Astigmatism
Cylindrical Lens: f = 50mm
Leica - Camera Port: Astigmatismu
Measurement - Setup: Not Def.
Leica - Microscope: Leica DMI
Camera - Type: Photron SA1
Particles - Manufacturer: Microparticles
Solution - Name: No Def.
Leica - Modus: Fluorescence
Camera - Gain: 2
Particles - Material: Polystyrol
Solution - Type: Not Def.
Leica - Filter Cube: CY3
Camera - Gamma: 1
Particles - Dye: PS-FluoRot
Solution - S. Tension [mN/m]: 0
Leica - FL Light Intensity: 100%
Camera - Contrast: 0
Particles - Diameter [µm]: 2
Solution - Viscosity [m2/s]: 0
Lamp - Intensity: 4
Camera - Brightness: 0
Particles - Dispersität: Monodispers
Objective: Olympus:
Camera - Upper Default: 0
Particels - Distribution: On Slide
Objective Slide: 24 x 60mm
Camera - Frame Rate: 50
FD: Round 6
Camera - Exposure Time: 0.02
File Path Control: C:\Users\straub\Desktop
File Ending: .csv
Comments:

Estimated Picture Count: 0
Pictures taken by Camera: 0
Z-Axis Position (mm): 0
Speed Count: 0
Min Speed Count: 0
Max Speed Count: 0
Max Z-Travel [mm]: 0
X-Axis Position (mm): 0
X-Speed µm/s: 0
X-Min Speed µm/s: 0
Max X-Travel [mm]: 0
X-Max Speed µm/s: 0
Y-Axis Position (mm): 0
Y-Speed µm/s: 0
Y-Min Speed µm/s: 0
Y-Max Speed µm/s: 0
Max Y-Travel [mm]: 0
Temperature [C]: 0
Feuchte [%]: 0
Debug Info Z: 0
Debug Info XYZ: 0

Figure A.4.: Graphical user interface of the written control software. The inner tabular structure offers different control options. The other data is, independent of the chosen tab, always visible.

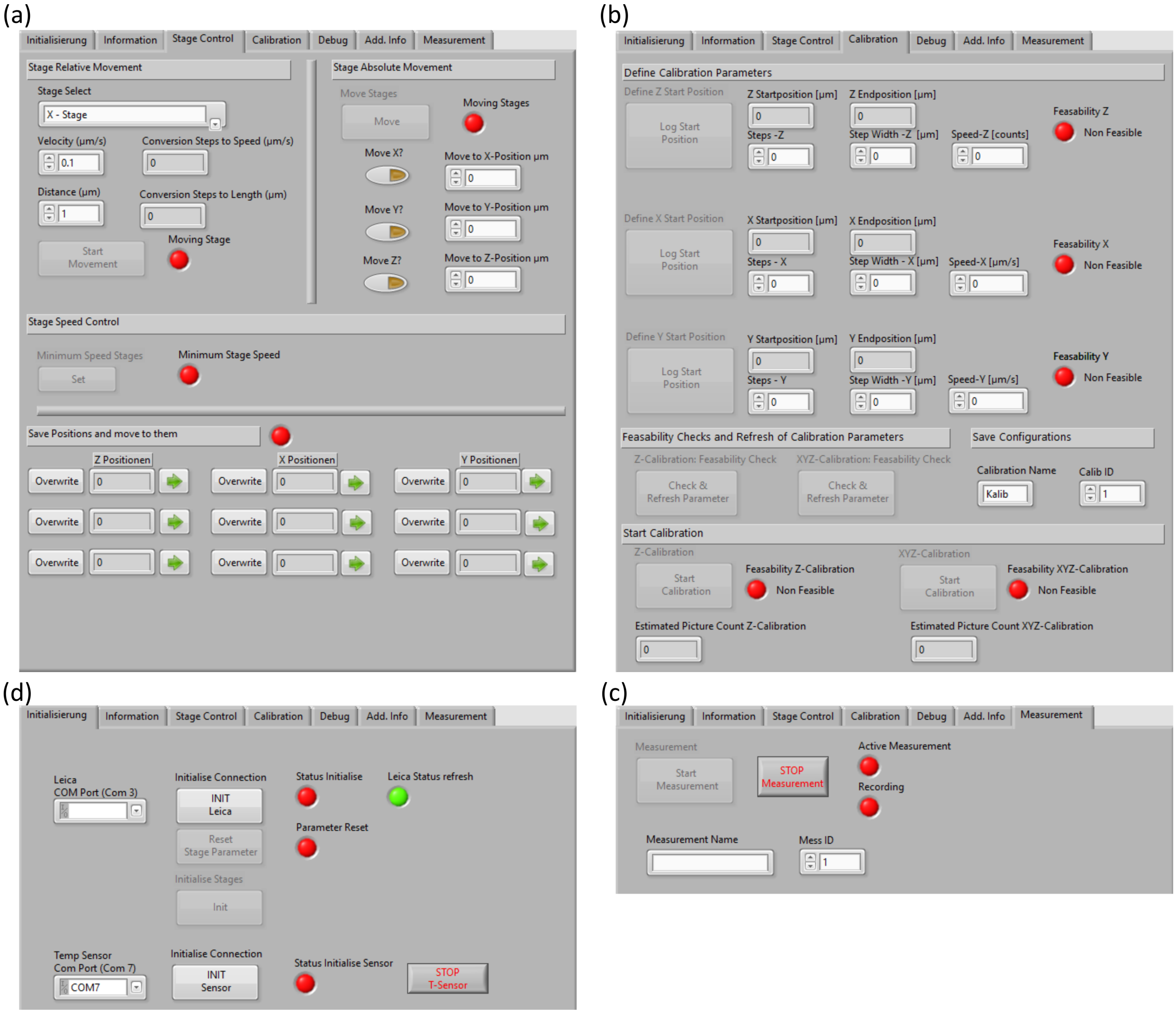

Stage Select: X - Stage
Velocity (µm/s): 0.1
Conversion Steps to Speed (µm/s): 0
Distance (µm): 1
Conversion Steps to Length (µm): 0
Move to X-Position µm: 0
Move to Y-Position µm: 0
Move to Z-Position µm: 0
Z Startposition [µm]: 0
Z Endposition [µm]: 0
Steps -Z: 0
Step Width -Z [µm]: 0
Speed-Z [counts]: 0
X Startposition [µm]: 0
X Endposition [µm]: 0
Steps - X: 0
Step Width - X [µm]: 0
Speed-X [µm/s]: 0
Y Startposition [µm]: 0
Y Endposition [µm]: 0
Steps - Y: 0
Step Width -Y [µm]: 0
Speed-Y [µm/s]: 0
Calibration Name: Kalib
Calib ID: 1
Estimated Picture Count Z-Calibration: 0
Estimated Picture Count XYZ-Calibration: 0
Leica COM Port (Com 3)
Temp Sensor Com Port (Com 7): COM7
Measurement Name
Mess ID: 1

Figure A.5.: Different open tabs of the graphical user interface. (a) Control options of the motorized stages. (b) Possible calibration routines. (c) Options to initialize the connection to the microscope and the temperature sensor. (d) Option to start measurements.

A.2.3. Data–sheet

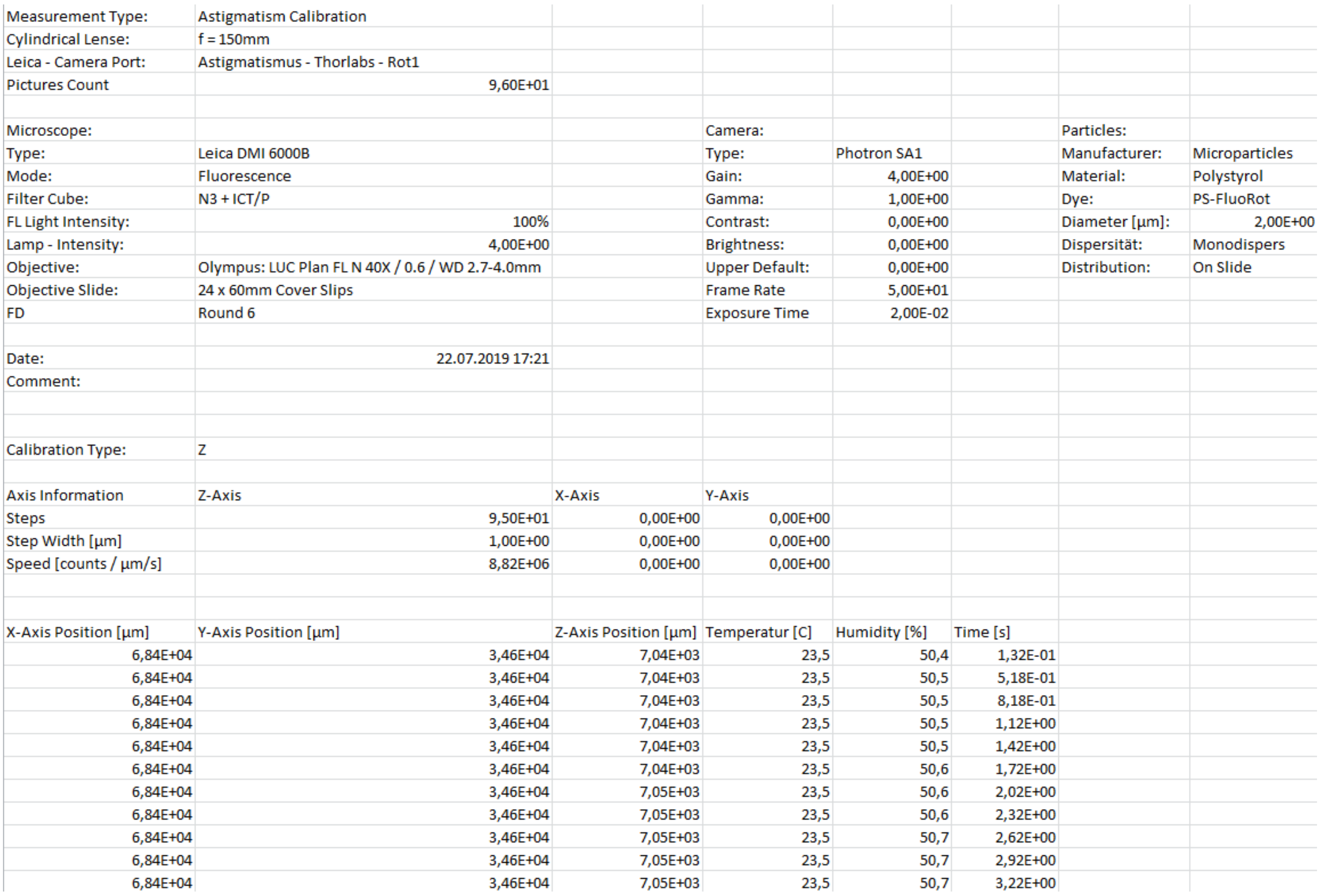

Measurement Type:	Astigmatism Calibration						
Cylindrical Lense:	f = 150mm						
Leica - Camera Port:	Astigmatismus - Thorlabs - Rot1						
Pictures Count	9,60E+01						
Microscope:			Camera:			Particles:	
Type:	Leica DMI 6000B		Type:	Photron SA1		Manufacturer:	Microparticles
Mode:	Fluorescence		Gain:	4,00E+00		Material:	Polystyrol
Filter Cube:	N3 + ICT/P		Gamma:	1,00E+00		Dye:	PS-FluoRot
FL Light Intensity:	100%		Contrast:	0,00E+00		Diameter [µm]:	2,00E+00
Lamp - Intensity:	4,00E+00		Brightness:	0,00E+00		Dispersität:	Monodispers
Objective:	Olympus: LUC Plan FL N 40X / 0.6 / WD 2.7-4.0mm		Upper Default:	0,00E+00		Distribution:	On Slide
Objective Slide:	24 x 60mm Cover Slips		Frame Rate	5,00E+01			
FD	Round 6		Exposure Time	2,00E-02			
Date:	22.07.2019 17:21						
Comment:							
Calibration Type:	Z						
Axis Information	Z-Axis	X-Axis	Y-Axis				
Steps	9,50E+01	0,00E+00	0,00E+00				
Step Width [µm]	1,00E+00	0,00E+00	0,00E+00				
Speed [counts / µm/s]	8,82E+06	0,00E+00	0,00E+00				
X-Axis Position [µm]	Y-Axis Position [µm]	Z-Axis Position [µm]	Temperatur [C]	Humidity [%]	Time [s]		
6,84E+04	3,46E+04	7,04E+03	23,5	50,4	1,32E-01		
6,84E+04	3,46E+04	7,04E+03	23,5	50,5	5,18E-01		
6,84E+04	3,46E+04	7,04E+03	23,5	50,5	8,18E-01		
6,84E+04	3,46E+04	7,04E+03	23,5	50,5	1,12E+00		
6,84E+04	3,46E+04	7,04E+03	23,5	50,5	1,42E+00		
6,84E+04	3,46E+04	7,04E+03	23,5	50,6	1,72E+00		
6,84E+04	3,46E+04	7,05E+03	23,5	50,6	2,02E+00		
6,84E+04	3,46E+04	7,05E+03	23,5	50,6	2,32E+00		
6,84E+04	3,46E+04	7,05E+03	23,5	50,7	2,62E+00		
6,84E+04	3,46E+04	7,05E+03	23,5	50,7	2,92E+00		
6,84E+04	3,46E+04	7,05E+03	23,5	50,7	3,22E+00		

Figure A.6.: Data–sheet.

A.3. Influence of surfactants on forced wetting

A.3.1. Velocity and deviation fields

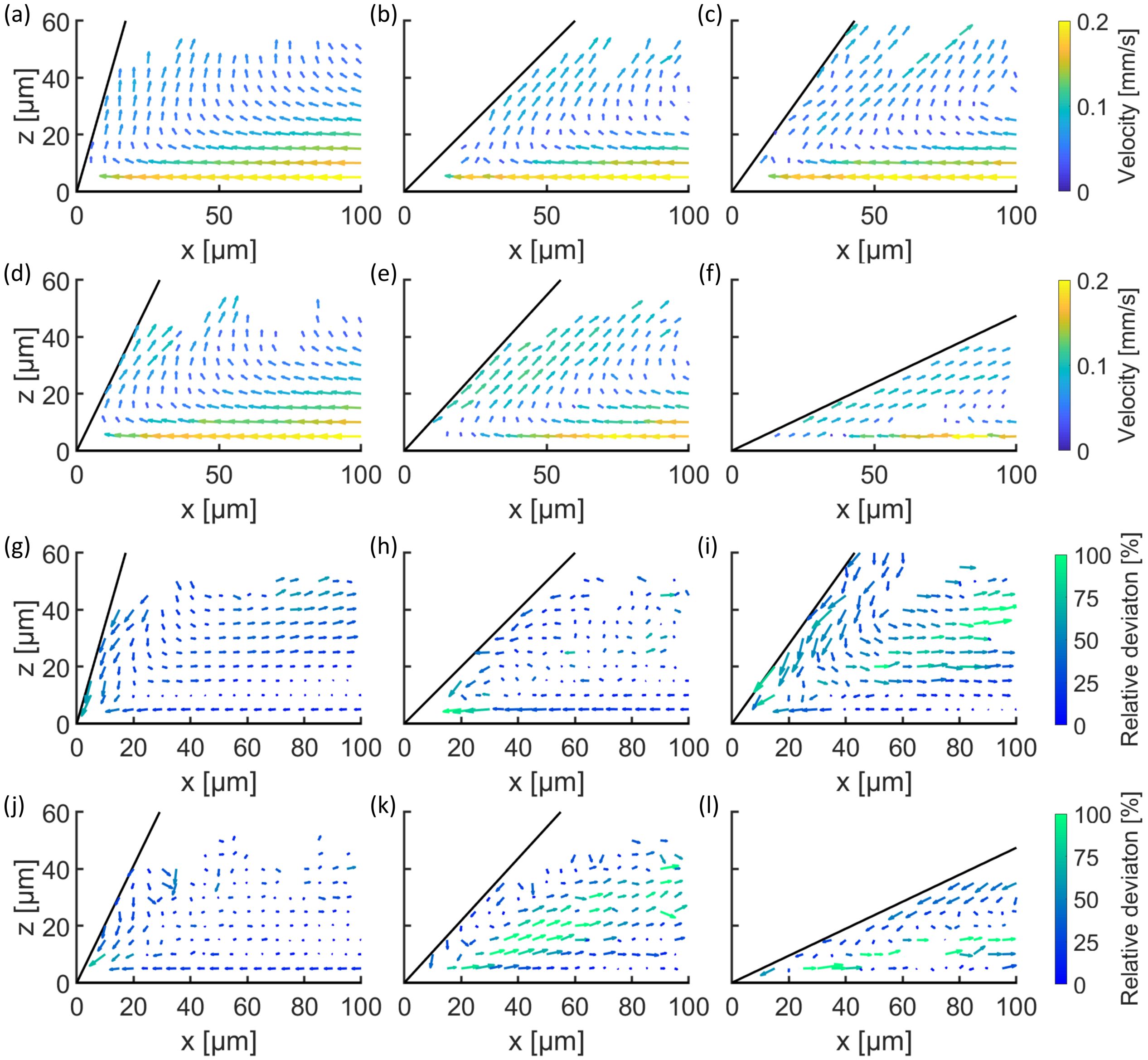

Figure A.7.: (a-c) Velocity and (g-i) deviation fields of 5, 15 and 30 % CMC $\mathrm{C}_{12}\mathrm{E}_5$ solutions with receding contact angles of 76°, 46° and 47°. (d-f) Velocity and (j-l) deviation fields of 5, 15 and 30 % CMC $\mathrm{C}_8\mathrm{E}_3$ solutions with receding contact angles of 61°, 47° and 25°. Partially adapted from [170] (under review) ©2020 American Physical Society (CC BY 4.0).

A.4. Table of components

A.4.1. Confocal microscope

Table A.1.: Confocal microscope: table of components

Number	Type	Manufacturer	Information
A.1.1	Agilent 33512B	Keysight (A.7.2)	Two channel waveform generator,
A.1.2	Agilent DSO5014A	Keysight (A.7.2)	Oscilloscope, 4 channel, 100 MHz
A.1.3	EL-10-30-C	Optotune AG (A.7.3)	Electrically focus tunable lens
A.1.4	CXYZ1/M	Thorlabs (A.7.4)	xyz–translation Mount
A.1.5	MBT402D/M, MBT501	Thorlabs (A.7.4)	5–Axis Stage Kit
A.1.6	C1515/M	Thorlabs (A.7.4)	Mounting Post Bracket
A.1.7	PSHA/M	Thorlabs (A.7.4)	Adjustable Height Collar
A.1.8	CLS–SL	Thorlabs (A.7.4)	Scan lens for telecentric system
A.1.9	ITL200	Thorlabs (A.7.4)	Tube lens for telecentric system
A.1.10	TTL200–A	Thorlabs (A.7.4)	Tube lens
A.1.11	CRM1P/M	Thorlabs (A.7.4)	Precision rotation mount
A.1.12	60 mm Cage System	Thorlabs (A.7.4)	Optomechanical components to mount tube and scan lenses
A.1.13	S130C	Thorlabs (A.7.4)	Power meter
A.1.14	SH1/M	Thorlabs (A.7.4)	Optical beam shutter
A.1.15	DMSP550	Thorlabs (A.7.4)	Dichroic mirror
A.1.16	NDC-100C-4	Thorlabs (A.7.4)	Unmounted Round Variable ND Filters
A.1.17	ACXXX-XXX-A-ML	Thorlabs (A.7.4)	Achromatic corrected lenses with antireflective coating
A.1.18	FELH0550	Thorlabs (A.7.4)	Longpass filter
A.1.19	dynAXIS XS	Scanlab (A.7.5)	Galvanometer scanner
A.1.20	dynAXIS XS driver	Scanlab (A.7.5)	Driver card for galvanometer scanner (A.1.19)
A.1.21	Linos Microbench	Qioptiq (A.7.6)	Optomechanical system
A.1.22	G040-XXX-000	Qioptiq (A.7.6)	Pinholes, without reflection
A.1.23	G065-118-000	Qioptiq (A.7.6)	Motorized rotation mount powered by a step motor
A.1.24	N-BK7	Qioptiq (A.7.6)	50:50 Beam splitter with antireflex coating
A.1.25	G340-523-000	Qioptiq (A.7.6)	Silver mirrors
A.1.26	G063-730-000	Qioptiq (A.7.6)	Kinematic mirror mount

Continued on next page

Confocal microscope: table of components – continued from previous page

Number	Type	Manufacturer	Information
A.1.27	G063-XXX-000	Qioptiq (A.7.6)	Achromatic corrected lenses with antireflective coating
A.1.28	NI BNC–2120	National Instruments (A.7.7)	Shielded connector block BNC–2120
A.1.29	PCIe-6323	National Instruments (A.7.7)	Multifunction I/O–module
A.1.30	xyz–unit	Owis (A.7.8)	Previous version of MVT 40C–XYZ
A.1.31	HTM 100	Owis (A.7.8)	Elevator stage
A.1.32	HTM 100 controller	Owis (A.7.8)	controller box for HTM 100 (A.1.31)
A.1.33	PLD–2S–220	EOPC (A.7.9)	Control unit for resonant scanners A.1.34
A.1.34	SC 30	EOPC (A.7.9)	Resonant scanners, 15.7 kHz, mirror size $4 \times 5\,\text{mm}^2$
A.1.35	P–726 PIFOC	Physik Instrumente (A.7.10)	High–load objective scanner
A.1.36	E-754	Physik Instrumente (A.7.10)	Digital motion controller for P–726 PIFOC (A.1.35)
A.1.37	U–751	Physik Instrumente (A.7.10)	Piezoelectric xy–stage with and 25 mm travel range
A.1.38	C-867.2U2	Physik Instrumente (A.7.10)	Motion controller for xy–stage (A.1.37)
A.1.39	PD72Z4CA0	Physik Instrumente (A.7.10)	Objective scanning system 400 µm travel range; includes E–709 motion controller
A.1.40	Power supply	MPIP (A.7.11)	Power supply for galvanometer scanner (A.1.19)
A.1.41	Remote control	MPIP (A.7.11)	Target value control for resonant scanner (A.1.33)
A.1.42	Shutter controller	MPIP (A.7.11)	Controller box for shutter (A.1.14)
A.1.43	Filterwheel controller	MPIP (A.7.11)	Filter wheel controller box for microstep controller (A.1.50)
A.1.44	Temperature sensor CLSM	MPIP (A.7.11)	Temperature and humidity sensor
A.1.45	Housing box	MPIP (A.7.11)	Housing box
A.1.46	Cobolt Samba	Cobolt (A.7.12)	Laser, wavelength 532 nm, max. 100 mW

Continued on next page

Confocal microscope: table of components – continued from previous page

Number	Type	Manufacturer	Information
A.1.47	Guardian Al-6	Newport (A.7.13)	Active isolation optical table
A.1.48	NX 4	IDT (A.7.14)	High–speed camera
A.1.49	DG5102	Rigol (A.7.15)	Waveform generator
A.1.50	SMC 11	Nanotec A.7.16	Compact microstep controller
A.1.51	S4LFT1254/121	Sill Optics (A.7.17)	F–theta lens
A.1.52	KEL-SNAP 24	Icotek (A.7.23)	Cable entry system
A.1.53	SH0011, SH0131	Schaumstoffe Helgers (A.7.24)	Adsorption foam

Concluded

A.4.2. Astigmatism particle tracking velocimetry

Table A.2.: Astigmatism particle tracking velocimetry: Table of components

Number	Type	Manufacturer	Information
A.2.1	RLA150/M, RC2/M	Thorlabs (A.7.4)	Dovetail optical rail
A.2.2	SM1A50	Thorlabs (A.7.4)	Leica DMI Microscope Camera Port Adapter
A.2.3	Photron Fastcam SA 1.1	Photron (A.7.27)	High–speed camera
A.2.4	Active isolation table	No information	Active isolation table with pneumatic self–levelling
A.2.5	Housing	MPIP (A.7.11)	Housing box
A.2.6	MB1515/M	Thorlabs (A.7.4)	Aluminium breadboard
A.2.7	Leica DMI 6000B	Leica (A.7.25)	Inverted research microscope
A.2.8	TV adapter	Leica (A.7.25)	High speed camera connector, 1X 1"
A.2.9	SM1 lens tubes	Thorlabs (A.7.4)	Optomechanical tube system components and adapter rings
A.2.10	DLM1/M	Thorlabs (A.7.4)	Rotation mount for the cylindrical lens (A.2.11)
A.2.11	ACY254-XXX-A	Thorlabs (A.7.4)	Achromatic cylindrical lenses with antireflective coating
A.2.12	Temperature sensor	MPIP (A.7.11)	Temperature and humidity sensor
A.2.13	PCIe–6361	National Instruments (A.7.7)	Multifunction I/O Device

Continued on next page

APTV: table of components – continued from previous page

Number	Type	Manufacturer	Information
A.2.14	SCB-68A	National Instruments (A.7.7)	Shielded connector block
			Concluded

A.4.3. Experimental setup

Table A.3.: Experimental setup: table of components

Number	Type	Manufacturer	Information
A.3.1	LPS-45	Physik Instrumente (A.7.10)	Piezoelectric stage
A.3.2	E-871.1A1	Physik Instrumente (A.7.10)	Motion controller for piezoelectric stage (A.3.1)
A.3.3	7VT174-5	Standa (A.7.26)	Aluminium Ball Bearing Vertical Stage
A.3.4	K 25-FGS	Owis (A.7.8)	Kinematic mirror mount
A.3.5	FGS 6-10	Owis (A.7.8)	Finethread screw
			Concluded

A.4.4. Miscellaneous devices and components

Table A.4.: Table of miscellaneous devices and components

Number	Type	Manufacturer	Information
A.4.1	Arium®611	Sartorius (A.7.18)	Ultra–pure water system, resistivity of 18.2 MΩ
A.4.2	Arium®pro VF/UF & DI/UV	Sartorius (A.7.18)	Ultra–pure water system, resistivity of 18.2 MΩ
A.4.3	6.5 X UltraZoom, 3 mm FF, Coax	Navitar (A.7.29)	Tubus with zoom option
A.4.4	M Plan APO 2 X	Mitutoyo (A.7.28)	M Plan Apo 2 X objective for Bright Field Observation
			Continued on next page

Table of miscellaneous devices and components – continued from previous page

Number	Type	Manufacturer	Information
A.4.5	MT 120S-50-D56-XYZ-MS	Owis (A.7.8)	Three–axes table
A.4.6	OCA35	DataPhysics (A.7.30)	Contact angle measurement device
A.4.7	DCAT 11EC	DataPhysics (A.7.30)	Dynamic contact angle measuring devices and tensiometer
A.4.8	IntraLED 5	FiberOptic (A.7.31)	LED cold light source
A.4.9	CS2100M-USB	Thorlabs (A.7.4)	2.1 MP Monochrome sCMOS Camera
A.4.10	USC200T	VWR (A.7.32)	Ultrasonic Cleaner
A.4.11	EX225D/AD	OHAUS (A.7.33)	Fine balance
A.4.12	PS20	Pyser optics (A.7.19)	Calibration slide
A.4.13	Stage Micrometer 3	POG (A.7.34)	Calibration slide
A.4.14	BNC cables	RS Components (A.7.20)	Electrical resistance 50 Ω
A.4.15	Aluminum profiles	Bosch Rexroth (A.7.21)	Aluminium profiles
A.4.16	LUCPLFLN40X	Olympus (A.7.35)	Objective; NA=0.6; immersion medium: air
A.4.17	LUCPLFLN20X	Olympus (A.7.35)	Objective; NA=0.45; immersion medium: air
A.4.18	UMPLANFL20X	Olympus (A.7.35)	objective; NA=0.46; immersion medium: air
A.4.19	UPLSAPO60XO	Olympus (A.7.35)	Objective; NA=1.35; immersion medium: oil
A.4.20	MPLAPON50X	Olympus (A.7.35)	Objective; NA=0.95; immersion medium: air
			Concluded

A.5. Table of consumable materials

Table A.5.: Table of consumable materials

Number	Type	Manufacturer	Information
A.5.1	0107242	Marienfeld (A.7.39)	Precision cover glasses thickness No. 1.5H
A.5.2	Eppendorf Research®plus	Eppendorf (A.7.38)	Pipettes with various volumes
A.5.3	epT.I.P.S.®Standard	Eppendorf (A.7.38)	Pipette tips
A.5.4	448931-10G	Sigma–Aldrich (A.7.36)	(trichloro(1H, 1H, 2H, 2H–perfluorooctyl)silane
A.5.5	32221-2.5L-M	Sigma–Aldrich (A.7.36)	Ethanol puriss. p.a., absolute, $\geq$99.8 % (GC)
A.5.6	A/0600/17	Fisher Scientific (A.7.37)	Acetone, $\geq$99.8 %
A.5.7	P/7500/17	Fisher Scientific (A.7.37)	Propan-2-ol, $\geq$99.8 %
A.5.8	76437-1G	Sigma–Aldrich (A.7.36)	Dodecyl pentaglycole, BioXtra, $\geq$99.8 % (GC)
A.5.9	90455-5ML	Sigma–Aldrich (A.7.36)	Octyl triglycole, BioXtra, $\geq$99.8 % (GC)
A.5.10	JW14	MPIP (A.7.11)	Silica particles labelled with rhodamine B
A.5.11	S/7120/53	Fisher Scientific (A.7.37)	Sodium thiocyanate anhydrous
A.5.12	450510-100ML	Sigma–Aldrich (A.7.36)	Deuterium oxide, purity 99 %
A.5.13	Polystyrene particles	MPIP (A.7.11)	4 µm sized monodisperse polystyrene particles labelled with rhodamine B
A.5.14	PS–FluoRot–X.X	microParticles (A.7.22)	Florescent labelled monodisperse spherical polystyrene particles, various diameters
A.5.15	Immersol 518 F	Zeiss (A.7.41)	immersion oil with refractive index of 1.518
			Concluded

A.6. Table of software

Table A.6.: Table of used software.

Number	Type	Manufacturer	Information
A.6.1	LabVIEW	National Instruments (A.7.7)	Used Versions: 2017-2020
A.6.2	Matlab	Mathworks (A.7.40)	Used Versions: 2017-2020
A.6.3	OWISoft	Owis (A.7.8)	Control software for the elevator stage (A.1.31)
A.6.4	PIMikroMove	Physik Instrumente (A.7.10)	Control software for the used motorized stages of the manufacturer Physik Instrumente
A.6.5	Motion Studio x64	IDT (A.7.14)	Control software for the high–speed camera (A.1.48)
A.6.6	PFV	Photron (A.7.27)	Photron Fastcam Viewer, Version 3.6.7.0
A.6.7	LAS V3	Leica (A.7.25)	Leica Application Suit V3
A.6.8	Thorcam	Thorlabs (A.7.4)	Control software for the webcam (A.4.9)
A.6.9	Cobolt Monitor	Cobolt (A.7.12)	Control software for the laser (A.1.46)

A.7. Table of manufacturers

In the following, all manufacturers of used components are listed.

Table A.7.: Manufacturer information

Number	Manufacturer	Address
A.7.1	AHF analysentechnik AG	Tübingen, Germany
A.7.2	Keysight	Santa Rosa, California, USA
A.7.3	Optotune AG	Dietikon, Switzerland
A.7.4	Thorlabs GmbH	Munich, Germany
A.7.5	Scanlab GmbH	Puchheim, Germany
A.7.6	Qioptiq Photonics GmbH & Co. KG	Göttingen, Germany
A.7.7	National Instruments	Austin, Texas
A.7.8	Owis GmbH	Staufen i. Br., Germany
A.7.9	EOPC	Ridgewood, NY, USA
A.7.10	Physik Instrumente	Karlsruhe, Germany
A.7.11	Max Planck Institute for Polymer Research	Mainz, Germany
A.7.12	Cobolt	Solna, Sweden
A.7.13	Newport	Irvine, California, USA
A.7.14	Integrated Design Tools, Inc.	Pasedena, US
A.7.15	Rigol	Beijing, China
A.7.16	Nanotec Electronic GmbH	Feldkirchen, Germany
A.7.17	Sill Optics GmbH & Co. KG	Wendelstein, Germany
A.7.18	Sartorius AG	Göttingen, Germany
A.7.19	Pyser optics	Kent, United Kingdom
A.7.20	RS Components GmbH	Frankfurt a. M., Germany
A.7.21	Bosch Rexroth AG	Lohr am Main, Germany
A.7.22	microParticles GmbH	Berlin, Germany
A.7.23	Icotek GmbH	Eschach, Germany
A.7.24	Schaumstoffe Helgers GmbH	Eschweiler, Germany
A.7.25	Leica Mikrosysteme Vertrieb GmbH Mikroskopie und Histologie	Wetzlar, Grmany
A.7.26	Standa Ltd	Vilnius, Lithuania
A.7.27	Photron Deutschland Gmbh	Reutlingen, Germany
A.7.28	Mitutoyo Europe GmbH	Neuss, Germany
A.7.29	Navitar	Rochester, New York 14623 USA
A.7.30	DataPhysics Instruments GmbH	Filderstadt, Germany
A.7.31	FiberOptic P. + P. AG	Spreitenbach, Germany

Continued on next page

Manufacturer information – continued from previous page

Number	Manufacturer	Address
A.7.32	VWR International GmbH	Darmstadt, Germany
A.7.33	OHAUS Europe GmbH	Nänikon, Switzerland
A.7.34	POG Präzisionsoptik Gera GmbH	Löbichau, Germany
A.7.35	Olympus Deutschland GmbH	Hamburg, Germany
A.7.36	Sigma–Aldrich Chemie GmbH	Taufkirchen, Germany
A.7.37	Fisher Scientific GmbH	Schwerte, Germany
A.7.38	Eppendorf AG	Hamburg, Germany
A.7.39	Paul Marienfeld GmbH & Co.KG	Lauda-Königshofen, Germany
A.7.40	The MathWorks GmbH	Aachen, Germany
A.7.41	Carl Zeiss AG	Oberkochen, Germany
		Concluded

A.8. Technical drawings

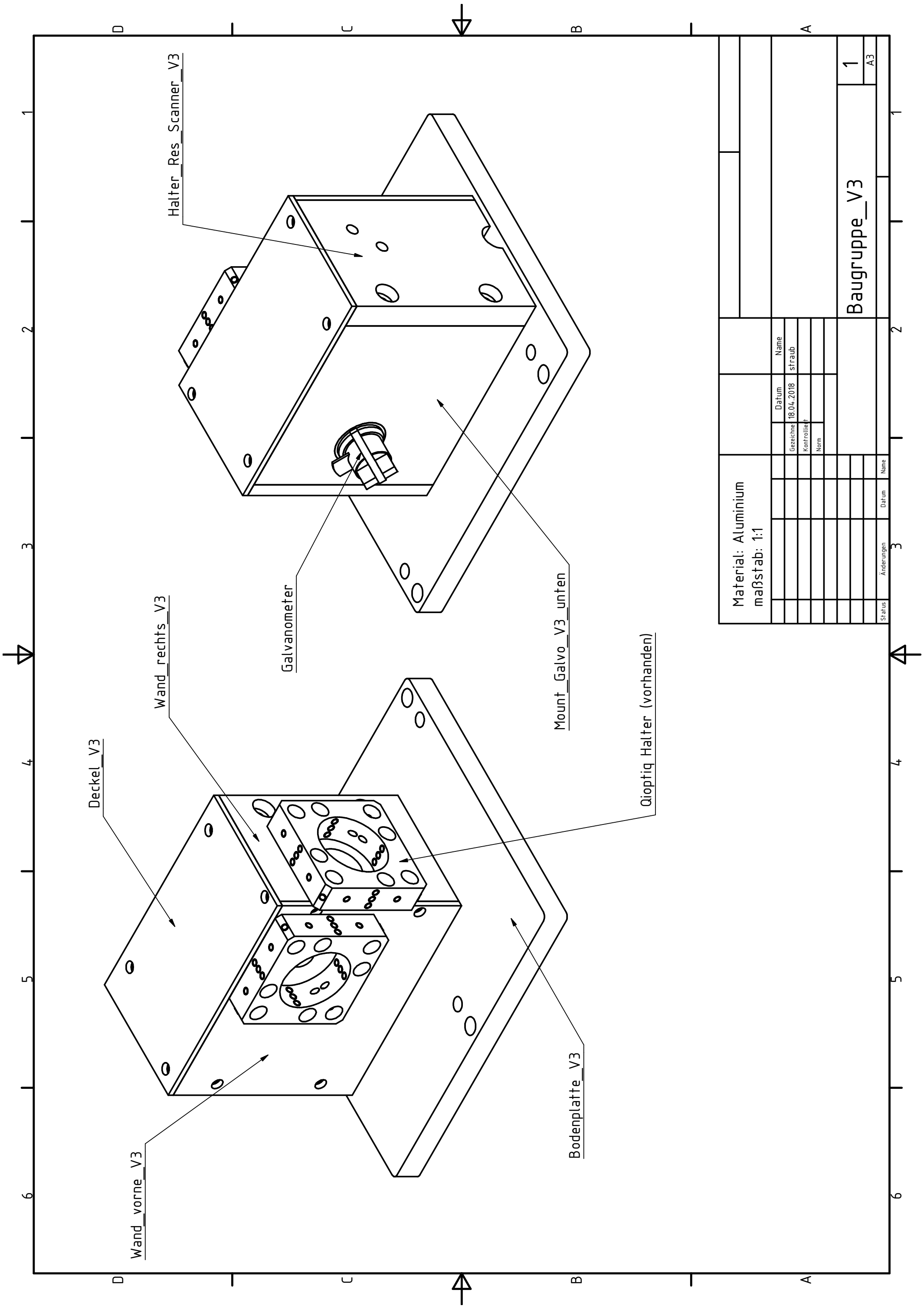

Figure A.8.: Assembly group of scan cube B

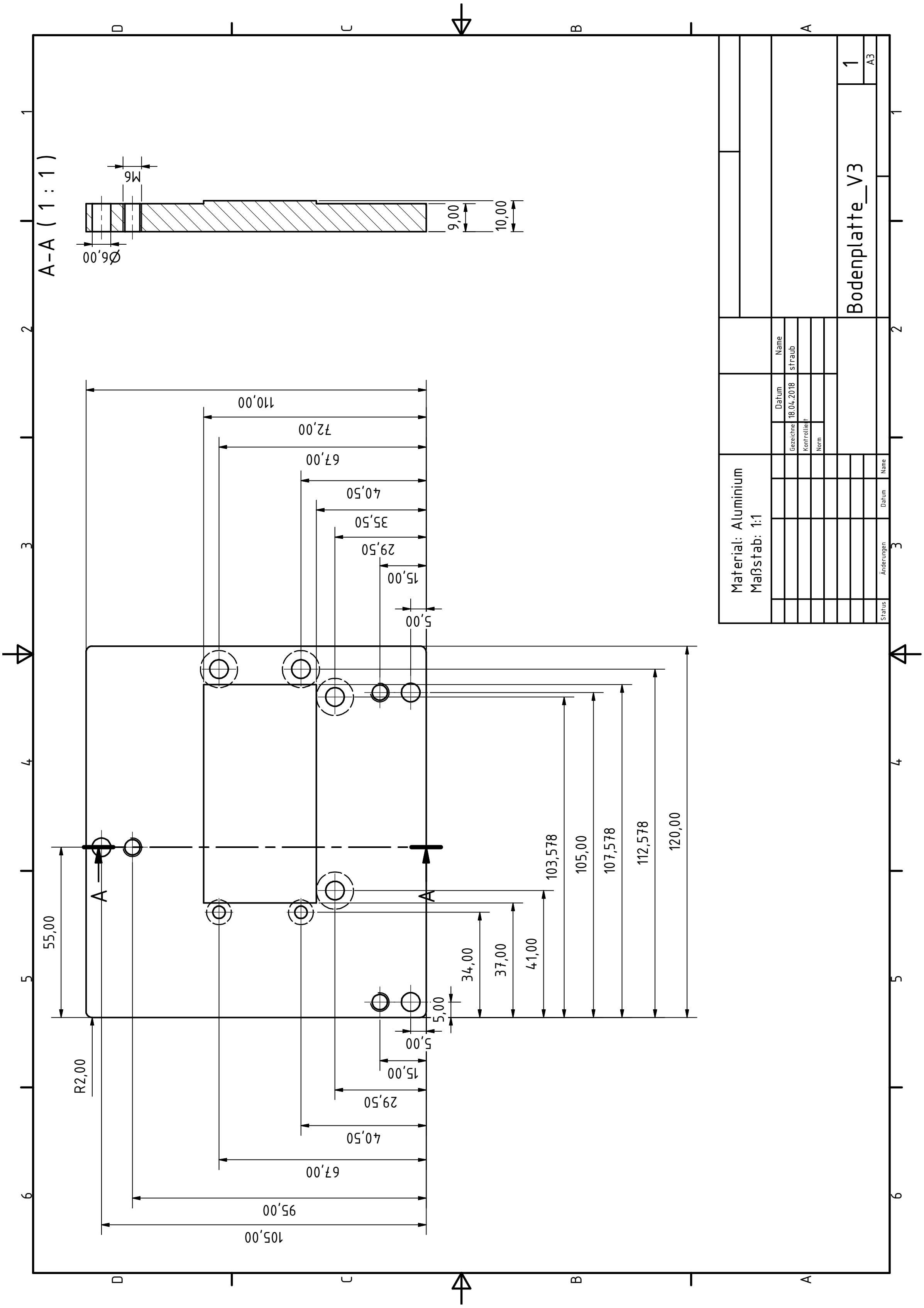

Figure A.9.: Scan cube B: Base plate; side 1

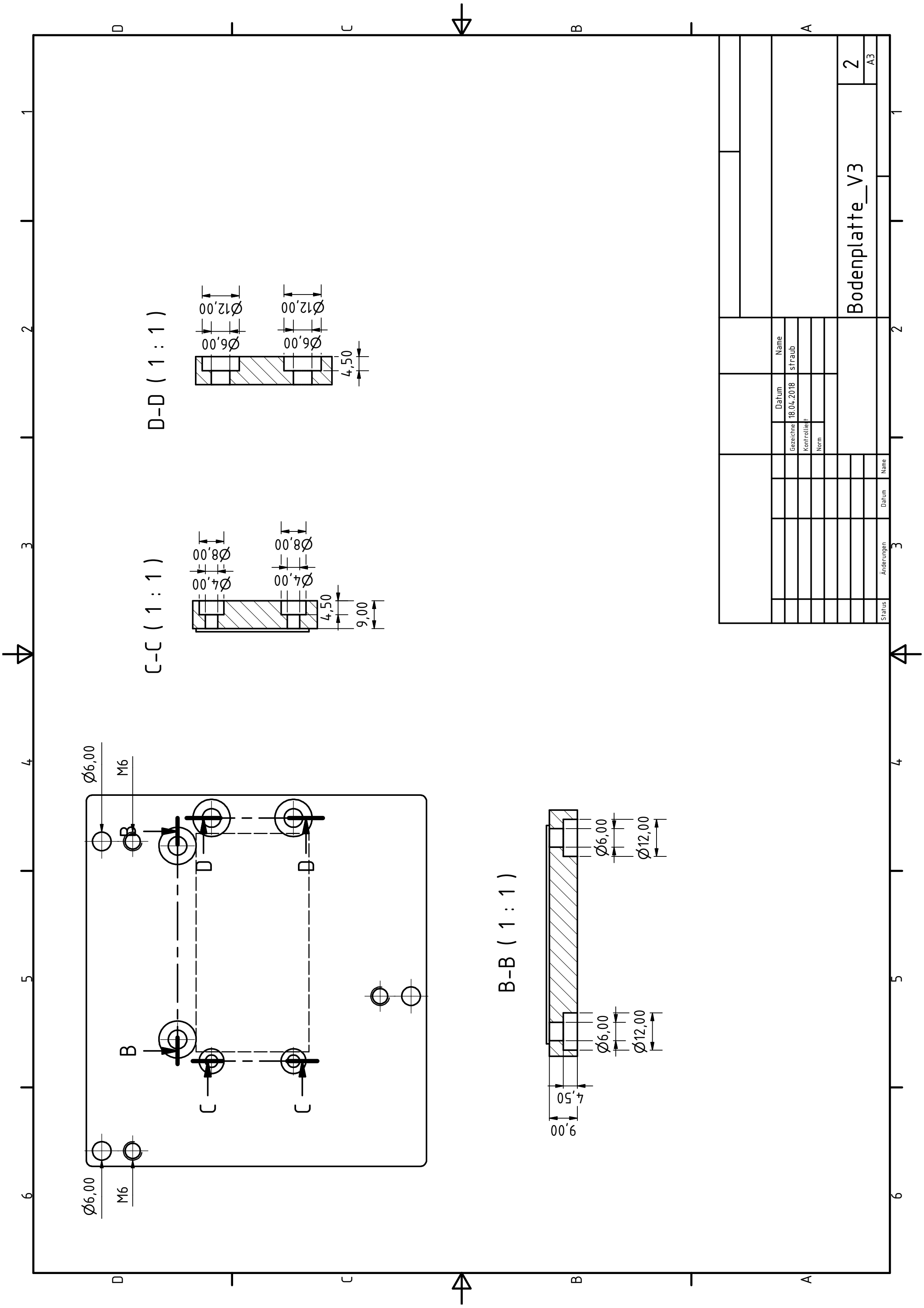

Figure A.10.: Scan cube B: Base plate; side 2

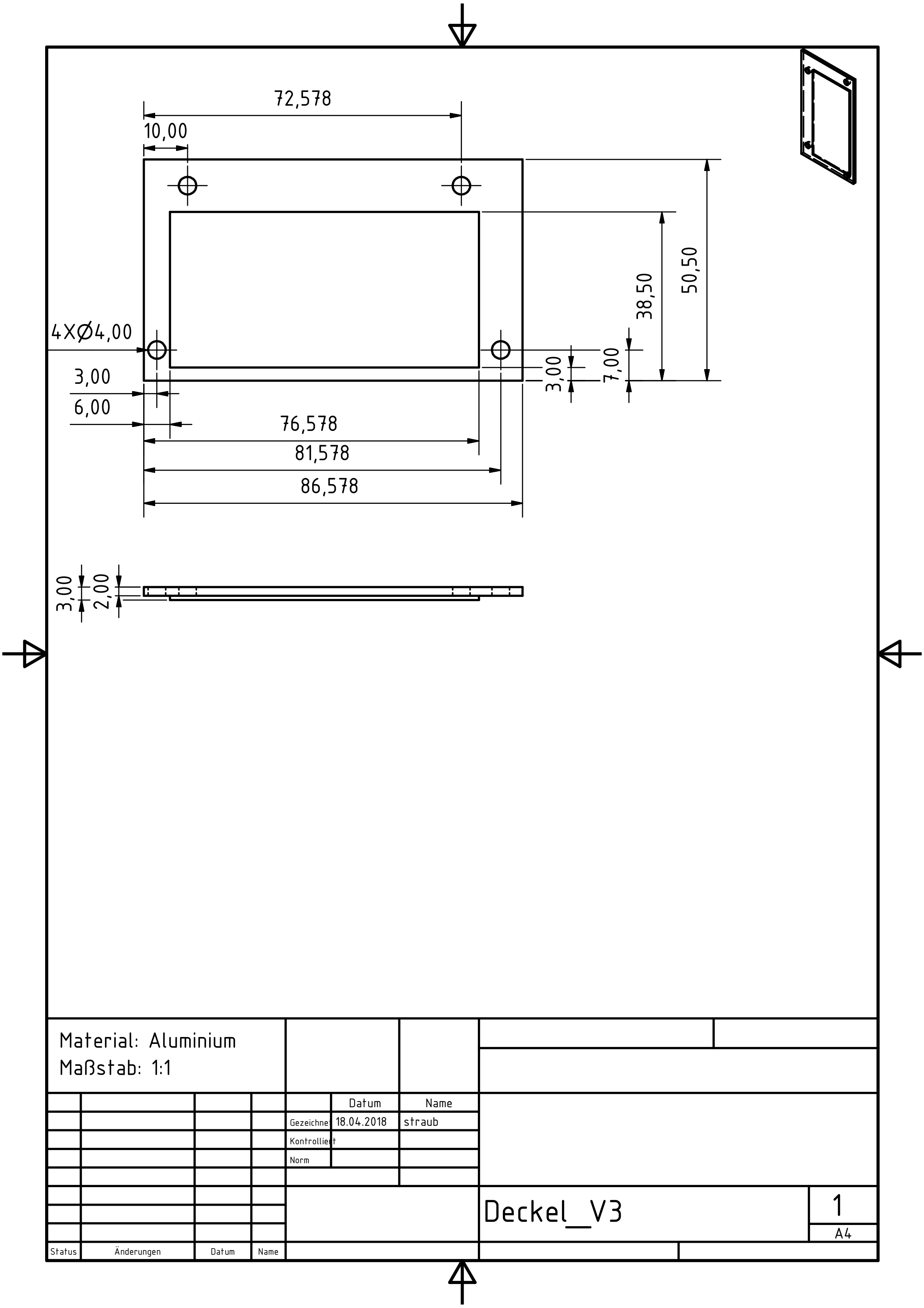

Figure A.11.: Scan cube B: Lid

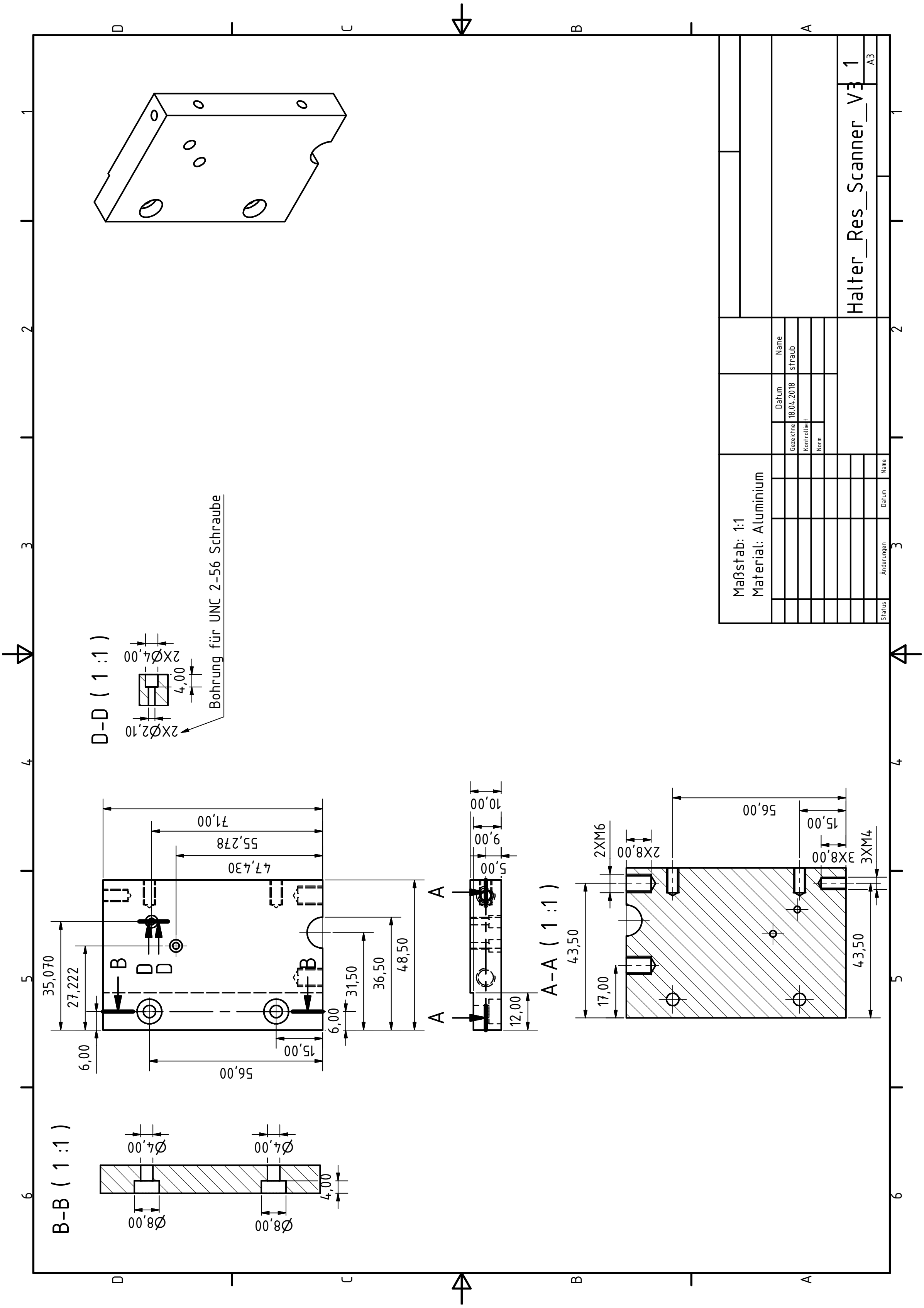

Figure A.12.: Scan cube B: Resonant scanner mount

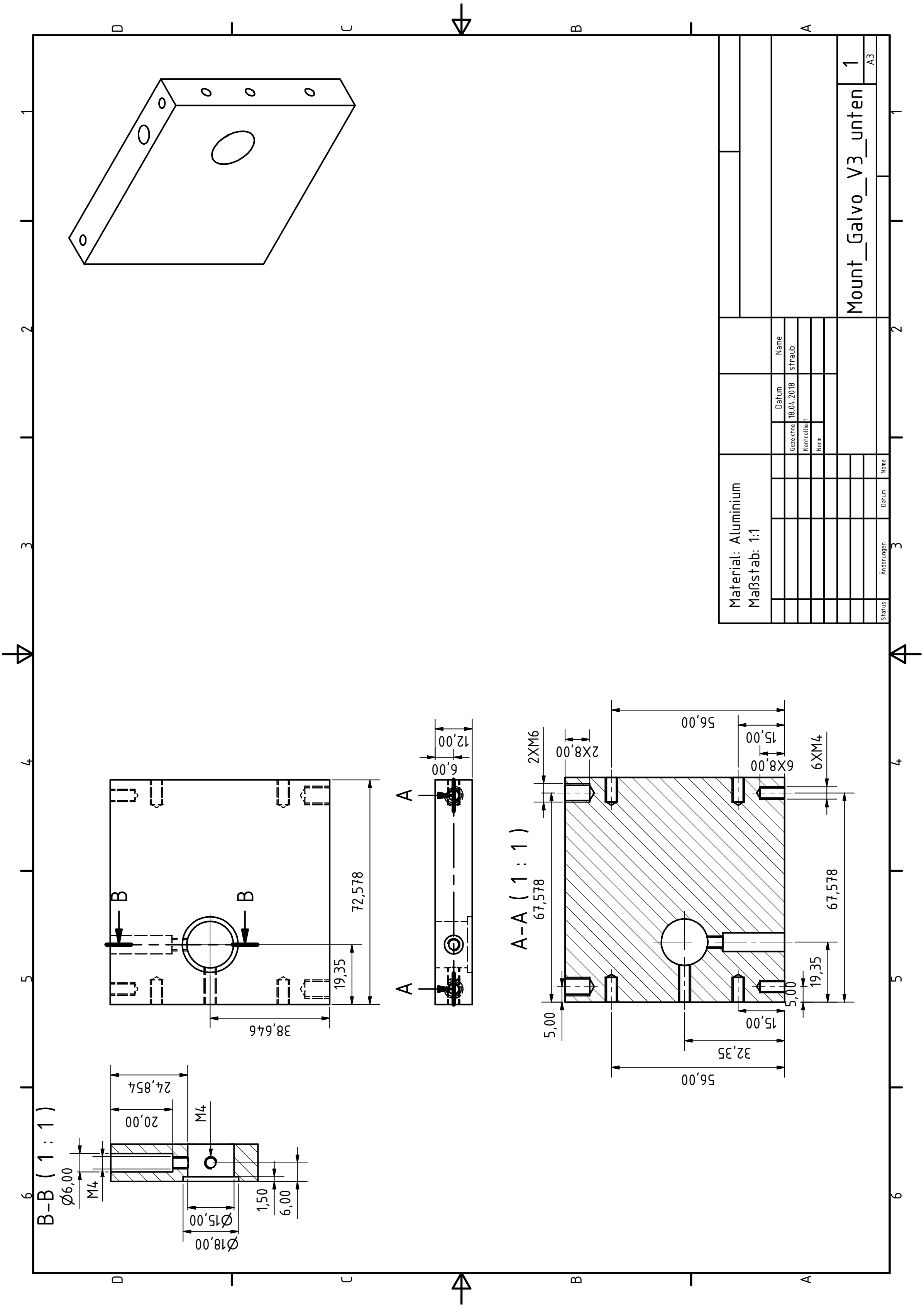

Figure A.13.: Scan cube B: Galvanometer scanner mount

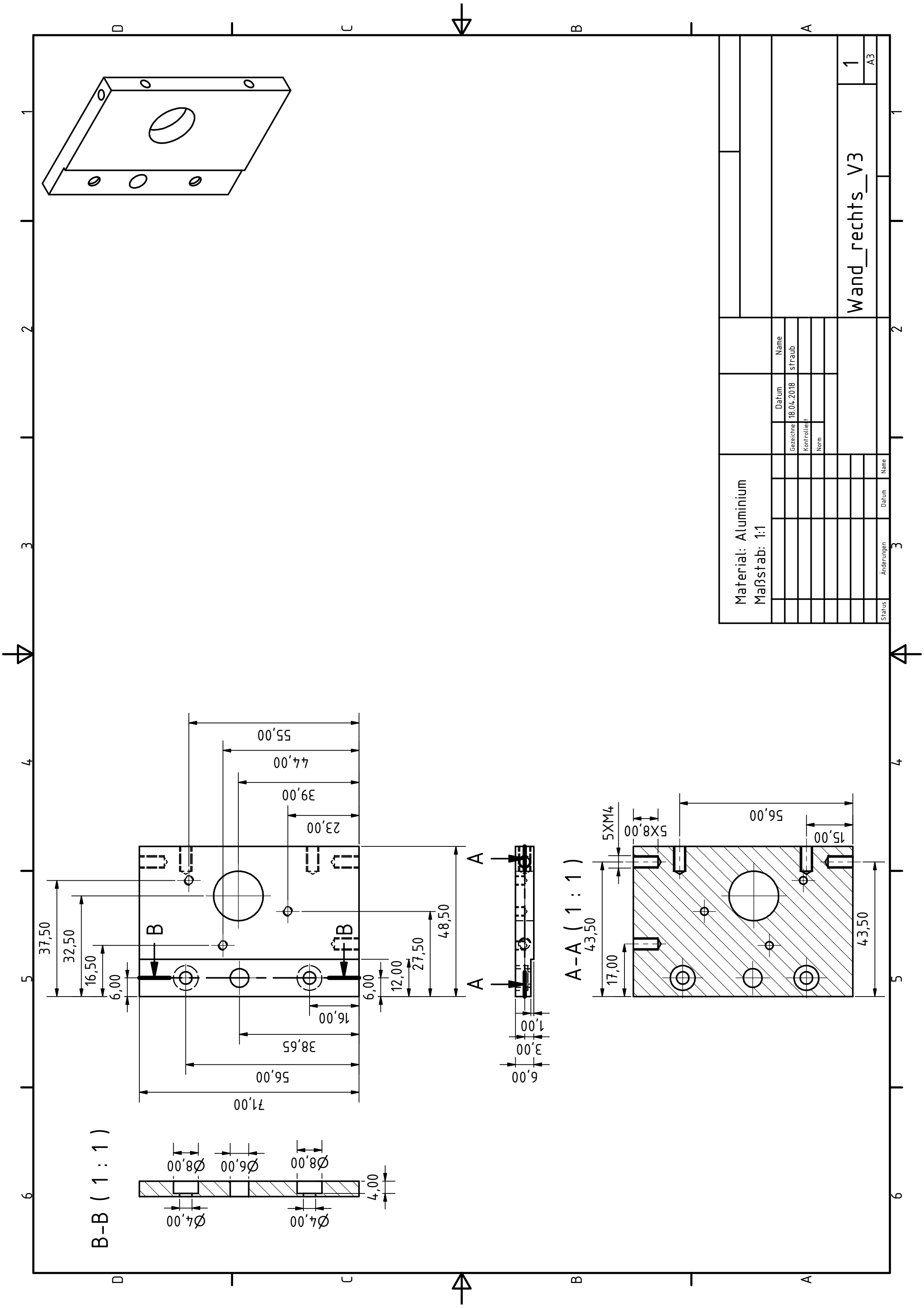

Figure A.14.: Scan cube B: Right wall

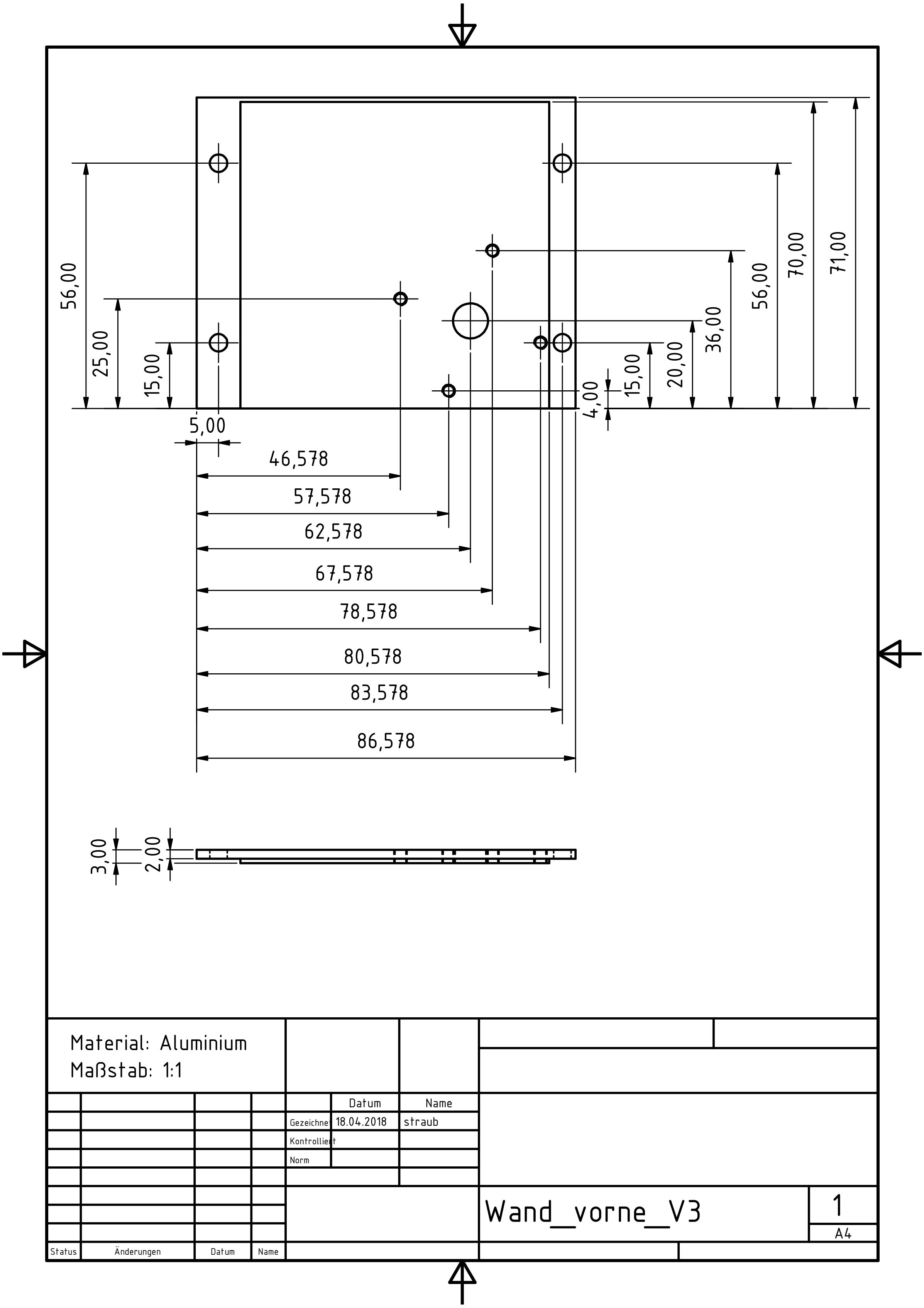

Figure A.15.: Scan cube B: Front wall; side 1

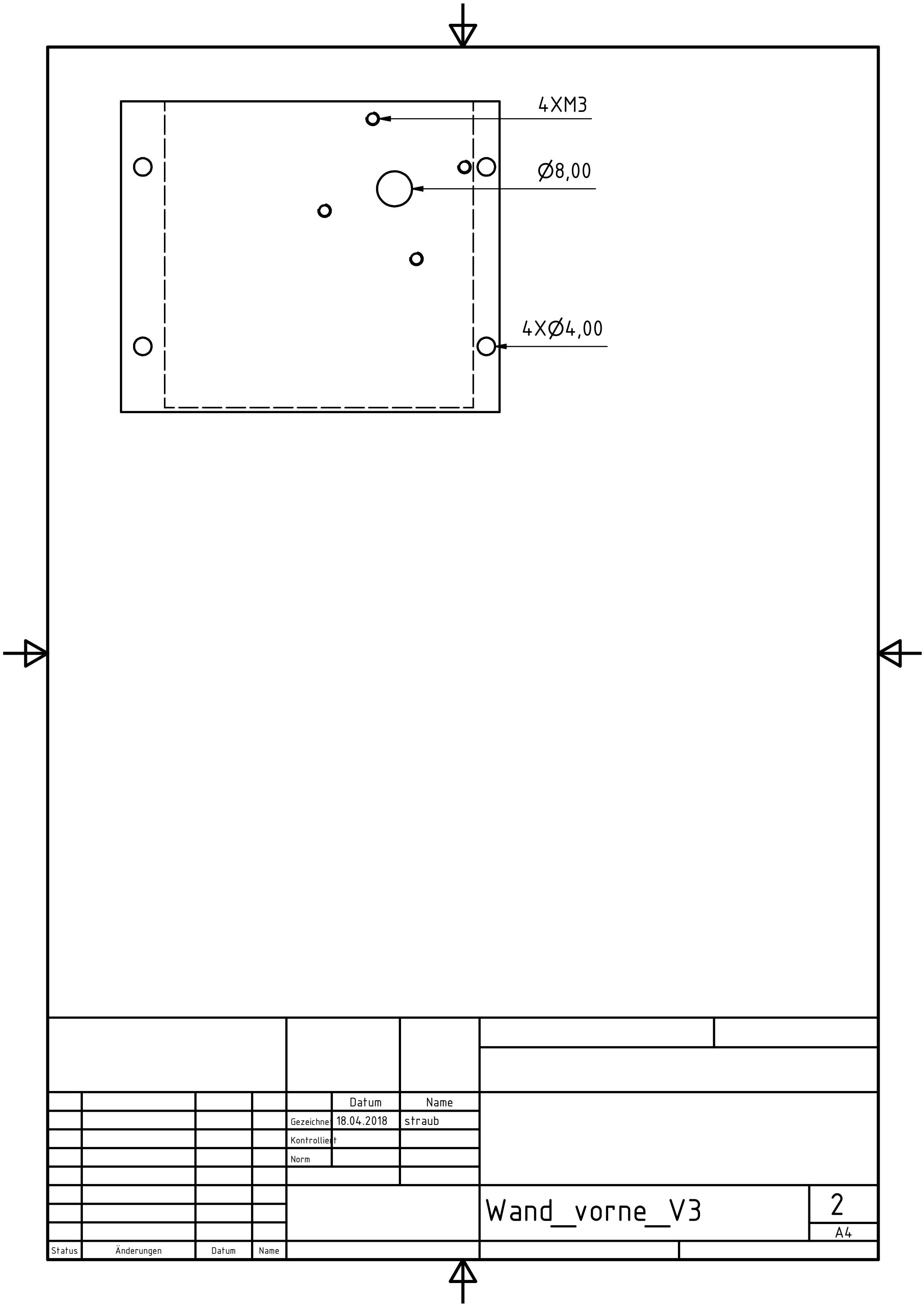

Figure A.16.: Scan cube B: Front wall; side 2

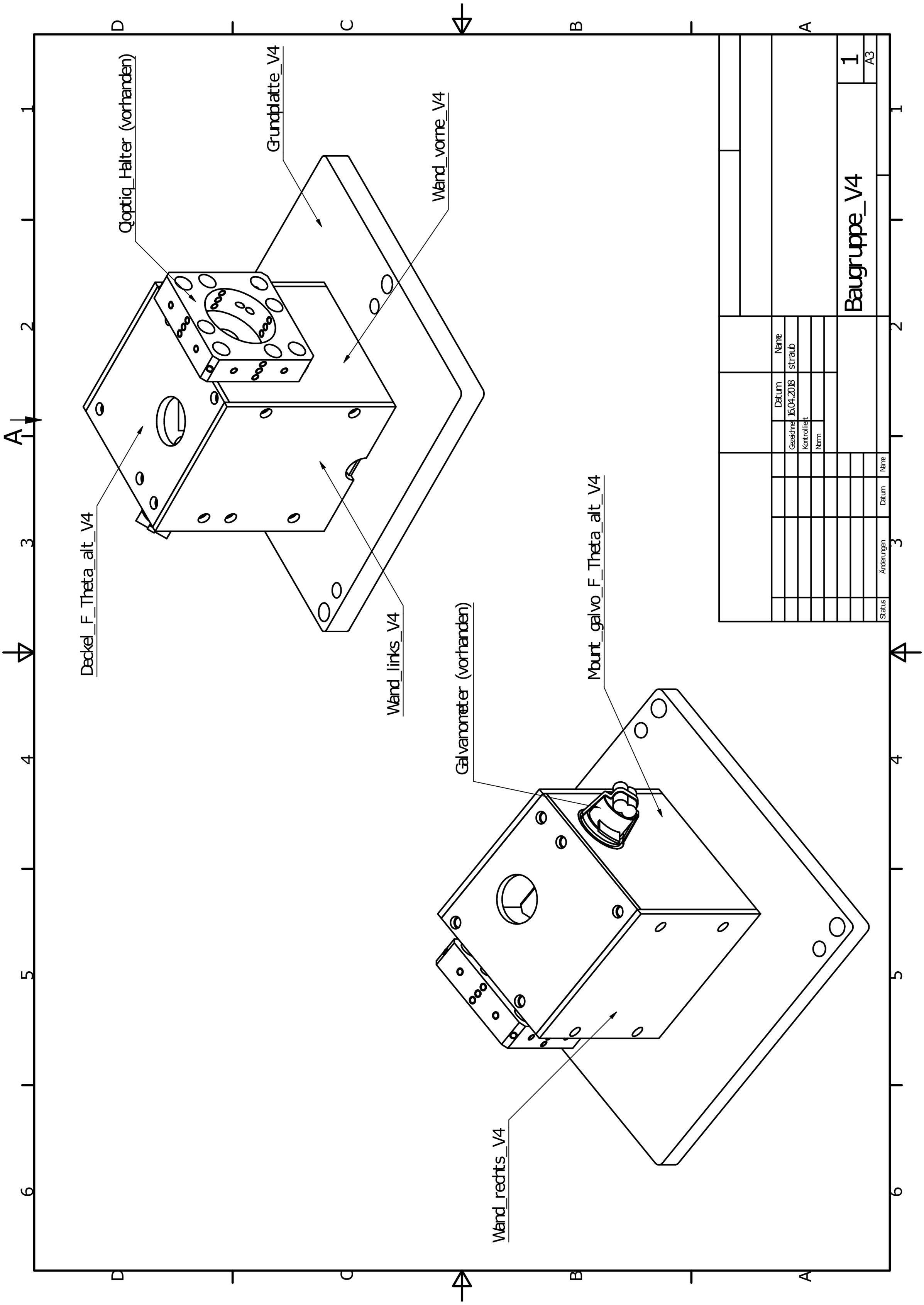

Figure A.17.: Assembly group of scan cube A

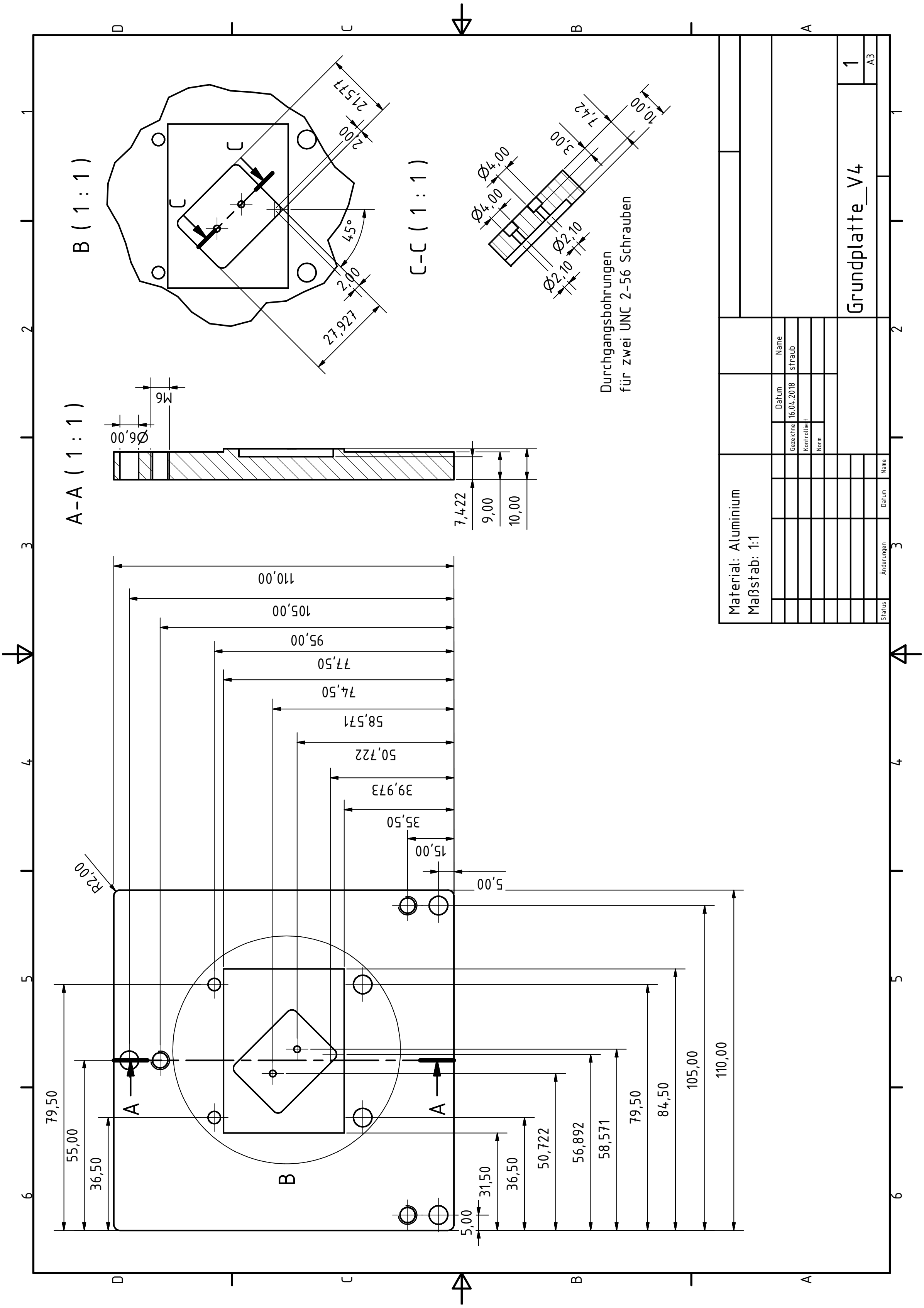

Figure A.18.: Scan cube A: Base plate; side 1

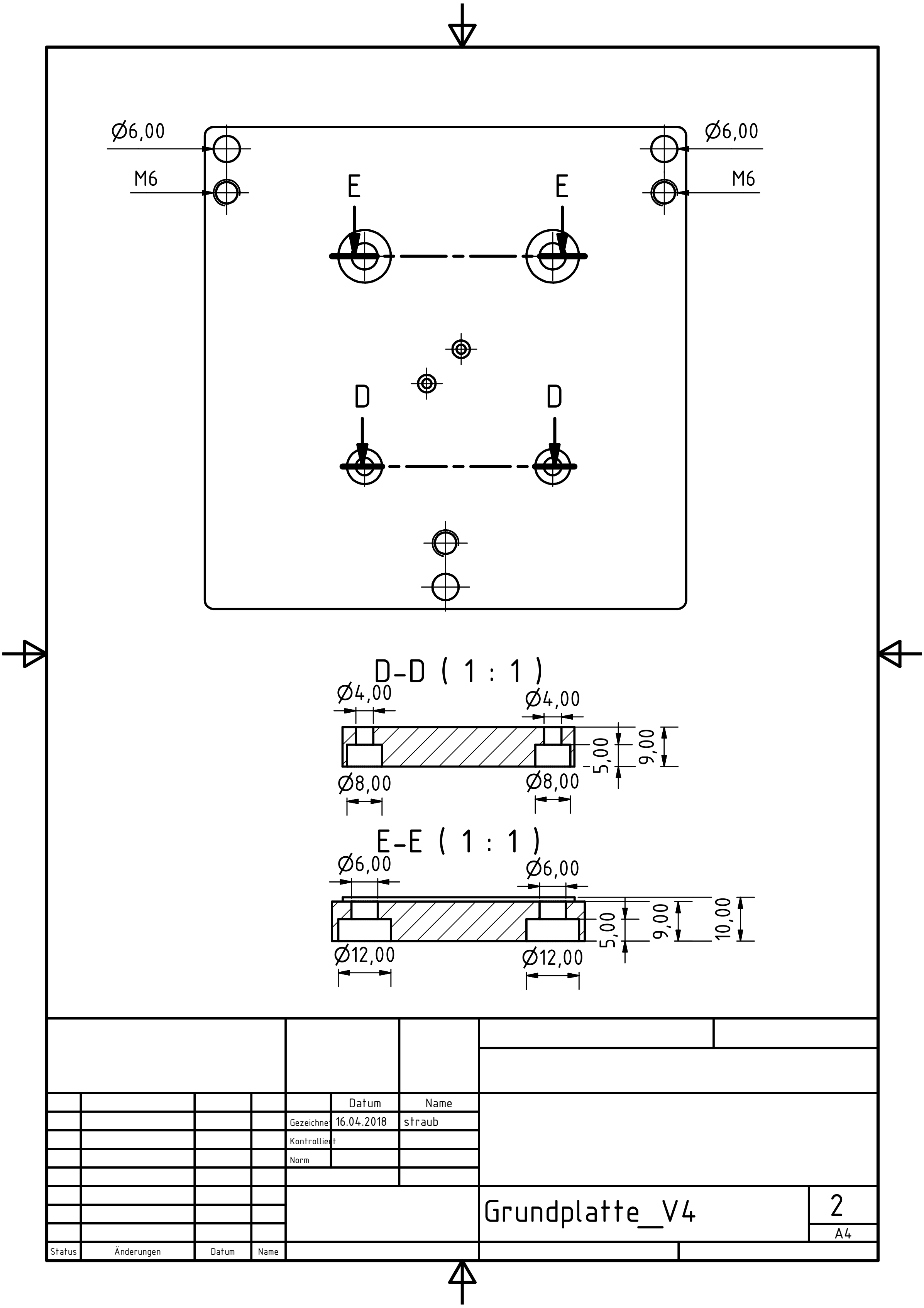

Figure A.19.: Scan cube A: Base plate; side 2

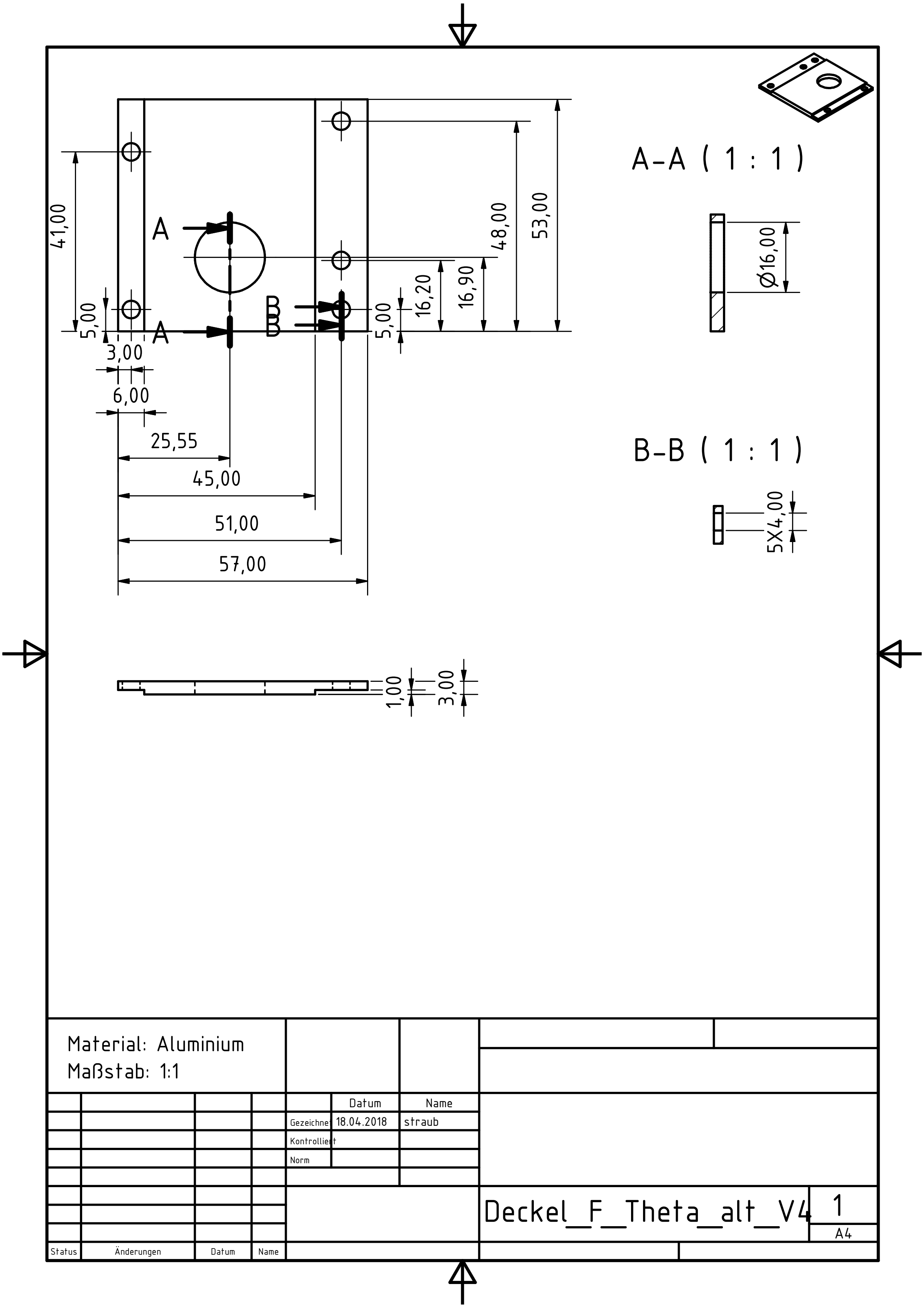

Material: Aluminium
Maßstab: 1:1

	Datum	Name
Gezeichnet	18.04.2018	straub
Kontrolliert		
Norm		

Deckel_F_Theta_alt_V4 1
A4

Figure A.20.: Scan cube A: Lid

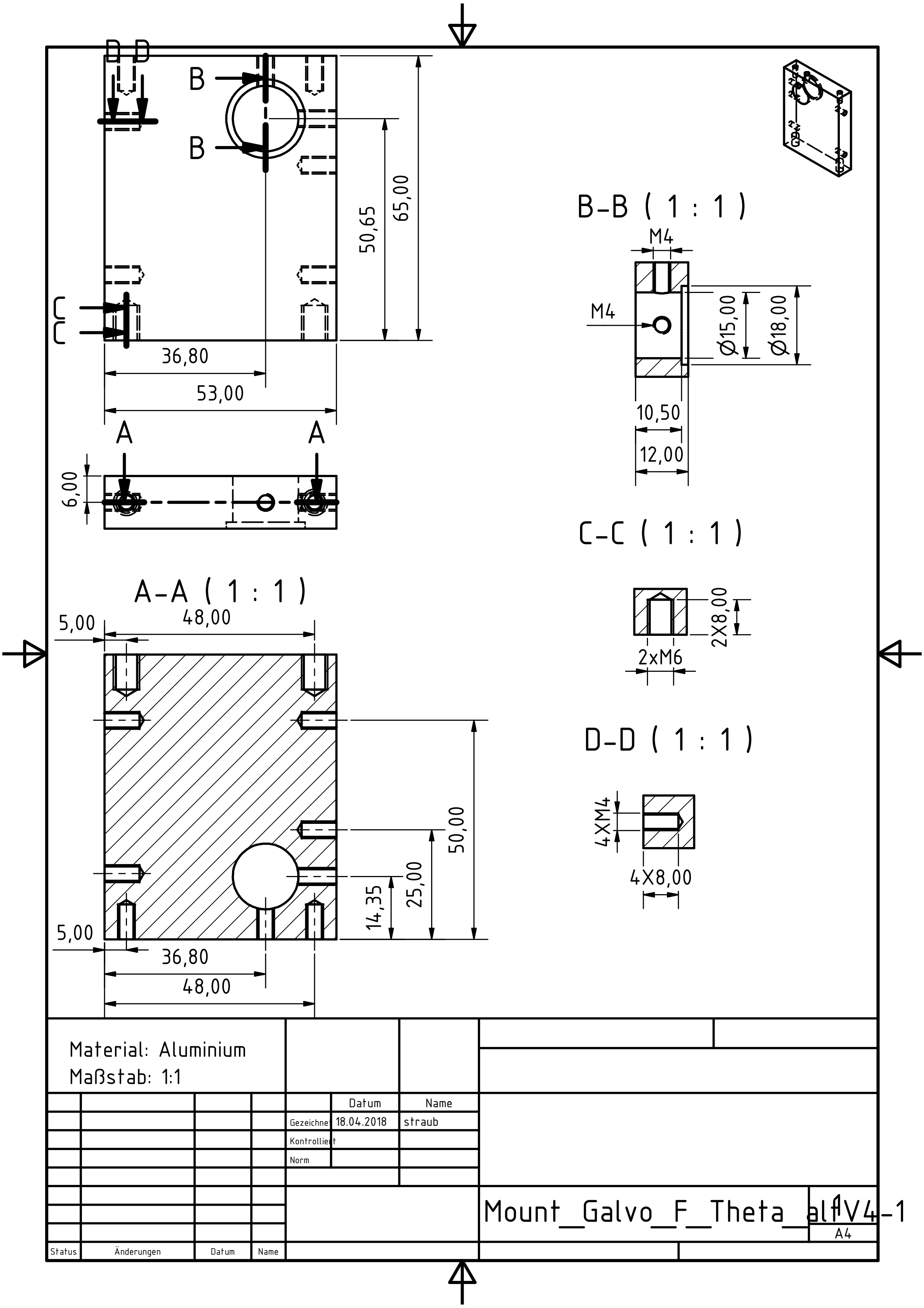

Figure A.21.: Scan cube A: Galvanometer scanner mount

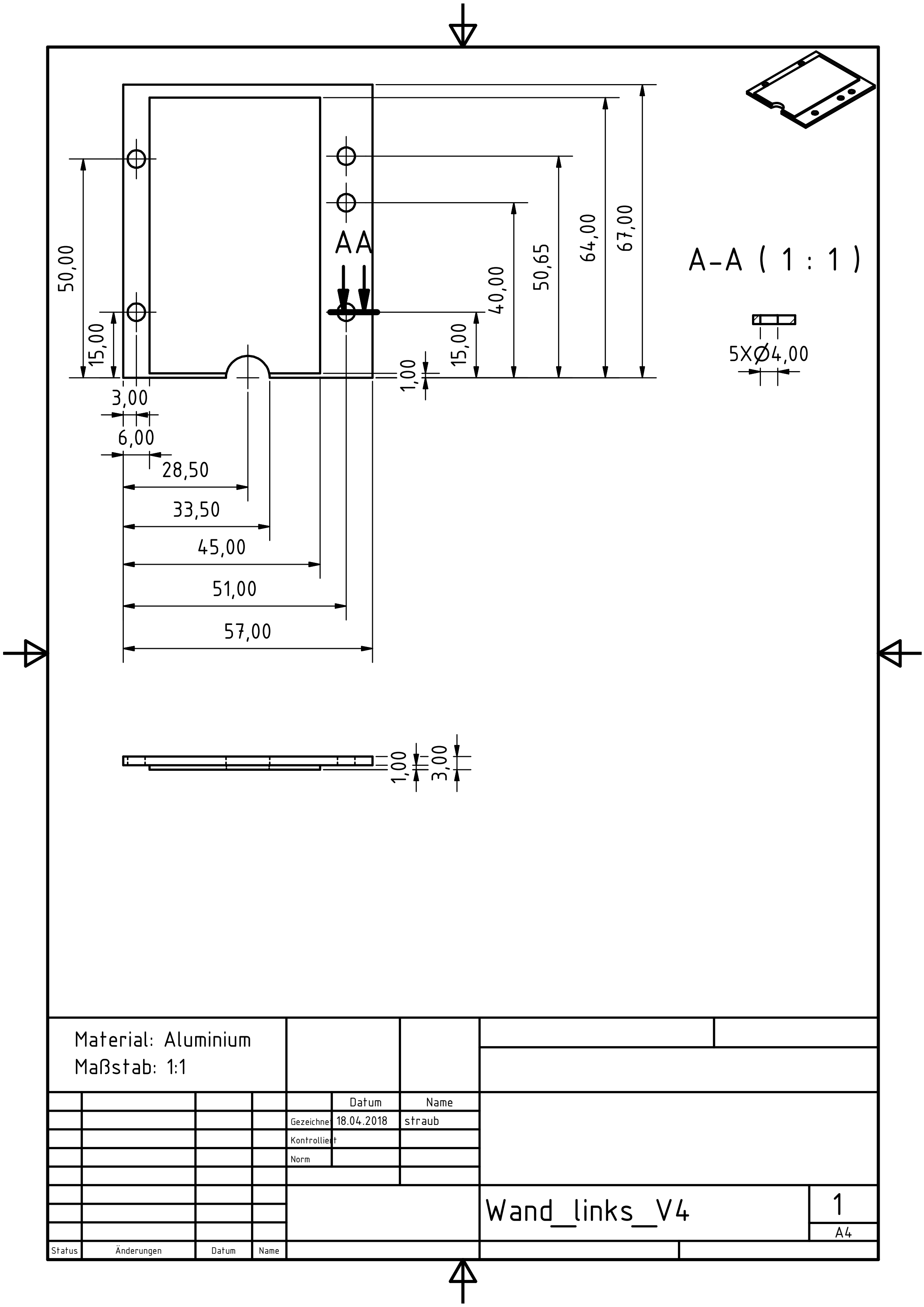

Figure A.22.: Scan cube A: Left wall

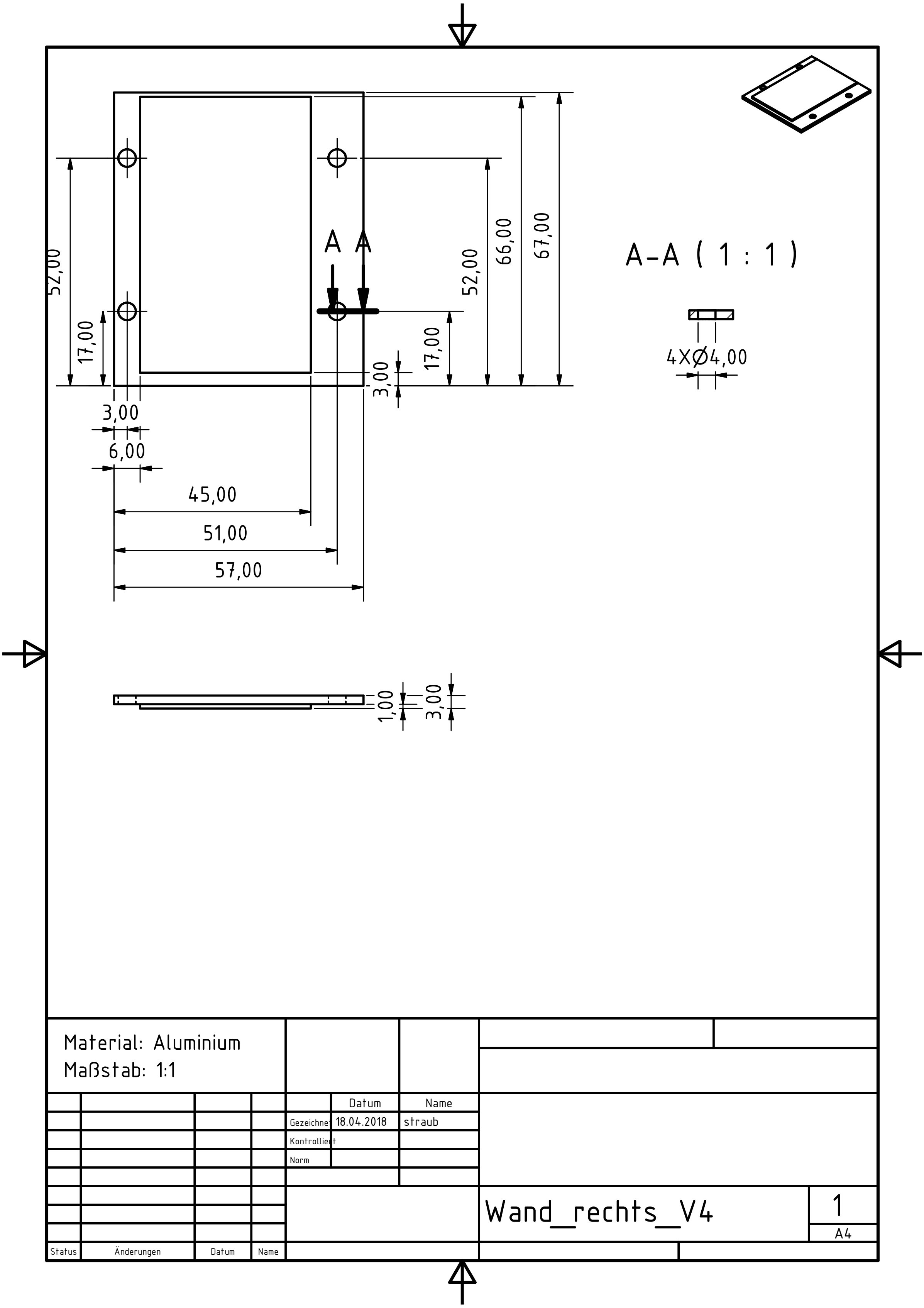

Material: Aluminium
Maßstab: 1:1

	Datum	Name
Gezeichnet	18.04.2018	straub
Kontrolliert		
Norm		

Wand_rechts_V4

1

A4

Status Änderungen Datum Name

Figure A.23.: Scan cube A: Right wall

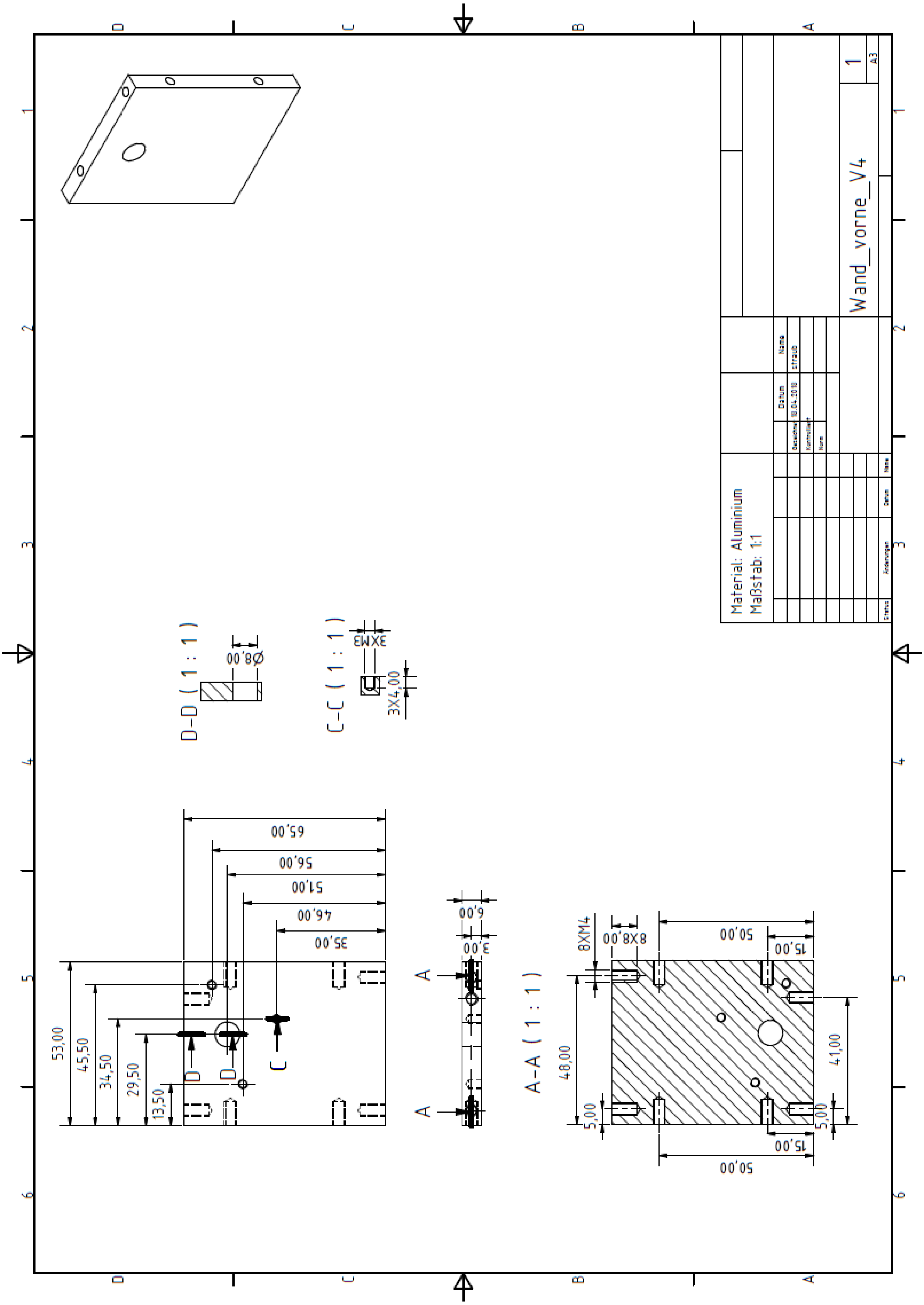

Figure A.24.: Scan cube A: Front wall